Gr/SiOx Blend Anode Lithiation: A Comprehensive Investigation of High-Energy Lithium-Ion Batteries

Von der Fakultät für Ingenieurwissenschaften
der Universität Bayreuth
zur Erlangung der Würde

Doktor-Ingenieur (Dr.-Ing.)

genehmigte Dissertation

von

Julian Knorr, M.Sc.

aus

Fürstenfeldbruck

Erstgutachter:	Prof. Dr.-Ing. Michael A. Danzer
Zweitgutachter:	Prof. Dr.-Ing. Jan Philipp Schmidt
Tag der mündlichen Prüfung:	17.10.2025

Lehrstuhl für Elektrische Energiesysteme

Universität Bayreuth

2025

Abstract

Battery electric vehicles have the potential to significantly reduce greenhouse gas emissions. However, numerous challenges remain to be addressed in order to achieve performance and comfort levels comparable to those of combustion engine powered vehicles, particularly in terms of driving range, recharge capability, and longevity. One of the primary requirements for battery electric vehicles is the provision of an adequate driving range. In order to satisfy this, it is necessary to integrate new active materials into lithium-ion batteries. The combination of electrodes comprising graphite and SiO_x represents one of the most promising options for anode materials. This type of electrode combines the high specific capacity of silicon with the structural stability and long lifetime of graphite. However, the combination of two active materials with disparate thermodynamic and kinetic properties introduces an increased complexity to the electrochemical behavior, which requires a comprehensive understanding to guarantee optimal functionality.

This thesis examines the lithiation behavior of Gr/SiO_x blend anodes with the aim of enhancing the performance of the battery cell. The objective is to ascertain the extent to which degree each of the active materials is lithiated throughout the entire charge and discharge process and to determine how the lithiation influences the cell voltage. To achieve this objective, multiple thermodynamic and kinetic effects are examined for cells containing Gr/SiO_x blend anodes.

In addition to the inherent differences in the working potentials of graphite and silicon, the hysteresis of silicon exerts a considerable influence on the thermodynamics of Gr/SiO_x blend anodes. Therefore, it is necessary to analyze the hysteresis effect to gain a deeper understanding of the lithiation behavior in blend anodes. Electrochemical tests at the electrode and cell levels demonstrate the voltage profile that occurs when transitioning from charging to discharging and vice versa during the cycling process. The hysteresis transition is found to be strongly dependent on the degree of lithiation of each active material. As only silicon exhibits a significant intrinsic hysteresis, the hysteresis transition is observed to pause while graphite is active. This results in the formation of a distinctive voltage profile, which is contingent upon the initial state of charge of the transition. An additional phenomenon that affects the lithiation behavior is the formation of crystalline silicon, which induces a memory effect in Gr/SiO_x blend anodes. Partial cycling of the cells without fully discharging them results in the trapping of lithium in the crystalline phase of silicon. As the reversion of this phase occurs at a different potential than the formation, this memory effect results in alterations to the voltage profile. This has an impact on the estimation of internal battery states and causes a reduction of the available energy of the partial cycles. The analysis of this phenomenon with varying parameters reveals an increasing trend with the partial cycle count and identifies a critical range for the state of charge.

A further significant aspect of this thesis is the investigation of the kinetic behavior in Gr/SiO_x blend anodes, with a particular focus on the effects of increased charge rates. In order to ascertain which material is preferably lithiated at elevated charging currents, two methodologies

are presented. The first method employs a non-destructive approach to identify alterations in the lithiation across a range of charge rates during the charging process to a specific state of charge. A qualitative determination of the graphite lithiation subsequent to a charge process up to 25 % state of charge is feasible by analyzing the dimensions of a particular graphite plateau within the voltage profile of the hysteresis transition. It can thus be concluded that SiO_x is preferably lithiated at increased charge rates, as evidenced by the observation of a smaller graphite plateau in the discharging voltage profile. This assumption is corroborated by X-ray diffraction analysis of the graphite lithiation. The second method enables direct measurements of the graphite and SiO_x lithiation throughout the entire charging and discharging process. An experimental setup is constructed, comprising a pure graphite and a pure SiO_x half-cell connected in parallel. The configuration permits direct measurement of the current ascribed to each material, thus enabling the determination of the lithiation distribution. An increase in the lithiation rate corroborates the findings of the first method and demonstrates an increased SiO_x lithiation throughout the entirety of the charging process.
The provided analysis enhances the comprehension of the thermodynamic and kinetic effects that influence the lithiation behavior of Gr/SiO_x anodes. This facilitates the integration in high-energy lithium-ion batteries with enhanced performance, whereby the internal state estimation of battery management systems is improved and the precision of electrochemical simulation modelling is optimized.

Kurzfassung

Batteriebetriebene Elektrofahrzeuge haben das Potenzial, den Ausstoß von Treibhausgasen erheblich zu verringern. Allerdings sind noch zahlreiche Herausforderungen zu bewältigen, um das gewohnte Performanz- und Komfortniveau von Fahrzeugen mit Verbrennungsmotor zu erreichen, insbesondere in Bezug auf Reichweite, Aufladefähigkeit und Langlebigkeit. Eine der wichtigsten Anforderungen an batteriebetriebene Elektrofahrzeuge ist die Bereitstellung einer ausreichenden Reichweite. Um diese Anforderung zu erfüllen, ist es notwendig, neue Aktivmaterialien in Lithium-Ionen-Batterien zu integrieren. Elektroden, bestehend aus einer Kombination von Graphit und SiO_x, stellen eine der vielversprechendsten Optionen für Anodenmaterialien dar. Dieser Elektrodentyp verbindet die hohe spezifische Kapazität von Silizium mit der strukturellen Stabilität und der langen Lebensdauer von Graphit. Die Verwendung zweier Aktivmaterialien mit unterschiedlichen thermodynamischen und kinetischen Eigenschaften führt jedoch zu einer erhöhten Komplexität des elektrochemischen Verhaltens, was ein umfassendes Verständnis erfordern, um eine optimale Funktionalität zu gewährleisten.

In dieser Arbeit wird das Lithiierungsverhalten von Gr/SiO_x Blendanoden untersucht, um die Performanz der Batteriezelle zu verbessern. Ziel ist es, festzustellen, in welchem Maße jedes der Aktivmaterialien während des gesamten Lade- und Entladevorgangs lithiiert wird und wie die Lithiierung die Zellspannung beeinflusst. Um dieses Ziel zu erreichen, werden verschiedene thermodynamische und kinetische Effekte an Zellen mit Gr/SiO_x Blendanoden untersucht.

Neben den Unterschieden in den Arbeitspotenzialen von Graphit und Silizium übt die Hysterese von Silizium einen erheblichen Einfluss auf die Thermodynamik von Gr/SiO_x Blendanoden aus. Daher ist es notwendig, den Hystereseeffekt zu analysieren, um ein tieferes Verständnis des Lithiierungsverhaltens in Blendanoden zu erlangen. Elektrochemische Tests auf Elektroden- und Zellebene zeigen das Spannungsprofil, welches während der Zyklisierung beim Übergang vom Laden zum Entladen und umgekehrt auftritt. Es wurde festgestellt, dass dieser Hystereseübergang stark vom Lithiierungsgrad der Aktivmaterialien abhängt. Da nur Silizium eine signifikante intrinsische Hysterese aufweist, konnte festgestellt werden, dass der Hystereseübergang pausiert, während Graphit aktiv ist. Dies führt zur Ausbildung eines veränderten Spannungsprofils, das vom ursprünglichen Ladungszustand des Übergangs abhängt. Ein weiteres Phänomen, welches sich auf das Lithiierungsverhalten auswirkt, ist die Bildung von kristallinem Silizium, das in Gr/SiO_x Blendanoden einen Memory-Effekt hervorruft. Teilzyklen ohne eine vollständige Entladung der Zellen führen zum Einschluss von Lithium in der kristallinen Phase des Siliziums. Da die Bildung dieser Phase bei einem anderen Potenzial als die Rückbildung erfolgt, führt dieser Memory-Effekt zu Veränderungen des Spannungsprofils. Dies hat Auswirkungen auf die Schätzung der internen Batteriezustände und führt zu einer Verringerung der verfügbaren Energie der Teilzyklen. Eine Variation der Testparameter zeigt einen zunehmenden Trend des Memory-Effekts mit steigender Anzahl der Teilzyklen und identifiziert einen kritischen

Ladezustandsbereich.
Ein weiterer wesentlicher Schwerpunkt dieser Arbeit ist die Untersuchung des kinetischen Verhaltens in Gr/SiO_x Blendanoden, mit besonderem Augenmerk auf die Auswirkungen erhöhter Laderaten. Um festzustellen, welches Material bei erhöhten Ladeströmen bevorzugt lithiiert wird, werden zwei Methoden vorgestellt. Die erste Methode verwendet einen zerstörungsfreien Ansatz, um Veränderungen der Lithiierung bis zu einem bestimmten Ladezustand bei unterschiedlichen Ladeströmen zu ermitteln. Eine qualitative Bestimmung der Graphitlithiierung nach einem Ladevorgang bis zu 25 % Ladezustand ist durch die Analyse der Ausprägung eines bestimmten Graphitplateaus innerhalb des Spannungsprofils des Hystereseübergangs möglich. Daraus lässt sich schließen, dass SiO_x vorzugsweise bei höheren Laderaten lithiiert wird, was durch die Beobachtung eines kleineren Graphitplateaus im Entladespannungsprofil belegt wird. Diese Aussage wird durch die Röntgendiffraktionanalyse der Graphitlithiierung bestätigt. Die zweite Methode ermöglicht direkte Messungen der Graphit- und SiO_x-Lithiierung während des gesamten Lade- und Entladevorgangs. Es wird ein Versuchsaufbau verwendet, der eine Halbzelle aus reinem Graphit und eine Halbzelle aus reinem SiO_x beinhaltet, welche parallel verschaltet sind. Die Konfiguration ermöglicht die direkte Messung des Stroms, der jedem Material zugeordneten ist, und erlaubt so die Bestimmung der Lithiierungsverteilung. Das Erhöhen der Lithiierungsrate bestätigt die Ergebnisse der ersten Methode und zeigt eine verstärkte SiO_x-Lithiierung während des gesamten Ladevorgangs.
Die durchgeführten Untersuchungen verbessern das Verständnis der thermodynamischen und kinetischen Effekte, die das Lithiierungsverhalten von Gr/SiO_x Blendanoden beeinflussen. Dies erleichtert die Integration in hochenergetische Lithium-Ionen-Batterien mit verbesserter Performanz, wodurch die interne Zustandsschätzung von Batteriemanagementsystemen und die Genauigkeit der elektrochemischen Simulationsmodellierung optimiert wird.

Acknowledgements

This dissertation summarizes the research I carried out during three years of my doctoral studies at the BMW Group in collaboration with the Chair of Electrical Energy Systems at the University of Bayreuth. I am deeply grateful for the opportunity to conduct my work in an innovation-driven company, complemented by the strong academic support of a leading university.

First and foremost, I would like to express my sincere gratitude to Prof. Dr.-Ing. Michael A. Danzer for his invaluable academic supervision. His prompt and insightful feedback was instrumental in advancing this work and provided continuous guidance throughout my doctoral journey. I am also thankful to Prof. Dr.-Ing. Jan Philipp Schmidt for kindly serving as the second reviewer of this thesis.

My heartfelt appreciation goes to Dr. rer. nat. Barbara Rödl at BMW for her unwavering support and regular exchange of ideas. Her openness and encouragement allowed me to pursue every research initiative that came to mind. I am equally grateful to Dr.-Ing. Alexander Adam and Lukas Maul, who, without formal obligation, generously acted as co-mentors and were always available for insightful technical discussions.

I would also like to acknowledge my numerous colleagues across various BMW departments, the vibrant BMW doctoral network spanning diverse fields of research, and the team at the University of Bayreuth. Their collaboration and positive spirit created an inspiring environment that made research both productive and enjoyable.

Finally, I owe profound gratitude to my family and friends for their constant encouragement and belief in my goals. Their support and motivation were essential in completing this dissertation.

Contents

List of Abbreviations

Abbreviation	Decription
a	amorphous
BEV	Battery electric vehicle
BMS	Battery management system
BoL	Begin of life
c	crystalline
CE	Coulombic efficiency
CEI	Cathode electrolyte interface
C-rate	(Dis-)Charge rate
DFN	Doyle-Fuller-Newman
DMC	Dimethyl carbonate
EC	Ethylene carbonate
ECM	Equivalent circuit model
EMC	Ethyl methyl carbonate
EoL	End of life
FEC	Fluoroethylene carbonate
Gr	Graphite
HOMO	Highest occupied molecular orbial
ICEV	Internal combustion engine powered vehicle
LAM	Loss of active material
LCO	Lithium cobalt oxide
LE	Loss of electrolyte
LFP	Lithium iron phosphate
Li	Lithium

Abbreviation	Decription
LIB	Lithium-ion battery
LiD	Lithium deposition
LLI	Loss of lithium inventory
LMR	Lithium-manganese-rich
LUMO	Lowest unoccupied molecular orbial
NCA	Lithium nickel cobalt aluminium oxide
NMC	Lithium nickel manganese cobalt oxide
NMR	Nuclear magnetic resonance
OCP	Open-circuit potential (electrode level)
OCV	Open-circuit voltage (full-cell level)
p2D	Pseudo two-dimensional
PC	Propylene carbonate
PE	Polyethylene
PP	Polypropylene
PVDF	Polyvinylidene fluoride
SEI	Solid electrolyte interface
SEM	Scanning electron microscopy
Si	Silicon
SiC	Silicon embedded in carbon matrix
SiO_x	Silicon oxide
SoC	State of charge (full-cell level)
SoH	State of health
SoL	State of lithiation (electrode level)
SSE	Solid-state electrolyte
TEM	Transmission electron microscopy
TMO	Transition metal oxide
XRD	X-ray diffraction

List of symbols

Symbol	Description	Unit
F	Faraday constant	A s mol
i	Instantaneous current density	A/m^2
i_0	Exchange current density	A/m^2
I_{cell}	Current of the full cell	A
M	Variable metal or metalloid	-
n	Number of electrons	-
Q	Capacity	A h
Q_{ref}	Reference capacity	A h
$Q_{ref,BoL}$	Reference capacity at begin of life condition	A h
R	Internal cell resistance	Ω
R_{BoL}	Internal cell resistance at begin of life condition	Ω
R_G	Universal gas constant	Ω
SoC	State of charge	%
SoH_Q	State of health regarding the capacity	%
SoH_R	State of health regarding the resistance	%
T	Absolute temperature	K
U_{cell}	Cell voltage	V
U_{OCV}	Open-circuit voltage	V
x	Amount of oxygen in SiOx ($0 \leq x \leq 2$)	-
α_a	Anodic current coefficient	-
α_c	Cathodic current coefficient	-

δ	Index number of overlithiated phase	-
η	Overpotential	V
η_j	Local surface overpotential	V
σ_e	Electronic conductivity	S/cm
σ_{Li}	Li-ion conductivity	S/cm
Φ_{An}	Anode potential	V
$\Phi_{An,OCP}$	Anode open-circuit potential	V
Φ_{Ca}	Cathode potential	V
$\Phi_{Ca,OCP}$	Cathode open-circuit potential	V

1 Introduction and context

Battery electric vehicles (BEVs) have become a significant component of the automotive market. In the forerunner country Norway, 96.4 % of new car registrations were purely electric in September 2024 and it is anticipated that this number will reach 100 % in 2025 [1]. Although the initial motivation for the incorporation of BEVs was the reduction of CO_2 emissions, drivers are increasingly appreciating the comprehensive performance capabilities that these vehicles possess. The instant availability of the maximum torque during acceleration, the low cost of recharging, the quiet driving experience, and energy recuperation during braking are among the key advantages of BEVs. Nevertheless, numerous challenges must yet be overcome for BEVs to achieve wide acceptance and to be able to compete with internal combustion engine powered vehicles (ICEVs) in most regions of the world. In addition to the aforementioned advantages of electric vehicles, customers also expect a satisfactory performance and driving experience from their electric vehicles. The most significant factors influencing the adoption of electric vehicles are cost reduction, an extended driving range to mitigate range anxiety, a reduced fast-charging duration with a sufficient fast-charging infrastructure, and an extended battery lifespan [2–5]. For those without prior experience of driving a BEV, a sufficient driving range presents a significant factor, whereas for those who are more familiar with BEVs, a short fast-charge duration with good infrastructure availability is of greater relevance [2]. With the exception of the fast-charging infrastructure, which is still found to be insufficient for 40–60 % of customers [6], these performance factors directly address the high-voltage battery pack and especially the battery cells, with the objective of overcoming the existing challenges. Consequently, high-performance battery cells require a high energy density for an increased driving range and a high power density to enable a short fast-charging duration. In addition to the satisfactory attributes of the battery cells, a high-performance battery system also ensures an exact estimation of the remaining driving range and the maximum available capacity throughout the battery's entire lifespan.
Lithium-ion batteries (LIBs) currently represent the dominant technology in the BEV market, primarily due to their high specific energy density >150 Wh/kg in comparison to other battery technologies, such as lead-acid and nickel-metal hydride batteries [7]. However, the selection of the most suitable components for a LIB remains a topic of ongoing research and debate. In general, the design of a battery cell inherently involves a trade-off between competing design parameters, whereby the enhancement of one parameter inevitably results in the impairment of one or multiple other parameters. It is therefore evident that the ideal battery cell remains unattainable the time being, and that considerations must be made in accordance with the requirements of the intended application. The most prevalent trade-off

between providing a high energy density and a high power density involves precisely the two primary customer requirements. Enhancing the driving range is accompanied by an extended charging time and conversely, whereas enhancing the fast-charging capability diminishes the driving range, provided that the remaining design parameters are maintained. A comparison of several design parameters is provided in Fig. 1.1 for an energy density and a power density focused design.

As a sufficient driving range is a major entry barrier for hesitant BEV customers, preferably above 400 miles [8], car manufacturers are focusing their efforts on developing vehicles with high battery capacity without a significant increase in the fast-charging duration. While a high amount of nickel in the positive electrode provides a high energy density, the use of silicon (Si) in the negative electrode fulfills the same objective. With 3579 Ah/g, the specific capacity of silicon is approximately ten times that of the standard material, graphite (Gr) [9–12]. Therefore, further research is required to enhance understanding of silicon as an active material and facilitate its use in high-energy LIBs for peak performance. Ultimately, this will increase the driving range of BEVs, improve the acceptance of BEVs, and reduce global emissions.

Although pure silicon offers one of the highest specific capacities among potential active anode materials, it is challenging to produce stable electrodes with a long lifespan. This is attributed to the significant volume expansion that silicon experiences during the cycling process, which can lead to pulverization, particle cracking, and a loss of electrical contact [13–16]. These negative side effects collectively diminish the available capacity, thereby counteracting the primary advantage of silicon. To utilize the high specific capacity of silicon while maintaining a long lifetime, variations of the silicon material or a combination of graphite and silicon are often employed.

This work focuses on a particular type of electrode, namely a Gr/silicon oxide (SiO_x) blend anode, which employs a combination of graphite and SiO_x. The primary active material, graphite, accounts for the majority of the capacity and provides structural stability and high conductivity for the electrode [17; 18]. The incorporation of a small quantity of SiO_x into the electrode can be regarded as a capacity boost to the total capacity, while the volume expansion remains controllable by the surrounding graphite. The combination of silicon and oxygen results in a reduction of the specific capacity and a reduced initial efficiency compared to that of pure silicon, yet it exhibits a less pronounced degradation [19–21].

Given the disparate thermodynamic and kinetic characteristics of the two active materials, graphite and SiO_x, the lithium (Li) storage and extraction is more complex than in electrodes comprising a single active material. The objective of this work is to gain a deeper understanding of the thermodynamic and kinetic effects on the lithiation behavior in Gr/SiO_x blend electrodes. Consequently, the performance of high-energy LIBs can be enhanced by optimizing the functions of the battery management system (BMS) and the precision of electrochemical simulation models.

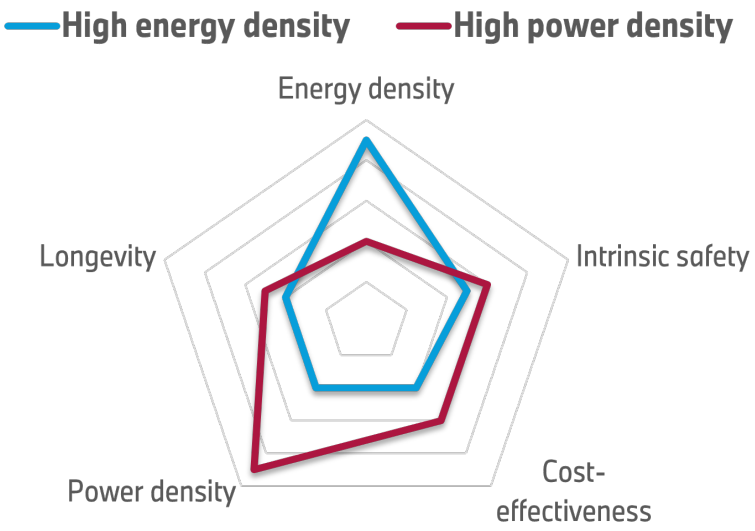

Figure 1.1: Qualitative comparison of various parameters of LIBs for a high energy density design (blue) and a high power density design (red) [22–25].

1.1 Context of electrochemical energy storage

In order to understand the distinctive lithiation behavior of Gr/SiO_x blend anodes, it is essential to elucidate the fundamental principles that govern lithium-ion batteries. This section provides a comprehensive overview of the components and the operating principles of a LIB. Moreover, the advantages and disadvantages of different cell formats are presented, and the various degradation processes are described.

1.1.1 Components of a lithium-ion battery

This section outlines the distinctive characteristics of the different components that comprise a LIB. These include the two electrodes (anode and cathode) that facilitate lithium storage, the separator that ensures electrical isolation, the electrolyte that enables lithium-ion transfer between the electrodes, and the current collector that establishes electrical contact.

Anode

The definition of the anode used in battery research deviates from the accepted electrochemical definition. The term “anode” refers to the electrode where the oxidation reaction occurs and electrons are emitted. In the context of battery cells, however, the term “anode” is consistently used to refer to the negative electrode, irrespective of whether the oxidation or reduction reaction is occurring. Therefore, the anode is the electrode that stores Li-ions in a fully charged state and exerts an influence on the rate capability, energy density, cycle

lifetime, and the power density of a LIB [26; 27]. An ideal anode must meet several criteria. These include a high reversible gravimetric and volumetric capacity, a low potential against the cathode material, a high rate capability, a long cycle life, excellent abuse tolerance, low cost, and environmental compatibility [28].

Lithium metal anode Regarding the energy density as one of the most significant requirements, particularly in the context of BEVs [27], the optimal anode is a pure lithium metal anode devoid of any additional active material. This type of anode not only provides the highest possible specific capacity of 3862 mAh/g [27–29], but also the lowest possible anode potential of 0 V vs. Li/Li^+ [28]. Any active material with a lower working potential than this threshold would result in the deposition of metallic lithium on the surface of the anode particle, similar to the working principle of the lithium metal anodes. During charging, additional lithium deposits on the surface of the lithium metal anode, which is stripped back during discharging. However, this also presents one of the primary disadvantages associated with this anode type. The constant lithium deposition and stripping results in significant volume changes, which lead to an increased internal cell pressure and the potential cracking of the electrode or the passivation layer surrounding the anode [28]. Furthermore, lithium deposition must not occur in a homogeneous manner, as this can result in the growth of lithium dendrites. In the worst case, these dendrites have the potential to cause internal short circuits if their growth reaches the cathode and electrical contact is created [28; 30].

Intercalation anode materials The most prevalent anode material in current use is graphite, which belongs to the class of carbon-based anode materials [26–28; 31]. In addition to graphite, this class contains graphene and non-graphitic hard carbon [32]. Through an intercalation process, graphite is capable of storing Li-ions in its crystalline structure between the hexagonal graphene layers. In order to store a single Li-ion, a total of six carbon atoms are required, which results in the low theoretical specific capacity of 372 mAh/g [13; 33–36]. The intercalation process to obtain fully lithiated graphite can be described as follows:

$$6\,C + Li^+ + e^- \underset{\text{Discharging}}{\overset{\text{Charging}}{\rightleftharpoons}} LiC_6 \tag{1.1}$$

Despite the relatively low specific capacity of graphite, its numerous advantages justify the common use. With an average potential of ~100 mV, graphite has one of the lowest potentials versus lithium [27; 37], which increases the overall cell voltage and consequently the energy density. Moreover, graphite offers comprehensive safety features [27], excellent electronic conductivity [14; 17; 18; 27; 32], and high structural stability due to its minimal volume expansion of ~10 % [18]. Additionally, graphite exhibits an enhanced lifetime due to minimal degradation [14; 21; 27] and a low cost, which results from the widespread availability [14; 27; 30; 32]. However, the low potential vs. Li/Li^+ presents a risk of lithium deposition if the anode potential drops below 0 V. Consequently, the same risk of an electrical short circuit

exists as with lithium metal anodes, where dendrite growth may occur [27; 32].

A second category of intercalation active materials are titanium-based materials, including lithium titanate ($Li_4Ti_5O_{12}$) and titanium dioxide (TiO_2). This type of anode exhibits a lower specific capacity than graphite, with a value of 175–330 mAh/g [28; 30] and an anode potential above 800 mV vs. Li/Li^+ [28]. Nevertheless, it is employed in applications that require extreme safety standards, such as those in the military and aviation industries [26; 27]. Additionally, titaneous anodes demonstrate an excellent cycle life [27; 28], low cost [28], low toxicity [27; 28], and high power density [28]. Furthermore, the volume expansion of titaneous anodes is even less than that of graphite, with a mere 2–3 %. Besides the low energy density, the only major disadvantage is the low electronic conductivity [27; 28; 30; 31].

Alloy anode materials The most promising class of anode materials is that of alloys, which contain metals and semimetals from the groups *IV* and *V* of the periodic table [30]. Due to their high theoretical specific capacity, these materials are able to meet the needs of increased energy density, particularly in the context of BEVs [27]. Potential alloy materials include aluminum, tin, zinc, germanium, phosphor, and magnesium [27; 28; 30–32]. The theoretical specific capacity is in the range of 400–2300 mAh/g, which is significantly higher than that of graphite [27; 32]. In their fully lithiated state, zinc reaches 409 mAh/g (LiZn) [27], tin reaches 994 mAh/g ($Li_{4.4}Sn$) [26; 27], germanium reaches 1624 mAh/g ($Li_{4.4}Ge$) [27], and magnesium reaches 3350 mAh/g (Li_3Mg) [38]. Furthermore, alloys offer the additional benefit of good processing quality [32]. Nevertheless, despite their high specific capacity, alloys possess numerous disadvantages. The primary disadvantage is the considerable volume change that occurs during the charging process. The volume expansion ranges from 96 % for aluminum to 260 % for tin [38]. Consequently, structural issues emerge, resulting in an unstable passivation layer and, ultimately, a capacity loss [9; 13; 28; 32]. Additionally, alloy anode materials exhibit poor electrical conductivity and a low diffusion rate [27; 32]. The average anode potential is below 1 V vs. Li/Li^+ (e.g. Sn = 0.6 V and P = 0.9 V), which is higher compared to that of graphite and reduces the energy density. However, this also reduces the risk of lithium deposition and the related safety concerns [27; 28; 32].
The most relevant alloy material, that has not yet been mentioned, is silicon. With a theoretical capacity of 3579 mAh/g at room temperature ($Li_{15}Si_4$) and 4200 mAh/g at 415 °C ($Li_{22}Si_5$) [14; 39–41] in combination with a volume expansion of ~280 % ($Li_{15}Si_4$) [20; 42–44], both the advantage and disadvantages exceed any other alloy material. Given that it is the second most abundant element in the Earth's crust [13; 26; 45], it is a low-cost anode material option [9; 46] with a specific capacity that is close to that of pure lithium metal. Nevertheless, the considerable volume expansion, coupled with the relatively low electrical conductivity of $\sim 1 \cdot 10^{-3}$ S/m [9] and a substantial voltage hysteresis of ~300 mV [47], presents significant challenges to the integration of silicon as an anode material.
In order to offset the considerable increase in volume and mitigate the accompanying nega-

tive consequences, several electrode design methods have been investigated for silicon. The substitution of nanostructure for mirco-Si particles does not directly offset the volume expansion. Nevertheless, the use of silicon nanoparticles, nanowires, nanotubes, or nanoporous networks can withstand the volume expansion due to their reduced dimensions [14; 16; 48–50]. The risk of pulverization and cracking is markedly reduced when the structure size is below 150 nm [49; 51]. Furthermore, the lithium diffusion is enhanced within the silicon nanostructures due to the reduction in transmission path length [16]. An alternative approach involves the combination of silicon with additional materials, which serve to compensate for the volume expansion but simultaneously reduce the theoretical specific capacity. This group comprises SiO_x and silicon embedded in a carbon matrix (SiC). The quantity of oxygen (x) in SiO_x is within the range of $0 > x > 2$ [29; 47; 52]. Accordingly, the specific capacity is dependent on the amount of oxygen, as detailed in Section 1.2.3. A frequently reported value for the actual reversible capacity of SiO_x is ~1400 mAh/g [46; 53; 54], which is also used for calculations presented in this work. The formation process results in the generation of Li-silicates and Li_2O as irreversible side products [19; 21; 49; 55]. These side products surround the remaining pure silicon and function as a buffer against the volume expansion, reducing it to ~160 % [20; 21]. However, this results in a substantial reduction in the initial coulombic efficiency (CE) [20; 21]. Additionally, the Li_2O acts as a lithium diffusion channel, thereby enhancing the rate capability of SiO_x [21]. The carbon matrix surrounding the pure silicon in SiC produces a comparable effect to that of the oxygen in SiO_x, as it creates void spaces to accommodate the volume expansion [14; 56]. Furthermore, it enhances electronic conductivity and improves the cycle life [21; 37; 56]. An alternative method, which is becoming increasingly prevalent in commercial applications, is to combine one of the aforementioned silicon species with graphite particles in order to exploit the advantages of both active materials. The so-called blend electrode benefits from the high structural integrity, the good electronic conductivity, and the buffer against volume expansion that is provided by graphite [39; 46; 50; 57; 58]. Concurrently, even minor quantities of silicon-based materials enhance the specific capacity of the blend electrode and mitigate the proclivity for lithium deposition, due to the overall higher anode potential of silicon [16; 36; 46; 50; 58].

Transition metal oxides Transition metal oxides (TMOs) are the third major class of anode materials and are part of conversion-type transition-metal compounds, which also contain transition metal phosphides, nitrides, and selenides [27; 28; 32]. In TMOs, lithium is stored and extracted according to the following equation [28]:

$$\mathrm{M}_x\mathrm{O}_y + 2y\,\mathrm{Li}^+ + 2y\,\mathrm{e}^- \underset{\text{Discharging}}{\overset{\text{Charging}}{\rightleftharpoons}} y\,\mathrm{Li}_2\mathrm{O} + x\,\mathrm{M} \tag{1.2}$$

The variable integers x and y change according to the specific metal M. The advantages and disadvantages of TMOs are comparable to those of the alloy materials. TMOs exhibit a substantial enhancement in the specific capacity relative to graphite, with values ranging

from 500 to 1200 mAh/g [27; 28; 30]. For instance, Fe_3O_4 exhibits a specific capacity of ~926 mAh/g [30; 32]. Moreover, TMOs have a very low productions cost, making this class of anode materials highly profitable [30; 32]. Nevertheless, the disadvantages include poor electronic and ionic conductivity [30; 32], a large volume expansion in the fully charged state (<200 %), which results in an unstable passivation layer and electrode pulverization [28; 30], poor rate performance [32], and an extreme potential hysteresis of several hundred to 2 V [27; 32]. This hysteresis markedly diminishes the discharge voltage, which has a negative impact on the energy density.
The principal advantages and disadvantages of the three anode material classes are presented in Table 1.1.

Table 1.1: Benefits and limitations of active anode materials, including graphite, alloy materials, and transition metal oxides.

Anode material	**Benefits**	**Limitations**
Graphite	(1) Low anode potential (< 0.2 V)	(1) Low specific capacity (372 mAh/g)
	(2) High structural integrity	(2) High risk of lithium deposition
	(3) High electronic conductivity	
Alloys	(1) Very high specific capacity (400–3579 mAh/g)	(1) Large volume expansion (up to 280 %)
	(2) Reduced risk of lithium deposition	(2) Increased cell degradation and reduced lifetime
	(3) Partially inexpensive (e.g. Si)	(3) Low electronic conductivity
Transition metal oxides	(1) High specific capacity (500–1200 mAh/g)	(1) Large voltage hysteresis (up to 2 V)
	(2) Low cost	(2) Low coulombic efficiency
		(3) Increased cell degradation and reduced lifetime

Solid electrolyte interface The aforementioned passivation layer plays a pivotal role in the functioning of the anode. Electrolyte decomposition occurs at the interphase between the anode surface and the electrolyte when the anode potential drops below the stability window of the electrolyte [14; 52; 59; 60]. Given that this threshold is reached at 1 V vs. Li/Li^+ for the majority of electrolytes utilized in LIBs, this decomposition occurs for all pertinent anode materials [14; 60; 61]. The consequence of this decomposition is the formation of the passivation layer, which is typically referred to as the solid electrolyte interface (SEI) and covers the entirety of the anode particle surface. The SEI comprises a variety of organic and inorganic components, including Li_2CO_3 and lithium alkyl carbonates. A detailed overview of possible SEI components is provided by An et al. [60]. The SEI is formed during the initial charge process, when Li-ions are transferred from the cathode to the anode for the first time,

thereby enabling direct anode-electrolyte contact. This process is consequently also referred to as the formation of the battery cell and is responsible for the initial capacity loss, which is irreversibly stored in the SEI [14; 60]. To prevent further SEI formation in the subsequent cycles, the SEI must exhibit substantial electronic insulation [14; 60]. However, in order to permit further Li-ion transfer, the SEI must exhibit high ionic conductivity [52; 60; 61].

Cathode

In the context of battery cells, the positive electrode is referred to as the cathode. In order to achieve a high cell voltage and consequently a high energy density, an ideal cathode must provide a high operating potential vs. Li/Li^+. In addition to this characteristic, the same requirements apply to cathodes as previously outlined for anodes. As the raw anode materials lack lithium, the cathode serves as the initial source of lithium [31]. The active material of cathodes is typically composed of lithium transition metal oxides and exhibits either a layered, spinel, or olivine structure. [26; 62; 63].

Layered transition metal oxides The most prominent class of cathode materials are layered TMOs. The chemical composition of this class can be described as $LiMO_2$, with M representing a transition metal or the combination of several transition metals (M = Co, Ni, Mn, Al, ...). The proportion of all transition metals is equal to one. Similar to the anode material graphite, the TMOs also form layers in between which lithium is stored in a one-atom-thick layer. This enables two dimensional lithium diffusion [62; 63].
In 1991, the first commercial LIB produced by Sony employed the use of the layered TMO $LiCoO_2$ (LCO) as the cathode material [26; 63]. LCO offers one of the highest theoretical capacities for cathode materials, with a value of 274 mAh/g [26; 64]. However, it is essential to restrict the upper cutoff voltage to prevent the structural rearrangement of the active material and the subsequent degradation [63]. At an upper cutoff voltage of 4.2 V, only half of the lithium can be extracted, resulting in $Li_{0.5}CoO_2$ and a realistic, reversible specific capacity of 135–150 mAh/g [63; 64].
As an improvement of $LiCoO_2$, a combination of nickel, cobalt and manganese is currently being utilized of commercial and automotive applications. This combination is typically referred to as $LiNi_xCo_yMn_zO_2$ (NMC) with $x + y + z = 1$. NMC is able to provide either a high energy or high power density, depending on the chosen design parameters [26; 31; 64]. With a relatively high cutoff potential of 4.3 V, a realistic specific capacity of 160–220 mAh/g is achievable, combining the advantages of all three transition metals [26; 31; 63]. Cobalt is able to enhance the rate capability [65], however, it is associated with a considerable expense in raw materials and a high level of toxicity [31; 63]. The addition of nickel increases the available energy, as a larger proportion of lithium is extracted at a lower but structurally stable potential. This addresses the aforementioned issue with cobalt [65]. Furthermore, it enhances the rate capability [66], although it concurrently diminishes the cyclic

and thermal stability of the cathode [63; 66]. The third transition metal, manganese, decreases the specific capacity [67], however, it increases the structural stability and lowers the cost [63; 67]. A variety of combinations of the three transition metals are possible, with a tendency towards a higher nickel content in order to increase the energy density. NMC111 ($LiNi_{0.33}Co_{0.33}Mn_{0.33}O_2$) was originally used with an equal share of all transition metals. The transition to NMC622 ($LiNi_{0.6}Co_{0.2}Mn_{0.2}O_2$), NMC811 ($LiNi_{0.8}Co_{0.1}Mn_{0.1}O_2$), and nowadays even to NMC955 ($LiNi_{0.9}Co_{0.05}Mn_{0.05}O_2$) [68] achieves high energy densities.
An alternative to NMC that has been demonstrated to be effective is the substitution of manganese with aluminum, which results in the chemical composition $LiNi_xCo_yAl_zO_2$ (NCA). The type of cathode material exhibits a comparable energy density and cost as NMC, thereby also being used in automotive applications [65]. It has the advantage of a higher capacity retention and higher power, compared to NMC with a comparable nickel content [65]. However, NMC exhibits enhanced cycle life and thermal stability compared to NCA [65].
The combination of lithium-manganese-rich (LMR) and NMC (LMR-NMC) has recently gathered considerable interest within the battery research community. With a specific capacity of up to 280 mAh/g, LMR-NMC exhibits a notable enhancement over the conventional cathode materials [69; 70]. The challenges that must be overcome for this material to be widely used include capacity fading caused by a cyclic voltage drop, a low rate capability, structural instability and the release of oxygen in the first cycles [69; 70]. Furthermore, LMR-NMC exhibits a considerable potential hysteresis [70].

Spinel cathode materials The second class of cathode materials is characterized by its spinel structure, which includes primarily $LiMn_2O_4$. The spinel structure provides a high lithium diffusivity [64; 66], and also allows for lithium diffusion in all three dimensions [62; 63]. Consequently, this class of cathode materials exhibits a high power density. Moreover, the material is capable of reaching high operation potentials [26] and has a relatively low material cost [26; 31; 64]. Conversely, $LiMn_2O_4$ exhibits a substantial decline in cyclic capacity fade [31; 63; 64] and offers a specific capacity of only 100–120 mAh/g [26].

Polyanionic olivine cathode materials Polyanionic lithium metal phosphates with an olivine structure represent the third significant category of cathode materials. Lithium iron phosphate (LFP), $LiFePO_4$, is the most promising candidate, attracting interest due to being the most cost-efficient cathode material with a high cycle life [26]. The olivine structure forms continuous parallel channels that permit only one-dimensional lithium diffusion [62]. With a theoretical specific capacity of 170 mAh/g, LFP occupies a central position among cathode materials in terms of specific capacity. However, LFP has the advantage of a low cost [26; 31; 64], increased safety features [26; 64], high thermal stability [26; 63], and high durability combined with a long cycle life [26; 31; 63; 64]. In addition to the diminished specific capacity in comparison to TMOs, LFP exhibits poor electronic conductivity [26; 31] and a lower working potential (~3.5 V), which further reduces the energy density [26; 63; 64].

Additionally, the potential of LFP exhibits a hysteresis and a substantial potential plateau. This consequently gives rise to an increased complexity in the estimation of the remaining energy of a LIB [63; 71; 72].

Binder and conductive additives In addition to the active material, minor quantities of binder and conductive additives are added in the anode and cathode manufacturing process to enhance the cell performance. Binders are added to improve the cohesion of the individual particles and improve the structural stability of the anode [26; 73]. Polyvinylidene fluoride (PVDF) is typically employed as a binder [26]. The addition of conductive additives, such as carbon black, serve to enhance the electrical conductivity of the material, thereby ensuring that particles located at a distance from the electrical terminate maintain sufficient electrical contact [73]. Binders and conductive additives are especially important for silicon anodes, given the inherent limitations in electrical conductivity and the considerable mechanical stress imposed by volume expansion.

Electrolyte

The electrolyte is responsible for the transition of Li-ions between the anode and cathode without allowing the transport of electrons. Accordingly, a high Li-ion conductivity ($\sigma_{\mathrm{Li}} > 1 \cdot 10^{-4}$ S/cm) and a low electronic conductivity ($\sigma_e < 1 \cdot 10^{-10}$ S/cm) over the entire temperature range of the cell is essential [26; 61; 74]. The additional requirements for an ideal electrolyte include a high chemical and thermal stability [74; 75], high safety features [61; 74; 75], low toxicity, and low cost [74; 75]. Furthermore, the electrolyte must exhibit a low viscosity to facilitate optimal Li-ion diffusion [26; 61; 74], and a substantial voltage stability window to prevent the decomposition of the electrolyte [60; 74; 75].
The electrolyte is comprised of three primary components: the solvents, the lithium salt and possible additives. In typical Li-ion batteries, carbonate ester and ether are employed as liquid, nonaqueous, organic solvents [74; 75]. Furthermore, the solvent must possess a high dielectric constant, which is necessary to achieve an adequate concentration of dissolved salt [74; 75]. The most common examples are propylene carbonate (PC), ethylene carbonate (EC), dimethyl carbonate (DMC), diethyl carbonate (DEC), and ethyl methyl carbonate (EMC). A combination of these solvents is often employed in electrolytes, to leverage the advantages of different solvents and fulfill various requirements simultaneously. For instance, EC offers a high dielectric constant, whereas DMC exhibits a low viscosity [75]. However, all carbonate solvents are highly flammable, which presents a significant safety risk for the safety of Li-ion batteries. The lithium salt serves as a source for Li-ions, thereby enhancing ionic conductivity. The most effective and widely used salt is $LiPF_6$ [74]. Nevertheless, even $LiPF_6$ can present safety concerns if the battery is exposed to moisture or if the operating temperature exceeds 60 °C, at which point it reacts with the carbonate solvents [61; 74]. Potential alternatives include $LIBF_4$ and $LiClO_4$ [75]. Additives, with typically amounts below 5 wt%, assist in

fulfilling the requirements of the electrolyte, for example, by reducing the flammability [74]. One potential additive is fluoroethylene carbonate (FEC). Moreover, additives facilitate the formation of a robust SEI [74]. As aforementioned, the electrolyte decomposes on the surface of the electrodes if the electrode potential falls outside of the electrolyte stability window. The typical cathode materials operate at voltages below the highest occupied molecular orbial (HOMO) of 4.7 V [60; 61], which prevents electrolyte decomposition on the cathode surface and the formation of a SEI. However, with the lowest unoccupied molecular orbial (LUMO) of typical electrolytes is approximately 1 V, which means that all commonly used anode materials operate at potentials below this threshold. Consequently, an SEI is created during the initial charge process of the cell formation [14; 60; 61]. A distinctive voltage profile at ~0.8 V can be observed for silicon and graphite, which is linked to the formation of the SEI [61; 76].
A promising advancement in the electrolyte development is the use of solid-state electrolytes (SSEs). The utilisation of an SSE has the potential to enhance the energy density and improve the safety of LIBs by substituting the highly flammable liquid electrolyte with a solid polymer electrolyte or an inorganic electrolyte, typically consisting of oxides or sulfides [26; 77; 78]. Nevertheless, several challenges remain to be addressed before SSEs can compete with liquid electrolyte in terms of performance. These include issues related to electrode contact, cyclic stability, and ion conductivity [77].

Separator

As indicated by its name, the separator functions as a structural and electrical insulator between the anode and cathodes. To prevent internal short-circuits between the two electrodes, the separator must be electronically insulating while still providing a sufficient ionic conductivity. The requirements for a commercially used separator are as follows: a thickness <25 µm, a porosity in the range 40–60 %, quick and complete wetting with electrolyte, chemical stability for a minimum of ten years, a pore size below 1 µm, sufficient mechanical strength to withstand assembly and operation, and a thermal stability of ~5 % shrinkage after 60 min at 90 °C [26; 79–81]. In commercial applications, typical separators are composed of polypropylene (PP), polyethylene (PE), or a combination of both [81]. An alternative to PP and PE is presented by glass fiber separators, which demonstrate enhanced porosity, ionic conductivity, and thermal and mechanical stability [82]. However, the markedly increased thickness and weight of glass fiber separators restrict their commercial application due to the reduction in volumetric and gravimetric energy density.

Current collector

The function of the current collectors is to provide the electrical contact between the cell terminals and the active anode and cathode material, facilitating the electron flow within

the battery cell. In typical LIBs, the current collectors are composed of a thin copper or aluminum foil for the anode and cathode, respectively [83; 84]. The active material is coated on top of the current collector during the manufacturing process. It is therefore essential that a good adhesion is achieved in order to prevent the loss of electrical contact. Furthermore, the current collector materials must exhibit high electric conductivity and electrochemical inactivity [73; 84]. In the case of the cathode, this is provided by aluminum, which is additionally inexpensive [84]. However, aluminum is not a suitable material for the anode, as it alloys with lithium at the low anode working potentials [73; 83]. Therefore, copper is frequently employed as the material for the anode current collector, given its electrochemical stability at low potentials. However, it is more expensive than aluminum [73]. The thickness of the current collectors depends on the selected cell design, but is typically $\leq 10\,\mu m$. Given that the current collector does not contribute to the available cell capacity, a thinner current collector enhances the energy density. However, this simultaneously increases also the electrical resistance, which would be disadvantageous for a cell with a high power density.

The aforementioned descriptions of the different battery components illustrate the manner in which material selection impact the configuration of the battery cell. As illustrated in Fig. 1.1, enhancing a single design parameter inevitably compromises at least one other parameter. For instance, the use of NMC as the cathode material has the effect of increasing the energy density, but also of increasing the cost. It is therefore evident that the optimal materials have yet to be identified, and that a well-considered selection must be made when designing a LIB.

1.1.2 LIB cell formats

For commercial and particularly automotive applications, three principal categories of battery cell formats are in use: cylindrical, prismatic, and pouch cells. Each format offers a distinct set of advantages and disadvantages when designing a battery cell.

Cylindrical cell

In cylindrical cells, the anode, cathode, and separator layers are wound together into a jelly roll and sealed in a stainless steel can [85–87]. This design, particularly the robust casing, exhibits resilience against high internal pressure [87; 88]. In contrast to prismatic and pouch cells, no additional mechanical constraints are required to accommodate this swelling effect [89]. The structural stability of cylindrical cells is particularly suitable for the utilisation of anodes comprising silicon, as it is capable of compensating for the large volume expansion of silicon or SiO_x [20; 21; 39; 42]. The major disadvantage of this structural stability is an increased weight of the battery cell, which results in a low energy density [88]. Furthermore, the energy density is diminished in battery packs due to the unavoidable empty spaces

between the cells inherent to the cylindrical format. Additionally, cylindrical cells exhibit temperature gradients along the diameter of the cell, with the hot-spot being in the core of the jelly roll [90]. A schematic of a cylindrical cell and the jelly roll is displayed in Fig. 1.2 a).

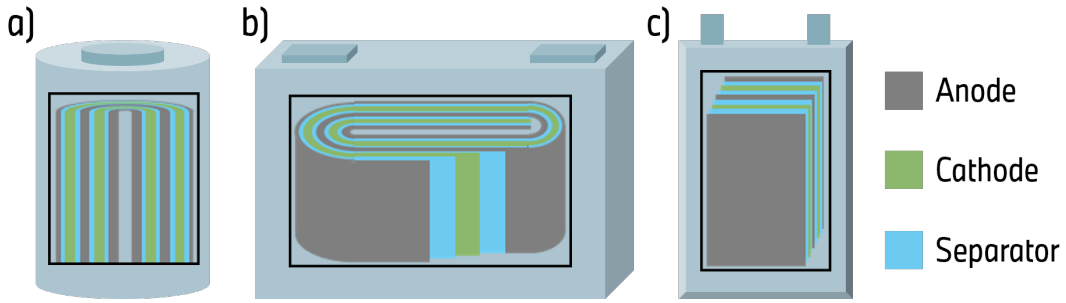

Figure 1.2: Schematic illustration of the major cell formats for commercial and automotive battery cells. a) Cylindrical cell with a jelly roll electrode. b) Prismatic cell with a winding-type electrode setup. c) Stacked multi-layer pouch cell.

Prismatic cell

In prismatic cells, the anode, cathode, and separator are encased in a rigid structure crafted from aluminum or stainless steel [86]. The active materials and the separator are either wound up into a flat jelly roll or stacked on top of each other [86; 87]. The current is distributed through two external tabs, one positive and one negative, which also results in an increased temperature in these regions [90]. The prismatic design offers the advantage of high energy density in a compact design, which can easily be assembled in modules or battery packs, while avoiding significant void spaces between the individual cells [88]. However, prismatic cells require external bracing to address the swelling effect that occurs upon repeated charging and discharging [89; 91; 92]. In comparison to cylindrical and pouch cells, the prismatic cell design results in an elevated manufacturing cost [88]. Fig. 1.2 b) illustrates the structure of a prismatic cell with a flat jelly roll.

Pouch cell

Pouch cells offer the highest energy density among the three cell types while simultaneously exhibiting a low manufacturing cost [87; 88]. It is possible to construct multi-layer pouch cells by stacking multiple layers of anodes, cathodes, and separators, or to create single-layer pouch cells by using a single layer. However, the stack or stacks are only enclosed in a laminate film of aluminum composite foils [85–87]. This casing is not designed to protect the battery from structural damage, which could potentially lead to thermal runaway [87; 93]. Moreover, the casing permits even more pronounced swelling effects than those observed in prismatic cells [87; 89; 91]. It is therefore essential to provide external bracing for pouch cells. As with prismatic cells, the greatest heat generation occurs in the region adjacent to the cell

tabs [90]. Fig. 1.2 c) illustrates a multi-layer pouch cell.

Experimental cell

The limited space in compact application systems often requires a cell format with diminished dimensions. These requirements can be met by the coin cell format, which employs a single stack of an anode, separator, and cathode with a circular configuration. To guarantee electrical contact, the electrodes are braced together by a spring. However, this cell format is not solely employed in small applications, but is also used for experimental cells to gain insights into the electrochemical behavior or to test novel material compositions [94; 95]. Coin cells have the advantage of an easy assembly process and only a minimal quantity of active electrode material is required. An additional application of coin cells is the assembly of half-cells, which comprise either an anode or a cathode as the working electrode and a pure lithium electrode as the counter electrode. This configuration permits the isolation of the anode or cathode potential, due to the constant potential of the pure lithium electrode. As only the difference between the electrode potentials is measurable in full cells, this increases the knowledge of the individual electrodes. To further mitigate the impact of polarization effects, the system can be augmented with a third electrode, which is also composed of pure lithium. The reference electrode is employed solely for the purpose of potential measurement, and does not facilitate an additional current flow. This three-electrode system is often referred to as a T-cell configuration. An illustration of a T-cell setup for an anode half-cell is provided in Fig. 1.3.

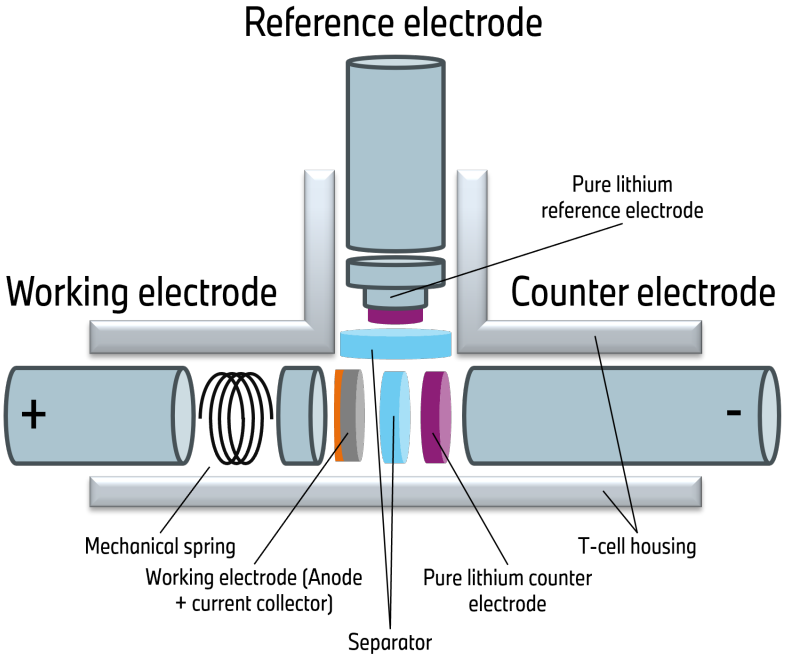

Figure 1.3: Schematic drawing of the classical T-cell setup of an experimental anode half-cell with a lithium reference electrode.

1.1.3 General definitions

Lithiation and delithiation

Lithiation describes the reduction reaction, whereby Li-ions react with an electron and are stored in the active material of the electrodes. In contrast, delithiation describes the oxidation reaction where the stored lithium is extracted from the electrode, resulting in a Li-ion and an electron. In this work, the terms ”lithiation” and ”delithiation” are used to describe the processes occurring at the electrode level and in experimental half-cells.

Charging and discharging

The terms ”charging” and ”discharging” describe the direction of Li-ion and electron transport. In this work, they are used in the context of full cells, which contain an anode and a cathode. During the charge process, energy is stored in the battery cell. Li-ions are delithiated from the cathode, transported by the electrolyte through the separator, and lithiated into the anode. Simultaneously, electrons move from the cathode to the anode through the electrical path. The current is defined as positive during charging. In contrast, the discharge process describes the opposite of the charging process, whereby energy is provided by the battery.

Capacity

The capacity of battery cells is defined as the maximum electric charge that can be extracted reversibly. The capacity of a battery cell is typically expressed in ampere-hours [Ah], which describes the duration for which the battery can be discharged at a given current. For example, a battery with a capacity of 1 Ah can be discharged for one hour at a current of 1 A. However, the total capacity of a battery cell is dependent on various external and operational factors, including ambient temperature, applied current, and voltage window. In this work, the reference capacity, Q_{ref}, is determined during a discharge process at an ambient temperature of 25 °C with a charge rate (C-rate) of C/3. The discharge process is terminated when the minimum operational voltage is reached.

C-rate

The C-rate provides a method for describing the current relative to the reference capacity of a battery cell. The C-rate is defined as the duration necessary to fully charge or discharge the cell with the respective current, I_{cell}. For example, at a C-rate of 1C, the cell is fully discharged within 1 h. Consequently, the corresponding current at a rate of 1C is precisely equal to the reference capacity of the cell. Increasing the C-rate by a specific factor, increases the current

and reduces the (dis-)charging time by the same factor.

$$\text{C-rate} = \frac{I_{\text{cell}}}{Q_{\text{ref}}} \tag{1.3}$$

Open-circuit voltage and open-circuit potential

The open-circuit voltage (OCV) is defined as the voltage measured between the terminals of the battery at open-circuit conditions, when the cell is not exposed to any current. It can be measured incrementally at multiple points throughout the charging and discharging process after a significant relaxation period or by the use of a very low (dis-)charging current. The second case is typically referred to as pseudo OCV due to the persistence of a minor polarization resulting from the internal cell impedance, however, to a negligible amount. The OCV is defined as the difference between the cathode open-circuit potential (OCP) and the anode OCP, represented by Φ_{Ca} and Φ_{An}, respectively.

$$U_{\text{OCV}} = \Phi_{\text{Ca,OCP}} - \Phi_{\text{An,OCP}} \tag{1.4}$$

State of charge and state of lithiation

The state of charge (SoC) is defined as the percentage of the currently available capacity, Q, in relation to the reference capacity of the battery cell.

$$SoC = \frac{Q}{Q_{\text{ref}}} \cdot 100\,\% \tag{1.5}$$

The available capacity, Q, is typically calculated through integration of the measured current, which is also referred to as coulomb counting. In applications where an accurate current measurement is not feasible, the SoC is often estimated through OCV comparison with a predefined reference or through model-based approaches that also use the OCV as an input [96–98].
While the SoC is used at the full cell level, the state of lithiation (SoL) describes the counterpart at the electrode level. In this work, the SoL is correlated with the upper and lower cutoff voltages of the electrode. For instance, the SoL is set to 0 % at the upper cutoff potential for an anode half-cell and reaches 100 % when reaching the lower cutoff potential.

State of health

The state of health (SoH) is a term used to describe the degradation of a battery cell and to define when the end of life (EoL) criterion is met. Two methods exist for determining the SoH of a battery. The first method is capacity-based and compares the reference capacity to the begin of life (BoL) condition, which typically demonstrates a decline over the battery's

lifetime.

$$SoH_{\mathrm{Q}} = \frac{Q_{\mathrm{ref}}}{Q_{\mathrm{ref,BoL}}} \cdot 100\,\% \tag{1.6}$$

The second method describes the changes in the internal cell resistance, R. An increased degradation correlates hereby with an increased resistance, which results in increased losses and a reduced efficiency [99].

$$SoH_{\mathrm{R}} = \frac{R}{R_{\mathrm{BoL}}} \cdot 100\,\% \tag{1.7}$$

1.1.4 Lithium-ion transport process

The ionic path of a battery cell is significantly more complex than the electrical path, considering the extraction and insertion of Li-ions from the anode and cathode, in conjunction with the Li-ion transport through the electrolyte and separator. Fig. 1.4 illustrates the entire Li-ion (and electron) transport process during a charge process. The discharge process is not explicitly depicted, however, it can be deduced by simply reversing all elements of the charge process.

In the electrical path, electrons generated by the oxidation reaction in the cathode dur-

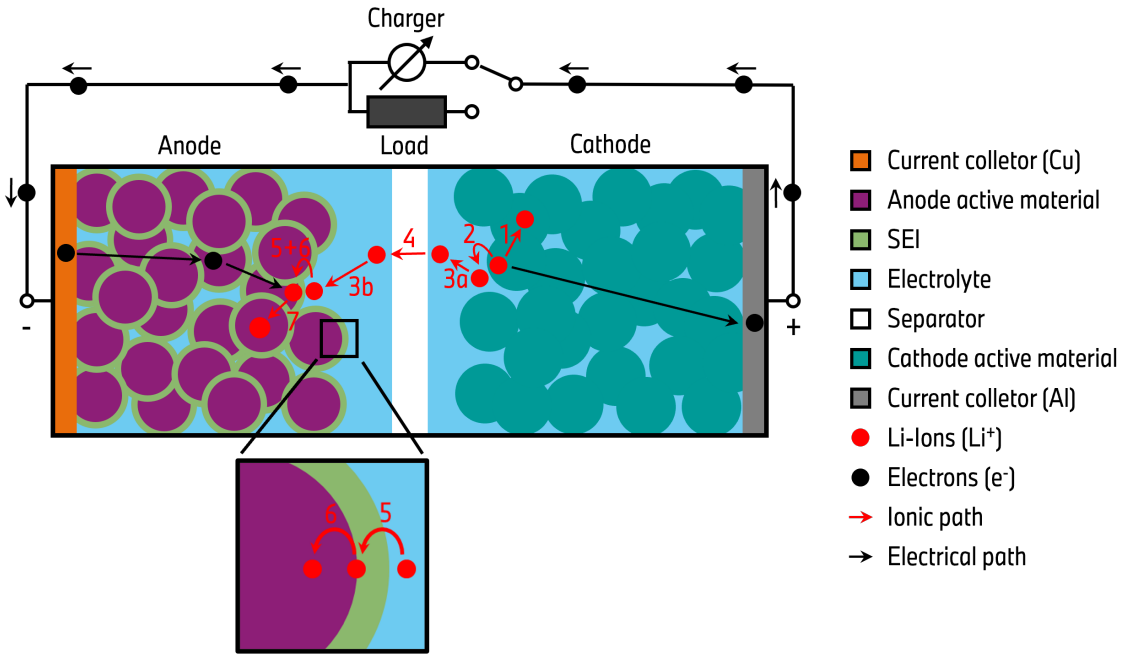

Figure 1.4: Schematic structure of a lithium-ion battery including all components. The electrical and ionic path for a charging process is indicated. The electrical path (black) shows the electron transport from the cathode to the anode. The ionic path (red) includes: (1) Solid diffusion cathode. (2) Charge transfer cathode. (3a) Electrolyte diffusion cathode-separator. (3b) Electrolyte diffusion separator-anode. (4) Separator transition. (5) SEI transition. (6) Charge transfer anode. (7) Solid diffusion anode.

ing charging are transported through the cathode material and conductive additives to the

aluminum current collector and subsequently to the positive cell terminal. From there, the electron flow facilitates the transfer of electrons to the negative cell terminal through the electrical connection, passing through the copper current collector to the designated anode particle where the reduction reaction for a Li-ion occurs.
The ionic path consists of seven discrete steps, which occur during the charge process. In the following, the path of the Li-ions is described, commencing at the cathode. Given that lithium is extracted and accommodated at the particle surface, the stored lithium must be initially migrate from the core of the cathode particles to the surface (1). This diffusion process is driven by a concentration gradient that arises when the initial Li-ions are extracted from the cathode surface. The delithiation process from the cathode represents the second step and is commonly referred to as charge transfer (2), which involves the oxidation of stored lithium into a Li-ion and an electron. In the third and forth steps, the Li-ion migration through the electrolyte (3a, 3b) and the porous separator (4) until they reach the anode surface. The Li-ions are surrounded by solvent molecules while traversing the electrolyte. The lithiation process is more complex in comparison to the cathode due to the presence of the SEI surrounding the anode particles, as illustrated in the zoom plot in Fig. 1.4. The Li-ion must first overcome the SEI (5) before the charge transfer process (6) on the actual anode particle surface can occur. The aforementioned processes provide a certain resistance for the Li-ions, which results in a higher concentration of Li-ions on the outer layer than on the inner layer for the SEI and the anode particle, respectively. Once the Li-ions accommodated inside the anode particle, solid-body diffusion occurs towards the core of the anode particles (7), due to the increase in concentration close to the particle surface [73].

Electrochemical reaction kinetics

In an equilibrium state, the cell voltage U_{cell} is equal to the OCV, as defined in Eq. (1.4). However, as it is the case with all electrical systems, applying a current inevitably results in the generation of internal losses. The various steps of the Li-ion transport processes contribute to the overall internal losses, which accumulate to the total cell polarization η. Accordingly, the cell voltage can be described as:

$$U_{\text{cell}} = U_{\text{OCV}} - \eta \tag{1.8}$$

In accordance with the first law of thermodynamics, the efficiency of any process has to be below 100 %. Given that the charge process requires the input of electric energy, while the discharge process yields energy, $\eta < 0\,\text{V}$ during charging and vise versa $\eta > 0\,\text{V}$ during discharging. Although a LIB cannot be described by a pure ohmic resistance, the polarization is predominantly influenced by the applied current. However, the polarization is also dependent on the temperature and the SoC of the cell, or more specifically, the SoL of the active materials [100]. Two principal methodologies exists for the modeling of a LIB, electrochemical simulation and equivalent circuit modeling.

Electrochemical simulations are based on the fundamental equations that represent the processes of the lithium-ion and electrical transport. These equations are parameterized with specific material parameters (e.g. the electrical conductivity of the anode active material), estimated parameters derived from measurements (e.g. the porosity of the electrode), or parameters that must be fitted by comparing the simulation results with measurements. The most relevant example of these electrochemical equations is the Butler-Volmer equation, which describes the charge transfer processes at the electrode/electrolyte surface [101]:

$$i = i_0 \left[\exp\left(\frac{\alpha_a n F}{R_G T} \eta_j \right) - \exp\left(-\frac{\alpha_c F}{R_G T} \eta_j \right) \right] \tag{1.9}$$

The instantaneous current density i is a function of the exchange current density i_0 and the local surface overpotential η_j [101; 102]. The exchange current density i_0 describes the magnitude of the anodic and cathodic current densities at equilibrium potential, which is dependent on the SoL of the electrode [101]. The local surface overpotential η_j represents the difference between the potential of the solid (active material) and liquid (electrolyte) phases [102]. At equilibrium, where $\eta_j = 0$, the anodic and cathodic current densities are of equal value and in opposite directions, indicating that the same amount of Li-ions are delithiated and lithiated at all times. A specific overpotential causes this equilibrium to shift towards increased lithiation during charging and an increased delithiation during discharging. The transfer coefficients for the anodic and cathodic current, α_a and α_c, respectively, are typically both set to $\alpha_a = \alpha_c = 0.5$ for LIBs [103]. In this context, F represents the Faraday constant, R represents the universal gas constant, and T represents the absolute temperature in kelvins. The factor n is equal to the number of electrons participating in the reaction, which can be removed from the equation for LIBs since only one electron is involved. The Butler-Volmer equation, in conjunction with the remaining equations, is frequently employed in pseudo two-dimensional Doyle-Fuller-Newman models to describe the entirety of the lithium transport process. These models simulate the lithium-ion transport for multiple particles simultaneously throughout the thickness of the electrodes [104; 105]. Given that the ionic resistance is typically higher than the electrical resistance, particles located in close proximity to the separator are preferably lithiated due to the shorter ionic path [83; 106].

The equivalent circuit model (ECM) offers a more simplistic approach to modeling the kinetics of a LIB, which is often sufficient for most applications. In an ECM, each of the lithium transport processes is represented by an electrical element. These elements are connected in series, together with a voltage source that represents the OCV. In ECMs for battery cells, some of the transport processes depicted in Fig. 1.4 can be consolidated into a single pure ohmic resistance [100]. This comprises the electrical path of the electrons through the current collector and active material, the ionic path of the Li-ions through the electrolyte, and the transition of the Li-ions through the separator. As a result of the series connection, these ohmic resistances are combined into a single ohmic resistance. The charge transfer process and the SEI transition are typically represented by a parallel network of a resistance and a double layer capacity (RC network) [100; 107]. The resistance represents the actual transition,

either through the SEI or into the particle for the SEI transition and the charge transfer process, respectively. The capacity describes the concentration difference of Li-ions on either sides of the respective layer. For instance, a greater concentration of Li-ions is present outside of the anode particles than inside at the particle surfaces during charging, due to the restricted kinetics of the charge transfer process. For the remaining process, the solid diffusion, a nonlinear Warburg impedance is often parameterized to represent this slow process [108]. In real batteries, each process occurs simultaneously many times with slightly varying parameters, due to the different positions and sizes of the particles. However, these processes are typically summarized in the ECM into a single element. An example for the series connection of an ECM is illustrated in Fig. 1.5.

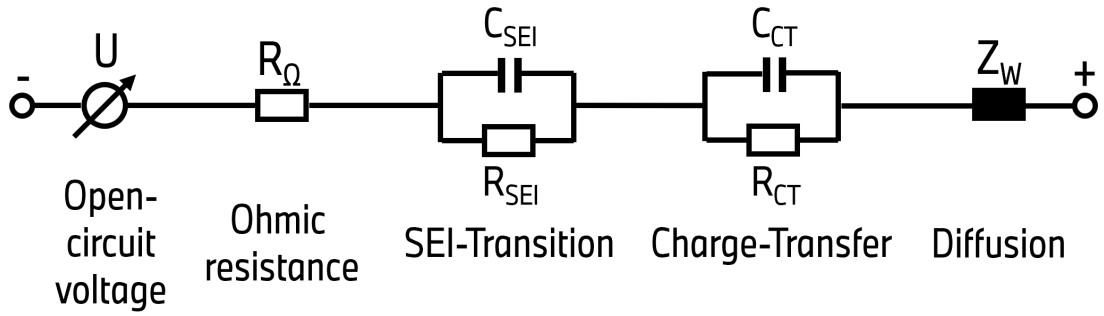

Figure 1.5: Equivalent circuit model of a LIB including the open-circuit voltage, the ohmic resistance, two RC-networks attributed to the charge transfer and the SEI-transition, and the diffusion impedance.

1.1.5 Degradation of lithium-ion batteries

The repeated charging and discharging of LIBs results in the degradation of the battery cell. This aging process is an unavoidable consequence of the battery's operational lifetime. However, the rate at which the degradation occurs can be influenced by adjusting external and internal conditions. The performance of the battery can be influenced by a number of different mechanisms, which act in either of two ways. These two methods were previously defined by the SoH_Q in Eq. (1.6), which tracks the available capacity of the cell, and the SoH_R in Eq. (1.7), which describes the internal resistance increase of the cell. However, due to the typically fixed lower cutoff voltage, an increased cell resistance also has a negative effect on the available capacity [109; 110]. It is therefore essential to gain a comprehensive understanding of the various aging mechanisms in order to adjust the operational parameters in a manner that will limit aging to a bare minimum. The origin of the disparate aging mechanisms can be attributed to either cyclic or calendaric aging, which results in a loss of lithium inventory (LLI), loss of active material (LAM), loss of electrolyte (LE), or a combination of these processes. In addition to experimental techniques such as cell opening, X-ray diffraction (XRD), scanning electron microscopy (SEM) or transmission electron microscopy (TEM), the analysis of the

OCV and its derivatives can effectively identify the specific aging mechanism [99; 109]. The following provides an overview of some of the most significant aging mechanisms:

- **SEI growth.** The SEI growth is frequently reported to represent a significant factor contributing to battery aging [99; 110]. This process occurs continuously throughout the entire lifetime of a battery cell and is categorized as calendaric aging. SEI growth describes the same mechanism as the SEI formation process that occurs during the initial charge phase (see Section 1.1.1). Although the SEI provides protection for the anode surface from electrolyte contact, it is still possible that some electrolyte makes contact, resulting in the formation of additional SEI [99]. The decomposition of the electrolyte results in the consumption of both Li-ions and electrolyte, which gives rise to LLI and LE. As the increased thickness of the SEI also impedes the Li-ion transport and reduces the porosity, it also increases the internal resistance [99]. The SEI growth is accelerated at elevated temperatures and high SoC [99]. In addition to the calendaric effect, the volume expansion of the active materials during lithiation can cause cracks in the SEI or even particle cracking [99; 110]. These cracks are then filled with electrolyte, resulting in new SEI formation. This effect is significantly increased for silicon anodes, due to the severe volume expansion of ~280 % [15; 49; 110; 111].
- **Loss of active material.** An additional consequence of the volume expansion is the loss of active material. Volume expansion can result in the particles losing electrical contact with their neighboring particles or the current collector [99; 109; 110]. This results in a reduction in the available storage capacity of the respective electrode (LAM) and the complete loss of the lithium stored in the particle at the moment of losing electrical contact (LLI). Furthermore, the significant volume expansion of silicon increases the likelihood of electrical contact loss and may also result in the pulverization of the particles [9; 16; 36; 111].
- **Lithium deposition.** Lithium deposition (LiD) is a process that can be attributed to cyclic aging, particularly in the context of fast charging. It occurs when the rate of lithium intercalation is insufficient to match the rate of Li-ion transport to the surface of anode particle. This results in an increased polarization, which in turn leads to a reduction in the anode potential. Once the local anode potential drops below 0 V vs. Li/Li^+, the deposition of metallic lithium on the surface of the anode particle becomes energetically a more favorable process than the conventional intercalation or alloying mechanisms [112–114]. As the deposited lithium metal is situated between the anode particles and the SEI, this does not directly result in the LLI. In the subsequent discharge step or relaxation, the metallic lithium may be stripped again from the particle or intercalated into the particle, respectively, becoming available for further cycling [114; 115]. However, increased LiD carries the risk of creating dead lithium, either by breaking the SEI and resulting in new SEI formation between the metallic lithium and the electrolyte, or by losing electrical contact for some part of the metallic lithium during the stripping process [114]. In extreme circumstances, LiD can result in the

formation of dendrites which may lead to an internal short circuit if the dendrites penetrate the porous separator and reach the cathode surface [114; 116]. The likelihood of LiD is increased at high charging currents, low temperatures, and when the cell is overcharged [110].

- **Cathode dissolution.** The dissolution of active cathode material represents a significant aging mechanism at the cathode. This phenomenon occurs for transition metal oxides and lithium manganese oxide, resulting in LAM [110]. It is also possible that the dissolved metals may pass through the separator, thereby enhancing the SEI growth at the anode, which is often referred to as cross-talk [110]. It is further possible that the dissolved metals react with the electrolyte, forming a cathode electrolyte interface (CEI) in an irreversible side reaction [110]. Analogous to the SEI, the CEI causes polarization and increases the internal resistance. As with all chemical processes, the cathode dissolution is also enhanced at elevated temperatures [99].

It is imperative to avoid these aging mechanisms in order to prevent the so called "roll-over effect", whereby cells are unable to compensate for the existing degradation and undergo a drastic decline in capacity [17].

1.2 Context of lithium-ion active materials: Formation and lithiation

In order to analyze the lithiation behavior of Gr/SiO_x blend anodes with the intention of enhancing their performance, it is necessary to have a comprehensive understanding of the thermodynamics that describe the lithiation behavior of the pure materials. This section presents a description of the various lithiation phases observed in graphite and silicon, as well as the formation process for silicon and SiO_x.

1.2.1 Lithiation of graphite

Graphite is composed of a hexagonal planar graphene layer structure, wherein lithium is intercalated between the layers [27; 117; 118]. At a state of full lithiation, six carbon atoms can accommodate one lithium-ion (LiC_6), resulting in a theoretical capacity of 372 mAh/g and the formation of a lithium layer in between each graphene layer [117–119]. Prior to reaching this full lithiation, different intercalation configurations exist, often referred to as stages or phases. These stages facilitate the optimal arrangement of lithium for the storage of Li-ions, resulting in one or multiple empty graphene layers devoid of intercalated lithium [31; 118]. A typical sequence of stages during the lithiation process is as follows: 1L - 4 - 3 - 2L - 2 - 1 [117; 118; 120]. The n-th stage describes a stage where every n-th graphene layer is filled with lithium. L-stages are distinguished by their liquid-like state, which is less organized than that observed in the remaining stages [118]. The identification of the different graphite phases

can be achieved through experimental analysis methods, including XRD, neutron diffraction, and Raman spectroscopy [118; 120]. Furthermore, the lithiation of graphite can be discerned through optical analysis, as the color of the material shifts from black or grey to gold upon lithiation [121].
Two distinct intercalation models have been proposed for graphite. The original model by Hofmann and Rüdorff [122] offers an explanation for graphite lithiation based on a combination of fully lithiated and completely empty layers, which represent the different stages. However, this model has the disadvantage of being unable to account for the phase transition, whereby entire layers must undergo simultaneous delithiation and lithiation [118]. Accordingly, the currently prevailing Daumas-Hérold-Model, which was first proposed in 1969 [123], postulates that graphite undergoes lithiation through the formation of small lithium domains situated between the flexible graphite layers [117; 118; 124]. This model posits that each layer is lithiated to a certain extent, while the necessary number of empty layers between the domains remains locally still intact [118].
Fig. 1.6 illustrates the pseudo OCP of a graphite anode half-cell during lithiation. The figure illustrates the various stages and the corresponding chemical degree of lithiation. Moreover, the lithium configuration in accordance with the Daumas-Hérold-Model is visualized for the non-liquid stages. The profile of the anode potential shows the distinctive graphite plateaus, which can be ascribed to specific phase transitions [117; 124]. Graphite is mainly active at potentials below 0.22 V [125]. At higher potentials, the particles are lithiated in the unorganized 1L stage [118]. Subsequently, the first graphite plateau describes the phase transition from 1L to 4, which can be translated to LiC_{72} to LiC_{36} [117; 120]. This plateau is situated within the potential range of 0.19–0.22 V [125; 126]. Following the first plateau, a relatively prolonged region with a voltage decline is evident. This region is associated with the phase transitions 4 - 3 - 2L, or accordingly, LiC_{36} - LiC_{24} - LiC_{18} [117–119]. Following on this voltage decline, the second graphite plateau is observed, which describes the 2L - 2 phase transition from LiC_{18} to LiC_{12}, typically occurring at a potential range of 0.11–0.14 V [117; 118; 125; 126]. The remaining 50 % SoL represent the final phase transition, 2 - 1, which results in the formation of the fully lithiated LiC_6 [117; 118]. This plateau occurs at a potential of 0.08–0.10 V [125; 126].

One of the advantages of graphite is that it exhibits a relatively small intrinsic hysteresis of only ~20 mV between lithiation and delithiation [47; 118; 127; 128]. A slight hysteresis is reported by Allart et al. [117] in the region of the the phase transition 4 - 3 - 2L with the voltage decline. This can be attributed to the presence of diverse configurations at these stages, which results in mixed stacking patterns for lithiation and delithiation. Nevertheless, the potential plateaus exhibit only a slight hysteresis, which was associated with reversible processes occurring during the respective phase transitions.

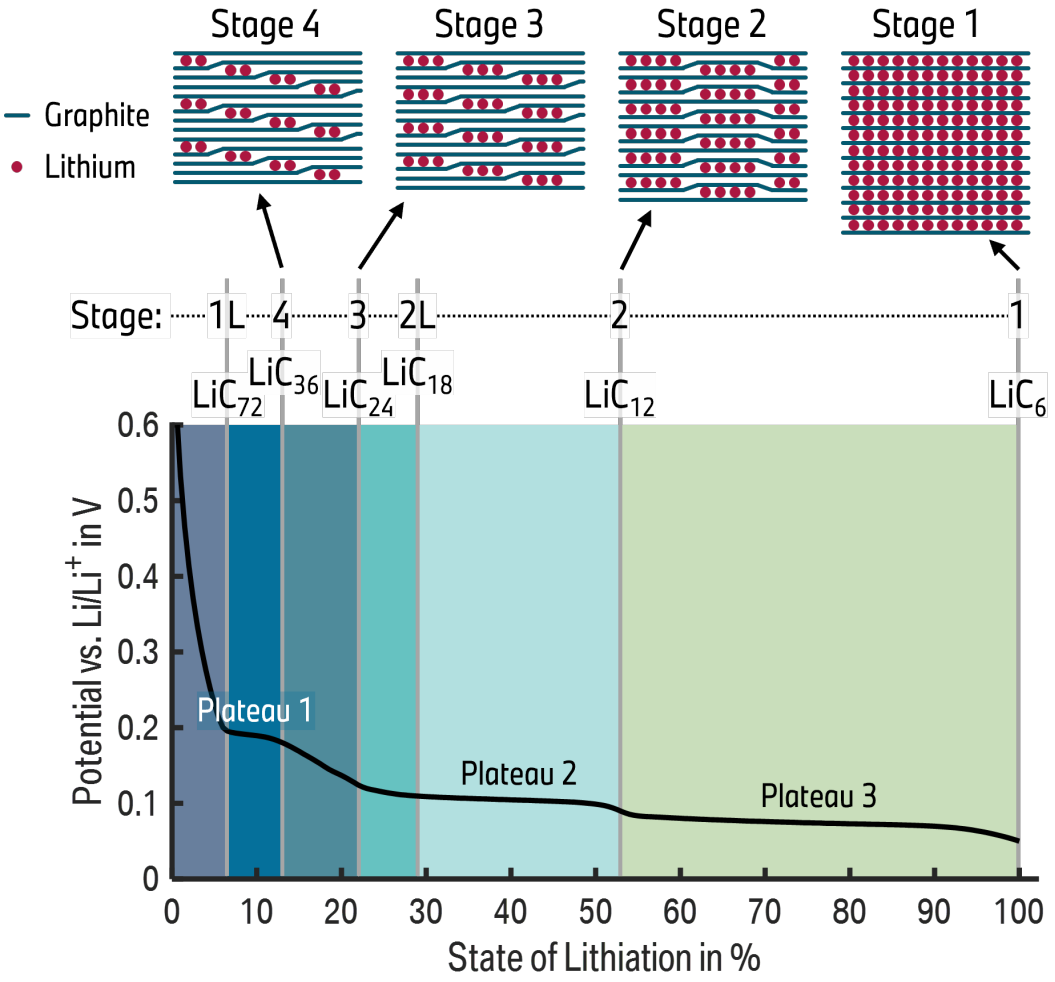

Figure 1.6: Anode potential during lithiation of a graphite electrode. The three graphite plateaus, the degree of lithiation, and the stage designation is indicated in the graphic. Additionally, the lithium arrangement between the graphene layers is illustrated for the ordered stages.

1.2.2 Lithiation and formation of silicon

As previously stated in Section 1.1.1, the lithium insertion into silicon is not an intercalation process, but an alloying process. The Li-Si alloy typically exhibits an unordered amorphous (a) state. However, this amorphous state is only attained subsequent to the formation process of the silicon electrode. Prior to the formation process, silicon exists in a crystalline (c) form [10]. Consequently, silicon undergoes an amorphization process during the initial lithiation process of the cell formation. This results in the characteristic silicon formation profile, which exhibits a large plateau at ~0.1 V vs. Li/Li^+ until the amorphization is complete [10]. The SEI formation occurs concurrently with the amorphization. Given the considerable volume expansion of silicon, it is probable that the SEI will undergo multiple cracking and reforming processes during the initial lithiation phase. Ultimately, this process should yield a stable SEI when full lithiation is reached [13; 14]. Once formation is complete, the potential profile

remains stable at an overall level that is slightly lower than that of graphite. In comparison to the active potential range of graphite (0–0.22 V vs. Li/Li^+), silicon is active across a broader potential range. During lithiation, silicon is lithiated between 0–0.8 V, with a significant proportion of the lithiation occurring above the graphite threshold of 0.22 V, but also a notable fraction occurring at similar potentials to graphite [34; 125]. The intrinsic hysteresis of silicon is known to increase the active potential range of silicon during delithiation, to levels almost completely above the graphite threshold of 0.22 V. Silicon exhibits significantly low SoLs at potentials above 1 V for silicon [10; 15]. The silicon hysteresis has been frequently reported to be ~250 mV [128; 129], a value that is markedly higher than the ~20 mV observed for graphite [47; 118; 127; 128].

Although the relaxation of silicon is relatively slow in comparison to other active materials, the voltage deviation between lithiation and delithiation remains at approximately 100 mV and can therefore be classified as a true thermodynamic hysteresis [129; 130]. The precise cause of the silicon hysteresis remains a topic of debate in the literature [128; 131]. A number of potential explanations have been put forth, including mechanical and kinetic causes. One frequently proposed explanation is internal mechanical stress [10; 132]. Köbbing et al. [130] states a hysteresis model that is based on mechanical stress from the interaction of the SEI with the particle surface, resulting from the volume expansion of silicon. The kinetic reasons can be explained by the breaking of Si-Si bonds to insert further Li-ions, which results in a significant kinetic resistance [129]. Durdel et al. [15] posit that the hysteresis can be attributed to the slow voltage relaxation of silicon, whereby the charge transfer requires a substantial polarization, irrespective of the applied C-rate.

Similar to graphite, distinct lithiation phases have also been reported for silicon. However, not all of these phases exhibit the same reversible reaction when the direction of the current flow is reversed. An overview of the entire lithiation and delithiation process of silicon is provided in Fig. 1.7. As aforementioned, fully delithiated silicon (a-Si) exhibits an amorphous state following the formation process. Upon lithiation, the potential undergoes a continuous decrease, reaching the phase a-Li_2Si between anode potentials of (200–250 mV vs. Li/Li^+) [133; 134]. Further lithium insertion results in the phase a-$Li_{3.5}Si$ at potentials of approximately 100 mV [133; 134]. Additional lithiation then leads to a phase transition of silicon from the prior amorphous phase to a crystalline phase. For a-$Li_{3.5}Si$, the formation of the metastable crystalline phase c-$Li_{3.75}Si$ or c-$Li_{15}Si_4$ is kinetically more advantageous [133–135]. This phase also describes the theoretical specific capacity of 3579 mAh/g for silicon at room temperature [13; 14]. The crystallization process is reported to occur at a potential below 50 mV [18; 125; 136–138] or 60 mV [133; 139]. This crystalline phase is facilitated by the presence of isolated Si-anions [10; 137]. The isolated anions are created by breaking the Si-Si bonds within larger silicon clusters during (de-)lithiation. Furthermore, Ogata et al. [133; 134] have reported an overlithiated crystalline phase, designated as c-$Li_{3.75+\delta}Si$ ($\delta = 0.2 - 0.3$), which is observed to occur at an even lower potential, below 50 mV. Ogata et al. posit that this phase is more favorable than breaking additional Si-Si bond to create new crystalline silicon.

The crystallization does not occur instantaneously once the potential drops below 50 mV.

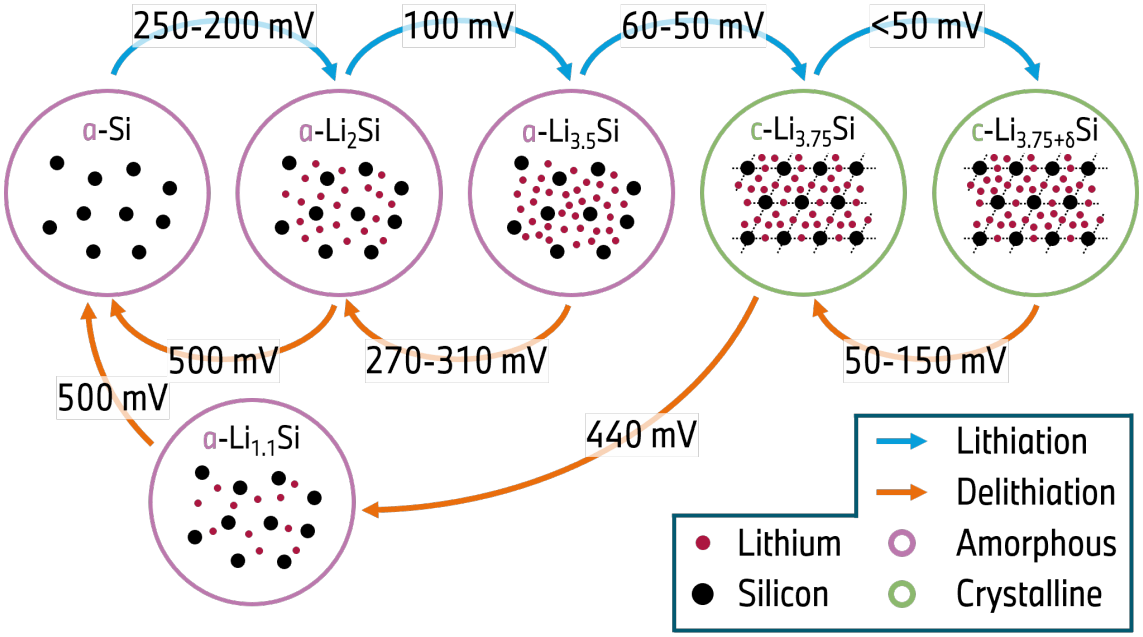

Figure 1.7: Description of the lithiation process of silicon according to [133]. This includes the amorphous and crystalline phase transitions that silicon experiences during lithiation and delithiation.

Rather, it occurs gradually during the lithiation at these low potentials [133]. The formation and reformation of the crystalline phase is often accompanied by the strong degradation of silicon, which may be a contributing factor in the SEI cracking and the resulting additional SEI formation [134; 138; 140]. The existence of the crystalline phase in silicon can be identified through analytical methods such as XRD [137; 141], SEM [136], or nuclear magnetic resonance (NMR) [134] .

The delithiation process can occur along different pathways, contingent on whether the crystalline phase transition has occurred during the prior lithiation step or not. These different pathways are also visualized in Fig. 1.7. The delithiation of purely amorphous silicon occurs via a symmetrical phase transition, analogous to the lithiation process. However, the delithiation occurs at a higher potential due to the hysteresis. The highest lithiated phase a-$Li_{3.5}Si$ is reduced to a-Li_2Si at potentials of 270–310 mV, and then further delithiated to a-Si at potentials above 500 mV [35; 133; 134]. In contrast, crystalline silicon is not transferred back to the a-$Li_{3.5}Si$ phase, resulting in an asymmetric additional hysteresis [10]. The overlithiated phase is initially reverted to c-$Li_{3.75}Si$ at relatively low potentials of 50–150 mV [133; 134]. The product of the decrystallization process is a-Li_xSi, which is formed at relatively high potentials of ~440 mV [12; 18; 35; 133; 142]. The amount of lithium x is inconsistent in the literature, with values ranging from 1.1 [133] to 2 [35; 141]. After returning to the amorphous phase, a-Li_xSi is reduced to fully delithiated a-Si at potentials exceeding 500 mV.

The consequences of this phase transition from amorphous to crystalline will be examined in greater detail in Section 2.1.

1.2.3 Lithiation and formation of silicone oxide

As aforementioned, SiO_x represents a viable alternative to pure silicon anodes, which serves to mitigate the disadvantages while also limiting the advantages of silicon. The volume expansion of SiO_x upon lithiation is less pronounced, which results in an improved lifetime due to a reduction in particle cracking or SEI growth. However, SiO_x exhibits a diminished specific capacity and an initial efficiency that is inferior to that of pure silicon [19; 20]. These attributes are dependent on the amount of oxygen in SiO_x, which is within a range of $0 \leq x \leq 2$. The SiO_x itself is inherently thermodynamically unstable, existing as a composition of pure silicon and SiO_2 prior to the formation process [21]. The oxygen does not directly contribute to the available capacity of the anode, but rather provides a buffering effect against the volume expansion, reducing it to ~160 % [20; 21; 39]. Consequently, the oxygen engages in a series of reactions with lithium and silicon, yielding a range of side products that are predominantly irreversible [20; 21; 135]. This results in a considerable LLI, given that lithium is involved in all side reactions, which accounts for the low initial efficiency. The formation of these side products occurs concurrently with the SEI formation, particularly during the initial lithiation step. The resulting structure can be described as a core-shell comprising side products, covering the remaining pure silicon particles [21; 143]. The side products are denser materials than fully lithiated $Li_{3.75}Si$, and thus allow the core-shell to compensate for the volume expansion of the pure silicon particle in the core [20; 76].
The side products can be classified into two categories: lithium silicates and Li_2O. The Li-silicates encompass numerous chemical compositions, comprising lithium, silicon, and oxygen. The most prevalent Li-silicate is Li_4SiO_4 [20; 21; 135; 143–145]. Besides that, $Li_2Si_2O_5$, Li_2SiO_3 and $Li_6Si_2O_7$ are some common examples of other lithium silicates that result from the formation of SiO_x [20; 135; 143]. While Li-silicates are not completely irreversible, they are chemically stable until reaching potentials above 4.0 V, which is outside of the active range of LIBs [20; 21; 135]. The formation of Li-silicates occurs within a potential range of 0.35–0.5 V vs. Li/Li^+ [20; 144]. The second side product, Li_2O, does not consume any silicon and therefore does not result in LAM. Nevertheless, it does lead to significant LLI [19; 20; 55]. However, Li_2O has the advantage of improving the rate performance, as it has a high lithium diffusivity and acts as a lithium diffusion channel towards the pure silicon particles [21].
The numerous variables involved in the formation of SiO_x make it exceedingly challenging to calculate the specific capacity of SiO_x. These variables include the amount of oxygen x, the distribution between Li_2O and Li-silicate formation, and the specific Li-silicates that are present after the formation process. A range for the initial and reversible specific capacities is provided in Section 2.2. This calculation was performed for SiO ($x = 1$) and under the assumption that only the Li-silicate Li_4SiO_4 exists. The edges of the specific capacity ranges are defined for the extreme cases, where only one side product category, either Li_2O or Li_4SiO_4, is created during the formation. In reality, however, there will always be a combination of both side products. The actual specific capacities will therefore lie somewhere between the following ranges:

- Initial specific capacity: 2318–3496 mAh/g
- Reversible specific capacity: 1710–2280 mAh/g

Following the formation process, SiO_x exhibits an electrochemical behavior analogous to that of pure silicon anodes. The pseudo OCP profile of a pure SiO_x anode is illustrated in Fig. 1.8, which also depicts the potential hysteresis between lithiation and delithiation.

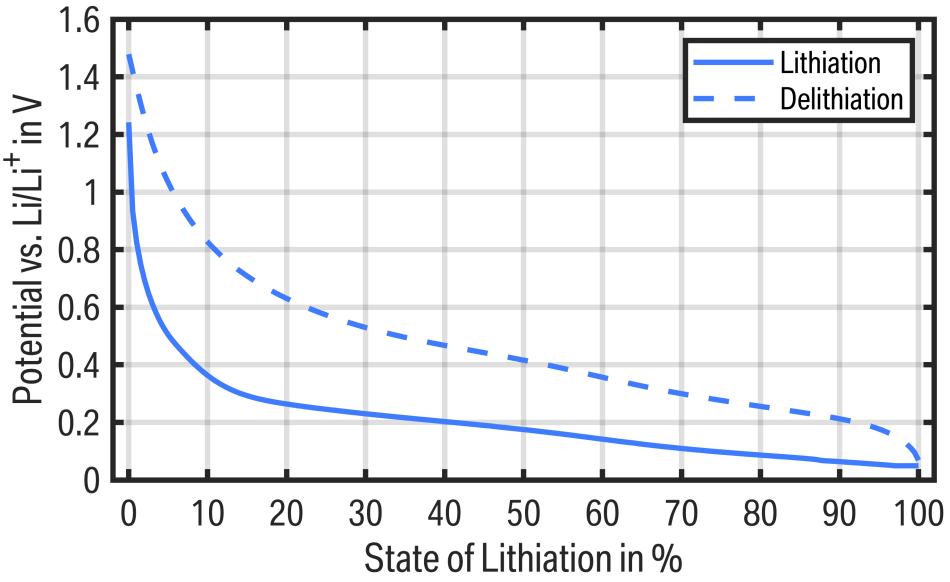

Figure 1.8: Pseudo open circuit potential of an SiO_x anode.

1.3 Motivation and research questions

Given the complex electrochemical behavior exhibited by a single anode material, as previously outlined, it becomes evident that a comprehensive investigation is imperative to gain insight into the interaction between graphite and SiO_x in blend anodes. The partially overlapping regions of the pure material anode potentials, in conjunction with the intrinsic silicon hysteresis, inevitably impact the thermodynamic effects in blend electrodes, thereby influencing the lithiation behavior. Moreover, it can be anticipated that the kinetic behavior of the two active materials will differ, which will consequently impact the lithiation behavior of the blend electrode. To gain a detailed comprehension of the lithiation behavior of Gr/SiO_x blend anodes, including thermodynamic and kinetic effects, this thesis addresses the following research questions:

1. How much lithium is stored in each active material throughout the entirety of the charging and discharging process?
2. What is the effect of the charging and discharging history on the lithiation behavior?
3. What is the impact of the charge rate (slow charging vs. fast charging) on the lithiation

behavior?

4. How is the cell voltage influenced in Gr/SiO_x blend electrodes?

By responding to these questions, it is feasible to track of lithium storage in Gr/SiO_x blend electrodes across all operational scenarios. Furthermore, improvements in matching the cell voltage with the specific lithiation characteristics of the graphite and SiO_x can be achieved. An enhanced comprehension of the lithiation behavior facilitates optimized performance of high-energy LIBs, particularly during operation. This understanding improves the accuracy of the internal battery state estimation, including the SoC and SoH estimation, which are major functions of BMSs. Moreover, the insights gained can be used to enhance fast-charging protocols. These protocols are typically designed to reach low anode potentials without causing the aging mechanism of LiD. This is done in order to reduce the charging time while maintaining a sufficient battery lifetime. As these protocols are typically based on electrochemical simulation models, an improved comprehension of the lithiation behavior, especially the kinetic aspects, will result in a higher quality of the simulation models. This will facilitate a reduced fast-charging time.

1.4 Outline of this work

This section outlines the structure of this cumulative thesis, which is based on three scientific publications. Furthermore, it provides a thematic classification of the manner in which each publication addresses the different research questions.
Chapter 2 is primarily devoted to a presentation of the three publications. Section 2.1 presents the work, entitled ”Lithium trapping induced memory effect of Gr/SiOx blend anodes in lithium-ion batteries subjected to repeated partial cycling”. The study describes a thermodynamic phenomenon exhibited by silicon, which gives rise to a memory effect in blend electrodes. This phenomenon is contingent upon the specific history of charging and discharging cycles. The crystalline silicon phase transition that is responsible for this effect introduces crystalline silicon as a third active material species to the blend electrode, thereby affecting the lithiation distribution. Additionally, the memory effect exerts a considerable influence on the cell voltage, which must be accounted for in order to maintain an accurate SoC estimation.
In order to provide insights into the kinetics that affect the lithiation behavior, the research article ”Effect of different charge rates on the active material lithiation of Gr/SiOx blend anodes in lithium-ion cells” is presented in Section 2.2. This article introduces a non-destructive method for analyzing the lithiation distribution between graphite and SiO_x at different C-rates during charging. This method allows for the determination of the active material that is preferably lithiated at elevated C-rates, which directly affects the lithiation distribution between graphite and SiO_x.

Section 2.3 presents the third study, entitled "Active material lithiation in Gr/SiOx Blend Anodes at Increased C-Rates". This work builds upon the findings of the second study by measuring the precise current flow through each active material at different C-rates in an experimental half-cell setup, comprising of a pure graphite and a pure SiO_x half-cell. These additional insights into the kinetic effects throughout the entire SoC range serve to corroborate the findings of the second study. The results are further employed for the optimization of an electrochemical simulation model, enabling a comparison of the precise lithiation behavior in addition to the conventional approach of aligning the anode potential.
Chapter 3 provides a comprehensive discussion of the entire thesis, including the individual contribution of each research article to the objective of this work. Section 3.1 is devoted to the discussion of thermodynamic effects, offering further insights that facilitate the contextualization of the research articles' findings. Section 3.2 covers the kinetic effects in a similar manner to the previous section. The entire thesis is summarized in Section 3.3. Additionally, this section presents an overview of how each research question is answered and an outlook on the further research questions to pursue in this area.

2 Published results

This chapter covers the cumulative part of this thesis. It comprises the three peer-reviewed research articles that constitute the primary results of this thesis. Prior to each research article, a concise summary of the findings is provided, along with a classification within the broader context of this work and a description of the contribution of each author.

2.1 Lithium trapping induced memory effect of Gr/SiOx blend anodes in lithium-ion batteries subjected to repeated partial cycling

The incorporation of SiO_x into the anode introduces multiple challenges that have an impact on the performance of LIBs. The thermodynamic influences are largely contingent upon the intrinsic hysteresis of silicon and the overall different working potentials of SiO_x and graphite. However, in addition to these considerations, silicon presents another challenge that must be addressed, namely the crystalline phase transition that occurs in silicon upon reaching high degrees of lithiation. This section presents a study investigating the influence of the crystalline phase transition of silicon on the operation of LIBs containing a Gr/SiO_x blend anode. It is imperative to gain a comprehensive understanding of this phenomenon in order to ensure the accuracy of voltage-based SoC and SoH estimation, given the considerable alterations in the voltage profile resulting from this phase transition.
As previously described in Section 1.2.2, silicon is known to undergo a phase transition from an amorphous to a crystalline state. This transition occurs at an anode potential below 50 mV vs. Li/Li^+ or at an equivalent high full cell SoC [18; 136; 137]. This phenomenon has been extensively investigated in the literature on pure silicon half-cells. This work makes a novel contribution to the field by examining the impact of this effect on blend anodes in full cell operation.
The study demonstrates that partial cycling without fully discharging the cells results in a significant memory effect, comparable to that observed in nickel-cadmium and nickel-metal hydride batteries [146–149]. This memory effect arises as Li-ions become trapped in the crystalline phase of silicon. Given that this phase is reverted at a considerably higher potential of 440 mV vs. Li/Li^+, it is necessary for the cells to be sufficiently discharged in order to regain the trapped capacity [12; 133; 142]. Given that graphite is the primary active material and its working potential is below 220 mV, these potentials are only reached at considerably low full cell SoCs. The crystallization of silicon has a considerable impact on

the cell voltage during discharging in the lower SoC range, where silicon is primarily active. In this range, the voltage is reduced until the crystalline phase is fully reverted. This has an impact on the performance of the battery cell, influencing the observed capacity retention of the partial cycles. Furthermore, it gives rise to an error in voltage-based SoC and SoH estimation, and reduces the available discharge energy. However, all of these consequences dissipate after a single full discharge cycle, which makes it necessary to fully understand the memory effect to sufficiently revert it.
Upon repeated partial cycling, the amount of lithium that becomes trapped in the crystalline phase increases. It is demonstrated that as the number of cycles increases, the amount of trapped lithium converges towards a cell specific saturation. Furthermore, the study encompasses a variation of the SoC range throughout the cycling process, thereby enabling the identification of a critical SoC range. No significant correlation is observable between variations in the ambient temperature and the (dis-)charging C-rate, thereby confirming that the memory effect is solely affected by the thermodynamics of the blend anode. To validate the findings, the main test scenario is repeated for a total of five cell types.
An additional analysis of Gr/SiO_x anode half-cells with a variation of the upper and lower cutoff potential serves to corroborate the aforementioned findings. Moreover, evidence of an additional crystalline phase is identified, which may exist prior to the formation of the crystalline phase c-$Li_{3.75}Si$. Nevertheless, the confirmation of this phase's existence remains to be seen.
The findings of this study provide an insight into the lithiation behavior of Gr/SiO_x blend anodes in real-world scenarios, where the battery cell is not fully discharged in every cycle. It is imperative to consider the impact of the additional asymmetric voltage hysteresis, resulting from the crystalline phase of silicon in order to improve the accuracy of BMS functions for internal state estimation. Furthermore, the distinct voltage profile of the crystalline silicon phase in comparison to graphite and amorphous SiO_x results in the blend anode being divided into three effective active material species. Therefore, the memory effect influences the voltage profile and has an impact on the lithiation behavior.

Publication notes

The article "Lithium trapping induced memory effect of Gr/SiO_x blend anodes in lithium-ion batteries subjected to repeated partial cycling" is presented in the following. The article was submitted to the *Journal of Power Sources* for peer review in October 2024 and got accepted in November 2024 [150]. The permanent web link to this publication is available under `https://doi.org/10.1016/j.jpowsour.2024.235936`. To support the main article, additional information is provided in the Supplementary material, including a method to determine the silicon capacity share by OCV analysis and further voltage measurements .

Author contribution

J.K. and A.A. developed the concept of the study. J.K. and H.C.H designed, carried out and analyzed the electrochemical test on full cell and half-cell level, respectively. J.K. carried out the visualization of the the data. J.K. wrote the manuscript, assisted by H.C.H. in the section about half-cell assembly. A.A., B.R., T.W., M.H, and M.A.D. reviewed and edited the manuscript and provided supervision for the research project. All authors discussed and commented on the results.

Journal of Power Sources 629 (2025) 235936

Contents lists available at ScienceDirect

Journal of Power Sources

journal homepage: www.elsevier.com/locate/jpowsour

Lithium trapping induced memory effect of Gr/SiO_x blend anodes in lithium-ion batteries subjected to repeated partial cycling

Julian Knorr [a,b,*], Hao-Chen Hsiao [c], Alexander Adam [c], Barbara Rödl [a], Thomas Waldmann [d,e,f], Markus Hölzle [d], Michael A. Danzer [b,g]

[a] BMW Group, Research and Technology Centre, Parkring 19, 85748, Garching, Germany
[b] Chair of Electrical Energy Systems (EES), University of Bayreuth, Universitätsstraße 30, 95447, Bayreuth, Germany
[c] BMW Group, Battery Cell Competence Centre, Lemgostraße 7, 80935, Munich, Germany
[d] Zentrum für Sonnenenergie- und Wasserstoff-Forschung Baden-Württemberg (ZSW), Lise-Meitner-Straße 24, 89081, Ulm, Germany
[e] Helmholtz Institute Ulm for Electrochemical Energy Storage (HIU), Helmholtzstraße 11, 89081, Ulm, Germany
[f] Institute of Surface Chemistry and Catalysis, Ulm University, Albert-Einstein-Allee 47, 89081, Ulm, Germany
[g] Bavarian Center for Battery Technology (BayBatt), University of Bayreuth, Universitätsstraße 30, 95447, Bayreuth, Germany

HIGHLIGHTS

- Partial cycling of Gr/SiO_x anodes in full cells causes a memory effect.
- Lithium is trapped in the fully lithiated crystalline phase of silicon.
- A full discharge cycle allows the trapped lithium to be recovered.
- Variations in temperature, cycle number, and C-rate are conducted.
- The critical state of charge range for partial cycling is determined.

GRAPHICAL ABSTRACT

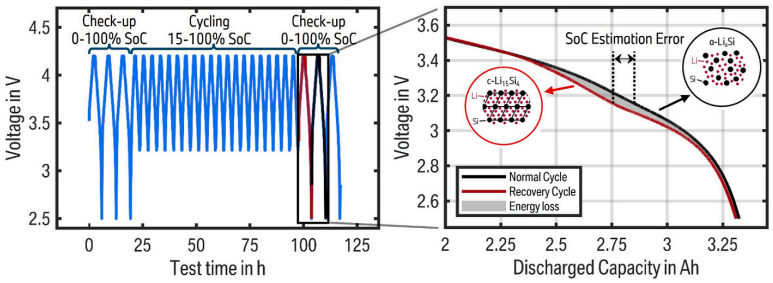

ARTICLE INFO

Keywords:
Lithium-ion battery
Gr/SiOx blend anode
Memory effect
Lithium trapping
Capacity recovery

ABSTRACT

The use of silicon-based secondary anode materials in blend anodes alongside graphite is becoming increasingly prevalent in commercial lithium-ion batteries also used more and more in automotive applications. In addition to the accelerated degradation of silicon due to its significant volume expansion, the crystalline phase transition of fully lithiated silicon results in alterations to the voltage profile during discharging. This study examines the impact of this phase transition on the operation and state estimation of battery cells using such silicon-containing graphite/SiO_x blend anodes. A memory effect of trapping lithium in the crystalline phase occurs when the cell is subjected to partial cycling without being fully discharged. However, this effect can be cancelled out by a single deep discharge. To gain further insights, a variation in cycle numbers, state of charge range during cycling, charge and discharge current, and the operation temperature is conducted. In order to validate the findings, a variety of commercial and automotive cells and blend anode half-cells are analyzed.

* Corresponding author. BMW Group, Research and Technology Centre, 85748, Garching, Germany.
E-mail address: Julian.Knorr@bmw.de (J. Knorr).

https://doi.org/10.1016/j.jpowsour.2024.235936
Received 19 October 2024; Received in revised form 21 November 2024; Accepted 23 November 2024
0378-7753/© 2024 Elsevier B.V. All rights are reserved, including those for text and data mining, AI training, and similar technologies.

1. Introduction

The market share of battery electric vehicles (BEVs) has exhibited a notable increase in recent years, with a substantial rise in the number of BEVs sold from 2.1 million in 2018 to 13.7 million in 2023 [1]. In order to extend the range of BEVs, new materials are investigated to enhance the energy density of lithium-ion batteries (LIBs). Among the active materials for the negative electrode, silicon (Si) is the most promising candidate, exhibiting a specific capacity of 3579 mAh/g at room temperature, which is about ten times higher than that of today's state-of-the-art material graphite (Gr) [2–4]. Moreover, silicon has a considerably low working potential, ranging from 0.2 to 0.6 V, which is essential for achieving a high energy density [5–7]. However, silicon experiences a significant volume expansion upon (de-)lithiation of ~280 % at full lithiation [8–10]. This results in the loss of active material and loss of lithium (Li) inventory, due to pulverization of Si-particles [7,11], particle cracking [4,12], loss of electrical contact [5,13], solid electrolyte interface (SEI) growth [14], and an overall unstable solid electrolyte interface [10,15,16]. The consequence of this degradation is a rather fast reduction of the available capacity, which counteracts the primary advantage of Si. A number of methods have been developed to avoid the adverse effects associated with volume expansion. Increasing the surface area to volume ratio by the implementation of nanoparticles reduces the strain during lithiation but results in a lower volumetric energy density [17]. Nevertheless, it has been demonstrated that such nanoparticles can withstand pulverization and cracking below a certain diameter [5,9,15].

The use of silicon oxide (SiO_x) or silicon embedded in a carbon matrix (SiC) instead of pure silicon particles presents an alternative with an intrinsically lower specific capacity, but with marked benefits in view of volume expansion [6,10,15,18]. The formation of Li-silicates and Li_2O as irreversible side products of SiO_x [19,20] results in an effective reversible specific capacity of ~1400 mAh/g [12,21,22]. To ensure longevity while still providing a capacity boost, commercially available cylindrical LIBs often employ a blend anode with SiO_x as a secondary active anode material in addition to graphite. This approach combines the high specific capacity of SiO_x with the high conductivity and structural stability of graphite which can further buffer the volume expansion of silicon [21,23–25].

The differences in the working potential between SiO_x and graphite in combination with the intrinsic hysteresis of SiO_x between lithiation and delithiation has an influence on the interplay between the two active materials. Cycling a LIB with a Gr/Si blend anode without fully charging or discharging the cell can result in disparate cell voltages at the same state of charge (SoC) due to the hysteresis of silicon [3,26]. In our previous research, we demonstrated that the SiO_x in Gr/SiO_x blend anodes undergoes preferential lithiation at increased C-rates at room temperature [27,28]. This leads to a different state of lithiation (SoL) of SiO_x and graphite at the same cell SoC, which remains even after prolonged relaxation periods due to the hysteresis of SiO_x [27]. Richter et al. [14] showed the inverse effect at extremely low temperatures of −20 °C in cells with Gr/Si anodes. However, the voltage discrepancies can occur even at a similar SoL for silicon. This phenomenon, which has been reported in numerous studies on silicon half-cells, typically occurs following the phase transition from fully lithiated amorphous (a) silicon to crystalline (c) $Li_{15}Si_4$ [2,11,13,17,29–39]. In general, silicon is in an amorphous state after formation while undergoing (de-)lithiation [34]. Two amorphous phase transitions occur during the lithiation process. Initially, fully delithiated a-Si forms a-Li_2Si [29,30] at a potential range of 250–200 mV vs. Li/Li^+ [29]. Upon further lithiation, the second phase transition to a-$Li_{3.5}Si$ occurs at approximately 100 mV vs. Li/Li^+ [29]. As the SoL is increased further, it is kinetically more preferable to rapidly [34,39] form the metastable [29,33] crystalline phase c-$Li_{3.75}Si$, often referred to as c-$Li_{15}Si_4$, rather than to increase the amount of Li in the amorphous state [17,29]. The formation of c-$Li_{15}Si_4$ is more likely to occur in regions with isolated silicon anions, which are created during lithiation by breaking the Si-Si bonds of larger silicon clusters with extended networks [29]. This crystalline phase transition occurs below a potential of 60 mV [33,38] to 50 mV vs. Li/Li^+ [2,29,31,32].

Ogata et al. [29,30] reported the formation of an overlithiated crystalline phase c-$Li_{3.75+\delta}Si$ with $\delta = 0.2–0.3$, which occurs when the SoL is increased further, to potentials below 50 mV vs. Li/Li^+. The formation of this c-$Li_{3.75+\delta}Si$ phase was found to be more favorable than the process of breaking additional Si-Si bonds to create the phase c-$Li_{3.75}Si$ from a-$Li_{3.5}Si$ [29]. In the absence of a crystalline phase during lithiation, the delithiation process shows the characteristic symmetrical hysteresis of silicon at its higher potential [30].

The reduction of a-$Li_{3.5}Si$ to a-Li_2Si occurs within the range of 270–310 mV vs. Li/Li^+ [29,36], followed by a return to fully delithiated a-Si at approximately 500 mV vs. Li/Li^+ [29,36]. However, the Li stored in a crystalline phase is delithiated at different potentials, creating an additional asymmetric voltage hysteresis [30,34]. The overlithiated crystalline phase is reduced back to c-$Li_{3.75}Si$ in the range of 50–150 mV vs. Li/Li^+ before any other Li is delithiated from silicon [29,30]. The transition back to an amorphous state, occurs at a significantly higher potential of around 440 mV vs. Li/Li^+ [2,11,29,35,36], which is at a higher level than the transition from a-$Li_{3.5}Si$ to a-Li_2Si. In addition, this decrystallization does not result in the amorphous phase a-$Li_{3.5}Si$ from which it was originally formed, but rather in a less lithiated phase. Two different phases are reported, namely a-Li_2Si [36,37] and a-$Li_{1.1}Si$ [29]. Caused by this effect, fully lithiated silicon exists at potentials as high as 440 mV vs. Li/Li^+, despite almost half of the Li is delithiated from amorphous Si. It is highly likely that this crystalline phase is formed in blend anodes containing graphite and silicon, given that the phase transition LiC_{12} to LiC_6 occurs at a potential plateau around 80 mV vs. Li/Li^+ [40,41]. Even minor polarization and concentration gradients can reduce the potential to a level below the threshold of 50–60 mV vs. Li/Li^+ for the formation of c-$Li_{3.75}Si$ [29,30]. For the same reason, c-$Li_{3.75}Si$ may also exist at potentials slightly above 440 mV vs. Li/Li^+ [11,35]. The crystalline phase was confirmed by several analytical methods. Specific peaks in the X-ray diffraction (XRD) spectrum are observable [32,37], dark spots in scanning electron microscopy (SEM) images indicate the existence of the crystalline phase [31] and the overlithiated phase c-$Li_{3.75+\delta}Si$ is detectable by nuclear magnetic resonance (NMR) [30].

The influence of the aforementioned characteristic on the potential of Gr/SiO_x anodes, combined with the intrinsic hysteresis of silicon [3,26,42], presents a significant challenge to the battery management system (BMS). A specific open-circuit voltage (OCV) does not directly correlate to a specific SoC for these blend anodes. Unlike laboratory battery test stands with a high accuracy in current measurements, the operation in BEVs does not allow coulomb counting to estimate the SoC, without a significant cumulative error over time [43–45].

The available online methods for estimating the SoC employ the OCV in two possible ways. The first is through direct comparison with a OCV lookup table after relaxation [43,44,46]. The second is as a foundation of model-based approaches that represent the entire electrochemical processes within the battery [43–46]. Beside the known dependencies of cell degradation and ambient temperature [43,45,47], the presence of a crystalline silicon phase can influence the OCV-SoC characteristic and, consequently, the SoC estimation. Similar to the SoC, the state of health (SoH) estimation is sensitive on OCV changes as it depends directly on OCV comparison after relaxation [48] or on OCV based peak comparison in incremental capacity analysis [46,49]. It is therefore necessary to track changes of the OCV over time to achieve an accurate SoC and SoH estimation, with the goal of improving the lifetime, safety, and performance of BEVs [43,44,49].

The memory effect was first observed for batteries in nickel cadmium (NiCd) and nickel metal hydride (NiMH) cells [50–54]. In such cells, repeated partial cycling results in a transient reduction in available capacity, which recovers following a slow, deep discharge [50,53]. In contrast, LIBs were long considered memoryless. However, Sasaki et al. [55] observed a memory effect in the cathode material $LiFePO_4$ (LFP),

whereby a single cycle in a lower SoC range resulted in changes to the voltage profile. The recovery of the available capacity after a substantial rest period was recently reported by Solchenbach et al. [56], resulting from an in-plane $LiPF_6$ gradient in cylindrical cells with Gr/Si anodes and a high excess of electrolyte. A memory effect for LIBs half-cells with pure silicon was also observed by Ulldemolins et al. [39] and Wen et al. [11], which is caused by the previously described crystalline phase transition. Similar observations were made for Gr/Si blend anode in half-cells [57]. To the best of our knowledge, this has not been investigated yet for SiO_x and on full cell level.

This study examines the induced memory effect of trapped Li in the crystalline phase of silicon for commercial and automotive LIBs with Gr/SiO_x anodes. The influence of the OCV and the resulting effect on the SoC estimation, the capacity retention and energy losses are presented. A series of parameter variations are conducted, including variations in the SoC range during cycling, the number of consecutive cycles, the C-rate during charging and discharging, and the temperature during operation. Moreover, the study includes measurements on anode half-cells with Gr/SiO_x blend anodes, providing additional insights.

2. Experimental

2.1. Commercial and automotive cells

To preclude the possibility that the results are attributable to a cell-specific effect, a total of five different commercial or automotive cell types are analyzed. These cell types vary in format, area of application, and manufacturer, and contain >5 wt% of SiO_x or a comparable amount of pure Si. However, from an operational standpoint, the capacity share between silicon and graphite is of particular interest. The pseudo OCV during discharging can be used to determine the capacity share of Si. We showed in our previous work that graphite is delithiated prior to silicon [28]. Given that graphite exhibits a distinct voltage profile with multiple phase transitions [58], it is possible to determine the SoC range at which graphite is mainly delithiated. This allows for an estimation of the capacity share of SiO_x and graphite. A detailed description of this calculation is presented in the Supplementary Materials section S1. The relevant cell parameters for each of the five cells are provided in Table 1, including the cell format, the nominal capacity, the operating voltage, the calculated silicon capacity share, and the gravimetric and volumetric energy density.

MoliCel M35A cells with a high energy density are used as the primary cell type in this work (Cell A), due to its high amount of SiO_x in the range of 10–14 wt%, determined by SEM with energy dispersive X-ray (EDX) analysis. This is in accordance with the high calculated silicon capacity share of 26.0 ± 0.5 %. Cell A is used for the majority of the parameter variation, while the other cell types are employed to show that the effect exists not only for one cell type. The MoliCel P45B (Cell B) is produced by the same manufacturer as Cell A. However, its design is more oriented towards providing high power than high energy, with a slightly lower amount of SiO_x. Cell C is manufactured by Murata/Sony and bears the identification US18650VTC6, with SiO_x as a secondary active anode material and the same cylindrical 18650 format as Cell A. To ensure that this effect is not exclusive to SiO_x but also exists in blend electrodes using pure silicon besides graphite, the SDI 30Q is used as Cell D. According to Bazlen et al. [59], this cell contains nano-Si in addition to graphite. The fifth cylindrical cell is a large-format automotive cell, further referred to as Cell E. This cell is produced at a BMW in-house prototype line, with the sole purpose of research and development. Full disclosure of all specific cell parameters is not possible, due to confidentiality reasons. Therefore, the results of Cell E are either presented as approximate values or by normalization.

2.2. Anode half cells

Additionally to cells A-E, a Gr/SiO_x blend electrode consisting of 7.6 wt% SiO_x (d50 ~5 µm) and 87.4 wt% graphite (~20 µm), is utilized for the anode half-cell study. The lithium predoped SiO_x secondary particle contains nano-sized Si, SiO_2, silicates and is coated with a thin carbon layer to improve its electrical conductivity. The electrode coating mixture of 1 wt% conductive carbon, 0.5 wt% carboxymethyl cellulose (CMC), and 3.5 wt% polyacrylate-based binder has a mass loading of ~10 mg/cm^2 and is pressed to a thickness of ~60 µm.

Prior to cell assembly, the electrodes are dried in a vacuum oven at 120 °C for at least 12 h. Two types of separators are employed in this work, namely a tri-layer PP/PE/PP separator (17 mm diameter, Celgard 2325, Celgard LLC, USA) and a glass fiber separator (16.5 mm diameter, 260 µm, GF/A Whatman, USA). Both separators are dried under vacuum in a glass oven (B-585, BÜCHI Labortechnik GmbH, Germany) for at least 12 h. The drying temperature for the tri-layer separator is 60 °C and for the glass fiber 300 °C. The cells are prepared in a dry room with a dew point < -50 °C. One piece of each type of separator is sandwiched between a lithium metal (300 µm thick, 16 mm in diameter) and Gr/SiO_x blend electrode disc (15 mm in diameter) in a CR2032 coin cell configuration. The tri-layer separator is facing to the SiO_x-graphite electrode. A commercially available electrolyte containing ethylene carbonate (EC), dimethyl carbonate (DMC), ethyl methyl carbonate (EMC) and fluoroethylene carbonate (FEC) is added in an amount of 100 µl.

The SiO_x-graphite//Li cells are allowed to rest at OCV after cell assembly to ensure sufficient wetting of the electrodes. Formation is performed galvanostatically with two consecutive full cycles at a rate of C/10 between 0.03 and 1.0 V vs. Li/Li$^+$. A constant voltage (CV) step is incorporated at the end of the electrode lithiation (i.e., 0.03 V vs. Li/Li$^+$) until the C-rate drops below C/50. The formation and subsequent half-cell measurement is performed isothermally at 25 °C using a battery test system (SL1130A, Keysight Technologies, United States) in a climatic chamber (customized model, Angelantoni Test Technologies, Italy).

2.3. Test procedure

All tests conducted in this study proceed with a consistent methodology. First, the available begin-of-test (BoT) capacity is determined through a capacity check-up. Subsequently, a specific number of cycles is conducted within the designated SoC range. The test is concluded with a second capacity check-up to determine the available end-of-test (EoT) capacity and to calculate the capacity retention, which is analogous to the state of health (SoH) of the cell.

The capacity check-up consists of three consecutive full cycles with a

Table 1
Specific parameters of the five cylindrical cells with a blend anode, used in this work. The share of the silicon capacity is calculated based on the pseudo OCV and the anode potential. The remaining parameters are derived from the specification provided by the cell manufacturers.

Cell	Format	Nom. Capacity	Operation voltage	Silicon capacity share	Gravimetric energy density	Volumetric energy density
A	18650	3.45 Ah	2.5–4.2 V	26.0 ± 0.5 % (SiO_x)	250 Wh kg^{-1}	700 Wh l^{-1}
B	21700	4.5 Ah	2.5–4.2 V	20.7 ± 0.5 % (SiO_x)	242 Wh kg^{-1}	643 Wh l^{-1}
C	18650	3.12 Ah	2.5–4.2 V	18.3 ± 0.5 % (SiO_x)	241 Wh kg^{-1}	631 Wh l^{-1}
D	18650	3 Ah	2.5–4.2 V	14.8 ± 0.5 % (nano-Si)	238 Wh kg^{-1}	646 Wh l^{-1}
E	4695	~30 Ah	2.8–4.2 V	15–20 % (SiO_x)	~300 Wh kg^{-1}	~800 Wh l^{-1}

constant-current constant-voltage (CCCV) charge step and a constant-current (CC) discharge step until the maximum or minimum cell voltage is reached, respectively. The CV phase of the charge step is terminated when the C-rate drops below C/50. Both the charge and discharge step use a C-rate of C/3. The available capacity, Q_{ref}, is determined during the final discharge step, as the preceding two cycles should be sufficient to eliminate all potential side effects that may affect the capacity of the cell.

During cycling, the upper or lower SoC deviate from 100 or 0 %, respectively. CCCV charging or discharging with a cutoff C-rate of C/10 is employed to set SoCs between 0 and 100 %. The voltage for each specific SoC is derived from the C/10 pseudo-OCV in the corresponding direction. It is essential to distinguish between charge and discharge OCV, as LIBs containing silicon have no unique OCV, due to the voltage hysteresis of silicon.

The test procedure of the reference case is conducted with the following parameters during cycling. Twenty cycles are performed between 15 and 100 % SoC at an ambient temperature of 25 °C, controlled by a climate chamber. A C-rate of C/2 is selected for charging and discharging, respectively. The lower SoC is set to approximately the center of the Si-range for cell A, as defined in section S1 in the Supplementary Materials.

The base test for cell A repeats this reference case five consecutive times, with a capacity check-up performed after each set of 20 cycles. In this way, all possible changes during the degradation process of the cell can be observed. Subsequently, each parameter is subjected to further variations to analyze its effect. This contains a variation in the number of cycles, a variation in the SoC range, a variation in the C-rate, and a variation in the temperature. The reference case is repeated for cells B to E, to eliminate the possibility of a specific effect, attributed to cell A. Furthermore, an additional lower SoC variation is conducted for cell E. The comprehensive test matrix is presented in Table 2.

The aforementioned anode half-cells are subjected to a similar test procedure. Fifteen consecutive cycles are conducted at 25 °C between different upper and lower cutoff potentials with a C-rate of C/10. The reduced C-rate compared to the reference case is required because coin cells typically exhibit an increased polarization compared to full cells. This is due to the overall configuration of the half cells, including the increased separator thickness. The upper cutoff potential is selected either at 400 mV vs. Li/Li^+, which is slightly below the potential of 440 mV vs. Li/Li^+ at which the crystalline phase is reverted to amorphous silicon [35,46], or at 270 mV vs. Li/Li^+, which is slightly above the potential at which graphite is active [40,60]. The lower cutoff voltage is set to either 60 mV vs. Li/Li^+ or 10 mV vs. Li/Li^+. According to the literature, at 10 mV vs. Li/Li^+ the crystalline phase transition of silicon is highly expected while at 60 mV vs. Li/Li^+ this transition should not have occurred yet [29,39]. The exact test specification is also described in Table 2.

Table 2
Overview of all conducted test scenarios, including the utilized cell, the number of cycles in between the check-ups, the employed SoC range during cycling, the C-Rate for charging and discharging, and the ambient temperature.

	Cell	# Cycles	SoC Range	C-Rate (Charge - Discharge)	Temperature
Reference case	Cell A	20	15–100 %	C/2 – C/2	25 °C
Base test/Aging	Cell A	5x 20	15–100 %	C/2 – C/2	25 °C
Number of cycles	Cell A	5	15–100 %	C/2 – C/2	25 °C
		50	15–100 %	C/2 – C/2	25 °C
		100	15–100 %	C/2 – C/2	25 °C
		200	15–100 %	C/2 – C/2	25 °C
SoC variation	Cell A	20	0–100 %	C/2 – C/2	25 °C
		20	5–100 %	C/2 – C/2	25 °C
		20	10–100 %	C/2 – C/2	25 °C
		20	20–100 %	C/2 – C/2	25 °C
		20	25–100 %	C/2 – C/2	25 °C
		20	30–100 %	C/2 – C/2	25 °C
		20	50–100 %	C/2 – C/2	25 °C
		20	70–100 %	C/2 – C/2	25 °C
		20	15–80 %	C/2 – C/2	25 °C
		20	15–60 %	C/2 – C/2	25 °C
		20	15–40 %	C/2 – C/2	25 °C
		20	30–70 %	C/2 – C/2	25 °C
C-rate variation	Cell A	10	15–100 %	C/10 – C/10	25 °C
		20	15–100 %	C/5 – C/5	25 °C
		20	15–100 %	1C–1C	25 °C
		20	15–100 %	2C–2C	25 °C
Temperature variation	Cell A	20	15–100 %	C/2 – C/2	10 °C
		20	15–100 %	C/2 – C/2	40 °C
Cell variation	Cell B	20	15–100 %	C/2 – C/2	25 °C
	Cell C	20	15–100 %	C/2 – C/2	25 °C
	Cell D	20	15–100 %	C/2 – C/2	25 °C
Cell-variation + SoC variation	Cell E	20	5–100 %	C/2 – C/2	25 °C
		20	10–100 %	C/2 – C/2	25 °C
		20	15–100 %	C/2 – C/2	25 °C
		20	20–100 %	C/2 – C/2	25 °C
		20	30–100 %	C/2 – C/2	25 °C
		20	40–100 %	C/2 – C/2	25 °C
		20	50–100 %	C/2 – C/2	25 °C
Anode half cell	7.6 wt% SiO_x	15	10–400 mV vs. Li/Li^+	C/10 – C/10	25 °C
		15	10–270 mV vs. Li/Li^+	C/10 – C/10	25 °C
		15	60–270 mV vs. Li/Li^+	C/10 – C/10	25 °C

3. Results and discussion

3.1. Influence of lithium trapping on the cell behavior

The memory effect of LIBs containing silicon as a secondary active anode material is evident when examining the discharge capacity during cycling. Fig. 1 illustrates the discharge capacity for each of the five sets of 20 cycles between 15 and 100 % SoC, in comparison to the discharge capacity of the third check-up cycles. The latter is employed to determine the available capacity Q_{ref}. While the discharge capacities of the check-ups demonstrate a nearly linear decline (R^2 = 98.4 %), it is evident that the capacity of the partial cycles (15–100 % SoC) exhibits an accelerated decrease but subsequently recovers a majority of the capacity loss during the check-ups. The actual loss of capacity between the check-ups can be attributed to the general degradation processes inherent in LIBs. Given the significant volume expansion that SiOx undergoes upon lithiation, the most likely processes are additional SEI growth and loss of active material due to particle cracking [15,16]. As the temperature and C-rate of the check-ups and cycling are identical or comparable, it can be assumed that the complete discharge during the check-up has a sort of recovery effect on the battery, thereby reversing the significant capacity loss observed during cycling. This behavior of the discharged capacity is comparable to the results observed in pure silicon half-cells [11,39].

This impression solidifies upon closer examination of the voltage behavior during discharging. The greater deviation is evident between the initial and final 15–100 % SoC cycles and between the first and the second full cycles of the check-up after cycling at the EoT condition. Fig. 2 shows the four aforementioned voltage profiles, in addition to the last full discharge step of the BoT check-up. All profiles are displayed over the discharged capacity during each individual cycle. As previously stated, graphite is predominantly delithiated at higher SoCs and SiO_x at lower SoCs [28], here indicated as Gr-range and Si-range, respectively.

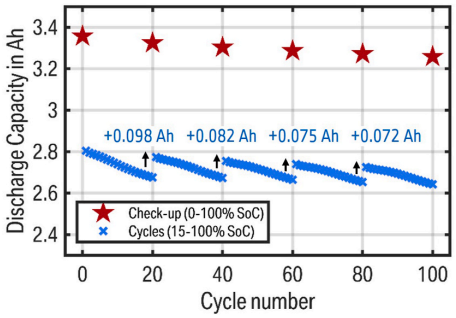

Fig. 1. Discharged capacity vs. cycle number in the base test with five sets of 20 cycles between 15 and 100 % SoC each and a check-up between each of the five sets. The discharged capacity of the third check-up cycle is indicated in red and represents the reference capacity of the cell at this specific point in time, which is used to calculate the SoH of a battery. The discharged capacity of all 100 cycles in blue illustrates the memory effect, exhibiting a rapid increase after each check-up before displaying a large decrease. (For interpretation of the references to colour in this figure legend, the reader is referred to the Web version of this article.)

In the Gr-range, neither the cycles nor the check-up exhibit any deviation. However, a reduction in voltage is observable in the Si-range with increasing cycle count. Therefore, this section is presented in more detail as a zoom plot in Fig. 2. The lower SoC of 15 % is set by a constant voltage phase at the corresponding voltage, resulting in a diminished discharge capacity for the last cycle. Similar voltage changes are present in the first cycle of the EoT check-up, which will henceforth be referred to as the recovery cycle. The voltage profile shows a decrease at the start of the Si-range, when being compared to the second cycle of the EoT check-up, further referred to as the normal cycle, or the BoT check-up. However, the steep decrease of the voltage reverses at approximately 3.1 V, reaching a near-plateau state, until it converges towards the profile of the normal cycle. Upon reaching a voltage below 2.9 V, only a minor deviation is observable between the recovery and normal cycle.

The described behavior presents a multifaceted influence on the battery operation. As previously stated, the first effect is a reduced cyclical capacity retention compared to the actual capacity retention ascertained during the check-ups. Secondly, a reduction in the voltage within the Si-range results in an error in the SoC estimation, when the SoC estimation is based solely on the cell voltage. As the same voltage is reached at a lower discharge capacity, the estimation results also in a lower value, given that high precision coulometry is only available for test stands. This is particularly crucial in BEVs, where reliable range estimation is a necessity. In the presented case, the remaining driving range will decline at a significantly accelerated rate during the first half of the Si-range and on the contrary will decline at a lower rate than the actual driving distance during the latter half. A third negative consequence is a minor energy loss between the recovery and normal cycle. This energy loss consists of two parts. Firstly, the lower voltage within the Si-range results in a decline in the energy. Secondly, the slightly reduced capacity of the recovery cycle compared to the normal cycle further reduces the discharged energy. Given the absence of a discernible distinction between the second and the third cycle of the EoT check-up, it can be reasonably inferred that this second energy loss can also be attributed to the partial cycling. It is either a secondary effect of the presented memory effect or might be explained by the diffusion of Li-ions into the anode overhang, which are only delithiated during consecutive discharge steps [61–63].

In general, batteries undergo an aging process upon repeated cycling [64,65]. Therefore, it is necessary to determine not only the capacity retention of the cycles between 15 and 100 % SoC, but also the capacity retention between the BoT and EoT check-up. It is essential to consider the overall degradation when evaluating the cyclical capacity retention, as this mitigates the severity to a certain extent. As previously stated, the third discharge cycle of the check-up is used for this determination. The capacity retention $rQ_{\text{Check-up}}$ describes the relation between Q_{ref} at EoT condition and Q_{ref} at BoT condition.

$$rQ_{\text{Check-up}} = \frac{Q_{\text{ref,EoT}}}{Q_{\text{ref,BoT}}} \tag{1}$$

A comparable calculation can be performed to determine the capacity retention during cycling rQ_{Cycling}, by comparing the discharged capacity of the first with the last partial cycle:

$$rQ_{\text{Cycling}} = \frac{Q_{\text{cycle,first}}}{Q_{\text{cycle,last}}} \tag{2}$$

$Q_{\text{cycle,first}}$ describes the discharge capacity of the first cycle, here between 15 and 100 % SoC and $Q_{\text{cycle,last}}$ describes the discharge capacity of the last, which is in this case the 20th, cycle. The maximum SoC error is described as:

$$SoC_{\text{Error,max}} = \frac{\max_x \left(Q_{\text{EoT,normal}}(U = x) - Q_{\text{EoT,recovery}}(U = x)\right)}{Q_{\text{ref,EoT}}}, \tag{3}$$

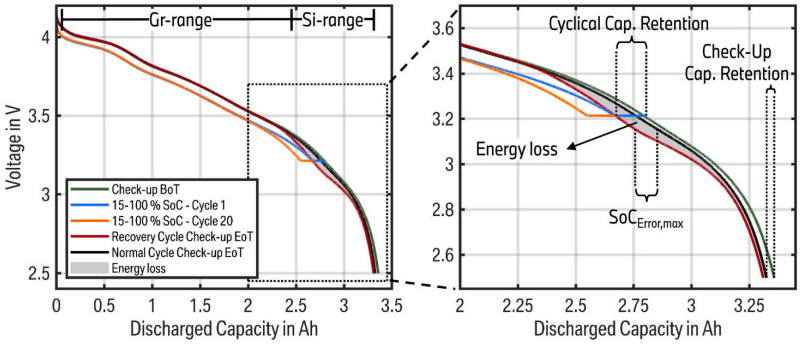

Fig. 2. Discharge voltage profile of all relevant cycles, influenced by the memory effect and displaying the recovery. A more detailed view is provided in a zoom plot on the right, in the range above 2 Ah, where notable deviations in voltage profiles are observed. The following cycles are presented in chronological order: Last cycle of the BoT Check-Up (grey), initial 15–100 % SoC cycle (blue), final 15–100 % SoC cycles (orange), first EoT check-up or recovery cycle (red), and second EoT check-up or normal cycle (red). Furthermore, the metrics used to assess the severity of the memory effect are visualized, including the check-up and cyclical capacity retention, the maximum SoC error, and the energy loss (red area). (For interpretation of the references to colour in this figure legend, the reader is referred to the Web version of this article.)

where $Q_{EoT,normal}(U = x)$ describes the discharge capacity when the voltage U is equal to x during the normal cycle of the EoT check-up. Similarly, $Q_{EoT,recovery}(U = x)$ describes the discharge capacity of the recovery cycle of the EoT check-up. In the presented case in Fig. 2, the $SoC_{Error,max}$ is equal to 2.55 % at a voltage of 3.15 V. The energy loss E_{loss} of the recovery cycle in relation to the normal cycle is defined by the subtraction of the respective energies:

$$E_{loss} = E_{normal} - E_{recovery} \tag{4}$$

$$E = \int_{t_{start}}^{t_{end}} U \cdot |I| \, dt \tag{5}$$

Eq. (5) is used to calculate E_{normal} and $E_{recovery}$ in Eq. (4). The integral is calculated from start to end of the respective discharge step. Absolut value of the current I is necessary, as the current is usually defined negative during discharging. In Fig. 2 the energy loss accounts for 0.6 %, or 73 mWh. All the metrics described for quantifying the memory effect are also indicated in the zoom plot in Fig. 2.

3.2. Crystalline silicon phase transition

The memory effect can be explained by reference to the previously mentioned phase transition of silicon from amorphous to crystalline that occurs when reaching a state of full lithiation. To confirm that the origin is indeed the phase transition, a test scenario with a pure graphite anode similar to the base test is analyzed, which does not indicate the presence of a memory effect. The voltage profiles of the recovery and normal cycle are displayed in Fig. S2 in the Supplementary Materials. To the best of our knowledge, a memory effect attributed to pure graphite anodes has also never been reported in the literature. Moreover, a change in the OCV is responsible for the changes in the voltage profile during the recovery cycle, which is confirmed by repeating the reference case with a relaxation interval every 2 % SoC.

While the phase transition was investigated in detail for pure silicon anode half-cells [11,29,39], the consequences for a full cell with a blend anode have not been examined yet. The phase transition from a-$Li_{3.5}Si$ to c-$Li_{3.75}Si$ occurs at an anode potential below 60 mV vs. Li/Li^+ [11,29,33]. In a blend anode in a full cell, this potential is typically not reached for the open circuit potential (OCP), as an SoC of 100 % is typically located before reaching fully lithiated graphite [30]. Consequently, the charging process terminates during the last graphite plateau of the phase transition from LiC_{12} to fully lithiated LiC_6 with an OCP of ~80 mV vs. Li/Li^+ [40,41]. However, with only a small polarization, the actual potential is likely to fall below the threshold of 60 mV vs. Li/Li^+, which permits for the phase transition of silicon to its crystalline form [30]. Fig. 3 shows the pseudo OCP during C/20 (de-)lithiation of harvested electrodes from cell A. Even at this C-rate of C/20, the potential falls slightly below 60 mV vs. Li/Li^+ at a fully cell SoC of 100 %. This is determined through the fitting of harvested electrode potentials to a C/20 pseudo OCV of cell A. Discharging the cell to 15 % SoC has to terminate at a potential below 440 mV vs. Li/Li^+, otherwise the crystalline phase will be reverted back to a-$Li_{1.1}Si$ during each cycle [29] and no memory effect would occur. This is demonstrated in Fig. 3 for cell A, where the potential at 15 % full cell SoC is indeed slightly below the threshold. Given that the SoC is set using a CV phase until a cutoff C-rate of C/10, it is reasonable to conclude that the anode potential remains largely below the threshold. Therefore, with each cycle, more Li is trapped in the crystalline phase of Si, which is not converted back to the amorphous phase. However, even a slightly lower SoC might recover the trapped Li during each cycle for cell A.

It is important to note that the anode potential in half-cells is not identical to that in full cells. The reason is that the anode/cathode interaction and the voltage range are different in both cell types. Accordingly, the full cell SoC illustrated in Fig. 3 is merely an approximation.

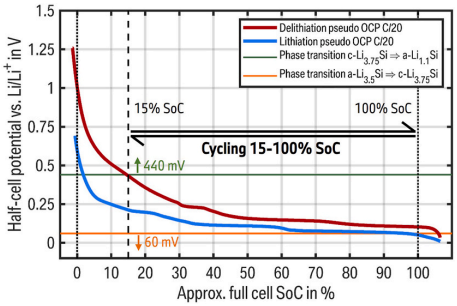

Fig. 3. Lithiation (blue) and delithiation (red) anode potential vs. Li/Li+ of harvested electrodes from cell A. The effective full cell SoC for both 0 and 100 % is indicated with dotted lines. The full cell SoC of 15 % is indicated with a dashed line, visualizing the potential range during the partial cycling in the reference case. The anode potential for the phase transition from a-$Li_{3.5}Si$ to c-$Li_{3.75}Si$ below 60 mV is indicated in orange, while the reverse transition from c-$Li_{3.75}Si$ to a-$Li_{1.1}Si$ above 440 mV is represented in green. (For interpretation of the references to colour in this figure legend, the reader is referred to the Web version of this article.)

During the first full discharge, which is in this test scenario the recovery cycle of the EoT check-up, the anode potential rises above 440 mV vs. Li/Li^+, resulting in the back transformation to the amorphous silicon phase. This typically results in a plateau at 440 mV vs. Li/Li^+ until the phase transformation is completed [11,35]. This plateau can also be observed at full cell level in Fig. 2 in the range of 2.75–3 Ah of discharged capacity. The comparatively small voltage decrease instead of an exact plateau within this range can be attributed to the decreasing cathode potential. The observed memory effect can thus be fully explained by the phase transition of silicon from crystalline to amorphous.

This is a comparable reason to the cause of the memory effect for NiCd and NiMH cells, which can be explained by the formation of the γ-NiOOH phase [50,52,54] or the amorphous phase HNi_2O_3 [53]. Both phases are reversed upon deep discharge, similar to the c-$Li_{3.75}Si$ phase. On the contrary, the origin of the memory effect in LFP cells can be attributed to the two-phase equilibrium potential of LFP, which results in the voltage deviations [55].

3.3. Parameter variation on full cell level

In order to investigate the impact of the memory effect on the operation of batteries, particularly in the context of BEVs, a parameter variation is presented in the following section. The impact on the operation is determined by evaluating the changes in capacity retention, maximum SoC error, and energy loss, as described in Eqs. (1)–(5), in comparison to the reference case. The parameter variation includes alterations in the impact over aging, the number of cycles prior to recovery, the SoC range during cycling, the used C-rate, and the ambient temperature.

3.3.1. Memory effect upon aging

During the base test, the reference case is repeated five times with a check-up conducted between each set of cycling. This permits an analysis of the extend of Li trapping throughout cell degradation. Fig. 4a–c illustrate the three defined metrics to measure Li trapping. Fig. 4a shows the capacity retention in percent for the check-ups and the cycles of all five sections, according to Eq. (1) and Eq. (2), respectively. The capacity retention of the check-up is included in the figure since it is important to evaluate the cyclical capacity retention correctly. A reduction in the capacity retention during the check-ups indicates a degradation of the cell. Accordingly, the difference between the cyclical and check-up capacity retention is relevant when evaluating Li trapping. Fig. 4b

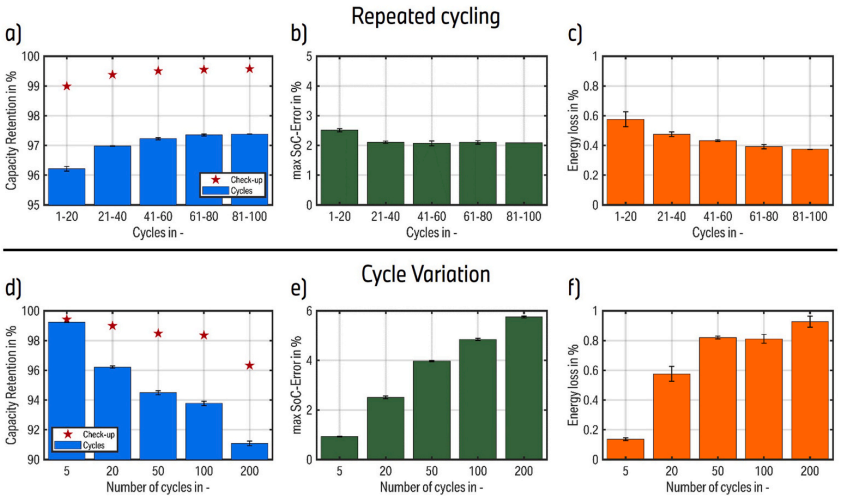

Fig. 4. Illustration of the metrics for quantifying Li trapping for the five sets of the reference case in the base test (a–c), as well as the variation in the number of cycles (d–f). (a) Capacity retention for the check-ups and the specific cycles in between the check-ups for each set of 20 cycles. (b) Maximum SoC-error between the recovery and normal cycle for each set of 20 cycles. (c) Energy loss of the recovery cycle, compared to the normal cycle, for each set of 20 cycles. (d) Capacity retention for the check-ups and the specific cycles in between the check-ups for each number of cycles in the cycle variation. (e) Maximum SoC-error between the recovery and normal cycle for each number of cycles in the cycle variation. (f) Energy loss of the recovery cycle, compared to the normal cycle, for each number of cycles in the cycle variation.

illustrates the maximum SoC error, as defined in Eq. (3), while Fig. 4c depicts the energy loss between the recovery and normal cycle during the EoT check-up according to Eq. (4). Similar plots to those presented in Fig. 4a–c are presented in subsequent sections for the remaining parameter variations.

The results of the repeated cycling demonstrate that aging has only a minor impact on the memory effect. A trend emerges, indicating that Li trapping has a progressively diminished impact with increasing lifetime. This trend is particularly evident between the first and the second set of 20 cycles. The first set exhibits the least capacity retention, the largest maximum SoC error, and the largest energy loss. Especially the maximum SoC error remains largely unchanged for the remaining sets, while the other metrics improve and appear to be converging with increasing set number. A comparable trend towards a reduction in the recovered capacity with increased aging is also evident in Fig. 1.

It can be inferred that there is a slight correlation between an improvement in the memory effect and increased aging, with the largest sensitivity observed during the initial cycles. It is unclear whether the number of cycles or the number of phase transitions from crystalline to amorphous during the recovery cycles is responsible for this effect. Similar results were also reported on pure silicon half-cell level, with a reduced memory effect with increased total cycle count [2,30,35].

3.3.2. *Variation in the number of cycles*

In this section, the number of repeated cycles before recovery is modified. All remaining test parameters are consistent with those of the reference case. The number of cycles varies from 5 to 200 cycles, as listed in Table 2. The results of the three metrics for this variation are visualized in Fig. 4d–f in a manner identical to that employed for the aging case in Fig. 4a–c. A clear dependency exists between the extend of Li trapping with the number of cycles. With increasing cycle number, all metrics indicate an increase in the amount of trapped Li. However, the amount of trapped Li appears to reach a maximum with increasing cycle count. The difference between capacity retention and check-up is approximately 4 % for the case 50, 100 and 200, with the energy loss exhibiting a slight increase. The SoC error is also not increasing in a linear fashion, with an additional error of 1 % for the case 200 cycles over the error of approximately 5 % during the initial 100 cycles. With a difference of 5 % between the capacity retention of the check-ups and the cycles and a maximum SoC error of approximately 6 % in the 200-cycle case, this cell appears to reach saturation between 5 and 6 % of trapped Li. The saturation is contingent upon the silicon capacity share, and thus will vary for cells with disparate silicon contents. Given a silicon capacity share of 25.5 % and a Si-range of 29.9 %, it can be assumed that approximately half of the silicon transitions to the crystalline phase, given that some of the remaining graphite will also be delithiated until 15 % SoC. Further details are presented in section S1 in the Supplementary Materials.

In summary, the impact of the memory effect increases with the number of cycles between the check-ups until reaching a saturation, which depends on the silicon content.

3.3.3. *Cell variation*

To ensure that the memory effect is not cell-specific for cell A, but rather a general occurrence of silicon in blend anodes, the reference case is repeated for all five cells listed in Table 1. Fig. 5 compares the resulting capacity retention, the maximum SoC error, and the energy loss. The maximum SoC error in Fig. 5b demonstrates that the memory effect occurs irrespective of the cell format, design, and silicon material. With the exception of cell C, the difference between the check-up and cyclical capacity retention in Fig. 5a is comparable for all remaining cells. The voltage profiles of cells B to E are presented in Fig. S3 of the Supplementary Materials. A comparable voltage deviation is observable during the recovery cycle, which indicates the presence of Li trapping. This suggests that the memory effect occurs in a similar manner in nano-Si as in SiO_x and independent of the cell format.

Cell C shows a significantly lower difference between the capacity retention of the check-up and cycles, yet also displays a strong cell degradation of ~2.5 % within the 20 cycles. Given that the crystalline phase transition is also associated with an increased cell degradation, it may be inferred that Cell C is less resistant to aging mechanisms as the remaining cells. As previously stated in Section 3.3.1, the memory effect is less pronounced in the presence of increased degradation, which also explains the reduced difference in the capacity retention. The largest

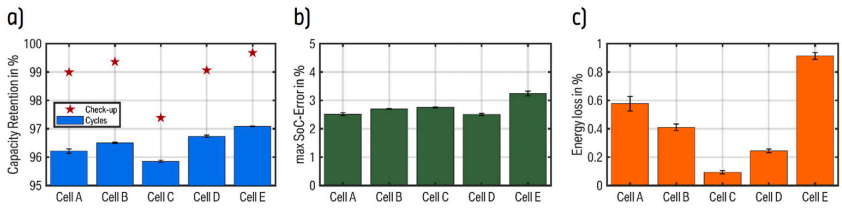

Fig. 5. Illustration of the metrics for quantifying Li trapping for the reference case of all cell types. (a) Capacity retention for the check-ups and the specific cycles in between the check-ups for each cell type. (b) Maximum SoC-error between the recovery and normal cycle for each cell type. (c) Energy loss of the recovery cycle, compared to the normal cycle, for each cell type.

deviation between the cells is observable in Fig. 5c for the energy loss. This can be primarily attributed to the discrepancy between the discharged capacity of the recovery and normal cycle. As aforementioned, the recovery cycle typically exhibits a slightly reduced discharged capacity than the normal cycle. The reason for this additional capacity regain between the recovery and normal cycle is yet to be elucidated and will be the subject to further investigation. The elevated cutoff voltage for Cell E is responsible for the observed increase in energy loss, as the recovery cycle is not yet fully completed. Moreover, the lower energy loss of cells C and D can be attributed to their discharge capacity, as evidenced by the recovery cycle exhibiting values closer to those of the normal cycle. The pronounced degradation of cell C, in particular, results in a discernible decline between the recovery and normal cycle in the EoT check-up. This further diminishes the energy loss, as the memory effect and the degradation cancel each other out.

3.3.4. SoC variation

Fig. 6 displays the three metrics for a variation in the SoC range during cycling for cells A and E, as listed in Table 2. The results demonstrate a pronounced dependence of this parameter. The most significant memory effect for cell A occurs at a lower SoC between 15 and 25 %, with an upper SoC of 100 %. All metrics show Li trapping in the cases 30–100 %, 15–80 %, and 30–70 %, however, to a lesser extent. For the remaining SoC ranges, little to no Li trapping is apparent in the displayed metrics in Fig. 6a–c, nor in an analysis of the voltage profiles. The SoC variation for cell E exhibits a similar behavior, illustrated in Fig. 6d–f, with a shift towards lower SoCs of 10–20 % for the most severe cases. This can be attributed to the lower amount of silicon in the blend anode.

At a lower SoC of 10 % or less, no discernible indication of Li trapping is observable. Nevertheless, a small increase of the lower SoC to ~15 % results in a considerable amount of Li trapping. Fig. 3 shows that the anode potential at a full cell SoC of 15 % is only slightly below the threshold of 440 mV vs. Li/Li^+ at which the crystalline phase c-$Li_{3.75}Si$ reverses to amorphous a-Li_xSi phase [11,29,35,36]. Consequently, the anode potential rises above 440 mV vs. Li/Li^+ at a full cell SoC below ~15 %, thereby recovering the trapped Li during each cycle and no difference is observable in the EoT check-up. There still exists a small amount of trapped Li for each cycle when the SoC reaches 100 %. However, this quantity exists in any full cycle and is therefore undetectable through voltage analysis. The same relation applies to the case 5–100 % SoC for cell E. Due to the lower amount of Si, the anode potential of 440 mV vs. Li/Li^+ is not reached in the case of 10–100 % SoC, resulting in a significant amount of trapped Li for this cell.

Increasing the lower SoC above 30 % for cell A, or above 20 % for cell E, results in a reduction of the memory effect, compared to the aforementioned SoC ranges that exhibit a pronounced memory effect. Since the upper SoC is maintained at 100 % and therefore an anode potential drop below 50 mV vs. Li/Li^+, it is reasonable to anticipate the occurrence of Li trapping. However, compared to the reference case, silicon is

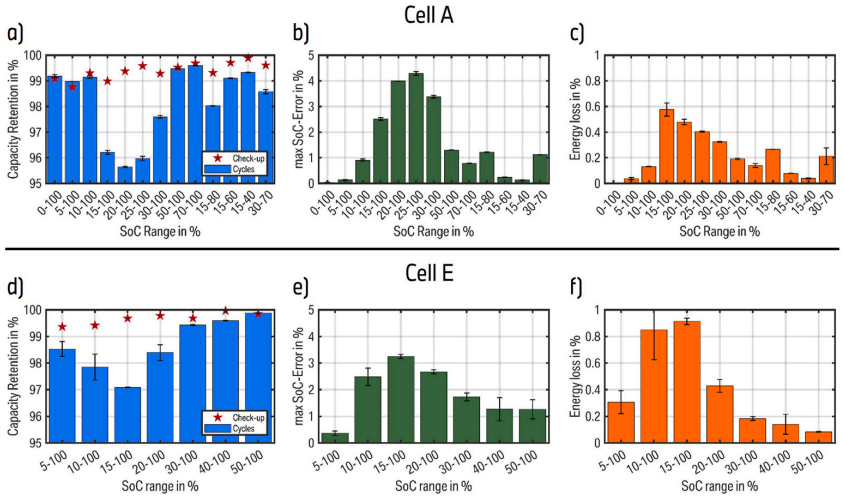

Fig. 6. Illustration of the metrics for quantifying Li trapping for the variation in the SoC range during cycling for Cell A (a–c) and cell E (d–f). (a) Capacity retention for the check-ups and the specific cycles in between the check-ups for each SoC range of cell A. (b) Maximum SoC-error between the recovery and normal cycle for each SoC range of cell A. (c) Energy loss of the recovery cycle, compared to the normal cycle, for each SoC range of cell A. (d) Capacity retention for the check-ups and the specific cycles in between the check-ups for each SoC range of cell E. (e) Maximum SoC-error between the recovery and normal cycle for each SoC range of cell E. (f) Energy loss of the recovery cycle, compared to the normal cycle, for each SoC range of cell E.

mostly not active during the cycling for these SoC ranges. As evidenced by the analysis of the pseudo OCV of cell A, only graphite is active during discharging to 30 % SoC. Therefore, silicon remains almost fully lithiated even at the higher rate of C/2 at a SoC higher than 30 %. This suggests that the silicon needs to be active to exhibit trapped Li. The certain reason for this relation cannot be given at this point and will be further investigated. One potential explanation is the breakage of Si-Si bonds in large silicon clusters to create isolated silicon anions. Ogata et al. [30] state that the formation of c-$Li_{3.75}Si$ is kinetically enhanced if isolated silicon anions exist. During lithiation, the larger Si-Si clusters are broken down into smaller clusters, which ultimately result in the formation of isolated silicon anions. In the case of a blend electrode, where silicon is not active above ~30 % SoC, these clusters are unable to be further broken down into smaller clusters, which hinders the transition to the crystalline phase. This also provides an explanation for the increase in the amount of trapped Li with each cycle in the critical scenarios, as an increased proportion of isolated anions is expected when the silicon is active.

The impact of varying the upper SoC on the memory effect is examined for cell A and displayed in Fig. 6a–c. At upper SoCs below 100 %, the effect initially decreases and then becomes nearly undetectable. At upper SoCs of 70 and 80 %, the three metrics show a discernible but reduced amount of trapped Li in comparison to the 100 % case with the same lower SoC. However, at upper SoCs below 70 %, the impact of the effect reduces to a similar degree as in the cases with lower SoCs below 15 %. This indicates that no memory effect exists. Given that the crystalline phase forms below an anode potential of 50 mV vs. Li/Li^+ [2,31,32], even with the polarization at a C-rate of C/2, the OCP needs to be near this value. For blend anodes containing silicon and graphite, the OCP reaches this threshold, even at SoCs below 100 %. This is attributed to the large voltage plateau of the graphite phase transition from LiC_{12} to LiC_6 at a potential of ~0.08 V at high lithiation [7]. Fig. 3 illustrates this plateau for cell A at a full cell SoC above 65 %. Therefore, when the charge step progresses to an SoC which is within this plateau, the anode potential with polarization drops below the threshold of 50 mV vs. Li/Li^+ to from crystalline Si. A charge step that terminates prior to this plateau, the anode potential does not decrease consistently below the threshold, resulting in the absence of Li trapping due to a lack of formation of the crystalline phase.

In summary, a critical SoC range for the upper and lower SoC exists, within which a pronounced memory effect occurs. The lower SoC must be sufficiently high to ensure that the anode potential remains below ~440 mV vs. Li/Li^+, while also being sufficiently low for silicon to be actively (de-)lithiated during each cycle. The upper SoC should be sufficiently high to terminate the charge process within the last graphite plateau. However, an increase in the upper SoC results in a more pronounced memory effect. Additionally, this critical SoC range depends on the silicon share of the blend anode.

3.3.5. *C-rate variation*

The variation of the C-rate, ranging from a low rate of C/10 to a high rate of 2C, demonstrates that there is nearly no rate dependency with regards to Li trapping. Fig. 7a–c shows the three metrics, which display no large deviation except in the case of a C-rate of C/10. However, this outlier, indicating a lower impact of Li trapping at this low rate, may be misleading due to the fact that only half the number of cycles are performed for this rate, due to limitations in the test duration. Projecting the 10 cycles of the C/10 case to the standard of 20 cycles would result in comparable values for all metrics to the remaining C-rates. This reinforces the strong dependency of the number of cycles. Since cell A is designed with a high energy density rather than providing a high power, the cells show increased degradation at higher rates, visible in Fig. 7a. This is most likely attributed to the deposition of metallic Li during charging, which occurs at anode potentials below 0 V vs. Li/Li^+ [66,67]. It is difficult to apply the common and simple Li deposition indication methods, due to the specific design of the cell tests. The use of CCCV charging hinders the analysis of discrepancies in the voltage relaxation [68–70]. Furthermore, the overall reduced capacity retention within each cycle, caused by the memory effect, precludes the use of the coulombic efficiency as an indicator [71,72]. However, under the assumption that Li deposition occurs, this ensures that the anode potential falls below the 50 mV threshold to form crystalline Si. Nevertheless, the results of the C-rate variation demonstrate that even at lower rates, the potential drops below this threshold, resulting in a comparable amount of trapped Li in the crystalline phase.

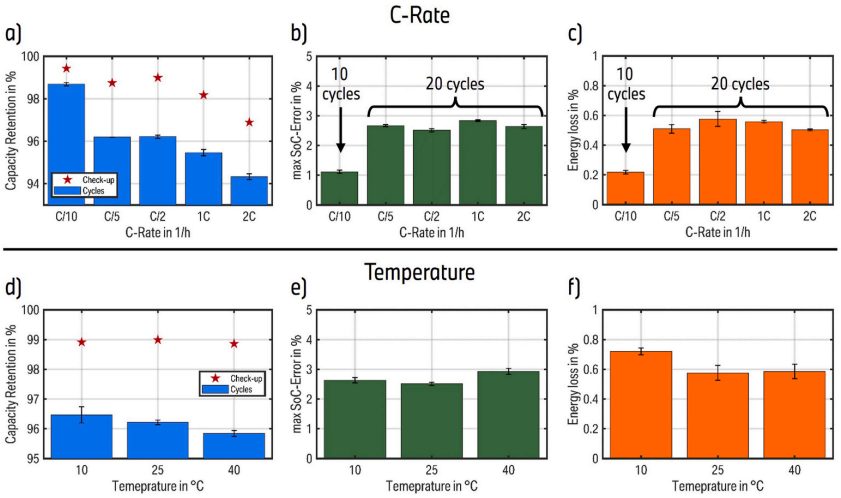

Fig. 7. Illustration of the metrics for quantifying Li trapping for the variation in the C-rate during (dis-)charging (a–c) and for the temperature variation (d–f). (a) Capacity retention for the check-ups and the specific cycles in between the check-ups for each C-rate. (b) Maximum SoC-error between the recovery and normal cycle for each C-rate. (c) Energy loss of the recovery cycle, compared to the normal cycle, for each C-rate. (d) Capacity retention for the check-ups and the specific cycles in between the check-ups for each ambient temperature. (e) Maximum SoC-error between the recovery and normal cycle for each ambient temperature. (f) Energy loss of the recovery cycle, compared to the normal cycle, for each ambient temperature.

3.3.6. Temperature variation

As with the C-rate variation, no large deviation is observable for cell A in the temperature variation between 10 and 40 °C. The capacity retention in Fig. 7d shows a small slight tendency towards an enhanced memory effect at higher temperatures, whereas the energy loss in Fig. 7f depicts the contrary tendency towards an increased effect at lower temperatures. The maximum SoC error in Fig. 7e shows no discernible trend with respect to temperature. Therefore, it can be concluded that nearly no temperature dependency exists. Both the C-rate and the temperature variation cause changes in the polarization, as a reduced temperature increases the internal resistance of the cell, similar to an increased C-rate [73]. Consequently, the polarization has most likely no effect on the amount of Li trapping.

3.4. Li trapping on anode half-cell level

The memory effect, caused by trapped Li in the fully lithiated crystalline phase, has been frequently reported and explained with pure silicon anode half-cells [11,29,39], but rarely with blend anode half-cells [57]. To demonstrate that the established SoC dependency also exist at half-cell level, a variation of the upper and lower cutoff potential is performed, as described in Table 2. Moreover, repeating the full cell tests in a comparable manner at the electrode level verifies that the observed memory effect can be attributed to the anode. The existence of the crystalline phase is additionally supported by the observation of a plateau at ~440 mV vs. Li/Li$^+$. The delithiation voltage profiles of the recovery and normal cycles during the EoT check-up are presented in Fig. 8. The first scenario outlines the anticipated worst case, with a lower cutoff potential of 10 mV vs. Li/Li$^+$ and an upper cutoff potential of 400 mV vs. Li/Li$^+$. A potential of 10 mV vs. Li/Li$^+$ is considerably below the threshold of 50 mV vs. Li/Li$^+$, whereas 400 mV vs. Li/Li$^+$ is only slightly below 440 mV vs. Li/Li$^+$, illustrated in Fig. 8a. Given the previous assumption of breaking the Si-Si clusters into isolated silicon anions, this potential range utilizes the majority of the Si-range without regaining the trapped Li. The results show increased amounts of all three metrics over any results of the cylindrical cells. The capacity retention between the first and fifteenth cycle account for 93.8 % with no appreciable degradation. Furthermore, the maximum SoC error and energy loss are found to be 5.8 % and 3.8 %, respectively. The maximum SoC error after 15 cycles of the half-cell is identical to that observed for 200 consecutive cycles of cell A. However, it should be noted that the energy loss cannot be calculated in a similar manner as presented in Eq. (4) due to the use of a pure Li metal counter electrode instead of an intercalation cathode. Therefore, the trapped Li increases the anode potential during the recovery cycle, rather than reducing the cell voltage. The overall lower voltage of an anode half-cell in comparison to a full cell, results in a significantly higher percentage of lost energy.

In the second scenario, illustrated in Fig. 8b, the upper cutoff potential is reduced to 270 mV vs. Li/Li$^+$, to utilize solely the graphite range, which is comparable to the case 30–100 % SoC for cell A. However, due to the visible degradation between the recovery and normal cycle, it is challenging to calculate a meaningful SoC error. Nevertheless, the voltage profile demonstrates a potential change in the recovery cycles with a clear but reduced characteristic, as anticipated from the results of the 30–100 % SoC case. However, the voltage profile exhibits a deviation from the expected plateau at approximately 440 mV vs. Li/Li$^+$. This plateau persists in a diminished form alongside an additional small plateau around 320 mV vs. Li/Li$^+$, which has not yet been reported.

The unexpected plateau observed at approximately 320 mV vs. Li/Li$^+$ also appears in the measurements of the third case, as shown in Fig. 8c, where the lower cutoff potential is increased to 60 mV vs. Li/Li$^+$. Given that the phase transition is known to occur below 50 mV vs. Li/Li$^+$ [2,29,31,32] or, in some cases below 60 mV vs. Li/Li$^+$ [33,38], limiting the cutoff potential to 60 mV vs. Li/Li$^+$ should not result in any crystalline silicon. This is supported by the observation that this test scenario

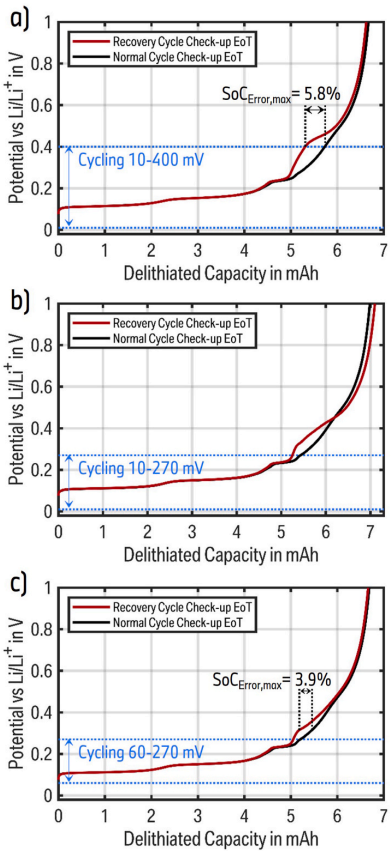

Fig. 8. Anode potential of the recovery cycle (red) and the normal cycle (black) in the EoT check-up for the cases (a) 10–400 mV vs. Li/Li + cycling, (b) 10–270 mV vs. Li/Li + cycling, and (c) 60–270 mV vs. Li/Li + cycling. The potential range during cycling is indicated in blue for each case. The maximum SoC error is visualized in (a) and (c). (For interpretation of the references to colour in this figure legend, the reader is referred to the Web version of this article.)

exhibits no voltage plateau at 440 mV vs. Li/Li$^+$, where the crystalline phase is otherwise reverted to an amorphous phase. However, the discernible shift in the voltage profile, with a maximum SoC error of 3.9 %, suggests the possibility of another phase transition occurring above 60 mV vs. Li/Li$^+$. This intermediate phase appears to be reverted at approximately 320 mV vs. Li/Li$^+$, rather than at 440 mV vs. Li/Li$^+$. It is conceivable that this is a lower lithiated crystalline phase than c-$Li_{3.75}Si$, given the similarity in the general behavior of this phase transition. Nevertheless, it is not possible at this stage to make any definitive statements. Further experiments are required to prove these assumptions and evaluate under which test scenarios this behavior is reproducible.

4. Conclusion

This work analyzes the impact of the phase transition of fully lithiated silicon anode material from the amorphous to the crystalline state in LIB cells containing Gr/SiO_x blend anodes at high SoC. It has been shown that:

- A crystalline phase transition at high states of lithiation is observable that impacts the operation of commercial and automotive batteries with Gr/SiO_x blend anodes.
- The phase transition is reversed only if the cells are discharged to SoC levels below 5–10 %, depending on the silicon content, leading to a memory effect for partial cycles.
- If unreversed, the crystalline phase changes the OCV characteristic, resulting in SoC and SoH estimation errors, a reduction in the discharge energy, and leads to a temporary loss of cyclable Li.
- The amount of trapped lithium shows a cumulative effect with the number of partial cycles and a dependency on their SoC range.
- If fully discharged, the phase transition is reversible, enabling an almost complete recovery of the trapped lithium.
- Partial cycling of Gr/SiO_x anode half-cells indicate an intermediate crystalline phase transition.

The anode potential repeatedly decreases below 60 mV during the cycling of Gr/SiO_x blend anodes, which results in the formation of the silicon crystalline phase c-$Li_{15}Si_4$. This changes the OCV in the lower SoC range, where silicon is predominantly active during discharging. These changes remain until the anode potential exceeds 440 mV, at which point the crystalline phase is reverted.

The results of electrochemical cell tests demonstrate that the described memory effect is present in all investigated cells containing different types of silicon alongside graphite. There is a notable correlation between the number of partial cycles before full discharge, with an increasing trend towards a higher cycle count. A critical SoC window for partial cycles is identified, wherein the lower SoC falls within the active Si-range but is not so low as to cause the recovery of the crystalline phase with each cycle. Furthermore, the upper SoC must be sufficiently high to facilitate the phase transition from amorphous to crystalline, thereby reaching a severe state of the memory effect. A slight correlation between battery degradation and the amount of trapped Li exists, with a lower SoH exhibiting less trapped Li. This suggests that the effect may decrease over the lifetime of the battery. The conducted experiments provide no evidence of a temperature- or C-rate-related dependency, both of which impact the polarization. The variations in the cutoff potentials observed in anode half-cells with blend electrodes suggest the potential existence of an intermediate crystalline phase, in addition to the well-documented c-$Li_{15}Si_4$. Further investigation is required to better comprehend the silicon lithiation behavior in blend electrodes.

In conclusion, the crystalline phase transition of silicon presents a significant challenge in the use of LIBs with Gr/SiO_x blend anodes in BEVs and other applications. The impact of the memory effect can be mitigated by limiting the upper SoC during charging, as this reduces the formation of crystalline silicon during each cycle. Moreover, it is advised that regular deep discharge cycles are conducted below the recovery threshold, to regain the trapped Li. If such operational adjustments are not feasible, it is essential that the BMS tracks the degree of lithiation of Si, especially at high SoCs. By adjusting the OCV accordingly, seamless operation as well as an accurate SoC and SoH estimation can be ensured.

CRediT authorship contribution statement

Julian Knorr: Writing – original draft, Visualization, Methodology, Investigation, Formal analysis, Conceptualization. **Hao-Chen Hsiao:** Writing – original draft, Methodology, Investigation, Formal analysis. **Alexander Adam:** Writing – review & editing, Formal analysis, Conceptualization. **Barbara Rödl:** Writing – review & editing, Supervision. **Thomas Waldmann:** Writing – review & editing, Supervision. **Markus Hölzle:** Writing – review & editing, Supervision. **Michael A. Danzer:** Writing – review & editing, Supervision.

Declaration of competing interest

The authors declare the following financial interests/personal relationships which may be considered as potential competing interests:

Julian Knorr reports a relationship with BMW Group that includes: employment. Hao-Chen Hsiao reports a relationship with BMW Group that includes: employment. Alexander Adam reports a relationship with BMW Group that includes: employment. Barbara Roedl reports a relationship with BMW Group that includes: employment. If there are other authors, they declare that they have no known competing financial interests or personal relationships that could have appeared to influence the work reported in this paper.

Table of abbreviations

a	Amorphous
BEV	Battery electric vehicle
BMS	Battery management system
BoT	Begin of test
c	Crystalline
CC	Constant-current
CCCV	Constant-current constant-voltage
EDX	Energy dispersive X-ray
EoT	End of test
Gr	Graphite
Li	Lithium
LIB	Lithium-ion battery
NMR	Nuclear magnetic resonance
OCP	(Half-cell) open-circuit potential
OCV	(Full-cell) open-circuit voltage
SEI	Solid electrolyte interface
SEM	Scanning electron microscopy
Si	Silicon
SiC	Silicon embedded in carbon matrix
SiO_x	Silicon oxide
SoC	State of charge
SoH	State of health
SoL	State of lithiation
XRD	X-ray diffraction

Appendix A. Supplementary data

Supplementary data to this article can be found online at https://doi.org/10.1016/j.jpowsour.2024.235936.

Data availability

Data will be made available on request.

References

[1] Trends in electric cars – Global EV Outlook 2024 – Analysis, IEA (n.d.). https://www.iea.org/reports/global-ev-outlook-2024/trends-in-electric-cars (accessed September 25, 2024).

[2] M. Wetjen, S. Solchenbach, D. Pritzl, J. Hou, V. Tileli, H.A. Gasteiger, Morphological changes of silicon nanoparticles and the influence of cutoff potentials in silicon-graphite electrodes, J. Electrochem. Soc. 165 (2018) A1503–A1514, https://doi.org/10.1149/2.1261807jes.

[3] A. Durdel, S. Friedrich, L. Hüsken, A. Jossen, Modeling silicon-dominant anodes: parametrization, discussion, and validation of a newman-type model, Batteries 9 (2023) 558, https://doi.org/10.3390/batteries9110558.

[4] N. Kirkaldy, M.A. Samieian, G.J. Offer, M. Marinescu, Y. Patel, Lithium-ion battery degradation: measuring rapid loss of active silicon in silicon–graphite composite electrodes, ACS Appl. Energy Mater. 5 (2022) 13367–13376, https://doi.org/10.1021/acsaem.2c02047.

[5] M. Ashuri, Q. He, L.L. Shaw, Silicon as a potential anode material for Li-ion batteries: where size, geometry and structure matter, Nanoscale 8 (2016) 74–103, https://doi.org/10.1039/c5nr05116a.

[6] M. Su, Z. Wang, H. Guo, X. Li, S. Huang, W. Xiao, L. Gan, Enhancement of the cyclability of a Si/Graphite@Graphene composite as anode for lithium-ion batteries, Electrochim. Acta 116 (2014) 230–236, https://doi.org/10.1016/j.electacta.2013.10.195.

[7] Z. Yang, S.E. Trask, X. Wu, B.J. Ingram, Effect of Si content on extreme fast charging behavior in silicon–graphite composite anodes, Batteries 9 (2023) 138, https://doi.org/10.3390/batteries9020138.

[8] J.W. Wang, Y. He, F. Fan, X.H. Liu, S. Xia, Y. Liu, C.T. Harris, H. Li, J.Y. Huang, S. X. Mao, T. Zhu, Two-phase electrochemical lithiation in amorphous silicon, Nano Lett. 13 (2013) 709–715, https://doi.org/10.1021/nl304379k.

[9] D. Rehnlund, F. Lindgren, S. Böhme, T. Nordh, Y. Zou, J. Pettersson, U. Bexell, M. Boman, K. Edström, L. Nyholm, Lithium trapping in alloy forming electrodes and current collectors for lithium based batteries, Energy Environ. Sci. 10 (2017) 1350–1357, https://doi.org/10.1039/C7EE00244K.

[10] T. Chen, J. Wu, Q. Zhang, X. Su, Recent advancement of SiOx based anodes for lithium-ion batteries, J. Power Sources 363 (2017) 126–144, https://doi.org/10.1016/j.jpowsour.2017.07.073.

[11] S. Wen, B. Lu, Y. Zhao, Y. Song, J. Zhang, Feigned death induced by partial delithiation in silicon composite electrodes, J. Power Sources 495 (2021) 229763, https://doi.org/10.1016/j.jpowsour.2021.229763.

[12] X. Gao, S. Li, J. Xue, D. Hu, J. Xu, A mechanistic and quantitative understanding of the interactions between SiO and graphite particles, Adv. Energy Mater. 13 (2023) 2202584, https://doi.org/10.1002/aenm.202202584.

[13] Y. Li, B. Lu, B. Guo, Y. Song, J. Zhang, Partial lithiation strategies for suppressing degradation of silicon composite electrodes, Electrochim. Acta 295 (2019) 778–786, https://doi.org/10.1016/j.electacta.2018.11.009.

[14] K. Richter, T. Waldmann, N. Paul, N. Jobst, R.-G. Scurtu, M. Hofmann, R. Gilles, M. Wohlfahrt-Mehrens, Low-temperature charging and aging mechanisms of Si/C composite anodes in Li-ion batteries: an operando neutron scattering study, ChemSusChem 13 (2020) 529–538, https://doi.org/10.1002/cssc.201903139.

[15] Y. Jin, B. Zhu, Z. Lu, N. Liu, J. Zhu, Challenges and recent progress in the development of Si anodes for lithium-ion battery, Adv. Energy Mater. 7 (2017) 1700715, https://doi.org/10.1002/aenm.201700715.

[16] A. Franco Gonzalez, N.-H. Yang, R.-S. Liu, Silicon anode design for lithium-ion batteries: progress and perspectives, J. Phys. Chem. C 121 (2017) 27775–27787, https://doi.org/10.1021/acs.jpcc.7b07793.

[17] E. Sivonxay, M. Aykol, K.A. Persson, The lithiation process and Li diffusion in amorphous SiO 2 and Si from first-principles, Electrochim. Acta 331 (2020) 135344, https://doi.org/10.1016/j.electacta.2019.135344.

[18] S.C. Jung, H.-J. Kim, J.-H. Kim, Y.-K. Han, Atomic-level understanding toward a high-capacity and high-power silicon oxide (SiO) material, J. Phys. Chem. C 120 (2016) 886–892, https://doi.org/10.1021/acs.jpcc.5b10589.

[19] M. Jiao, Y. Wang, C. Ye, C. Wang, W. Zhang, C. Liang, High-capacity SiOx (0≤ x≤ 2) as promising anode materials for next-generation lithium-ion batteries, J. Alloys Compd. 842 (2020) 155774, https://doi.org/10.1016/j.jallcom.2020.155774.

[20] M. Miyachi, H. Yamamoto, H. Kawai, T. Ohta, M. Shirakata, Analysis of SiO anodes for lithium-ion batteries, J. Electrochem. Soc. 152 (2005) A2089, https://doi.org/10.1149/1.2013210.

[21] S. Yoshida, T. Okubo, Y. Masuo, Y. Oba, D. Shibata, M. Haruta, T. Doi, M. Inaba, High rate charge and discharge characteristics of graphite/SiOx composite electrodes, Electrochemistry 85 (2017) 403–408, https://doi.org/10.5796/electrochemistry.85.403.

[22] C. Li, X. Zhang, K. Wang, X. Sun, Y. Ma, A 29.3 Wh kg−1 and 6 kW kg−1 pouch-type lithium-ion capacitor based on SiOx/graphite composite anode, J. Power Sources 414 (2019) 293–301, https://doi.org/10.1016/j.jpowsour.2018.12.090.

[23] N.-H. Yang, Y.-S. Wu, J. Chou, H.-C. Wu, N.-L. Wu, Silicon oxide-on-graphite planar composite synthesized using a microwave-assisted coating method for use as a fast-charging lithium-ion battery anode, J. Power Sources 296 (2015) 314–317, https://doi.org/10.1016/j.jpowsour.2015.07.066.

[24] P. Li, H. Kim, S.-T. Myung, Y.-K. Sun, Diverting exploration of silicon anode into practical way: a review focused on silicon-graphite composite for lithium ion batteries, Energy Storage Mater. 35 (2021) 550–576, https://doi.org/10.1016/j.ensm.2020.11.028.

[25] J. Guo, A. Sun, X. Chen, C. Wang, A. Manivannan, Cyclability study of silicon–carbon composite anodes for lithium-ion batteries using electrochemical impedance spectroscopy, Electrochim. Acta 56 (2011) 3981–3987, https://doi.org/10.1016/j.electacta.2011.02.014.

[26] S. Rodríguez-Cadavid, N. Bless, J. Poehler, J. Sabatier, P. Lanusse, C. Farges, BMS-oriented model for Li-ion batteries with mixed SiOx/graphite anodes, in: 2020 5th Int. Conf. Smart Sustain. Technol. Split, IEEE, 2020, pp. 1–6, https://doi.org/10.23919/splitech49282.2020.9243758.

[27] J. Knorr, A. Gomez-Martin, H.-C. Hsiao, A. Adam, B. Rödl, M.A. Danzer, Effect of different charge rates on the active material lithiation of Gr/SiOx blend anodes in lithium-ion cells, J. Energy Storage 86 (2024) 111151, https://doi.org/10.1016/j.est.2024.111151.

[28] J. Knorr, J. Li, M. Schamel, T. Kufner, A. Adam, M.A. Danzer, Active material lithiation in gr/SiOx blend anodes at increased C-rates, J. Electrochem. Soc. 171 (2024) 080512, https://doi.org/10.1149/1945-7111/ad68a9.

[29] K. Ogata, E. Salager, C.J. Kerr, A.E. Fraser, C. Ducati, A.J. Morris, S. Hofmann, C. P. Grey, Revealing lithium–silicide phase transformations in nano-structured silicon-based lithium ion batteries via in situ NMR spectroscopy, Nat. Commun. 5 (2014) 3217, https://doi.org/10.1038/ncomms4217.

[30] K. Ogata, S. Jeon, D.-S. Ko, I.S. Jung, J.H. Kim, K. Ito, Y. Kubo, K. Takei, S. Saito, Y.-H. Cho, H. Park, J. Jang, H.-G. Kim, J.-H. Kim, Y.S. Kim, W. Choi, M. Koh, K. Uosaki, S.G. Doo, Y. Hwang, S. Han, Evolving affinity between Coulombic reversibility and hysteretic phase transformations in nano-structured silicon-based lithium-ion batteries, Nat. Commun. 9 (2018) 479, https://doi.org/10.1038/s41467-018-02824-w.

[31] Y. Li, X. Zheng, Z. Cao, Y. Wang, Y. Wang, L. Lv, W. Huang, Y. Huang, H. Zheng, Unveiling the mechanisms into Li-trapping induced (ir) reversible capacity loss for silicon anode, Energy Storage Mater. 55 (2023) 660–668, https://doi.org/10.1016/j.ensm.2022.12.032.

[32] M.N. Obrovac, L. Christensen, Structural changes in silicon anodes during lithium insertion/extraction, Electrochem. Solid State Lett. 7 (2004) A93, https://doi.org/10.1149/1.1652421.

[33] M.T. McDowell, S.W. Lee, W.D. Nix, Y. Cui, 25th anniversary article: understanding the lithiation of silicon and other alloying anodes for lithium-ion batteries, Adv. Mater. 25 (2013) 4966–4985, https://doi.org/10.1002/adma.201301795.

[34] Y. Jiang, G. Offer, J. Jiang, M. Marinescu, H. Wang, Voltage hysteresis model for silicon electrodes for lithium ion batteries, including multi-step phase transformations, crystallization and amorphization, J. Electrochem. Soc. 167 (2020) 130533, https://doi.org/10.1149/1945-7111/abbbba.

[35] T. Schott, R. Robert, P.A. Ulmann, P. Lanz, S. Zürcher, M.E. Spahr, P. Novák, S. Trabesinger, Cycling behavior of silicon-containing graphite electrodes, Part A: effect of the lithiation protocol, J. Phys. Chem. C 121 (2017) 18423–18429, https://doi.org/10.1021/acs.jpcc.7b05919.

[36] M. Wetjen, D. Pritzl, R. Jung, S. Solchenbach, R. Ghadimi, H.A. Gasteiger, Differentiating the degradation phenomena in silicon-graphite electrodes for lithium-ion batteries, J. Electrochem. Soc. 164 (2017) A2840–A2852, https://doi.org/10.1149/2.1921712jes.

[37] J. Li, J.R. Dahn, An in situ X-ray diffraction study of the reaction of Li with crystalline Si, J. Electrochem. Soc. 154 (2007) A156, https://doi.org/10.1149/1.2409862.

[38] J. Saint, M. Morcrette, D. Larcher, L. Laffont, S. Beattie, J.-P. Pérès, D. Talaga, M. Couzi, J.-M. Tarascon, Towards a fundamental understanding of the improved electrochemical performance of silicon–carbon composites, Adv. Funct. Mater. 17 (2007) 1765–1774, https://doi.org/10.1002/adfm.200600937.

[39] M. Ulldemolins, F. Le Cras, B. Pecquenard, Memory effect highlighting in silicon anodes for high energy density lithium-ion batteries, Electrochem. Commun. 27 (2013) 22–25, https://doi.org/10.1016/j.elecom.2012.10.027.

[40] J. Schmitt, M. Schindler, A. Jossen, Change in the half-cell open-circuit potential curves of silicon–graphite and nickel-rich lithium nickel manganese cobalt oxide during cycle aging, J. Power Sources 506 (2021) 230240, https://doi.org/10.1016/j.jpowsour.2021.230240.

[41] D. Allart, M. Montaru, H. Gualous, Model of lithium intercalation into graphite by potentiometric analysis with equilibrium and entropy change curves of graphite electrode, J. Electrochem. Soc. 165 (2018) A380, https://doi.org/10.1149/2.1251802jes.

[42] L. Köbbing, A. Latz, B. Horstmann, Voltage hysteresis of silicon nanoparticles: chemo-mechanical particle-SEI model, Adv. Funct. Mater. 34 (2024) 2308818, https://doi.org/10.1002/adfm.202308818.
[43] D.N.T. How, M.A. Hannan, M.S.H. Hossain Lipu, P.J. Ker, State of charge estimation for lithium-ion batteries using model-based and data-driven methods: a review, IEEE Access 7 (2019) 136116–136136, https://doi.org/10.1109/ACCESS.2019.2942213.
[44] Z. Liu, X. Dang, B. Jing, A novel open circuit voltage based state of charge estimation for lithium-ion battery by multi-innovation kalman filter, IEEE Access 7 (2019) 49432–49447, https://doi.org/10.1109/ACCESS.2019.2910882.
[45] Y. Xing, W. He, M. Pecht, K.L. Tsui, State of charge estimation of lithium-ion batteries using the open-circuit voltage at various ambient temperatures, Appl. Energy 113 (2014) 106–115, https://doi.org/10.1016/j.apenergy.2013.07.008.
[46] C. Weng, J. Sun, H. Peng, A unified open-circuit-voltage model of lithium-ion batteries for state-of-charge estimation and state-of-health monitoring, J. Power Sources 258 (2014) 228–237, https://doi.org/10.1016/j.jpowsour.2014.02.026.
[47] C. Lin, Q. Yu, R. Xiong, L.Y. Wang, A study on the impact of open circuit voltage tests on state of charge estimation for lithium-ion batteries, Appl. Energy 205 (2017) 892–902, https://doi.org/10.1016/j.apenergy.2017.08.124.
[48] I. Baghdadi, O. Briat, P. Gyan, J.M. Vinassa, State of health assessment for lithium batteries based on voltage–time relaxation measure, Electrochim. Acta 194 (2016) 461–472, https://doi.org/10.1016/j.electacta.2016.02.109.
[49] X. Bian, L. Liu, J. Yan, Z. Zou, R. Zhao, An open circuit voltage-based model for state-of-health estimation of lithium-ion batteries: model development and validation, J. Power Sources 448 (2020) 227401, https://doi.org/10.1016/j.jpowsour.2019.227401.
[50] C. Vincent, B. Scrosati, Modern Batteries, Elsevier, 1997.
[51] R. Barnard, G.T. Crickmore, J.A. Lee, F.L. Tye, The cause of residual capacity in nickel oxyhydroxide electrodes, J. Appl. Electrochem. 10 (1980) 61–70, https://doi.org/10.1007/BF00937339.
[52] G. Davolio, E. Soragni, The 'memory effect' on nickel oxide electrodes: electrochemical and mechanical aspects, J. Appl. Electrochem. 28 (1998) 1313–1319, https://doi.org/10.1023/A:1003452327919.
[53] R.A. Huggins, Mechanism of the memory effect in "Nickel" electrodes, Solid State Ionics 177 (2006) 2643–2646, https://doi.org/10.1016/j.ssi.2006.03.005.
[54] Y. Sato, S. Takeuchi, K. Kobayakawa, Cause of the memory effect observed in alkaline secondary batteries using nickel electrode, J. Power Sources 93 (2001) 20–24, https://doi.org/10.1016/S0378-7753(00)00506-1.
[55] T. Sasaki, Y. Ukyo, P. Novák, Memory effect in a lithium-ion battery, Nat. Mater. 12 (2013) 569–575, https://doi.org/10.1038/nmat3623.
[56] S. Solchenbach, C. Tacconis, A.G. Martin, V. Peters, L. Wallisch, A. Stanke, J. Hofer, D. Renz, B. Lewerich, G. Bauer, M. Wichmann, D. Goldbach, A. Adam, M. Spielbauer, P. Lamp, J. Wandt, Electrolyte motion induced salt inhomogeneity – a novel aging mechanism in large-format lithium-ion cells, Energy Environ. Sci. 17 (2024) 7294–7317, https://doi.org/10.1039/D4EE03211J.
[57] M. Klett, J.A. Gilbert, K.Z. Pupek, S.E. Trask, D.P. Abraham, Layered oxide, graphite and silicon-graphite electrodes for lithium-ion cells: effect of electrolyte composition and cycling windows, J. Electrochem. Soc. 164 (2016) A6095, https://doi.org/10.1149/2.0131701jes.
[58] J.R. Dahn, Phase diagram of Li x C 6, Phys. Rev. B 44 (1991) 9170, https://doi.org/10.1103/PhysRevB.44.9170.
[59] S. Bazlen, P. Heugel, O. von Kessel, W. Commerell, J. Tübke, Influence of charging protocols on the charging capability and aging of lithium-ion cells with silicon-containing anodes, J. Energy Storage 49 (2022) 104044, https://doi.org/10.1016/j.est.2022.104044.
[60] C. Heubner, T. Liebmann, O. Lohrberg, S. Cangaz, S. Maletti, A. Michaelis, Understanding component-specific contributions and internal dynamics in silicon/graphite blended electrodes for high-energy lithium-ion batteries, Batter. Supercaps 5 (2022) e202100182, https://doi.org/10.1002/batt.202100182.
[61] B. Gyenes, D.A. Stevens, V.L. Chevrier, J.R. Dahn, Understanding anomalous behavior in coulombic efficiency measurements on Li-ion batteries, J. Electrochem. Soc. 162 (2014) A278, https://doi.org/10.1149/2.0191503jes.
[62] M. Lewerenz, J. Münnix, J. Schmalstieg, S. Käbitz, M. Knips, D.U. Sauer, Systematic aging of commercial LiFePO4|Graphite cylindrical cells including a theory explaining rise of capacity during aging, J. Power Sources 345 (2017) 254–263, https://doi.org/10.1016/j.jpowsour.2017.01.133.
[63] M. Lewerenz, G. Fuchs, L. Becker, D.U. Sauer, Irreversible calendar aging and quantification of the reversible capacity loss caused by anode overhang, J. Energy Storage 18 (2018) 149–159, https://doi.org/10.1016/j.est.2018.04.029.
[64] X. Han, L. Lu, Y. Zheng, X. Feng, Z. Li, J. Li, M. Ouyang, A review on the key issues of the lithium ion battery degradation among the whole life cycle, ETransportation 1 (2019) 100005, https://doi.org/10.1016/j.etran.2019.100005.
[65] M. Broussely, Ph Biensan, F. Bonhomme, Ph Blanchard, S. Herreyre, K. Nechev, R. J. Staniewicz, Main aging mechanisms in Li ion batteries, J. Power Sources 146 (2005) 90–96, https://doi.org/10.1016/j.jpowsour.2005.03.172.
[66] T. Waldmann, B.-I. Hogg, M. Wohlfahrt-Mehrens, Li plating as unwanted side reaction in commercial Li-ion cells – a review, J. Power Sources 384 (2018) 107–124, https://doi.org/10.1016/j.jpowsour.2018.02.063.
[67] A. Adam, J. Wandt, E. Knobbe, G. Bauer, A. Kwade, Fast-charging of automotive lithium-ion cells: in-situ lithium-plating detection and comparison of different cell designs, J. Electrochem. Soc. 167 (2020) 130503, https://doi.org/10.1149/1945-7111/abb564.
[68] M.C. Smart, B.V. Ratnakumar, Effects of electrolyte composition on lithium plating in lithium-ion cells, J. Electrochem. Soc. 158 (2011) A379–A389, https://doi.org/10.1149/1.3544439.
[69] C. Uhlmann, J. Illig, M. Ender, R. Schuster, E. Ivers-Tiffée, In situ detection of lithium metal plating on graphite in experimental cells, J. Power Sources 279 (2015) 428–438, https://doi.org/10.1016/j.jpowsour.2015.01.046.
[70] S. Schindler, M. Bauer, M. Petzl, M.A. Danzer, Voltage relaxation and impedance spectroscopy as in-operando methods for the detection of lithium plating on graphitic anodes in commercial lithium-ion cells, J. Power Sources 304 (2016) 170–180, https://doi.org/10.1016/j.jpowsour.2015.11.044.
[71] L.E. Downie, L.J. Krause, J.C. Burns, L.D. Jensen, V.L. Chevrier, J.R. Dahn, In situ detection of lithium plating on graphite electrodes by electrochemical calorimetry, J. Electrochem. Soc. 160 (2013) A588, https://doi.org/10.1149/2.049304jes.
[72] J.C. Burns, D.A. Stevens, J.R. Dahn, In-Situ detection of lithium plating using high precision coulometry, J. Electrochem. Soc. 162 (2015) A959, https://doi.org/10.1149/2.0621506jes.
[73] M. Petzl, M. Kasper, M.A. Danzer, Lithium plating in a commercial lithium-ion battery – a low-temperature aging study, J. Power Sources 275 (2015) 799–807, https://doi.org/10.1016/j.jpowsour.2014.11.065.

Supplementary Materials

S1. Calculation of the silicon capacity share

The partially overlapping anode potential of graphite (Gr) and silicon (Si) or SiOx presents a challenge in determining of the distribution between the two active materials in a blend anode. The distribution is expressed in either a gravimetric or a capacity-based manner. The gravimetric distribution can be determined through the use of analytical experiments, such as inductively coupled plasma-optical emission spectroscopy (ICP-OES), which allows for the determination of the Si weight percentage in the anode [1,2]. However, from an operational standpoint, the capacity share of Gr and Si is of greater interest, as it influences the cell voltage and other cell attributes [3]. This section presents a methodology for determining the capacity share of Si based on the pseudo open-circuit voltage (OCV).

The delithiation potentials of Gr and Si exhibit a more pronounced disparity due to the hysteresis of silicon [4]. Up to an anode potential of approximately 0.2 V, Gr is predominantly delithiated, whereas Si undergoes delithiation primarily above this potential. This potential threshold is reached at the end of the graphite plateau associated with the phase transition from LiC_{36} to LiC_{72} [5], which is also evident in the pseudo OCV during discharging. In order to ascertain the precise state-of-charge (SoC), a differential voltage analysis (DVA) is employed. Figure S1 illustrates the C/20 discharge pseudo OCV of the MoliCel M35A and the DVA, exemplifying of the describe process. The local minimum observed at approximately 32 % SoC indicates the phase transition of Gr from LiC_{36} to LiC_{72} [6]. The Si-range is defined as commencing once the derivative increases above the local maximum in the Gr-range, which occurs immediately prior to the graphite plateau being reached during discharging. In the case of the MoliCel M35A, the Si-range can thus be determined to be less than 29.9 % SoC.

In our previous work [7], we employed a SiOx and a Gr half-cell, connected in parallel, to determine the precise state-of-lithiation (SoL) of the two active materials. The setup was subjected to a series of cycles between an anode potential of 10 mV and 1.2 V. At the start of the Si-range during delithiation, Gr had an SoL of 8.2 %, whereas the SiOx had an SoL of 90.1 %. Therefore, it is inaccurate to attribute the entirety of the 29.9 % to the Si. However, at full cell level, the anode potential does not typically employ the full potential range of a half-cell. A pseudo OCV fitting with pseudo open-circuit potentials (OCP) of harvested MoliCel M35A electrodes yielded an anode utilization range from 1.3 % to 94.1 % SoL. At the start of the full-cell discharge at 94.1 % SoL, the experimental results demonstrated that the Gr and SiOx electrodes were lithiated at 92.5 % and 98.7 %, respectively. Similarly, at the end of the full-cell discharge (1.3 % SoL), the Gr electrode remained lithiated at 0.4 %, while the SiOx electrode was lithiated at 4.1 % [7]. Consequently, the remaining lithiation at the start of the Si-range must be adjusted to 8.4 % and 90.9 % for Gr and SiOx, respectively.

Utilizing this information, the capacity shares of Si x_{Si} and of Gr x_{Gr} are calculated as follows:

$$x_{\mathrm{Si}} = 1 - x_{\mathrm{Gr}} \tag{S1}$$

$$SoC_{\mathrm{Si-range}} = x_{\mathrm{Si}} * SoL_{\mathrm{Si}} + x_{\mathrm{Gr}} * SoL_{\mathrm{Gr}} \tag{S2}$$

$$x_{\mathrm{Si}} = \frac{SoC_{\mathrm{Si-range}} - SoL_{\mathrm{Gr}}}{SoL_{\mathrm{Si}} - SoL_{\mathrm{Gr}}} \tag{S3}$$

The $SoC_{\mathrm{Si-range}}$ is used to describe the SoC at the start of the Si-range, which, in the presented case, is 29.9 %. The previously determined SoLs at the start of the Si-range for Gr (9.3 %) and Si (91.3 %) are presented as SoL_{Gr} and SoL_{Si}, respectively. Eq. (S3) is derived from the rearrangement of Eqs. (S1)-(S2).

The Si capacity shares in Table 2 are based on the aforementioned calculation and the assumption that the remaining four cells exhibit a similar lithiation behavior as the MoliCel M35A. It can be reasonably assumed that the exact value of the capacity share will fall within a range of ± 0.5 % of the calculated value.

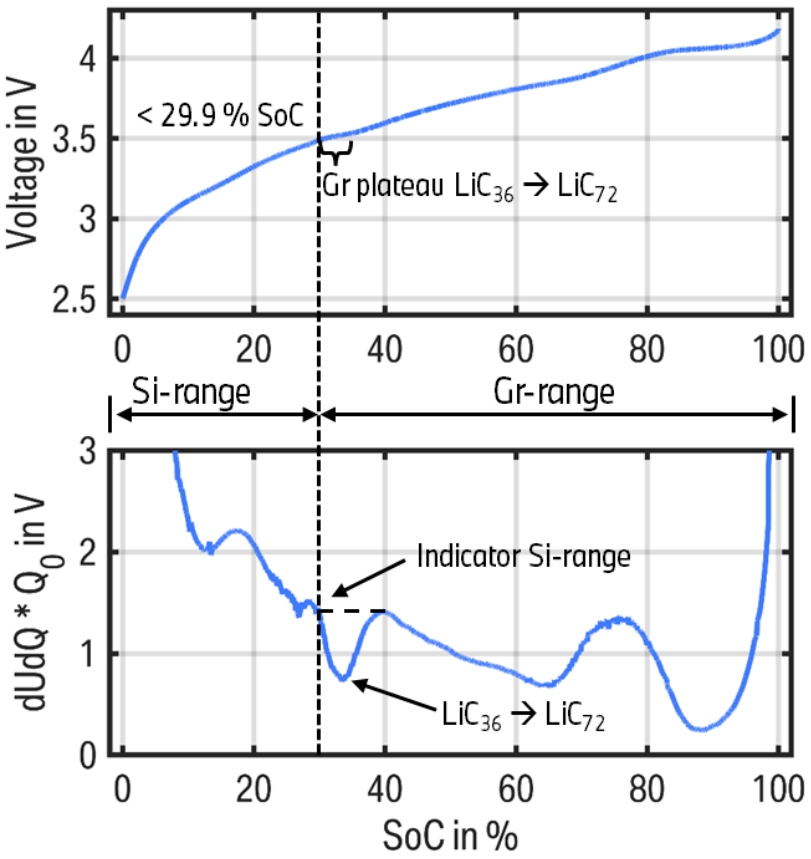

Figure S1: Illustration of the discharge C/20 pseudo OCV of the MoliCel M35A with the DVA below. The DVA is normalized with the nominal capacity. The graphite plateau of the phase transition from LiC36 to LiC72 is marked in both plots beside the indicator at which the Si-range starts with decreasing SoC. The indicator is based on the local maximum immediately preceding the graphite plateau at slightly higher SoCs.

S2. Lack of Li-trapping in cells with pure graphite anode

To support the assumption that the crystalline phase transition of silicon is the underlying cause for the memory effect, a full cell with a pure graphite anode is subjected to a comparable test scenario. As illustrated in Fig. S2, the first full discharge step of the check-up demonstrates no significant divergence from the second cycle. Therefore, the existence of a memory effect for a pure graphite anode could not be detected.

The cell used in this experiment is a multi-layer pouch cell comprising eleven symmetrical stacks of a graphite anodes and a nickel-manganese-cobalt-oxide cathodes arranged in a Z-fold configuration. The cell has a slightly higher nominal capacity of 4.2 Ah than the commercial cylindrical cells A-D. The upper and lower cutoff voltages are 4.2 and 2.8 V, respectively. During testing, the cell is subjected to 75 consecutive cycles within an SoC range of 10-100 %. This differs from the reference case. However, this SoC range with only 20 cycles results in a considerable amount of lithium trapping for cell E, as displayed in Fig. 6 d-e). The check-ups prior to and following the cycling process consists of three full cycles, analogous to the reference case.

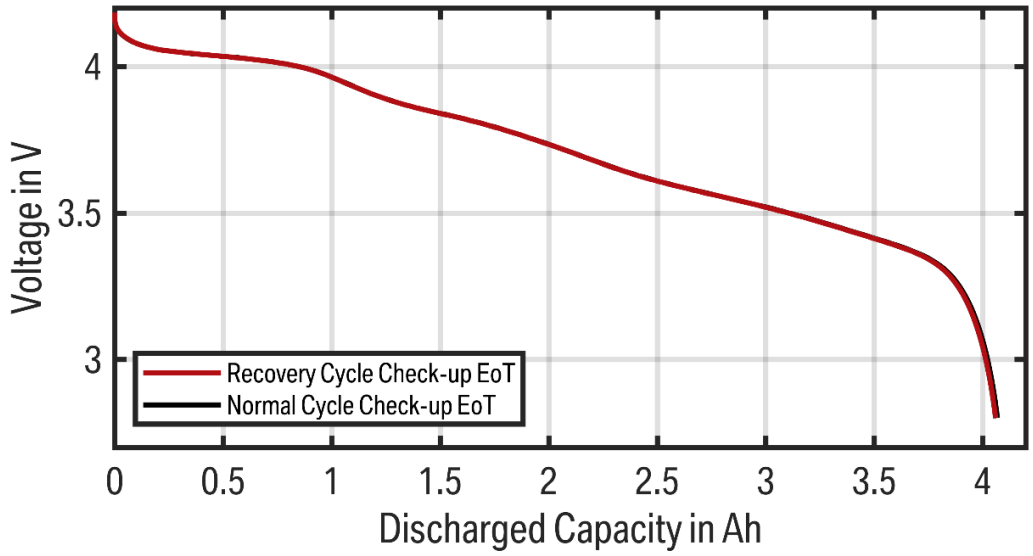

Figure S2: Illustration of the voltage profile of a full cell with a pure graphite anode. The first cycle after 75 cycles between 10-100 % SoC is shown in red and designated as the recovery cycle, analogous to the nomenclature employed in the main work. The second (normal) cycle of the check-up is shown in black, but it is nearly indistinguishable from the first cycle.

S3. Voltage profiles of the cell variation

The voltage profiles of the recovery and normal cycle of the cell variation is presented in Fig. S3. In the cell variation test (Section 3.3.3), cells B to E are subjected to the reference test case in order to compare the results to the reference case of the primary cell A.

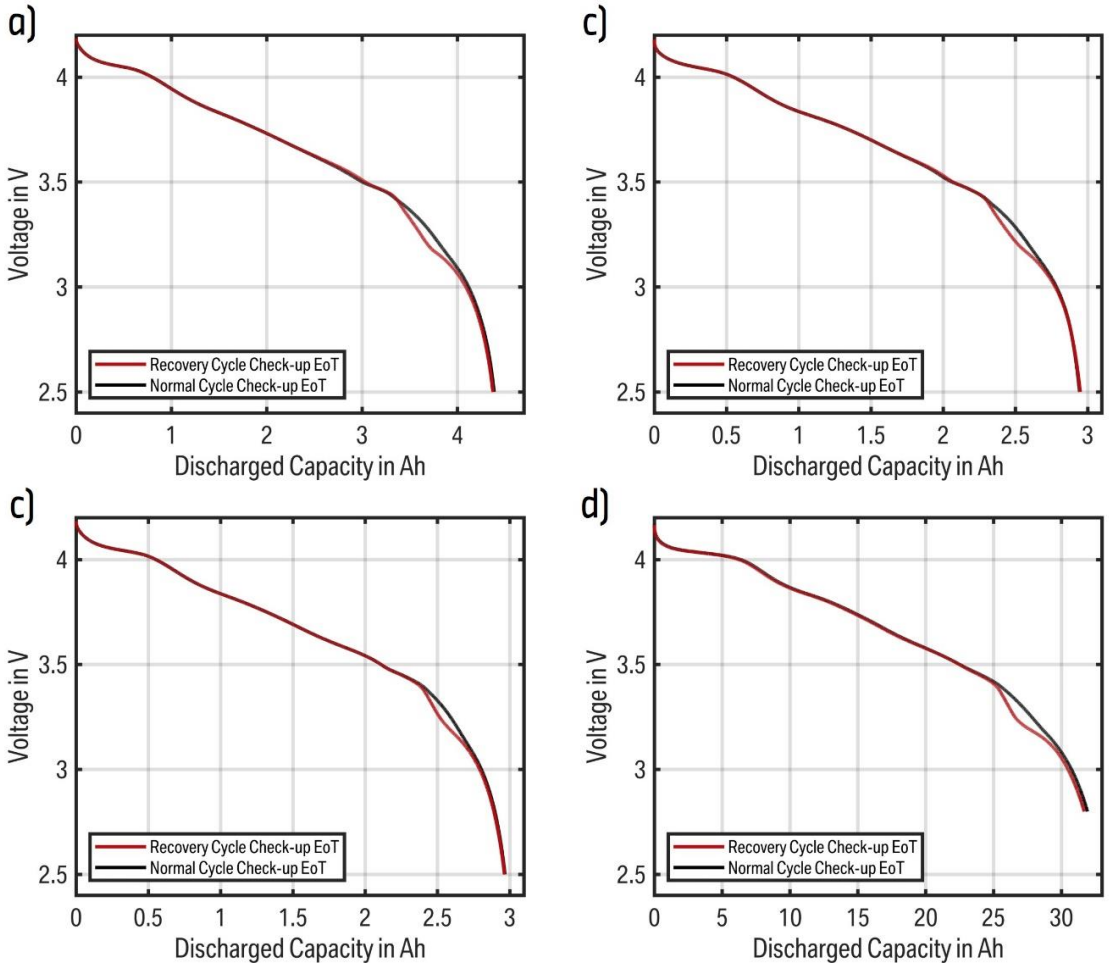

Figure S3: Illustration of the voltage profiles of the recovery and normal cycle of the cell variation. a) Cell B, b) Cell C, c) Cell D, and d) cell E.

References

[1] J. Schmitt, M. Schindler, A. Oberbauer, A. Jossen, Determination of degradation modes of lithium-ion batteries considering aging-induced changes in the half-cell open-circuit potential curve of silicon–graphite, J. Power Sources 532 (2022) 231296. https://doi.org/10.2139/ssrn.4014217.

[2] Y. Zheng, D. Yin, H.J. Seifert, W. Pfleging, Investigation of Fast-Charging and Degradation Processes in 3D Silicon–Graphite Anodes, Nanomaterials 12 (2021) 140. https://doi.org/10.3390/nano12010140.

[3] N. Kirkaldy, M.A. Samieian, G.J. Offer, M. Marinescu, Y. Patel, Lithium-ion battery degradation: Measuring rapid loss of active silicon in silicon–graphite composite electrodes, ACS Appl. Energy Mater. 5 (2022) 13367–13376. https://doi.org/10.1021/acsaem.2c02047.

[4] C. Heubner, T. Liebmann, O. Lohrberg, S. Cangaz, S. Maletti, A. Michaelis, Understanding Component-Specific Contributions and Internal Dynamics in Silicon/Graphite Blended Electrodes for High-Energy Lithium-Ion Batteries, Batter. Supercaps 5 (2022) e202100182. https://doi.org/10.1002/batt.202100182.

[5] J.R. Dahn, Phase diagram of Li x C 6, Phys. Rev. B 44 (1991) 9170. https://doi.org/10.1103/PhysRevB.44.9170.

[6] J. Schmitt, M. Schindler, A. Jossen, Change in the half-cell open-circuit potential curves of silicon–graphite and nickel-rich lithium nickel manganese cobalt oxide during cycle aging, J. Power Sources 506 (2021) 230240. https://doi.org/10.1016/j.jpowsour.2021.230240.

[7] J. Knorr, J. Li, M. Schamel, T. Kufner, A. Adam, M.A. Danzer, Active Material Lithiation in Gr/SiOx Blend Anodes at Increased C-Rates, J. Electrochem. Soc. 171 (2024) 080512. https://doi.org/10.1149/1945-7111/ad68a9.

2.2 Effect of different charge rates on the active material lithiation of Gr/SiO_x blend anodes in lithium-ion cells

This section presents a study that analyzes the lithiation behavior of LIBs with a Gr/SiO_x blend anode at increased C-rates. The objective of this study is to identify the active anode material that is most susceptible to lithiation when the charging current is increased. Obtaining this objective offers insights into the kinetic behavior, which can be used to correctly represent the lithiation behavior in simulation models by providing the necessary input for the kinetic parameters. This is particularly crucial for the design of fast-charging profiles to mitigate the risk of LiD. Furthermore, an accurate understanding of the lithiation distribution between graphite and SiO_x facilitates more precise voltage-based SoC estimation in partial cycles.
A commercial cylindrical full cell with a high SiO_x content is selected for the electrochemical measurements in this study, in order to achieve more pronounced indicators. The hysteresis transition from charging to discharging is utilized to draw conclusions about the lithiation behavior of the active materials. It is evident that the voltage profile of the hysteresis transition exhibits notable distinctions in response to the preceding charging current.
Charging until an SoC of 25 % results in an anode lithiation within the range of the first graphite plateau, as defined in Fig. 1.6. This graphite plateau is also clearly observable at the beginning of the hysteresis transition. As graphite is delithiated prior to SiO_x, due to the increased delithiation potential of SiO_x, the length of the graphite plateau allows for the identification of the quantity of lithiated graphite. The length of this plateau shows a notable correlation with the charging current. An increase in the charging current results in a reduction in its size. With the fixed full cell SoC at the end of the charging step, a diminished graphite plateau within the hysteresis transition is indicative of a reduction in graphite lithiation, which consequently results in an augmented SiO_x lithiation. Accordingly, an elevated charging current results in an increased SiO_x lithiation.
An explanation is provided based on the anode potentials of the raw materials and their kinetic behaviors, which implies an increased polarization of graphite in comparison to SiO_x. Given that both active materials behave like being connected in parallel, the increased graphite polarization results in a greater quantity of lithium being inserted into the SiO_x during charging at elevated C-rates. Due to the hysteresis of silicon, the anticipated balancing effects between SiO_x and graphite during the relaxation period also cease almost immediately. This allows for the presented method to be applied even after long relaxation periods.
The findings are corroborated by XRD analysis. The cells are charged to 25 % SoC with varying C-rates and subsequently opened at this SoC. The observed XRD peaks are indicative of the graphite lithiation, and demonstrate an enhanced degree of graphite lithiation after being charged with a lower C-rate.
The study presents a non-destructive method for analyzing the lithiation behavior in full cells, which indicates the active material that is most susceptible to lithiation. However, this method is limited in that it can only be used to analyze lithiation up to a specific SoC, and

the results cannot be directly transferred to the entire SoC range. Nevertheless, the findings provide substantial insights into the kinetics of Gr/SiO_x blend anodes and the resulting lithiation behavior.

Publication notes

The article "Effect of different charge rates on the active material lithiation of Gr/SiOx blend anodes in lithium-ion cells" is presented in the following. The article was submitted to the *Journal of Energy Storage* for peer review in November 2023 and got accepted in February 2024 [126]. The permanent web link to this publication is available under `https://doi.org/10.1016/j.est.2024.111151`.

Author contribution

J.K. developed the concept of the study. J.K. conducted the electrochemical measurements and evaluated that resulting data. A.G.M. conducted and evaluated the XRD measurements. J.K. and H.C.H. carried out the half-cell manufacturing and anode potential measurements. J.K. wrote the manuscript, assisted by A.G.M in the XRD sections. A.A., B.R., and M.A.D. reviewed and edited the manuscript and provided supervision for the research project. All authors discussed the data and commented on the results.

Journal of Energy Storage 86 (2024) 111151

Contents lists available at ScienceDirect

Journal of Energy Storage

journal homepage: www.elsevier.com/locate/est

Research Papers

Effect of different charge rates on the active material lithiation of Gr/SiOx blend anodes in lithium-ion cells

Julian Knorr [a,b,*], Aurora Gomez-Martin [c], Hao-Chen Hsiao [c], Alexander Adam [c], Barbara Rödl [a], Michael A. Danzer [b,d]

[a] BMW Group, Research and Technology Centre, 85748 Garching, Germany
[b] Chair of Electrical Energy Systems (EES), University of Bayreuth, Universitätsstraße 30, 95447 Bayreuth, Germany
[c] BMW Group, Battery Cell Competence Centre, 80788 Munich, Germany
[d] Bavarian Center for Battery Technology (BayBatt), University of Bayreuth, Universitätsstraße 30, 95447 Bayreuth, Germany

ARTICLE INFO

Keywords:
Lithium-ion battery
Gr/SiOx blend anode
Fast charging
Voltage hysteresis
Material lithiation
X-ray diffraction

ABSTRACT

Anodes with blended active materials, containing SiOx as a secondary material in addition to graphite, gain interest in research and commercial applications to increase the capacity of lithium-ion batteries. SiOx has the advantage of significantly higher specific capacity than graphite but the disadvantage of a reduced cycling and structural stability. To understand the processes involved for this type of blend anode, a detailed investigation of its electrochemical behavior is required. This work provides a non-destructive method for understanding the interaction between blend materials in cells containing silicon-based active material. This method helps to identify internal battery conditions and thereby optimize the battery performance. A cylindrical cell containing approximately 10 wt% of SiOx is used for electrochemical testing. By analyzing the voltage hysteresis, differences in the graphite lithiation are observable, which allows conclusions to be drawn about the SiOx lithiation. An increase in the charge rate leads to a decrease in graphite lithiation and consequently to an increase in SiOx lithiation. This effect is explained by the analysis of the pure material anode potentials. Validation of the effect is given by X-ray diffraction analysis to identify the state of graphite lithiation.

1. Introduction

Over the past decade, public awareness of environmental protection has increased, driving the integration of battery electric vehicles into the personal transportation industry. Limited battery cell capacity is still a major barrier that consumers are concerned about [1]. Increasing the energy density of lithium-ion batteries (LIBs) is therefore a focus of researchers and car manufacturers. The high theoretical capacity of silicon (Si) is one possibility for a future anode material to extend the driving range of electric vehicles.

Elementary silicon has a specific capacity, which is about ten times higher than that of graphite (Gr) [2]. Fully lithiated silicon forms $Li_{15}Si_4$ at room temperature [3], which results in a specific capacity of 3579 mAh/g, while fully lithiated Gr (LiC_6) has a specific capacity of 372 mAh/g. Furthermore, as the second most abundant element in the Earth's crust, Si is also cost efficient [4]. However, compared to Gr, Si has a volume expansion of ~300 % in the fully lithiated state [5]. This can lead to particle pulverization, unstable SEI and loss of electrical contact [3,6–8]. Other drawbacks include the low electronic conductivity and insufficient electrode loading of Si [4]. These drawbacks mitigate the positive effect of the high specific capacity and result in a poor cycle life.

The use of silicon oxide (SiOx) is an alternative to pure Si, that improves the negative aspects, but with a reduced reversible capacity. During the initial cycles, SiOx forms pure cyclable silicon and electrochemically inactive lithium silicates, mainly Li_4SiO_4, and Li_2O as largely irreversible by-products [9,10]. This by-product formation results in a comparatively low initial coulombic efficiency [9], but increases the cyclic stability of SiOx compared to pure Si [11]. The higher density of the by-products compared to lithiated silicon [5] further reduces the volume change in the fully lithiated state to ~150 % for SiO and ~100 % for SiO_2 [9]. With the amount of oxygen in the range of $0 \leq x \leq 2$ and an unclear distribution between the by-products Li_4SiO_4 and Li_2O, it is difficult to give an explicit value for the specific capacity of SiOx. Assuming only Li_2O as an extreme case of by-products and initial SiO ($x = 1$) particles, this results in a theoretical initial capacity of 3496 mAh/g

* Corresponding author at: BMW Group, Research and Technology Centre, 85748 Garching, Germany.
E-mail address: Julian.Knorr@bmw.de (J. Knorr).

https://doi.org/10.1016/j.est.2024.111151
Received 9 November 2023; Received in revised form 12 January 2024; Accepted 28 February 2024
Available online 5 March 2024
2352-152X/© 2024 Elsevier Ltd. All rights reserved.

and a theoretical reversible capacity, related to $Li_{15}Si_4$, of 2280 mAh/g. Assuming only Li_4SiO_4 as the other extreme case of by-products for SiO, this results in a theoretical initial capacity of 2318 mAh/g and a theoretical reversible capacity, related to $Li_{15}Si_4$, of 1710 mAh/g. The true theoretical capacities lie somewhere between these extreme values. This is in agreement with the results of Yan et al. [12] for $Li_{22}Si_5$, which exists in a fully lithiated state at 415 °C [4].

To further increase the stability and conductivity, blend anodes containing graphite and small amounts of Si or SiOx gain interest in research and commercial applications. This approach combines the advantages of both materials, the stability and conductivity of the graphite with a boost in cell capacity due to the silicon [13,14]. This type of blend anode is further referred to as Gr/SiOx. Even small amounts of 10 wt% SiOx as a secondary active material show a theoretical reversible capacity of 535 mAh/g, assuming a theoretical reversible capacity of 2000 mAh/g for SiOx. This is a 44 % increase over pure graphite with only 10 wt% of SiOx. It is known from blend cathodes that the potential of the individual active materials influences the voltage or State-of-Charge (SoC) range in which each material is de-/lithiated [15–17]. The generally higher anode potential of SiOx compared to Gr causes SiOx to be cycled preferentially in the lower SoC range, while Gr is active with increasing anode lithiation [18,19]. This effect is enhanced during delithiation due to the large voltage hysteresis of silicon [19,20]. This hysteresis is almost ten times higher for silicon than for graphite [21]. Lithiation differences between the active materials also occur when comparing slow and fast charging. Heubner et al. [20] showed increased graphite lithiation by analyzing the individual active material current in a parallel half-cell setup, when charging at an increased rate in the very low SoC range. Bazlen et al. [22] studied the differential voltage of full cells which resulted in an increased silicon lithiation after fast charging to 20 % SoC. Richter et al. [23] measured the graphite lithiation by operando neutron diffraction at very low temperatures. The results showed an increased graphite lithiation at higher charge rates due to the impaired kinetic behavior of silicon at very low temperatures.

In this work, the influence of increased charge rates on the lithiation behavior of Gr/SiOx blend anodes is thoroughly investigated. Therefore, a commercial cell with ~10 wt% SiOx is charged with different currents up to 25 % SoC to analyze the behavior in the low SoC range where silicon is active. The voltage hysteresis transition in the subsequent discharge process is analyzed to infer different States-of-Lithiations (SoL) between Gr and SiOx as a function of the charge rate beforehand. As a complementary approach, X-ray diffraction (XRD) analysis is used to determine the SoL of graphite and to validate the results of the voltage hysteresis. Furthermore, an explanation of the observed effects is given by the anode potential interaction of the active materials. This work provides a non-destructive and reproducible method for determining the preferred active material that is lithiated during fast charging. The method is applicable to any full cell containing blend anodes with Si or SiOx in addition to graphite. The obtained knowledge aids in understanding the individual cell behavior, improving intrinsic battery state estimation, and optimizing simulation models.

The experimental section describes the electrochemical cell test, the half-cell assembly procedure to obtain anode potentials for the pure materials Gr and SiOx and the procedure for cell opening and XRD analysis. The results section describes and explains the hysteresis effect and the XRD results that can be used to infer graphite lithiation. In addition, the lack of compensation processes between the active materials is explained, which allows the measurement of lithiation differences in full cells.

2. Experimental

2.1. Battery cell test setup

The electrochemical tests that are performed to investigate the fast charging behavior of lithium-ion battery cells containing silicon. A commercially available cylindrical cell (MoliCel M35A), hereafter referred to as MoliCel, is used for the electrochemical tests. This cell has the 18650 format (diameter: 18 mm, length: 65.0 mm) with a nominal capacity of 3.5 Ah. The cell contains a Gr/SiOx blend anode, which contains ~87 wt% graphite, ~10 wt% SiOx (corresponding to ~ 5 wt% pure silicon) and ~3 wt% of inactive components. The cathode consists of ~93 wt% nickel-cobalt-aluminum (NCA) as the active material and ~7 wt% of inactive components.

The electrochemical cell tests are performed on three cells simultaneously in a climate chamber at 25 °C. All cells have the same Begin-of-Life (BoL) condition, which includes only the manufacturer's formation process. For testing, the ACT0550 battery test system of PEC is used, which allows a maximum voltage of 5 V and a maximum current of 50 A per channel with a sufficient current accuracy of ±0.03 mA.

The cell test consists of three parts. First, the individual cell capacity is determined by a capacity check consisting of three consecutive full cycles. Each cycle uses a constant-current-constant-voltage (CCCV) charge protocol to the maximum voltage of 4.2 V with a cut-off charge rate of C/50, a constant-current (CC) discharge protocol to the minimum voltage of 2.5 V, and 30 min of relaxation between charging and discharging. The charge and discharge rates are set to C/3 based on the nominal cell capacity. The actual capacity of each cell is calculated during the third discharge step and further taken to calculate the current and to set the SoC via coulomb counting. In the second part, the pseudo open-circuit-voltage (OCV) is measured using the same procedures for two consecutive cycles, with the only difference of using a charge rate of C/10 for charging and discharging. Prior tests with the MoliCel revealed, that while C/10 is a relatively high rate for a pseudo OCV, it is low enough to assume that the overpotential can be neglected. When compared to C/20, only an average voltage deviation of 6.7 mV occurs. However, when compared to C/3, the average voltage deviation increases significantly to 76.3 mV. Hence, we assume that C/10 has only minor overpotential.

After these preparation steps, the actual cell test proceeds to analyze the voltage behavior at different charge rates. Five different currents are used, ranging from moderate currents similar to the pseudo-OCV measurement to fast charge rates that can theoretically charge the cell in 20 min (charge rates: C/10, C/3, 1C, 2C & 3C). This part can also be divided into three steps:

1. Charging from 0 % to 25 % SoC via coulomb counting using the specific charge rates. It is known that SiOx lithiation dominates in this low SoC range due to the overall higher open-circuit potential (OCP) of silicon compared to graphite [19,22,24,25].
2. Relaxation for 5 h to ensure sufficient homogenization of the cell.
3. Discharging with C/10 to analyze the hysteresis effects known for silicon [26] until reaching the pseudo-OCV with the same discharge rate of C/10. In this case, a CCCV discharging protocol is used to obtain a fully discharged cell and similar start conditions.

The three steps are repeated for each of the five charge rates, starting with the lowest C-rate to minimize stress and possible aging effects on the cell. The target SoC of 25 % is selected for this specific cell. It is dependent on the ratio of Gr to SiOx and has to be define for any type of cell individually. The process for defining the target SoC is explained in Section 3.2.

In this work, the term (dis)charge refers to the full cell, while (de) lithiation refers to the electrode/anode level.

2.2. Cell opening and XRD analysis

Ex-situ XRD analysis is used to further analyze the effects of fast charging on Gr/SiOx blend anodes. The aim is to qualitatively measure the degree of graphite lithiation after charging the cell at different charge rates. A total of four MoliCels at BoL is prepared using a similar

procedure as described in the last section. Two charge rates (C/10 & 3C) with the largest deviation are evaluated. The cells are charged to 25 % SoC, as specified in the previous section, at the respective charge rate. Two cells per considered rate are prepared and opened to ensure reproducibility of the results.

The cells with an SoC of 25 % are transferred into a glove box with an inert gas atmosphere (argon, MBraun). In the glove box, the cap assembly with the attached jelly roll is removed from the can and subsequently the jelly roll is disconnected from the cap assembly. The individual components (anode, cathode, and separator) are then separated from each other. For XRD measurements, a small sample ($\sim$1cm^2) of the partially lithiated anode material is cut from the center of the jelly roll. A similar spot is chosen for all cells for a better comparability.

Powder XRD (Bruker D8 Advance) measurements of harvested electrodes are performed with a Bragg-Brentano geometry between 15° and 100° at a step size of 0.005°s^{-1} using Cu-Kα radiation ($\lambda = 0.154$ nm) at 40 kV and 40 mA. The collected data is Rietveld-refined using Topas Academic V6 (Bruker AXS GmbH) to obtain lattice parameters. Sample preparation is performed inside the glove box under an argon atmosphere and an X-ray transparent dome is used to prevent contact with the ambient atmosphere during sample handling and XRD measurements.

2.3. Pure active material half-cell potential

To explain the measured full cell effects, the anode potentials of the pure materials is primarily used in the following of this work. The exact material composition of the Gr and SiOx used in the MoliCel is only known by the manufacturer specifications. For this reason, pure graphite and pure SiOx half-cells are produced to obtain detailed information about the anode potential of the pure materials. The assembly, formation and measurement of the anode potential is described in this section.

The half-cells are fabricated using Swagelok-type T-cells containing the active material (either pure graphite or pure SiOx) as the working electrode, pure lithium as the counter electrode and pure lithium as the reference electrode to measure the quasi OCP with negligible overpotentials between the working and reference electrodes. Three identical half cells are constructed for each of the pure materials.

The electrodes measure 12.7 mm in diameter. Copper foil of the same diameter and a thickness of 10 µm is used as the current collector. The active material weight averages 15.06 +/− 0.2 mg. With an active material content of 95 wt% and a specific capacity of 372 mAh/g [27,28], this results in an average cell capacity of 5.32 mAh or an average areal capacity of 4.20 mAh/cm^2 for the graphite electrodes. The SiOx electrodes used, measure an average active material weight of 1.85 +/− 0.1 mg. Due to the larger amount of binder materials and additives required for SiOx, the active material percentage is only 75 wt%. Using 2000 mAh/g as the specific reversible capacity of SiOx, an average cell capacity of 2.78 mAh or an average areal capacity of 2.19 mAh/cm^2 is calculated for the SiOx electrodes. This value of 2000 mAh/g is chosen based on the calculations mentioned in the introduction and represents an intermediate value between the extreme cases of Li_4SiO_4 and Li_2O by-product formation. A commercially available glass fiber separator with a diameter of 13 mm, slightly larger than the electrode diameter, is used to avoid short circuits. The thickness of the separator is 260 µm. A typical electrolyte for battery cells is used, which contains a 1.2 M $LiPF_6$ solution with a combination of the following solvents: ethylene carbonate (EC), dimethyl carbonate (DMC), ethyl methyl carbonate (EMC) and fluoroethylene carbonate (FEC). The specific ratio of EC/DMC/EMC/FEC cannot be disclosed here but should not affect the results of the OCPs. The half-cells are filled with a total of 160 µl of this electrolyte in total, equally divided between the working and the reference separators. Nanoscale carbon black and two different commercially available binders, namely polyacrylic acid and carboxymethyl cellulose, are used.

The formation and measurement of the OCP of the half-cells is performed with a potentiostat (BioLogic VMP3 potentiostat). The potentiostat has a maximum current of 400 mA with a resolution of 0.76 nA. The half-cells are cycled in a climate chamber at 25 °C. The upper and lower voltage cutoff limits for cycling of the SiOx half-cells are 1.5 V and 0.05 V vs. Li/Li$^+$, respectively. A smaller upper voltage limit of 1 V is used for the graphite half-cell. However, this reduced value has almost no effect on the OCP due to the steep gradient of Gr in this voltage range. The current is set to C/50 with respect to the calculated capacity for each half cell. Three consecutive cycles are used for the formation process. The pseudo-OCPs are taken from the third formation cycle, when the formation is expected to be complete.

3. Results and discussion

3.1. Pure active material quasi open-circuit potential

The graphite and SiOx OCP measurements are conducted as described in Section 2.3. For each material, the half-cell with the lowest overpotential is selected to best represent the correct OCP. The deviation among all cells remains below 5 mV consistently. Small variations between the cells may occur during the cell assembly because of differences in the anode coating, compression force, etc. During the formation, graphite shows coulombic efficiencies of 81.5 %, 91.4 % and 98.2 % for the first, second, and third cycles, respectively. Similarly, the coulombic efficiencies of the SiOx half-cell are 69.0 %, 93.0 % and 95.3 %. The initially low coulombic efficiency during the first formation cycles can be attributed to the formation of the solid electrolyte interface, surrounding the anode particles [29]. The reduced delithiation capacity of SiOx during the first cycle is due to the additional formation of lithium silicates and Li_2O [9]. The resulting pure active material potential curves of the third formation cycle for Gr and SiOx are visualized in Fig. 1, normalized to the SoL. The SoL is defined between the upper and lower cutoff potentials of the pure anode materials in the range of 0 % to 100 %. In the following sections, the OCPs for both materials are used to explain the effects of the electrochemical tests.

The OCP of SiOx in Fig. 1 clearly shows the hysteresis of SiOx with an average of 266 mV and a maximum of 563 mV at an SoL_{SiOx} of 2.5 %. In contrast, graphite shows almost no hysteresis with an average voltage difference between lithiation and delithiation of only 17 mV. The visible graphite plateaus at an anode potential of $\sim$0.19 V (Plateau 1), $\sim$0.11 V

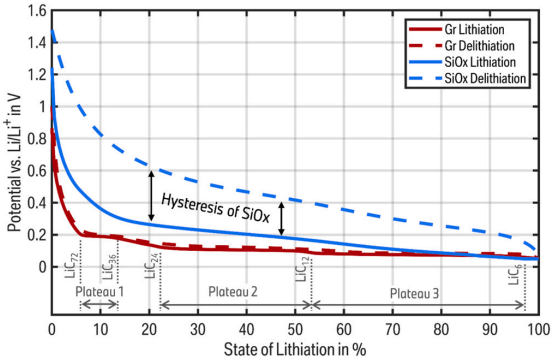

Fig. 1. Half-cell measurements of pure graphite (red) and pure SiOx (blue) anode potentials. The half-cells are cycled with a pure lithium counter electrode and an additional lithium reference electrode for the measurements. The solid lines show the potential in the lithiation direction, the dashed lines in the delithiation direction of the third formation cycle. The (de)lithiation rate is C/50 based on the calculated mass loading. The figure visualizes the overall increased potential and the hysteresis of SiOx compared to graphite. It also indicates the graphite plateaus associated with the graphite phase transitions. (For interpretation of the references to colour in this figure legend, the reader is referred to the web version of this article.)

(Plateau 2) and ~0.08 V (Plateau 3) describe the graphite phase transitions from LiC_{72} to LiC_{36}, LiC_{24} to LiC_{12} and LiC_{12} to LiC_6 in lithiation direction, respectively [30]. Fig. 1 also shows that SiOx has an overall higher working potential compared to Gr. Only 6 % of the lithiation for Gr occurs at an anode potential above 0.2 V or before the first graphite plateau. In contrast, for SiOx, the first 41 % of lithiation occurs at potentials higher than 0.2 V. In delithiation direction, this percentage increases to 92 %, while the Gr potential shows only a small deviation between lithiation and delithiation. This explains the clear separation of Gr and SiOx delithiation during a discharge process [19,20].

3.2. Voltage plateau in hysteresis transition

Fig. 2 shows the results of the electrochemical test with the MoliCel. The results show the cell voltage over SoC and time for one of the three cells tested in total. All three cells show the same effect with no significant deviation in the cell voltage. Fig. 2a shows the voltage response for all five charge rates used to reach the SoC of 25 % during the charge step. As expected, the cell voltage increases at higher charge rates, due to losses, caused by the internal cell impedance. At the end of charging there is a voltage difference of 425 mV between cases 1 (3C-charge) and 5 (C/10-charge).

Fig. 2b shows the relaxation process after charging the cells with different currents to 25 % SoC. Since the SoC does not change during relaxation, this part of the figure shows the voltage over time. The cells can be assumed to be fully relaxed after 5 h, with a voltage difference of 40 mV at the end of the relaxation period.

Fig. 2c shows the hysteresis transition during the C/10 discharge step. The hysteresis transition appears while discharging from 25 to 15 % SoC and terminates when the C/10 full cycle pseudo-OCV is reached. This effect is caused by the hysteresis of silicon [31]. During this transition, a plateau is clearly visible that varies in size depending on the charge rate used in the charge step. This plateau in the range of 3.44 V - 3.47 V is associated with the potential plateau of graphite, indicating the phase transition between the two lithiation states LiC_{72} and LiC_{36} [32], and is also shown in the first graphite plateau in Fig. 1 in the range of 5–15 % SoL_{Gr}. The explanation for the slight drop in the cell voltage is the cathode potential of NCA, which decreases constantly with higher lithiation and shows no plateau in this state of lithiation [33]. The low discharge rate of C/10 ensures that the overvoltage is minimized, and the cell voltage measurements can be directly associated with the anode potential. Since graphite is almost exclusively discharged before discharging silicon [20,34], the results show that the cell is at an SoL_{Gr} in the range of the first plateau (Fig. 1) at the beginning of the discharge step, regardless of the charge rate. Possible inhomogeneities between the lithiation of the graphite particles are sufficiently balanced after the relaxation step of 5 h. The length (SoC wise) of the plateau varies depending on the charge rate. The end of the plateau indicates the SoC at which the entire graphite plateau is delithiated, which corresponds to an SoL_{Gr} of 7.5 % (Fig. 1). During this plateau, the delithiation of the anode can be provided almost exclusively by graphite. This leads to the conclusion that there is a difference in the lithiation of graphite at the end of the charge step. Specifically, the use of a lower charge rate results in a larger graphite plateau during the hysteresis transition and therefore a higher graphite lithiation in contrast to higher charge rates. With the additional information that the SoC of 25 % is set using coulomb counting, this implies that the lithiation of SiOx must be lower to achieve the same cell capacity in all scenarios.

The reason to set the target cell SoC of 25 % is also explained by these results. Ideally, the charging process should stop during the lithiation of the first graphite plateau, regardless of the charge rate. This ensures that differences in the plateau lengths are observable. At lower target SoCs, SiOx lithiation becomes predominant due to the overall higher anode potential above the level of the first graphite plateau. Therefore, this method does not reveal any observable lithiation differences due to the minimal amount of lithiated graphite. At higher target SoCs, the here presented method remains usable, but with a reduced sensitivity. As shown later, SiOx is already lithiated at approximately 50 % at 25 % cell SoC. At higher SoCs and with decreasing anode potential, the SiOx lithiation slows down, resulting in less distinguishable graphite lithiation. To observe lithiation differences, it is necessary to analyze the SoC at the end of the first graphite plateau, as it is fully lithiated for any charge rate.

These observations show that a given SoC can result in different

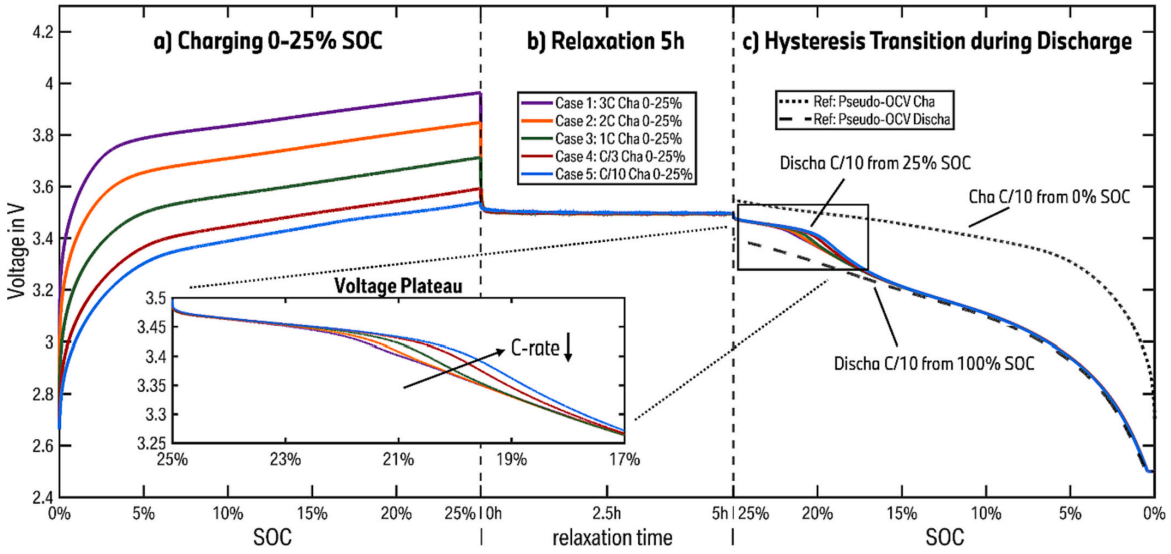

Fig. 2. Resulting cell voltage of the MoliCel test from C/10 (slow charge) to 3C (fast charge). b) Relaxation at 25 % SoC after the charge step. c) Discharging from 25 % to 0 % SoC with a current of C/10 independent of the charge rate. Discharging subsequent to a low charge rate shows a larger voltage plateau during the hysteresis transition compared to after a high charge rate. This indicates more lithiated graphite for the slow charge case at a 25 % SoC. For better visualization of the hysteresis transition, the pseudo-OCV in both directions (discharge/charge) is also presented.

combinations of SiOx and graphite lithiation to obtain the required anode lithiation at this SoC. A higher charge rate results in a higher proportion of SiOx and a lower proportion of the graphite being lithiated for the MoliCel. A possible reason can be the small SiOx particles of the MoliCel, which result in a lower resistance and therefore a better fast charge capability. Heubner et al. [20] and Yang et al. [35] assign this effect to better kinetics of silicon compared to graphite. Furthermore, an increased content of active Si content in blend anodes improves the charge rate capability [20,35].

Fig. 3 shows the same voltage measurement as in Fig. 2c with the additional information of the differential voltage analysis (DVA). The upper subplot shows again the cell voltage during the discharge step from 25 to 10 % SoC with the different lengths in the graphite plateau. The derivative of the voltage in the lower subplot is used to quantify the size of the plateau. The DVA is calculated from the voltage U and the SoC between the discrete steps n as follows:

$$\frac{dU(t)}{dSoC(t)} \approx \frac{\Delta U}{\Delta SoC} = \frac{U_{n+1} - U_n}{SoC_{n+1} - SoC_n} \tag{1}$$

This results in positive values although the cell voltage continuously decreases, because the SoC decreases likewise. At 15 % SoC, both the cell voltage and its derivative show no deviation, indicating the homogenization of all effects caused by the use of different charge rates and, therefore, the achievement of a similar distribution between SiOx and Gr lithiation. Due to the decrease of the cathode potential [33], the DVA will always be positive, although the anode potential is approximately constant in the range of the first plateau. For this reason, we define the plateau where the differential voltage is <0.02 V/%, which is the voltage derivative after homogenization. Using this definition, the two most extreme cases, 3C-charge and C/10-charge, have a plateau size of 2.47 % ΔSoC and 4.07 % ΔSoC, respectively. This indicates that the C/10 charge rate results in a higher SoL_{Gr} of approximately 1.60 % ΔSoC.

3.3. Blend electrode lithiation

3.3.1. Constant potential in blend electrodes

The explanation for the different lithiation states between the two anode materials is given by the assumption that the anode is represented by two anodes connected in parallel for each of the pure materials SiOx and Gr [31]. This electrical contact between the materials occurs either through the current collector, direct particle contact or conductive additive materials. This is a simplified first-order model of the anode which only gives an approximation of the real behavior, without considering effects like concentration gradients between the particles.

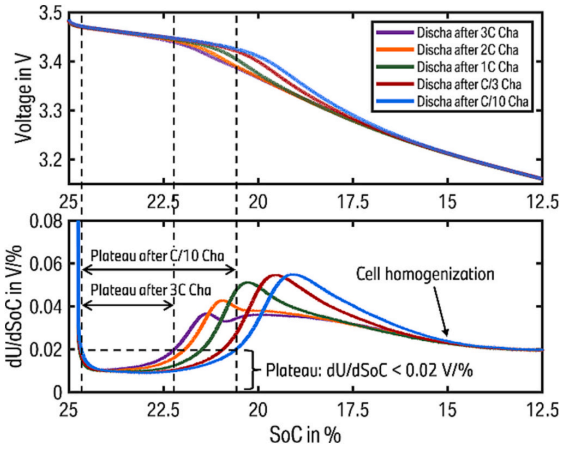

Fig. 3. Resulting cell voltage and differential voltage of the discharge step after charging to 25 % SoC with different rates (same data as in Fig. 2.c). The differential voltage is calculated with respect to the SoC. The length of the voltage plateau, indicating the discharged graphite plateau, is defined by a differential voltage less than 0.02 V/%. This allows a clear comparison between the different charge rates with respect to the graphite lithiation.

The model results in the following set of equations:

$$\Phi_{An} = \Phi_{Gr}(SoL_{Gr}, I_{Gr}) = \Phi_{SiOx}(SoL_{SiOx}, I_{SiOx}) \tag{2}$$

$$\Phi_{Gr} = OCP_{Gr}(SoL_{Gr}) - R_{Gr} \cdot I_{Gr} \tag{3}$$

$$\Phi_{SiOx,Lith} = OCP_{SiOx,Lith}(SoL_{SiOx}) - R_{SiOx} \cdot I_{SiOx} + H(SoL_{SiOx}) \tag{4}$$

$$\Phi_{SiOx,Delith} = OCP_{SiOx,Delith}(SoL_{SiOx}) - R_{SiOx} \cdot I_{SiOx} - H(SoL_{SiOx}) \tag{5}$$

$$I_{cell} = I_{Gr} + I_{SiOx} \tag{6}$$

$$SoC_{Cell} = SoL_{Gr} \cdot (Q_{Gr}/Q_{An}) + SoL_{SiOx} \cdot (Q_{SiOx}/Q_{An}) \tag{7}$$

Φ_{An}, Φ_{Gr} and Φ_{SiOx} describe the potential versus the equilibrium potential of lithium and Q_{An}, Q_{Gr} and Q_{SiOx} the capacity of the whole anode, Gr and SiOx, respectively. This model for a parallel connection of a SiOx and a Gr anode implies that both material particles have the same anode potential at all times (Eq. (2)) [20,31]. The potential of graphite is based on the OCP of graphite, which depends on the SoL of graphite and the voltage loss caused by the current flow related to the graphite particles, I_{Gr} (Eq. (3)). The current is considered positive during lithiation. The impedance of the graphite particles responsible for this voltage loss consists of the solid-electrolyte interface (SEI) resistance [36,37], the charge-transfer-resistance [36,38], resistances caused by diffusion processes [36], the electrolyte ionic resistance [38], and the electrical resistance [38]. For battery cells, this impedance is often approximated by a resistance connected in series with a series of one or multiple RC-networks [39,40]. For the sake of simplicity, the anode complexity is reduced to a single graphite particle with a constant resistance of R_{Gr}. This resistive loss decreases the anode potential, which is also the cause of the aging effect of lithium deposition when the potential drops below 0 V vs Li/Li^+ and metallic lithium is deposited on the anode particle surfaces [41,42]. The potential of SiOx is formed accordingly for lithiation (Eq. (4)) and delithiation (Eq. (5)). The non-linear term $H(SoL_{SiOx})$ accounts for a possible hysteresis transition, e.g., when switching from lithiation to delithiation while the cell is not fully charged. Immediately after switching from lithiation to delithiation, the term $H(SoL_{SiOx})$ has the full magnitude of the voltage hysteresis of SiOx at this SoL. It decreases towards 0 V during the delithiation process, at which point the hysteresis transition is completed. This hysteresis transition can be approximated by an exponential function [43,44]. Eqs. (2)–(5) state that the particle potentials Φ_{Gr} and Φ_{SiOx} must be equal after considering the polarization and the hysteresis effect of SiOx. However, this fact does not imply that the OCPs of SiOx and Gr are also identical. The total current for the whole cell is the sum of I_{Gr} and I_{SiOx} (Eq. (6)).

Since SiOx and graphite contribute with different proportions to the total cell capacity, the contribution must be taken into account for the SoC calculation (Eq. (7)). Q_{Gr}/Q_{An} and Q_{SiOx}/Q_{An} describe the contribution of graphite and SiOx to the cell capacity. Comparing the ~10 wt % of SiOx and an available discharge capacity, including all by-products and SEI formation, of 1400 mAh/g [18] with the 87 wt% of Gr and an available discharge capacity of 340 mAh/g [18], this results in 32 % of the capacity being contributed by the SiOx.

With the assumption that the overpotential in the C/10 slow charge case can be neglected, the anode potential is similar to the open circuit potential and must be constant for both materials according to Eq. (2). The slow charging case in Fig. 4 (upper part) shows the resulting anode potential for graphite and SiOx at an SoC of 25 % and also the lithiation contribution of the individual materials in a parallel connected anode model. At an anode potential of 0.18 V, graphite is 13 % lithiated and SiOx is 48 % lithiated. According to Eq. (5), this results in a cell capacity

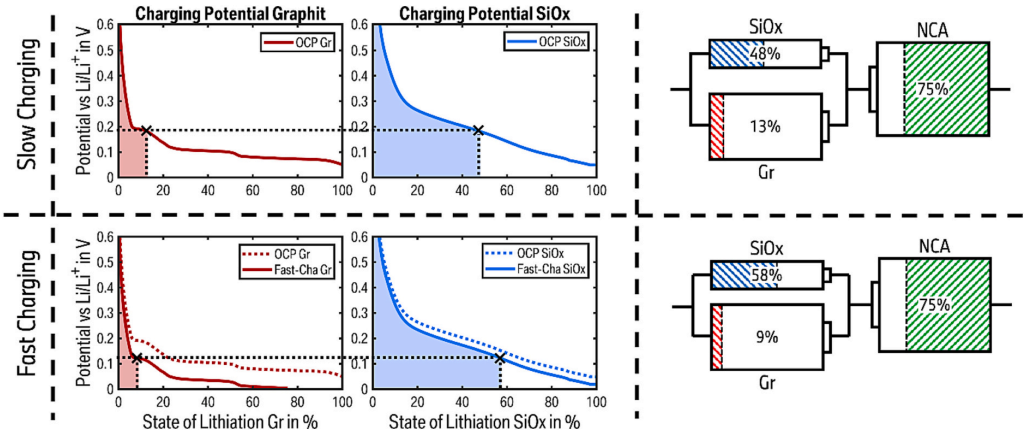

Fig. 4. Illustration of the lithiation distribution when charging to 25 % SoC with high or low charge rates. In both cases, 25 % of the total anode capacity is lithiated. The top row shows the slow charging case without significant overpotential, while the bottom row shows the fast charging case with an increased overpotential of Gr over SiOx. The left subplot in each row shows the graphite potential (red) and the right subplot the SiOx potential. The OCP is displayed alongside the fast charging potential in the fast charging case. The black dotted lines represent the constant anode potential at 25 % SoC of the full cell, which must be equal for both materials. To illustrate the lithiation differences at 25 % SoC, a simple lithiation model of each anode material and the cathode is shown on the right side of each row. In the slow charging case, the SoL_{SiOx} is 48 % and the SoL_{Gr} is 13 %. The lithiation distribution shifts towards a higher proportion of SiOx lithiation due to the increased overpotential of Gr compared to SiOx changes (SoL_{SiOx} = 58 %, SoL_{Gr} = 9 %). (For interpretation of the references to colour in this figure legend, the reader is referred to the web version of this article.)

of ~25 % SoC. At the beginning of the lithiation process, at higher anode potentials, the current is mainly distributed towards the SiOx due to the overall higher anode potential of SiOx and the rapid decrease of the graphite potential. In the region of the first graphite plateau (~0.19 V vs. Li/Li^+) the current is mainly distributed towards the graphite. This is in agreement with the results of Heubner et al. [20].

3.3.2. Active material rate performance on lithiation distribution

The use of higher charge rates for the charging process results in higher losses, due to the inner cell resistance, which causes the anode potential to drop according to Eqs. (2) and (3). The fast charging case in Fig. 4 (lower part) shows an estimation of how this affects the anode potential. The true anode potential is not measurable for full cells without a reference electrode. In a scenario where both materials have the same potential drop, the distribution between the SoL_{Gr} and SoL_{SiOx} would not change. Only the total anode potential would drop towards 0 V vs. Li/Li^+ during lithiation. With the results of different lengths in the voltage plateaus from the electrochemical cell test in Section 3.1, we know that an increased current leads to an increased SiOx lithiation. Under all previous assumptions and formulas, this can only be explained by a greater voltage loss of the graphite particles relative to the SiOx particles. This is consistent with the better rate performance of silicon compared to graphite [20,35]. If the potential drop of Gr were to be less than or equal to that of SiOx, no differences in lithiation would be visible in Fig. 2.

In the lower half of Fig. 4, this increased voltage loss of graphite is visualized by a constant potential drop of 7 mV compared to a potential drop of 3 mV for SiOx. In reality, the R_{SiOx} and R_{Gr} resistances depend on several factors such as the SoL, temperature or SEI-thickness due to aging. The voltage drop also depends on the actual current to the specific active material, which changes for different SoL regions caused by the OCP. With the increased potential drop of graphite, a higher portion of the SiOx lithiation occurs before the equilibrium potential reaches the first graphite plateau. The full cell is only charged to 25 % SoC in the experiment. The increased amount of SiOx lithiation, before the first graphite plateau is reached, causes the charging process to stop during the graphite lithiation of the first plateau at a lower SoL_{Gr} than at slow charge rates, as shown in the upper half of Fig. 4. This aligns with the results presented in Fig. 2, where a charge rate of 3C shows a small graphite plateau, while C/10 displays a large graphite plateau, close to the full plateau of the discharge pseudo-OCV. The potential drops of 3 mV and 7 mV are chosen for the sake of visualization. As mentioned earlier, more detail about the anode of the MoliCel is required to find the exact values. However, we found that in order to achieve the lithiation differences of the MoliCel, an increased potential drop of +4 mV for graphite is required. This value closely aligns with the measurements of the MoliCel.

The charging process stops at an anode potential of 0.12 V with the estimated overpotential, which is corresponds to an SoL_{Gr} of 9 % and an SoL_{SiOx} of 58 %. The calculated distribution according to Eq. (6) of 13 %/48 % and 9 %/58 % for the slow and fast charging case is calculated with the known information about the MoliCel mentioned in the experimental section. It is important to note that, since the anode potentials, shown before are measured using experimental cells, the actual anode potential of the MoliCel may differ slightly. This would also affect the lithiation distribution between SiOx and Gr.

3.3.3. Lithiation balancing between blended active materials

This section addresses the question on the absence of balancing processes during the 5 h relaxation period after fast charging to 25 % SoC. This question is valid under the assumption that graphite has a higher overpotential than SiOx in the case of fast charging. After the end of the charging step, this overpotential will disappear during the relaxation of the cell [45]. At full relaxation, this would result in a higher active material potential for graphite than for SiOx, similar to the OCP for each material respectively. Assuming a constant potential for both materials, this causes an exchange of lithium ions between the active materials, delithiating the SiOx and lithiating the Gr, until the rest potential is equalized again.

Heubner et al. [20] measured this balancing current in a setup with a graphite and a pure amorphous silicon half-cell connected in parallel. They compared the lithiation of this setup at 2C and 0.2C to a very low SoC. In this range a higher amount of graphite was lithiated due to the strong decrease of the graphite anode potential at very low SoL. During the relaxation after fast charging, they observed an exchange of lithium ions from the graphite to the silicon. This means that during relaxation,

graphite is delithiated and Si is lithiated. In the end, the same state was reached as during slow charging (0.2C).

The relevant distinction in the experiment of this work is that SiOx is preferentially lithiated at high charge rates when the cell is charged to higher SoCs, here 25 %. The spatial separation of the blend active materials can also influence the lithiation process. The reason for the absence of the balancing process is the hysteresis of SiOx. In fact, there is a balancing process that delithiates the SiOx and lithiates the Gr, driven by the potential difference after relaxation. But this change from lithiation to delithiation forces the SiOx potential into a hysteresis transition towards the much higher delithiation potential. This rapid increase of the SiOx potential leads to a constant anode potential between graphite and SiOx even after a very small amount of charge exchange and therefore stops the balancing process altogether, although there is still more SiOx lithiation than in the slow-charging case.

This balancing process is visualized in Fig. 5, which again shows the fast charging case to 25 % SoC. At the end of the fast charging step (Point 1), the potential of both active materials is 120 mV. After relaxation without balancing processes (Point 2), the potential difference is 40 mV. Graphite shows an increased potential due to its higher dissipation voltage. The potential difference triggers the balancing process until reaching an equalized rest potential. At an SoL_{SiOx} of 58 % the anode potential of SiOx in lithiation and delithiation direction is 120 mV and 370 mV, respectively. When changing from lithiation to delithiation, the potential of SiOx must change towards the delithiation OCP. This hysteresis transition is approximated by the non-linear term $H(SoL_{SiOx})$ in Eq. (5). This results in the rapid increase of the potential until the potential of SiOx and graphite are equalized (point 3). The graphite potential remains approximately the same because of the graphite plateau, that is reached during lithiation. The amount of delithiated SiOx is almost negligible due to the rapid increase of the SiOx potential during the hysteresis transition. Assuming a constant anode potential (Eq. (2)), the relaxation step (1–2) and the balancing step (2–3) occur simultaneously in the real scenario.

This SiOx hysteresis effect ensures that even after long relaxation periods, the different lithiation states between the slow and fast charging cases remain present and measurable. The relatively small hysteresis of Gr can be neglected here. Gr is lithiated during the fast charging of the cell and the balancing process during relaxation. Thus, Gr experiences no hysteresis transition and remains on its lithiation OCP. If Gr were the higher lithiated material during fast charging, the analysis of plateau lengths during the hysteresis transition would be insignificant. Technically, the small hysteresis of 17 mV on average, as shown in Fig. 1, would also stop the balancing, but this would result in only a minor difference between different charge rates.

3.4. XRD results of graphite lithiation

The hypothesis that a higher charge rate results in less graphite lithiation needs to be confirmed by a complementary approach. Ex-situ XRD analysis is used to qualitatively measure the SoL_{Gr} for anode samples which are lithiated to about 25 %. The absence of balancing effects, as explained above, allows this measurement even after rest periods of >5 h without significant changes in the lithiation state.

XRD analysis can be used to identify the graphite intercalation phase which is associated with a certain SoL. Characteristic reflections at specific diffraction angles indicate different intercalation stages of graphite upon lithiation [29,46]. The intercalation of Li^+-ions between adjacent graphene layers gradually occurs upon charging the cell. The (002) reflection position in XRD diffractograms is directly influenced by the average interlayer distance [29] and, in this case, lower 2θ-diffraction angles correspond to an expansion of the interlayer distance [32]. Silicon lithiation, on the contrary, cannot be analyzed by XRD due to the amorphous state of SiOx during lithiation in the voltage range of 0.05 V - 0.2 V [9,47]. However, with the SoC and therefore the total blend anode SoL set to 25 %, it is possible to draw conclusions about the silicon lithiation. A lower graphite lithiation measured by XRD directly implies a higher silicon lithiation.

Fig. 6 shows XRD analysis of the anodes for the two extreme cases, charging to 25 % SoC with a very low (C/10) and a very high (3C) charge rate. Due to the low SoC of 25 %, a phase close to LiC_{18} was found. Comparing the results with the theoretical position of graphite intercalation compounds LiC_{12}, LiC_{18} as well as that of fully delithiated graphite anodes at ~26.5° [30,32,46], it is clearly visible that the cells charged with a lower charge rate show the maximum reflection at a lower 2θ diffraction angle, indicating a higher graphite lithiation. In contrast, the two cells charged at 3C show the maximum of the (002) reflection at angles of 26.31° and 26.28°, respectively. Both cells show a secondary peak with a reduced intensity, slightly below 26°. According to Dahn et al. [29], this indicates that the graphite is in the region of the phase transition from LiC_{72} to LiC_{36}. The higher intensity around 26.3° suggests that graphite is lithiated at the beginning of the plateau for this phase transition, in the range of 8–10 % SoL_{Gr}. Charging with low charge rates of C/10 results in a larger shift to lower angles, being the (002) reflection at 25.86° and 25.92° for both cells. This corresponds to a lithiation close to the end of the first graphite plateau, where most of the

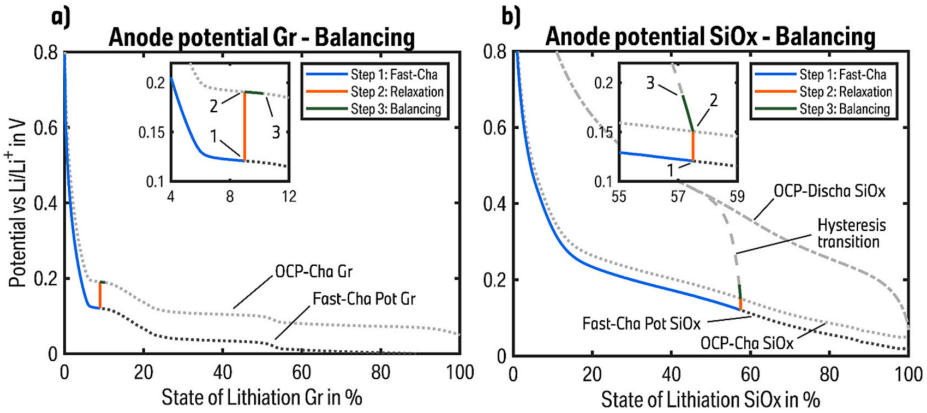

Fig. 5. Balancing effect of the anode potential after fast charging. (1) Same anode potential of Gr and SiOx when reaching 25 % SoC with a higher overpotential of Gr compared to SiOx. (2) Reaching the OCP after complete relaxation results in a potential difference with a higher potential of Gr. (3) The potential difference causes Gr to be lithiated and SiOx to be delithiated until a constant potential is reached. The hysteresis of the SiOx potential causes the potential to rise rapidly during delithiation, which stops the balancing effect even after a small amount of charge exchange between the materials.

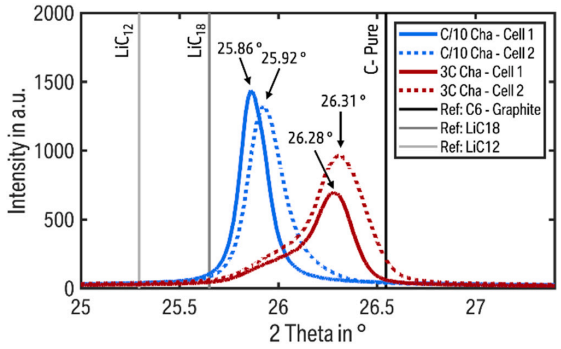

Fig. 6. Ex-situ XRD analysis results of cells charged at C/10 or 3C to 25 % SoC. The two cells charged with a low current of C/10 show (002) reflections (solid and dotted blue lines) close to the reference of a LiC_{18} lithiation phase. The two cells charged with a high current of 3C show a lower SoL_{Gr}, with their (002) reflections (solid and dotted red lines) close to the reference of fully delithiated graphite. (For interpretation of the references to colour in this figure legend, the reader is referred to the web version of this article.)

graphite lithiation is mainly LiC_{36} [29,48]. The Gr-OCP in Fig. 1 indicates a SoL_{Gr} between 11 and 13 %. These estimated SoL_{Gr} values for 3C and C/10 align with the assumptions of 9 % and 13 %, made in Section 3.3. The results show reproducible peaks in the diffraction angle between the different cells. The expected graphite phase for the low current is LiC_{36}, which is mainly present at the end of the first graphite plateau. This potential plateau indicates the graphite phase transition from LiC_{72} to LiC_{36} [29,30]. This expectation is derived from the larger graphite plateau in the discharge hysteresis transition (Fig. 2). The smaller graphite plateau at higher charge rates implies that some parts of the graphite has already changed phase from LiC_{72} to LiC_{36}, but the majority of the graphite is still in the LiC_{72} phase. This is consistent with the XRD results for 3C charging, where the main peak in the diffraction angle is close to fully delithiated graphite. However, there is also a small intensity visible at lower angles, indicating that a small amount of graphite has already transitioned to a higher lithiation phase, similar to the XRD results for the low charge rate.

This confirms the findings of the electrochemical analysis that a higher charge rate leads to an increase in SiOx and a decrease in graphite lithiation.

4. Conclusion

This study investigates the fast charging behavior of a commercial LIB cell containing a Gr/SiOx blend anode with respect to the anode lithiation. The results show that an increased charge rate implies an increased SiOx lithiation when charging to 25 % SoC. In the low SoC range, Si dominates the lithiation process over graphite due to the higher active material potential. A cylindrical cell containing approximately 10 wt% of SiOx is used for the electrochemical tests. The distribution between SiOx and Gr lithiation is analyzed by the voltage response during the hysteresis transition while discharging the cell after different charge rates. The size of a voltage plateau, that can be linked to the Gr transition from LiC_{72} to LiC_{36}, is used as an indicator of the Gr lithiation at 25 % SoC. Charging with a rate of 3C to 25 % SoC shows a smaller plateau in the following discharge step compared to charging with a C/10 rate. This effect is further validated using XRD measurements as a complementary approach to analyze the SoL_{Gr} and therefore draw conclusions on the SiOx lithiation. Both methods show similar results regarding the amount of lithiated graphite. An explanation is given by the constant potential of both active anode materials. Using the anode potentials of pure Gr and pure SiOx to estimate their interaction in a cylindrical cell shows a lithiation distribution in the slow charging case of 13 % Gr and 48 % SiOx at an SoC of 25 %. Assuming a higher overpotential of Gr compared to SiOx in a fast charging case, this distribution shifts to 9 % Gr and 58 % SiOx lithiation. This assumption is associated with a better rate capability of the SiOx particles for the examined MoliCel. After a sufficient relaxation period, this effect is only observable in the hysteresis transition and XRD measurements due to the absence of balancing effects. The hysteresis of SiOx prevents full anode balancing because of the rapid increase in the SiOx potential when changing from lithiation to delithiation. This allows a visible lithiation differences even after long relaxation periods.

The results of this study cannot be generalized for all cells with Gr/SiOx blend anodes. However, the presented method enables the analysis of any cell based on its lithiation behavior, which is strongly influenced by the electro-thermal and kinetic properties of the Gr and SiOx used. An increased fast charging capability of SiOx, e.g. by the use of nanoparticles, might enhance the shown effect. However, the use of large SiOx particles could even have the opposite effect of increasing graphite lithiation during fast charging. With the methods shown in this study, this could not be analyzed, because graphite has almost no hysteresis and therefore balancing processes would occur. Consequently, the aim of future work is to validate the electrochemical effect demonstrated here in various cells and under different cell parameters, such as temperature or target SoC.

Abbreviations

BoL	Begin-of-Life
CC	Constant current
CCCV	Constant current constant voltage
DVA	Differential voltage analysis
Gr	Graphite
Li	Lithium
LIB	Lithium-ion battery
NCA	Nickel-cobalt-aluminum
OCP	(Half-cell) open-circuit potential
OCV	(Full-cell) open-circuit voltage
SEI	Solid-electrolyte interface
Si	Silicon
SiOx	Silicon oxide
SoC	State-of-Charge
SoL	State-of-Lithiation
SoL_{Gr}	State-of-Lithiation of graphite
SoL_{SiOx}	State-of-Lithiation of silicon oxide
XRD	X-ray diffraction

CRediT authorship contribution statement

Julian Knorr: Conceptualization, Data curation, Formal analysis, Investigation, Methodology, Validation, Writing – original draft. **Aurora Gomez-Martin:** Data curation, Writing – original draft. **Hao-Chen Hsiao:** Data curation, Writing – review & editing. **Alexander Adam:** Methodology, Supervision, Writing – review & editing. **Barbara Rödl:** Supervision, Writing – review & editing. **Michael A. Danzer:** Supervision, Writing – review & editing.

Declaration of competing interest

The authors declare the following financial interests/personal relationships which may be considered as potential competing interests: Julian Knorr reports a relationship with Bayerische Motoren Werke AG that includes: employment. Aurora Gomez-Martin reports a relationship with Bayerische Motoren Werke AG that includes: employment. Hao-Chen Hsiao reports a relationship with Bayerische Motoren Werke AG that includes: employment. Alexander Adam reports a relationship with Bayerische Motoren Werke AG that includes: employment. Barbara Roedl reports a relationship with Bayerische Motoren Werke AG that

includes: employment.

Data availability

Data will be made available on request.

Acknowledgments

We would like to thank Johannes Wandt and Lukas Maul of the BMW Group for their helpful discussions on this topic.

References

[1] T.-C. Kuo, Y.-S. Shen, N. Sriwattana, R.-H. Yeh, Toward net-zero: the barrier analysis of electric vehicle adoption and transition using ANP and DEMATEL, Processes 10 (2022) 2334, https://doi.org/10.3390/pr10112334.
[2] Q. Huang, M.J. Loveridge, R. Genieser, M.J. Lain, R. Bhagat, Electrochemical evaluation and phase-related impedance studies on silicon–few layer graphene (FLG) composite electrode systems, Sci. Rep. 8 (2018) 1386, https://doi.org/10.1038/s41598-018-19929-3.
[3] Y. Jin, B. Zhu, Z. Lu, N. Liu, J. Zhu, Challenges and recent progress in the development of Si anodes for lithium-ion battery, Adv. Energy Mater. 7 (2017) 1700715, https://doi.org/10.1002/aenm.201700715.
[4] P. Li, H. Kim, S.-T. Myung, Y.-K. Sun, Diverting exploration of silicon anode into practical way: a review focused on silicon-graphite composite for lithium ion batteries, Energy Storage Mater. 35 (2021) 550–576, https://doi.org/10.1016/j.ensm.2020.11.028.
[5] T. Chen, J. Wu, Q. Zhang, X. Su, Recent advancement of SiOx based anodes for lithium-ion batteries, J. Power Sources 363 (2017) 126–144, https://doi.org/10.1016/j.jpowsour.2017.07.073.
[6] S. Chae, M. Ko, K. Kim, K. Ahn, J. Cho, Confronting issues of the practical implementation of Si anode in high-energy lithium-ion batteries, Joule 1 (2017) 47–60, https://doi.org/10.1016/j.joule.2017.07.006.
[7] A. Franco Gonzalez, N.-H. Yang, R.-S. Liu, Silicon anode design for lithium-ion batteries: progress and perspectives, J. Phys. Chem. C 121 (2017) 27775–27787, https://doi.org/10.1021/acs.jpcc.7b07793.
[8] M. Ashuri, Q. He, L.L. Shaw, Silicon as a potential anode material for Li-ion batteries: where size, geometry and structure matter, Nanoscale 8 (2016) 74–103, https://doi.org/10.1039/c5nr05116a.
[9] M. Jiao, Y. Wang, C. Ye, C. Wang, W. Zhang, C. Liang, High-capacity SiOx (0≤ x≤ 2) as promising anode materials for next-generation lithium-ion batteries, J. Alloys Compd. 842 (2020) 155774, https://doi.org/10.1016/j.jallcom.2020.155774.
[10] M. Miyachi, H. Yamamoto, H. Kawai, T. Ohta, M. Shirakata, Analysis of SiO anodes for lithium-ion batteries, J. Electrochem. Soc. 152 (2005) A2089, https://doi.org/10.1149/1.2013210.
[11] X. Yang, C. Zhan, D. Xu, D. Nan, R. Lv, W. Shen, F. Kang, Z.-H. Huang, SiOx@ Si-graphite microspheres for high-stable anode of lithium-ion batteries, Electrochim. Acta 426 (2022) 140795, https://doi.org/10.2139/ssrn.4118143.
[12] N. Yan, F. Wang, H. Zhong, Y. Li, Y. Wang, L. Hu, Q. Chen, Hollow porous SiO2 nanocubes towards high-performance anodes for lithium-ion batteries, Sci. Rep. 3 (2013) 1568, https://doi.org/10.1038/srep01568.
[13] W. Liu, J. Jiang, H. Wang, C. Deng, F. Wang, G. Peng, Influence of graphene oxide on electrochemical performance of Si anode material for lithium-ion batteries, J. Energy Chem. 25 (2016) 817–824, https://doi.org/10.1016/j.jechem.2016.06.006.
[14] E. Moyassari, T. Roth, S. Kücher, C.-C. Chang, S.-C. Hou, F.B. Spingler, A. Jossen, The role of silicon in silicon-graphite composite electrodes regarding specific capacity, cycle stability, and expansion, J. Electrochem. Soc. 169 (2022) 010504, https://doi.org/10.1149/ma2022-012421mtgabs.
[15] C. Heubner, T. Liebmann, C. Lämmel, M. Schneider, A. Michaelis, Insights into the buffer effect observed in blended lithium insertion electrodes, J. Power Sources 363 (2017) 311–316, https://doi.org/10.1016/j.jpowsour.2017.07.108.
[16] J.P. Schmidt, H.Y. Tran, J. Richter, E. Ivers-Tiffée, M. Wohlfahrt-Mehrens, Analysis and prediction of the open circuit potential of lithium-ion cells, J. Power Sources 239 (2013) 696–704, https://doi.org/10.1016/j.jpowsour.2012.11.101.
[17] A. Klein, P. Axmann, M. Wohlfahrt-Mehrens, Synergetic effects of LiFe0. 3Mn0. 7PO4–LiMn1. 9Al0. 1O4 blend electrodes, J. Power Sources 309 (2016) 169–177, https://doi.org/10.1016/j.jpowsour.2016.01.093.
[18] S. Yoshida, T. Okubo, Y. Masuo, Y. Oba, D. Shibata, M. Haruta, T. Doi, M. Inaba, High rate charge and discharge characteristics of graphite/SiOx composite electrodes, Electrochemistry 85 (2017) 403–408, https://doi.org/10.5796/electrochemistry.85.403.
[19] K.P. Yao, J.S. Okasinski, K. Kalaga, J.D. Almer, D.P. Abraham, Operando quantification of (de) lithiation behavior of silicon–graphite blended electrodes for lithium-ion batteries, Adv. Energy Mater. 9 (2019) 1803380, https://doi.org/10.1002/aenm.201803380.
[20] C. Heubner, T. Liebmann, O. Lohrberg, S. Cangaz, S. Maletti, A. Michaelis, Understanding component-specific contributions and internal dynamics in silicon/graphite blended electrodes for high-energy lithium-ion batteries, Batter. Supercaps. 5 (2022) e202100182, https://doi.org/10.1002/batt.202100182.
[21] D. Wycisk, M. Oldenburger, M.G. Stoye, T. Mrkonjic, A. Latz, Modified Plett-model for modeling voltage hysteresis in lithium-ion cells, J. Energy Storage 52 (2022) 105016, https://doi.org/10.1016/j.est.2022.105016.
[22] S. Bazlen, P. Heugel, O. von Kessel, W. Commerell, J. Tübke, Influence of charging protocols on the charging capability and aging of lithium-ion cells with silicon-containing anodes, J. Energy Storage 49 (2022) 104044, https://doi.org/10.1016/j.est.2022.104044.
[23] K. Richter, T. Waldmann, N. Paul, N. Jobst, R.-G. Scurtu, M. Hofmann, R. Gilles, M. Wohlfahrt-Mehrens, Low-temperature charging and aging mechanisms of Si/C composite anodes in Li-ion batteries: an operando neutron scattering study, ChemSusChem 13 (2020) 529–538, https://doi.org/10.1002/cssc.201903139.
[24] B. Liu, Y. Jia, J. Li, H. Jiang, S. Yin, J. Xu, Multiphysics coupled computational model for commercialized Si/graphite composite anode, J. Power Sources 450 (2020) 227667, https://doi.org/10.1016/j.jpowsour.2019.227667.
[25] J. Schmitt, M. Schindler, A. Oberbauer, A. Jossen, Determination of degradation modes of lithium-ion batteries considering aging-induced changes in the half-cell open-circuit potential curve of silicon–graphite, J. Power Sources 532 (2022) 231296, https://doi.org/10.2139/ssrn.4014217.
[26] V.A. Sethuraman, V. Srinivasan, A.F. Bower, P.R. Guduru, In situ measurements of stress-potential coupling in lithiated silicon, J. Electrochem. Soc. 157 (2010) A1253, https://doi.org/10.1149/1.3489378.
[27] P. Lian, X. Zhu, S. Liang, Z. Li, W. Yang, H. Wang, Large reversible capacity of high quality graphene sheets as an anode material for lithium-ion batteries, Electrochim. Acta 55 (2010) 3909–3914, https://doi.org/10.1016/j.electacta.2010.02.025.
[28] J.-M. Tarascon, M. Armand, Issues and challenges facing rechargeable lithium batteries, Nature 414 (2001) 359–367, https://doi.org/10.1038/35104644.
[29] J.R. Dahn, Phase diagram of Li x C 6, Phys. Rev. B 44 (1991) 9170, https://doi.org/10.1103/PhysRevB.44.9170.
[30] D. Allart, M. Montaru, H. Gualous, Model of lithium intercalation into graphite by potentiometric analysis with equilibrium and entropy change curves of graphite electrode, J. Electrochem. Soc. 165 (2018) A380, https://doi.org/10.1149/2.1251802jes.
[31] S. Rodríguez-Cadavid, N. Bless, J. Poehler, J. Sabatier, P. Lanusse, C. Farges, BMS-oriented model for Li-ion batteries with mixed SiOx/graphite anodes, in: 2020 5th Int. Conf. Smart Sustain. Technol. Split., IEEE, 2020: pp. 1–6. 10.23919/splitech49282.2020.9243758.
[32] C. Schmitt, A. Kube, N. Wagner, K.A. Friedrich, Understanding the influence of temperature on phase evolution during lithium-graphite (de-)intercalation processes: an operando X-ray diffraction study, ChemElectroChem 9 (2022) e202101342, https://doi.org/10.1002/celc.202101342.
[33] A. Zülke, Y. Li, P. Keil, R. Burrell, S. Belaisch, M. Nagarathinam, M.P. Mercer, H. E. Hoster, High-energy nickel-cobalt-aluminium oxide (NCA) cells on idle: anode-versus cathode-driven side reactions, Batter. Supercaps. 4 (2021) 934–947, https://doi.org/10.1002/batt.202100101.
[34] J. Park, S.S. Park, Y.S. Won, In situ XRD study of the structural changes of graphite anodes mixed with SiOx during lithium insertion and extraction in lithium ion batteries, Electrochim. Acta 107 (2013) 467–472, https://doi.org/10.1016/j.electacta.2013.06.059.
[35] Z. Yang, S.E. Trask, X. Wu, B.J. Ingram, Effect of Si content on extreme fast charging behavior in silicon–graphite composite anodes, Batteries 9 (2023) 138. https://doi.org/10.3390/batteries9020138.
[36] J.P. Schmidt, S. Arnold, A. Loges, D. Werner, T. Wetzel, E. Ivers-Tiffée, Measurement of the internal cell temperature via impedance: evaluation and application of a new method, J. Power Sources 243 (2013) 110–117, https://doi.org/10.1016/j.jpowsour.2013.06.013.
[37] W. Waag, S. Käbitz, D.U. Sauer, Experimental investigation of the lithium-ion battery impedance characteristic at various conditions and aging states and its influence on the application, Appl. Energy 102 (2013) 885–897, https://doi.org/10.1016/j.apenergy.2012.09.030.
[38] N. Ogihara, S. Kawauchi, C. Okuda, Y. Itou, Y. Takeuchi, Y. Ukyo, Theoretical and experimental analysis of porous electrodes for lithium-ion batteries by electrochemical impedance spectroscopy using a symmetric cell, J. Electrochem. Soc. 159 (2012) A1034, https://doi.org/10.1149/2.057207jes.
[39] X. Ding, D. Zhang, J. Cheng, B. Wang, P.C.K. Luk, An improved Thevenin model of lithium-ion battery with high accuracy for electric vehicles, Appl. Energy 254 (2019) 113615, https://doi.org/10.1016/j.apenergy.2019.113615.
[40] B.Y. Liaw, G. Nagasubramanian, R.G. Jungst, D.H. Doughty, Modeling of lithium ion cells—a simple equivalent-circuit model approach, Solid State Ionics 175 (2004) 835–839, https://doi.org/10.1016/j.ssi.2004.09.049.
[41] F. Katzer, M.A. Danzer, Analysis and detection of lithium deposition after fast charging of lithium-ion batteries by investigating the impedance relaxation, J. Power Sources 503 (2021) 230009, https://doi.org/10.1016/j.jpowsour.2021.230009.
[42] M. Petzl, M. Kasper, M.A. Danzer, Lithium plating in a commercial lithium-ion battery–a low-temperature aging study, J. Power Sources 275 (2015) 799–807, https://doi.org/10.1016/j.jpowsour.2014.11.065.
[43] V.A. Sethuraman, V. Srinivasan, J. Newman, Analysis of electrochemical lithiation and delithiation kinetics in silicon, J. Electrochem. Soc. 160 (2012) A394, https://doi.org/10.1149/2.008303jes.
[44] F. Xuyun, S. Zechang, A battery model including hysteresis for state-of-charge estimation in Ni-MH battery, in: 2008 IEEE Veh. Power Propuls. Conf., IEEE, 2008: pp. 1–5. https://doi.org/10.1109/vppc.2008.4677449.
[45] D.M. Bernardi, J.-Y. Go, Analysis of pulse and relaxation behavior in lithium-ion batteries, J. Power Sources 196 (2011) 412–427, https://doi.org/10.1016/j.jpowsour.2010.06.107.

[46] N.A. Cañas, P. Einsiedel, O.T. Freitag, C. Heim, M. Steinhauer, D.-W. Park, K. A. Friedrich, Operando X-ray diffraction during battery cycling at elevated temperatures: a quantitative analysis of lithium-graphite intercalation compounds, Carbon 116 (2017) 255–263, https://doi.org/10.1016/j.carbon.2017.02.002.
[47] J. Moon, H.C. Lee, H. Jung, S. Wakita, S. Cho, J. Yoon, J. Lee, A. Ueda, B. Choi, S. Lee, Interplay between electrochemical reactions and mechanical responses in silicon–graphite anodes and its impact on degradation, Nat. Commun. 12 (2021) 2714, https://doi.org/10.1038/s41467-021-22662-7.
[48] Q. Sun, G. Zeng, J. Li, S. Wang, M. Botifoll, H. Wang, D. Li, F. Ji, J. Cheng, H. Shao, Y. Tian, J. Arbiol, A. Cabot, L. Ci, Is soft carbon a more suitable match for SiO_x in Li-ion battery anodes? Small 19 (2023) 2302644 https://doi.org/10.1002/smll.202302644.

2.3 Active Material Lithiation in Gr/SiO_x Blend Anodes at Increased C-Rates

This section builds upon the findings of Section 2.2, in which the lithiation behavior of full cells was explored. The third research article, entitled "Active Material Lithiation in Gr/SiO_x Blend Anodes at Increased C-Rates", provides a precise analysis of the lithiation behavior in an experimental half-cell setup. The objective of this study is to gain comprehensive insights into the lithiation behavior of Gr/SiO_x blend anodes across the entire SoL range. In the experimental setup, a pure SiO_x and a pure graphite anode half-cell are connected in parallel, inspired by a comparable setup in the work of Heubner et al. [151]. This setup permits the precise measurement of the current contributed to each active material, thus enabling the calculation of each material's SoL.
Similar to the test protocol presented in Section 2.2, the lithiation behavior is analyzed for different lithiation rates. The results are in accordance with the prior findings that an increased C-rate is associated with an augmented SiO_x lithiation. The findings of this study demonstrate that this phenomenon occurs across the entire SoL range. It is only at significantly increased C-rates that an increased graphite lithiation can be observed within a limited range, where graphite first begins to undergo lithiation. However, during the subsequent relaxation period, the SiO_x lithiation exhibits a marked increase, that even exceeds the lithiation of the remaining C-rates. In contrast to the augmented graphite lithiation, it is demonstrated that the state of the augmented SiO_x lithiation persists during relaxation periods, as the silicon hysteresis prevents any balancing effects.
To extend the findings, a pseudo two-dimensional (p2D) Doyle-Fuller-Newman (DFN) simulation is performed to compare the electrochemical measurements of the parallel setup with a model of a Gr/SiO_x blend anode, which is similar to the electrodes that are used in real applications. The results of both the measurements and the simulation demonstrate a comparable lithiation behavior, with the sole distinction being enhanced balancing during the relaxation period following very high C-rates. This is due to the fact that a direct lithium exchange is feasible between graphite and SiO_x particles in the simulation. Moreover, the simulation allows for variations in the SiO_x content, thereby facilitating an investigation of the resulting lithiation behavior.
The combination of the full cell measurements presented in Section 2.2, the parallel half-cell setup, and the electrochemical simulation collectively substantiate the hypothesis that the kinetics of Gr/SiO_x blend anodes shift the lithiation distribution towards an enhanced SiO_x lithiation at elevated charging currents at room temperature. The presented methods provide insights into the fast-charge behavior of Gr/SiO_x blend anodes, which can be used to enhance the performance by improving the SoL estimation. This has a direct impact on the subsequent discharge voltage profile, which in turn affects the SoC estimation. The shown improvements to the simulation model can be employed in the design of fast-charging profiles with the objective of reducing the charging time or mitigating the risk of LiD. Furthermore, the direct

measurements of the active material lithiation corroborate the thermodynamic effects posited in the previous studies. These assumptions include the clear separation of graphite delithiation prior to SiO_x delithiation and the effect that the silicon hysteresis prevents possible balancing charge exchange from SiO_x to graphite due to the significantly increased delithiation potential of SiO_x.

Publication notes

In the following, the article entitled "Active Material Lithiation in Gr/SiOx Blend Anodes at Increased C-Rates" is presented in its accepted manuscript form. The article was submitted to the *Journal of The Electrochemcial Society* for peer review in May 2024 and got accepted in August 2024 [152]. The permanent web link to this publication is available under `https://doi.org/10.1149/1945-7111/ad68a9`. Parts of the publication have been presented on the 244th Meeting of The Electrochemical Society in Gothenburg (Sweden) in October 2023 [153]. To support the main article, additional information is provided in the Supplementary material, including an image of the test setup and validation measurements with a second set of experimental cells.

Author contribution

J.K. developed the concept of the study, designed the experimental setup, and assembled the experimental cells. J.K. and T.K. conducted the electrochemical measurements and evaluated that resulting data. J.L. carried out the electrochemical simulation. J.K., J.L., and M.S. discussed the simulation results. J.K. wrote the manuscript, assisted by M.S. in the section about the simulation. A.A. and M.A.D. reviewed and edited the manuscript and provided supervision for the research project. All authors discussed and commented on the results.

Active Material Lithiation in Gr/SiOx Blend Anodes at Increased C-Rates

Author Names: Julian Knorr[1,2,z], Jiahao Li[3], Maximilian Schamel[2,4], Thomas Kufner[1], Alexander Adam[3] and Michael A. Danzer[2,4]
Affiliation(s):
[1]BMW Group, Research and Technology Centre, 85748, Garching, Germany
[2]Chair of Electrical Energy Systems (EES), University of Bayreuth, Universitätsstraße 30, 95447, Bayreuth, Germany
[3]BMW Group, Battery Cell Competence Centre, 80788, Munich, Germany
[4]Bavarian Center for Battery Technology (BayBatt), University of Bayreuth, Universitätsstraße 30, 95447, Bayreuth, Germany
[z]Corresponding Author E-mail Address [julian.knorr@bmw.de]

Abstract
The energy density of lithium-ion batteries can be improved by adding silicon as a secondary active anode material alongside graphite. However, accurate state estimation of batteries with blend electrodes requires detailed knowledge of the interplay between the active materials during lithiation. Challenges arise from the current split between the active materials and the overlap of their working potentials. This study examines the lithiation behavior of blend anodes using a setup consisting of a pure graphite and a pure SiOx half-cell connected in parallel. The setup allows for current measurements of both active materials, the determination of the state of lithiation throughout the entire charging process and measurements of balancing effects between the active materials during relaxation periods. Analysis of the behavior at increased charge rates results in greater SiOx lithiation after similar charge throughput indicating better kinetics for SiOx compared to graphite. A Doyle-Fuller-Newman model of a blend anode is used to further investigate the experimental findings on the lithiation behavior and transfer them to blend electrodes. Simulation-based variations of the silicon content show that an increased SiOx content in blend anodes leads to improved rate capability.

Introduction
Over the past decade lithium-ion batteries (LIB) became more and more important due to the pursuit of carbon neutrality in the energy and transport sectors. As the market demands higher energy densities, new active materials are investigated. Silicon (Si) proves to be an interesting anode material with a theoretical specific capacity of 3579 mAh g^{-1}, which is about ten times greater than graphite (Gr), which is commonly used as an anode active material[1]. However, the large volume expansion of Si during lithiation significantly reduces the cycling stability due to particle cracking and the resulting increase in irreversible solid-electrolyte-interface (SEI) formation[1–3]. SiOx, nano-Si, or Si embedded in a porous carbon structure can be used to reduce these negative side effects[4–6]. Cell manufacturers are beginning to use these Si-based materials in blend anodes along with Gr to combine the advantages of both active materials. Gr, as the main material, provides a high structural stability, a high conductivity, and longevity[7]. The Si-based secondary active materials increase the cell's capacity. The interaction between both active materials presents new challenges, e.g., estimating the state of charge (SoC) on cell level or the state of lithiation (SoL) on electrode level. The individual SoLs diverge during charging

and discharging as the open-circuit potential (OCP) of both active material species differs greatly over the course of lithiation and delithiation. Si is primarily active in the lower SoC range, due to the higher average equilibrium potential compared to Gr[8–10]. The potential hysteresis of Si further increases this complexity, which results in an increased delithiation potential, resulting in a larger difference to the working potential of Gr[11]. A detailed understanding of the lithiation behavior is necessary to provide an accurate estimation of the SoC in full cells with blend anodes containing Si.

Bazlen et al.[8] investigated the capacity distribution between Si and Gr at different charge rates in full cells by analyzing the cell voltage and dilatation. Richter et al.[12] used simultaneous operando neutron diffraction at -21 °C to study the Gr lithiation. The experiment showed an increase in Gr lithiation at higher current rates (C-rate) due to kinetic limitations of Si at low temperatures. Heubner et al.[11,13,14] and Liebmann et al.[15] developed a method to measure the current density towards each active material in blend electrodes. They separated the active materials of blend electrodes and connected them in parallel, allowing for direct measurement of the current attributed to each active material. Using this method, the range at which Si or Gr is active during (de-)lithiation can be precisely identified. Chatzogiannakis et al.[16] analyzed the behavior of cathode blend electrodes using a similar setup, focusing on the effective C-rate on the individual active materials. In our previous work[17], we examined the dependency of the C-rate on the lithiation behavior of a full cell with a Gr/SiOx anode. The analysis of the voltage profile after partial lithiation showed that the SiOx lithiation increases with the C-rate during charging.

This work investigates the effect of the lithiation rate on the SoL of the active materials in Gr/SiOx blend anodes. To achieve this, measurements are conducted using a half-cell setup connected in parallel, inspired by the work of Heubner et al.[13]. The two active materials are separated into individual half-cells. Connecting the cells in parallel simulates the electric contact within a blend anode, while still allowing measurements of the current split between the active materials. The measured currents and calculated SoLs indicate which active material is preferably lithiated at higher lithiation rates and therefore shows an increased SoL at the same capacity throughput of the total setup. The lithiation rate varies between C/40 and 1C. The setup further provides a method to analyze balancing effects between the active materials during relaxation periods. An explanation of the lithiation and balancing behavior is provided by the analysis of the anode potential and the SiOx hysteresis. The measurements are also used to parameterize a pseudo two-dimensional (p2D) Doyle-Fuller-Newman (DFN) model. This model deciphers the lithiation process and allows the transfer of the results from a half-cells setup connected in parallel to real blend electrodes. Simulation-based parameter variations further help to understand the lithiation behavior of active materials in blend anodes.

In the layout of the work, firstly the experimental and simulation setup used to analyze the lithiation behavior of blend anodes is described. Secondly, the results of the measurements carried out are presented and the kinetics of the active materials at increased lithiation rates are discussed. Finally, the simulation results are compared with the measurements, and the impact of an increased SiOx content on the rate capability is discussed.

Experimental

Half-cell assembly. – SiOx and Gr half-cells are assembled in the T-cell setup under dry room conditions with a dew point of less than -50 °C. Electrodes with a diameter of 12.7 mm are punched out of coated anode sheets of each active material. The electrodes are dried at 60 °C for 24 h before assembly. The pure active materials, SiOx and Gr, as the working electrodes are countered by pure lithium (Li) metal with the same diameter. Additionally, a pure Li reference electrode is inserted into the setup.

Table 1 presents the specific parameters for the working electrodes and other components. The anode thickness, porosity, and the amount of binders and additive are the most significant differences between the electrodes of the SiOx and Gr half-cells. The particle sizes are estimated using cross-sectional scanning electron microscopy (SEM) from different cells with the same active materials. The low conductivity of SiOx[18] requires a higher amount of conductive additives than Gr to produce sufficient electrodes. The anode loading is selected in a way to match the weight proportion of SiOx in existing commercial cells, which typically contain 5 to 10 wt% of SiOx. This results in 8.5 wt% of SiOx in the active material masses for this setup, excluding the masses of binders and additives. Consequently, there is a significant difference in the electrode thickness. The porosity of the SiOx electrode is more than twice as high as that of the Gr electrode before formation. However, this large difference in porosity only exists at a very low SoL since the severe volume expansion of SiOx by around 150 % during lithiation[5] significantly reduces it.

A standard 1.2M $LiPF_6$ electrolyte for battery cells is used, which contains ethylene carbonate (EC), dimethyl carbonate (DMC), ethyl methyl carbonate (EMC) and fluoroethylene carbonate (FEC) solvents. Both types of cells use nanoscale carbon black as a conductive additive, along with commercially available polyacrylic acid and carboxymethyl cellulose as binders.

Table 1. Half-cell parameters for SiOx and Gr.

Parameter	SiOx	Graphite
Anode diameter	12.7 mm	12.7 mm
Anode thickness	25 µm	90 µm
Copper foil thickness	10 µm	10 µm
Anode weight	2.21 mg	18.9 mg
Anode loading	1.74 mg cm^{-2}	15.0 mg cm^{-2}
Active material proportion	75 %	95 %
Particle size	3-6 µm	8-15 µm
Theoretical reversible specific capacity	1995 mAh g^{-1}	372 mAh g^{-1}
Theoretical reversible capacity	3.31 mAh	6.68 mAh
Calculated porosity	65.1 %	25.1 %
Separator diameter	13 mm	13 mm
Separator thickness	260 µm	260 µm
Electrolyte volume	160 µl	160 µl

Half-cell formation process. – The prepared half-cells are subjected to three consecutive formation cycles immediately after assembly. Lithiation and delithiation are terminated using cutoff voltages of 10 mV and 1.2 V, respectively. The voltage during formation is measured between the working and reference electrode. The cells are lithiated and delithiated at a rate of C/40 with respect to the theoretical capacities. The specific theoretical capacity of Gr is 372 mAh/g[19,20], resulting in a theoretical capacity of 6.68 mAh with an anode mass of 18.9 mg and an active material share of 95 %.
It is impossible to give an explicit value for the specific capacity of SiOx due to the formation of irreversible by-products. Both active materials, Gr and SiOx, form a passivation layer, called SEI, surrounding the active material particle. This SEI results from electrolyte decomposition during the initial cycles of a battery cell[21,22]. Additionally, the oxygen in SiOx forms irreversible by-products that reduce the volume expansion of the particles[23,24]. These by-products mainly include Li_2O and the lithium silicate Li_4SiO_4[5,24,25]. Other lithium silicates, such as $Li_6Si_2O_7$ or $Li_2Si_2O_5$, also occur[23,26]. Besides cyclable Li, both types of by-products consume oxygen, and in the case of the lithium silicates also Si. The reversible specific capacity is defined by the distribution between Li-silicate and Li_2O formation in combination with the amount of oxygen in the SiOx particles. In our previous work, a range of the theoretical specific capacity was calculated for SiO particles (x=1) and the two extreme cases of by-product formation, with only one existing by-product[17]. The theoretical specific initial capacity and theoretical specific reversible capacity are in the ranges of 2318 to 3496 mAh/g and 1710 to 2280 mAh/g, respectively. The higher value corresponds to an exclusive formation of Li_2O, and the lower value corresponds to an exclusive Li_4SiO_4 formation. In this work, 2907 mAh/g and 1995 mAh/g are chosen for the calculation of the theoretical initial and reversible capacity, respectively, assuming an equal distribution between both by-products and SiO as the original material. The SiOx half-cell has a theoretical initial capacity of 4.82 mAh and a theoretical reversible capacity of 3.31 mAh, with an anode mass of 2.21 mg and an active material proportion of 75 %. These calculated values are also included in Table 1.
In previous experiments, it was observed that pure SiOx performs better when subjected to three consecutive formation cycles at a rate of C/40. This ensures that the formation process is sufficiently completed, and the low C-rate is necessary to reduce the polarization of the initial cycle. During this cycle, the conversion of crystalline to amorphous silicon occurs at low potentials[24,27]. The formation of the Gr half-cell is performed similarly to generate comparable results. The potentials of the third cycle are used as a pseudo OCP for (de-)lithiation. Zahner ZENNIUM PRO potentiostats are used for cycling and measuring. The tests are performed in a climate chamber at 25 °C.

Parallel half-cell setup. – Both cells are connected in parallel after formation completion. The entire setup is described in Fig. 1. A 1 Ω shunt resistance is connected in each parallel path. In total, three Zahner ZENNIUM PRO potentiostats are used to cycle and measure the parallel setup. The first potentiostat sets the current I_1 for the total setup and measures the voltage U_1 of the parallel setup. According to Kirchhoff's second law, the voltage of each parallel path is equal to the voltage U_1. The second potentiostat is utilized to measure the voltage across the shunt resistor in the SiOx path. According to Ohms law, $I_{SiOx} = U_2 / 1\ \Omega$, meaning that the measured voltage is equivalent to the current of the SiOx path. The Gr path is treated similarly,

with $I_{Gr} = U_3 / 1\ \Omega$. The shunt's resistance is selected in a way to have minimal impact on the electric path while still guaranteeing accurate measurements. From our experiences, this type of half-cells typically exhibits a resistance of 20-30 Ohms. This setup is based on the work of Heubner et at.[11,13] and ensures that a 1 Ω shunt resistor has a negligible influence on the electric path. A photograph of the entire setup is provided in the supplementary material in Fig. S1.

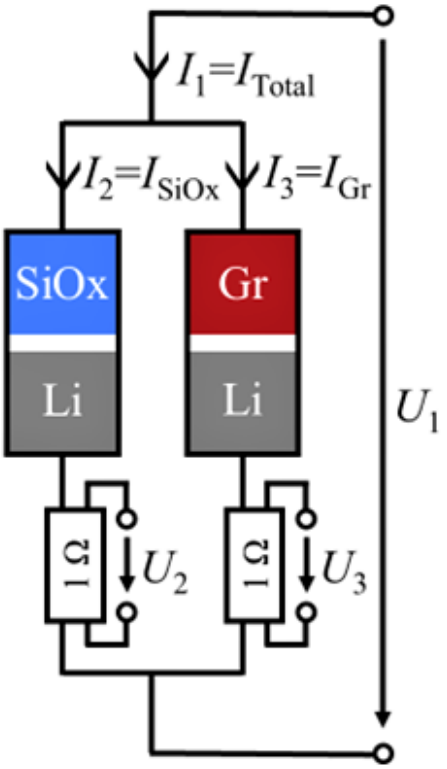

Figure 1. Schematic illustration of the experimental test setup. The SiOx and Gr half-cells are connected in parallel, each with a 1 Ω shunt resistor in the electrical path.

Test procedure. – The objective of this work is to analyze the SoL of both active materials in blend electrodes during lithiation. To achieve this, we compare different lithiation rates within the parallel setup, ranging from very low C-rates with almost no polarization to high rates with significant polarization for the used half-cells. The C-rates are defined based on the sum of both half-cell capacities, similar to a blend electrode. The reversible capacity is determined by using the third delithiation cycle. This experiment compares the lithiation rates of C/40, C/20, C/10, C/3 and 1C. The lithiation rates 1C and, to a certain extent, C/3 exhibit significant polarization, which was already observed in full cells during fast charging. For each cycle, a delithiation rate of C/40 is chosen to maximize the lifetime. Studying the delithiation rate is an additional research question, but not within the scope of this work. A relaxation period of 1 h after lithiation and delithiation enables the measurement of potential balancing effects between SiOx and Gr.

Simulation model. – The parallel half-cell setup described here provides insights into the active material lithiation of blend electrodes. It is important to note that setup is only a simplification of the actual behavior. To validate the measurements, a p2D DFN model is created and

parameterized to transfer the results to blend electrodes. The DFN model is commonly used to model the electrochemical behavior of Li-ion battery cells. In 1993, Doyle et al.[28] introduced the p2D model based on the porous-electrode theory of Newman and Tiedemann[29]. The DFN model consists of the Butler-Volmer kinetics for (de-)lithiation and considers electric conductivities, solid diffusion according to Fick's law, and electrolyte diffusion[30,31].

The simulation of a blend electrode instead of two pure active material half-cells connected in parallel requires some necessary changes in the parameterization. This causes a slightly different behavior than seen in the measurements but allows to draw conclusions about the lithiation in blend electrodes. These changes include a unique electrode thickness, the active material proportion, and a unique porosity for both active materials. In the simulation model, the two active materials allow for a direct exchange of Li ions through the electrolyte. However, in the parallel setup, this exchange is only possible between the Li metal counter electrodes.

The model used in this work consists of two p2D models on a single axis, each with its own kinetics for the corresponding active material[32]. This implies that both SiOx and Gr particles coexist at each position between the current collector and the separator, with a similar capacity share as in the experimental setup. Contrary to the experiment, the particles use the same electrolyte, enabling direct Li exchange between the different active materials. The blend electrode is countered by an infinite Li source. The model includes both lithiation and delithiation OCP for SiOx to consider the hysteresis of Si. To the best of our knowledge, there exists no universal solution yet to model the hysteresis of silicon. A hysteresis model based on the zero-state model of Plett[33] is used for each SiOx particle individually.

$$\frac{dS}{dT} = -K\left|\frac{dx}{dt}\right|\left(\operatorname{sign}\left(\frac{dx}{dt}\right) + S\right) \tag{1}$$

$$OCP_{\mathrm{SiOx}}(SoL_{\mathrm{SiOx}}) = OCP_{\mathrm{SiOx,avg}}(SoL_{\mathrm{SiOx}}) + S \cdot OCP_{\mathrm{SiOx,offset}}(SoL_{\mathrm{SiOx}}) \tag{2}$$

$$OCP_{\mathrm{SiOx,avg}}(SoL_{\mathrm{SiOx}}) = \frac{OCP_{\mathrm{SiOx,Delith}}(SoL_{\mathrm{SiOx}}) + OCP_{\mathrm{SiOx,Lith}}(SoL_{\mathrm{SiOx}})}{2} \tag{3}$$

$$OCP_{\mathrm{SiOx,offset}}(SoL_{\mathrm{SiOx}}) = \frac{OCP_{\mathrm{SiOx,Delith}}(SoL_{\mathrm{SiOx}}) - OCP_{\mathrm{SiOx,Lith}}(SoL_{\mathrm{SiOx}})}{2} \tag{4}$$

The variable S defines the state of the hysteresis transition, which has a range of $-1 \leq S \leq 1$. At $S = 1$, the potential equals the delithiation potential, and at $S = -1$, it equals the lithiation potential. x is the local current density in A/m^3 and K is used as a fitting parameter. The average of the lithiation and delithiation OCP is taken for Gr, as Gr has no significant rate-dependent hysteresis[34,35].

All simulation parameters are summarized in Table 2. The parameters are either taken directly from the experimental setup or fitted to match the measurements of the parallel half-cell setup. In the parallel setup, the porosity of the SiOx and Gr half-cell varies significantly. The value of 25.1 % is chosen for the simulation to ensure uniform porosity, which is similar to the Gr half-cell. During lithiation, SiOx expands to around 150 %[5], causing a significant reduction in the porosity of the SiOx half-cell at higher SoL_{SiOx}. The porosity of the Gr half-cell is comparable to that of real blend anodes. This parameter should be taken into account when comparing simulation results with measurements.

Table 2. p2D simulation parameters with the information of the origin from where the values are taken.

Parameter	Value	Origin
Anode thickness	90 µm	Experimental setup Gr half-cell
Active material proportion	95 %	Experimental setup Gr half-cell
Max. Li concentration in Gr	31507 mol m^{-3}	Theoretical value
Max. Li concentration in SiOx	278000 mol m^{-3}	Theoretical value
Porosity	25.1 %	Experimental setup Gr half-cell
Separator thickness	260 µm	Experimental setup
Electrode conductivity	100 S m^{-1}	Fitted parameter
Gr particle radius	10 µm	Fitted parameter
SiOx particle radius	5 µm	Fitted parameter
Exchange current density for Gr intercalation (50 % SoL)	4 A m^{-2}	Fitted parameter
Exchange current density for SiOx intercalation (50 % SoL)	6 A m^{-2}	Fitted parameter
Electrolyte volume fraction in separator	0.93	Experimental setup
Electrolyte volume fraction in electrode	0.25	Experimental setup
Diffusion Gr	4e-15 m^2 s^{-1}	Fitted parameter
Diffusion SiOx	8e-15 m^2 s^{-1}	Fitted parameter
Bruggeman exponent separator	1.6	Fitted parameter
Bruggeman exponent electrode	1.8	Fitted parameter
Factor *K* for hysteresis modeling	100	Fitted parameter

Results and discussion

Half-cell formation results. – The voltage of all formation cycles is displayed in Fig. 2a. During the first lithiation of SiOx, there is a voltage plateau at approximately 0.1 V. Silicon transitions from its crystalline phase to the amorphous phase during the first lithiation step, which causes this phenomenon[24,27]. Table 3 presents the lithiated and delithiated specific capacities, as well as the calculated coulombic efficiency (CE) of each cycle. The CE is defined as the lithiated capacity divided by the delithiated capacity for a single cycle and describes the reversible capacity in percent. The initial cycle exceeds the theoretical value of the specific capacity due to the SEI formation, resulting in a low CE below 90 %. Subsequent cycles exhibit specific capacities slightly lower than the theoretical value, but with CEs above 97 %, indicating a completed formation process.

The lower initial CE of the SiOx half-cell is explained by the formation of Li-silicates and Li_2O, in addition to the SEI. The specific capacities are lower than the previously defined theoretical values. However, the reversible specific capacity matches with the measurements from the literature[9]. One possible reason for the lower specific capacity could be a not completed formation of Li-silicates and Li_2O after the first cycle. This also explains the CE of around 92 % in the second and third cycle of SiOx compared to the graphite cell with a CE greater than 97 % in these cycles. However, the lower specific capacities suggest a high oxygen content with $x > 1$ in the SiOx.

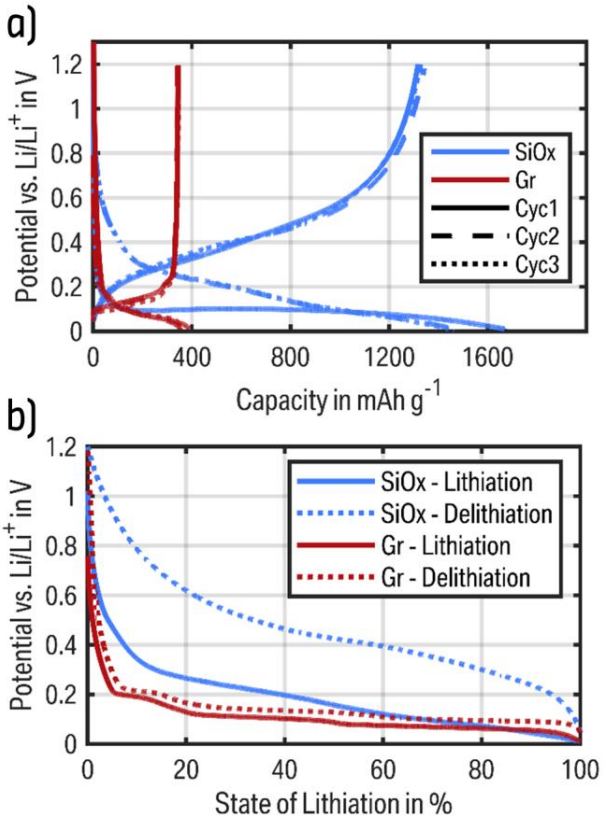

Figure 2. a) Formation cycles of Gr and SiOx half-cells. b) OCP of Gr and SiOx taken from the third formation cycle and normalized to the total charge throughput.

The nominal capacity and C-rate for the parallel setup are calculated using the absolute values of the delithiated capacity during the third formation cycle. The half-cells show a nominal capacity of 2.20 mAh and 6.22 mAh for SiOx and Gr, respectively. Therefore, the parallel setup has a total nominal capacity of 8.42 mAh, and a current of 1C is equal to 8.42 mA.

Fig. 2b displays the pseudo OCP of both materials for lithiation and delithiation. The x-axis is normalized to the capacity throughput of lithiation and delithiation, respectively. Graphite shows the plateaus during the phase transitions from LiC_{72} to LiC_{36} at around 0.2 V, from LiC_{24} to LiC_{12} at around 0.11 V, and from LiC_{12} to the fully lithiated LiC_6 at around 0.07 V[36]. The small voltage deviation between lithiation and delithiation of approximately 20 mV is mostly due to polarization effects, as Gr exhibits almost no intrinsic hysteresis[34,35]. In contrast, SiOx or silicon in general exhibit a significant voltage hysteresis. The pseudo OCP measurements show an average hysteresis of 285 mV, with an increasing trend towards lower SoLs. The cause of this hysteresis is still a matter of debate. Mechanical stress caused by the large volume expansion is often given as a reason[37,38]. Durdel et al.[39] proposed another explanation based on the strong relaxation behavior of Si. According to this hypothesis, charge transfer requires large overpotentials even at low (de-)lithiation rates. SiOx generally has a higher working potential than Gr, which is mostly active below potentials of 0.2 V. During lithiation of SiOx, only the upper 61 % of SoL are below this threshold. However, during delithiation, this percentage drops to 6 % due to the hysteresis of SiOx. This suggests that there are two distinct voltage regions where each material is active.

Table 3. Measurements of the specific capacities during (de-)lithiation for all three C/40 formation cycles. Additionally, the coulombic efficiency (CE) is given for each cycle.

Material	Cycle	Spec. capacity - Lithiation	Spec. capacity - Delithiation	CE
Graphite	1	389.9 mAh g-1	344.3 mAh g-1	88.3 %
	2	352.5 mAh g-1	342.3 mAh g-1	97.1 %
	3	355.5 mAh g-1	345.9 mAh g-1	97.3 %
SiOx	1	1668.5 mAh g-1	1317.6 mAh g-1	79.0 %
	2	1466.3 mAh g-1	1345.3 mAh g-1	91.8 %
	3	1442.5 mAh g-1	1327.0 mAh g-1	92.0 %

Parallel setup current measurements. – Fig. 3 shows the measurements obtained by connecting the cells in parallel and cycling them with different C-rates. The subplots a) to e) correspond to each lithiation rate from C/40 to 1C and display the lithiation step and the following 1 h relaxation. The set lithiation rate is visualized in grey, while the current split between the SiOx and Gr cell is visualized in blue and red, respectively. A higher absolute current indicates a greater contribution of the certain material in this region. Unlike full cells, a negative current indicates lithiation since a Gr or SiOx anode of a full cell appears as the cathode in a half-cell vs. lithium. Please note that in Fig. 3, the current is presented in mA rather than as a C-rate. The SiOx cell has approximately one-third of the capacity of the Gr cell, so a similar current represents a three times higher C-rate. Fig. 3a displays not only the lithiation current measurements but also the measurements during the subsequent C/40 delithiation process and the measured potential for the parallel setup.

Upon analysis of the C/40 measurements, it is evident that the expected behavior, according to the pseudo OCPs, is present. The potential measured is identical for both active materials, due to the parallel connection. The material with the lower potential gradient exhibits a higher lithiation. At a rate of C/40, the polarization is almost negligible, allowing to match anode potential ranges of the active materials to the measurements. At C/40, lithiation starts in a range where SiOx accounts for most of the current. The potential in this range exceeds 0.2 V. The SiOx pseudo OCP shows working potentials up to 39 % SoL above this level, while Gr only shows 2 % SoL. Therefore, most of the current is covered by SiOx. Additionally, there are three peaks of high Gr current regions with varying sizes, corresponding to the three Gr plateaus with almost constant potential. The transition between plateaus allows for further lithiation of SiOx as its OCP constantly decreases. Delithiation of Gr and SiOx is almost completely separated, with Gr being delithiated prior to SiOx. This can be explained by the SiOx hysteresis mentioned in the previous subsection. SiOx is delithiated at a working potential higher than 0.2 V, while Gr is already largely delithiated.

Increasing the lithiation rate terminates the lithiation process before reaching full lithiation due to the increased polarization causing the potential to reach 10 mV earlier. At C/20 and C/10, the overall behavior, is similar to the C/40 reference, with the major difference being that the SiOx current does not decrease as much during the graphite plateaus as in the C/40 case. This trend becomes more pronounced at C/3 and 1C lithiation. However, the lithiation terminates too early at these rates to make a sufficient statement, based only on the current measurements. The effective C-rate of each active material exceeds the set C-rate of the parallel setup if one material contributes more than its capacity share. This can result in high electrochemical stress,

especially in regions where one material is primarily active[15,16]. During the 1C lithiation of the parallel setup, SiOx exhibits a maximum current of 4.96 mA. This is equivalent to a C-rate of 2.3C, with the available capacity of the SiOx cell being 2.20 mAh. This is due to the preference to lithiate SiOx in low SoL regions and its lower capacity share of 26 %.

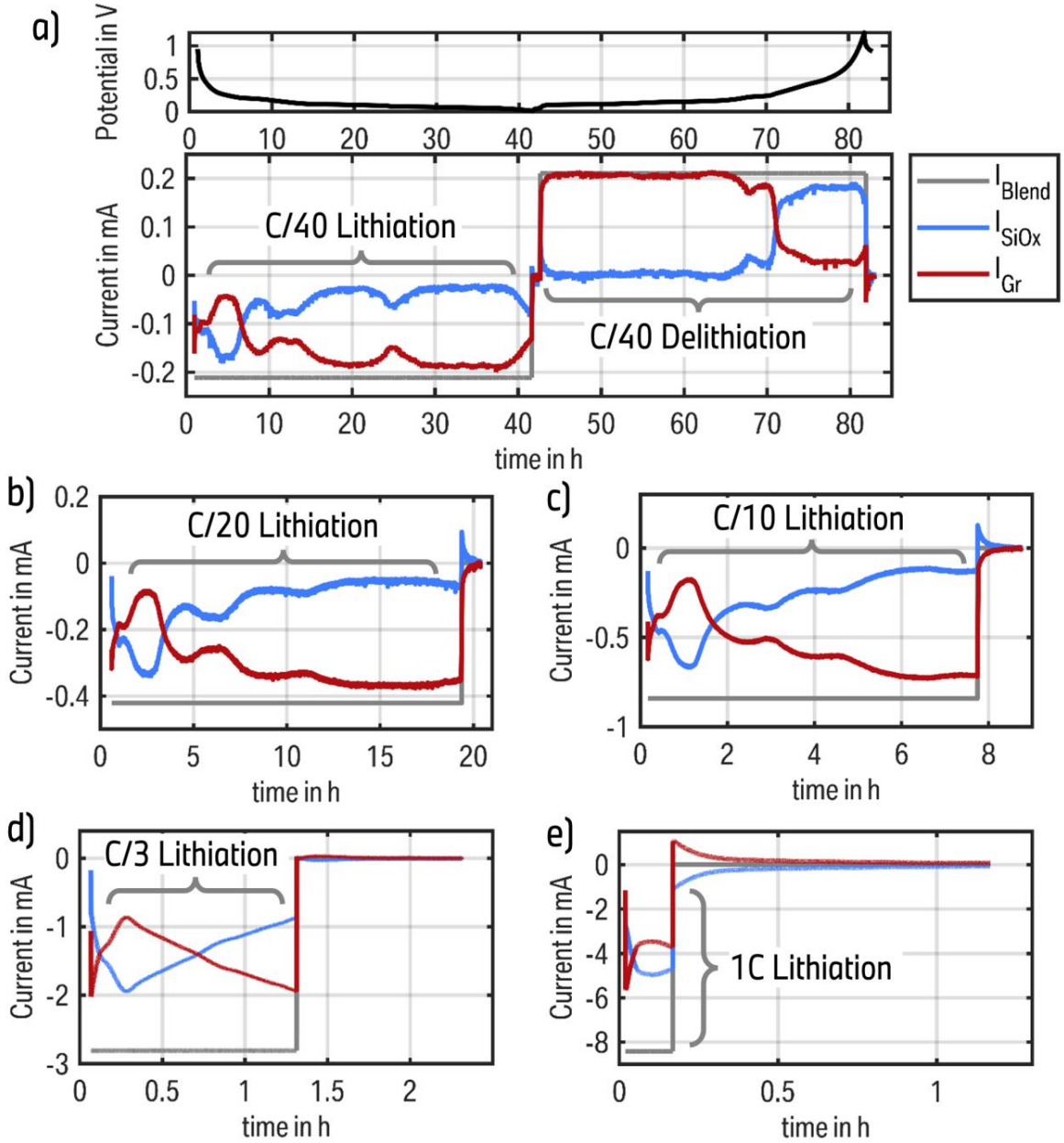

Figure 3. Measurements of all lithiation rates for the active material currents over time, with SiOx in blue and Gr in red. The set total current of the parallel setup is shown in grey. a) Current measurement of the C/40 lithiation step, followed by the C/40 delithiation step. The anode potential is displayed above the current measurement at different rates of the lithiation step: b) C/20, c) C/10, d) C/3, e) 1C. Subsequent to each lithiation step, a 1 h relaxation period is implemented.

A balancing current is observed at the start of the relaxation period after lithiation at rates of C/40, C/20, and C/10. This current delithiates the SiOx and lithiates the Gr, indicating a lower OCP of the SiOx cell. The balancing current continues until the OCP of both active materials is equal. However, this balancing current quickly drops to a negligible amount. At higher rates, the opposite balancing effect occurs, delithiating the Gr and lithiating the SiOx. The effect is barely noticeable after C/3 lithiation, but it becomes significant after 1C lithiation, with a maximum of 1.1 mA. This high balancing current indicates a substantial difference in the OCP between Gr and SiOx, which significantly affects the SoL of the active materials.
The current measurements align with the findings of Heubner et al.[11], where pure Si is connected in parallel to Gr instead of SiOx.

Lithiation behavior. – Fig. 4 displays the calculated SoL for the SiOx and Gr half-cells. Fig. 4a and Fig. 4b show the results during lithiation with low and high C-rates, respectively. The C/40 lithiation is given in both subplots as a reference. Fig. 4c shows the C/40 delithiation for all cycles following the varying lithiation rates. The SoL is defined for each active material with respect to the C/40 lithiation cycle. For instance, a SoL_{SiOx} of 20 % during C/3 lithiation equals 20 % of the maximum capacity stored in the SiOx during C/40 lithiation. The dashed grey lines indicate equal lithiation of both active materials. SiOx consistently exhibits higher lithiation than Gr, regardless of the charge throughput, due to the higher anode potential of SiOx. This effect is further enhanced during delithiation because of the higher delithiation potential. The lithiation curve of SiOx can be found above this dividing line, while the Gr curve is located below it. The progression over time during lithiation and delithiation is indicated by the black arrows.
The data presented in Fig. 4a demonstrates that a higher lithiation rate results in a greater SoL of the SiOx cell throughout the entire lithiation process. This effect is particularly noticeable in the SoL of the SiOx cell, which has a nominal capacity three times lower than that of the Gr cell. The largest difference between C/40 and C/10 lithiation occurs at the end of the second graphite plateau, with an increased SoL_{SiOx} of +11.3 % at a total capacity throughput of 4.5 mAh. The analysis in Fig. 4b shows a slightly different behavior for higher lithiation rates. The Gr lithiation exceeds here the C/40 reference in the initial stages of the lithiation process. Nevertheless, the SoL_{SiOx} at C/3 surpasses the reference again at approximately 1.5 mAh, following the trend that a higher C-rate results in an increased SiOx lithiation. The lithiation step is terminated at an SoL_{SiOx} higher than during C/10 lithiation. The large polarization during 1C lithiation terminates the lithiation step at a lower SoL_{SiOx} than in the C/40 reference. If the measurements could continue below the 10 mV threshold, it is expected that the behavior would be similar to the observe in the C/3 case. However, lithium plating below 0 mV[40] would distort the lithiation behavior.
This temporary effect of a lower SoL_{SiOx} at higher C-rates is a result of the increased polarization. The SiOx half-cell is primarily responsible for the observed polarization increase, as it is preferentially lithiated during these early stages of lithiation. When the combination of OCP and polarization drops below 0.2 V, it is thermodynamically feasible for Gr to be lithiated. This results in a small current to the Gr cell, which is not possible yet in the reference case. The potential of 0.2 V is reached at a total capacity throughput of 0.56 mAh and 0.20 mAh for the C/3 and 1C cases, respectively. This is the point at which the SoL_{SiOx} falls below the C/40

reference curve, which reaches a potential of 0.2 V after a total capacity throughput of 1.38 mAh.

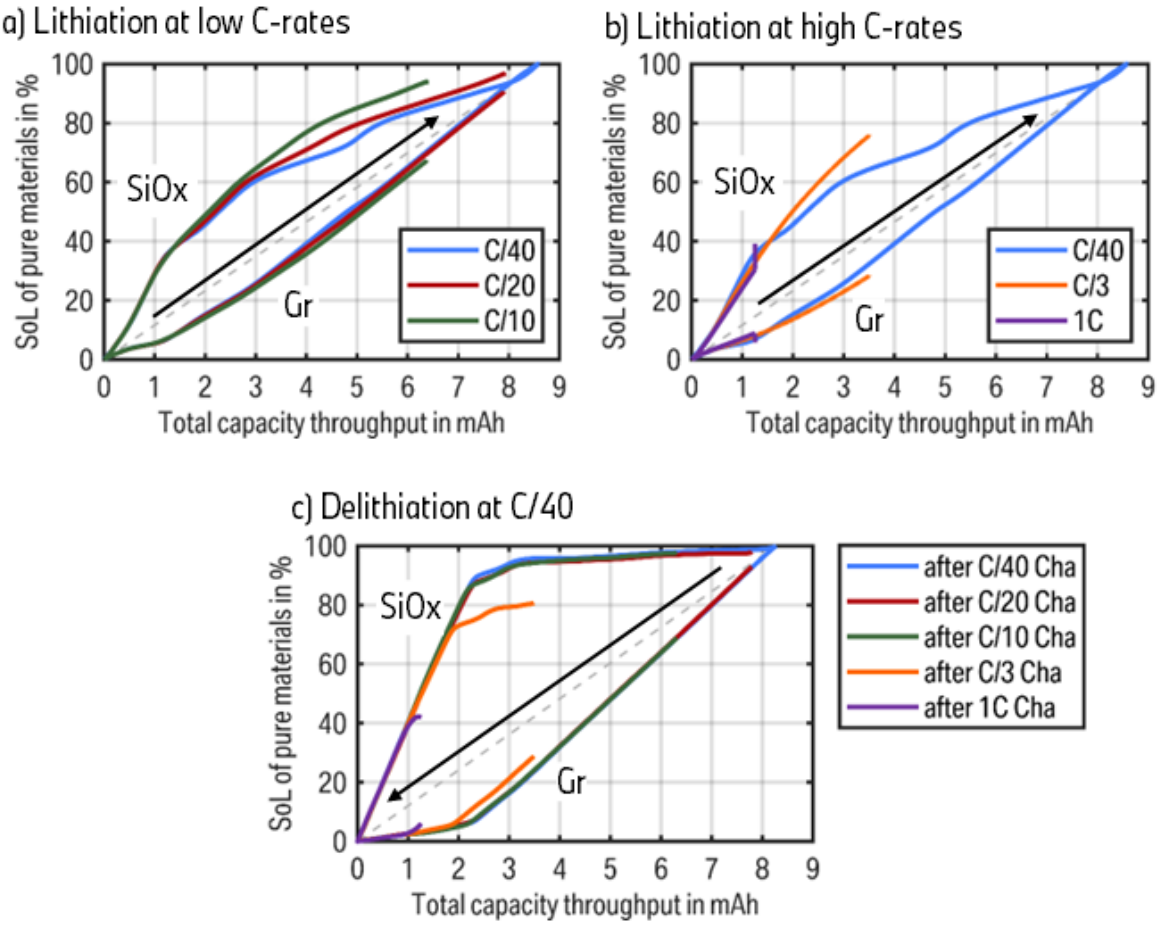

Figure 4. Continuous SoL of Gr and SiOx over the capacity throughput of the total parallel setup. The SoLs are normalized to the charge throughput of the C/40 measurement. The black arrow indicates the chronological procedure of the tests. a) Lithiation with low rates of C/40, C/20 and C/10. b) Lithiation with high rates of C/3 and 1C with C/40 as a reference. c) Delithiation with a rate of C/40 after all different lithiation steps.

At the end of the 1C lithiation, an interesting effect can be observed. A distinct vertical line is clearly visible, indicating a balancing effect during the 1 h relaxation period. SiOx undergoes further lithiation while Gr gets delithiated, as shown by the current measurements in Fig. 3e. The SoL_{SiOx} even exceeds the C/40 reference at this parallel setup capacity. This balancing effect will be further explained in the subsequent section.

The C/40 delithiation in Fig. 4c shows the expected behavior of Gr being delithiated first, followed by the SiOx delithiation. At low C-rates, the SiOx is almost fully lithiated, and only the reduced Gr lithiation accounts for the lower amount of total capacity throughput until the cutoff voltage is reached.

The reason for the preferred lithiation of SiOx at increasing lithiation rates is likely due to a reduced polarization compared to Gr. In the parallel connection, both half-cell active materials must have an identical potential. Therefore, when analyzing the lithiation behavior, both the OCP and the

polarization caused by the internal resistance must be considered. At low current, the polarization is low and the SoL-dependent OCP is the main factor influencing the current split in the parallel setup. In this case, the material with a lower OCP gradient is preferably lithiated. At higher C-rates, the impact of the internal resistance becomes more pronounced.
The measurements indicate that SiOx reaches a higher SoL at the same setup capacity at higher C-rates in comparison to the C/40 reference case. This could be indicative of a lower SiOx resistance compared to Gr. The reason for this could be enhanced material-specific transport properties, which would lead to the assumption that SiOx is more suitable for fast charging than Gr. This was demonstrated in our previous work on full cells with Gr/SiOx blend anodes[17]. Nevertheless, the reduced electrode thickness of SiOx must also be taken into account, which leads to shorter transport paths than in the Gr half-cell, possibly resulting in lower resistance.
However, the effect of a higher SoL_{SiOx} at elevated C-rates becomes apparent at increased setup capacity. One potential explanation is that the material-specific resistances are significantly influenced by the SoL, a phenomenon commonly observed in battery electrodes[41]. Further studies are required to investigate the resistance of each material as a function of SoL, which is beyond the scope of this work.
To preclude the possibility that the observations are a consequence of severe cell degradation, an additional C/40 cycle is conducted subsequent to the aforementioned test procedure. The delithiation capacity remains at 95.8 % in comparison with the initial C/40 cycle. Given that a C-rate of 1C is considerably high for the T-cell format, this degradation is sufficiently low to permit the observation to be interpreted as an effect of the interplay between SiOx and Gr.
To validate the discussed measurements, the entire procedure is repeated with a second set of pure material half-cells, and the results are provided in the supplementary material (Fig. S2 and Fig. S3).

Balancing effects during relaxation. – The balancing effects during the 1 h relaxation period need to be discussed in more detail. Both active materials have the same potential, and there should be no significant polarization after 1 h of relaxation. The expected behavior is that a similar SoL will be present at the end of the relaxation, regardless of the C-rate. Richter et al.[12] showed this effect at low temperatures, where Gr is lithiated over Si, due to kinetic limitations at these temperatures. Li ions are transferred from Gr to Si until a homogeneous state is reached. However, our measurements show a different behavior. Little to no balancing is observed at an increased SoL_{SiOx} at the end of lithiation (C/20, C/10 & C/3), which remains above the C/40 reference at the end of the relaxation step. In contrast, there is a balancing effect following 1C lithiation, which even exceeds the expected amount. At the end of the 1C lithiation step, the SoL_{SiOx} is well below the C/40 reference curve. However, it increases above this reference until the end of the relaxation, as illustrated by the vertical line in Fig. 4b. This substantial amount of charge exchange is also evident by observations of the current in Fig. 3e. The hysteresis of SiOx explains both unexpected balancing effects.
The current measurements during the relaxation, as shown in Fig. 3 a)-c), indicate that a small amount of SiOx is delithiated while Gr is lithiated for the same amount. This process stops almost immediately, before transferring a substantial amount of charge. The end of the balancing process indicates that the OCP of both cells is identical. However, the hysteresis stops this process long before reaching the reference. As the C-rate increases, SiOx is more lithiated and its OCP falls below the OCP of Gr at the end of the lithiation step. This leads to

the delithiation of SiOx and the lithiation of Gr until they reach a similar OCP. The delithiation of SiOx triggers a transition from the lithiation to the delithiation OCP, which is referred to as the hysteresis transition. Eqs. (1-4) describe this hysteresis transition. During the initial stages of the hysteresis transition, the potential increases rapidly, leading to a homogeneous anode potential even in the absence of significant charge transfer between the active materials, which stops the balancing effect.

Given that Gr has a negligible hysteresis compared to SiOx, an increased Gr lithiation results in balancing until the reference case is reached[12]. In the experiment, this only occurs after a lithiation rate of 1C. However, the balancing process continues beyond the reference to an even higher SoL_{SiOx}. The high lithiation gradient at this increased rate in combination with the hysteresis explains this effect and is described in detail in Fig. 5. Fig. 5a) illustrates a four-particle model comprising two SiOx and two Gr particles. One particle of each active material is positioned close to the separator and the other is close to the current collector. The particles situated closer to the separator are more lithiated when concentration gradients are present, as the ionic conductivity is significantly lower than the electrical conductivity[41]. Fig. 5b depicts the anode potential during the relaxation of all four particles until the OCP is similar. It should be noted that this visualization is not based on measurements and is solely intended to illustrate the effect. All processes a-d occur simultaneously but are presented here as separate steps for improved visualization. Point (a) describes the potential at the end of the 1C lithiation step. The transition from (a-b) represents the decrease in polarization until the potential equals to the OCP, resulting in different OCPs for all four particles in state (b). This causes balancing effects that lithiate particles with an OCP higher than the average OCP and delithiate particles with a lower OCP. Step (b-c) explains the balancing between two particles of the same material, while (c-d) describes the balancing between SiOx and Gr. The Gr particles end up at the same SoL at point (c) because Gr has no OCP hysteresis. This average SoL is analogous to the calculated SoL_{Gr} at the end of the 1C lithiation step. As previously stated, the hysteresis transition of SiOx (dotted line) stops any balancing processes almost immediately as the particle transitions from lithiation to delithiation. This results in different SoLs for the SiOx particles. It is important to note that the hysteresis transition shown is only an estimate and is not based on measurements for this specific SiOx half-cell. The OCP difference between the states (c) for Gr and SiOx particles remains significant. Consequently, during the second phase of the balancing process (c-d), the Gr is delithiated and the SiOx lithiated. The SiOx particle near the separator remains at a similar SoL due to the reversed hysteresis transition, which also exhibits significant potential differences. The SiOx particle near the current collector is lithiated by both graphite particles until all particles have the same OCP at point (d). The SoLs of all particles are selected such that the results match the measurements of the 1C lithiation. The only uncertainty is the SoL_{Gr} at point (a), as the data on Gr lithiation is an average and lacks further insights into the concentration gradient within the electrode.

This section describes how the balancing process can exceed the SiOx lithiation of the reference case. The second test setup in the supplementary material demonstrates similar behavior during 1C lithiation, but also to some extent in the C/3 case, despite the SoL_{SiOx} being already higher than the reference case before the relaxation begins.

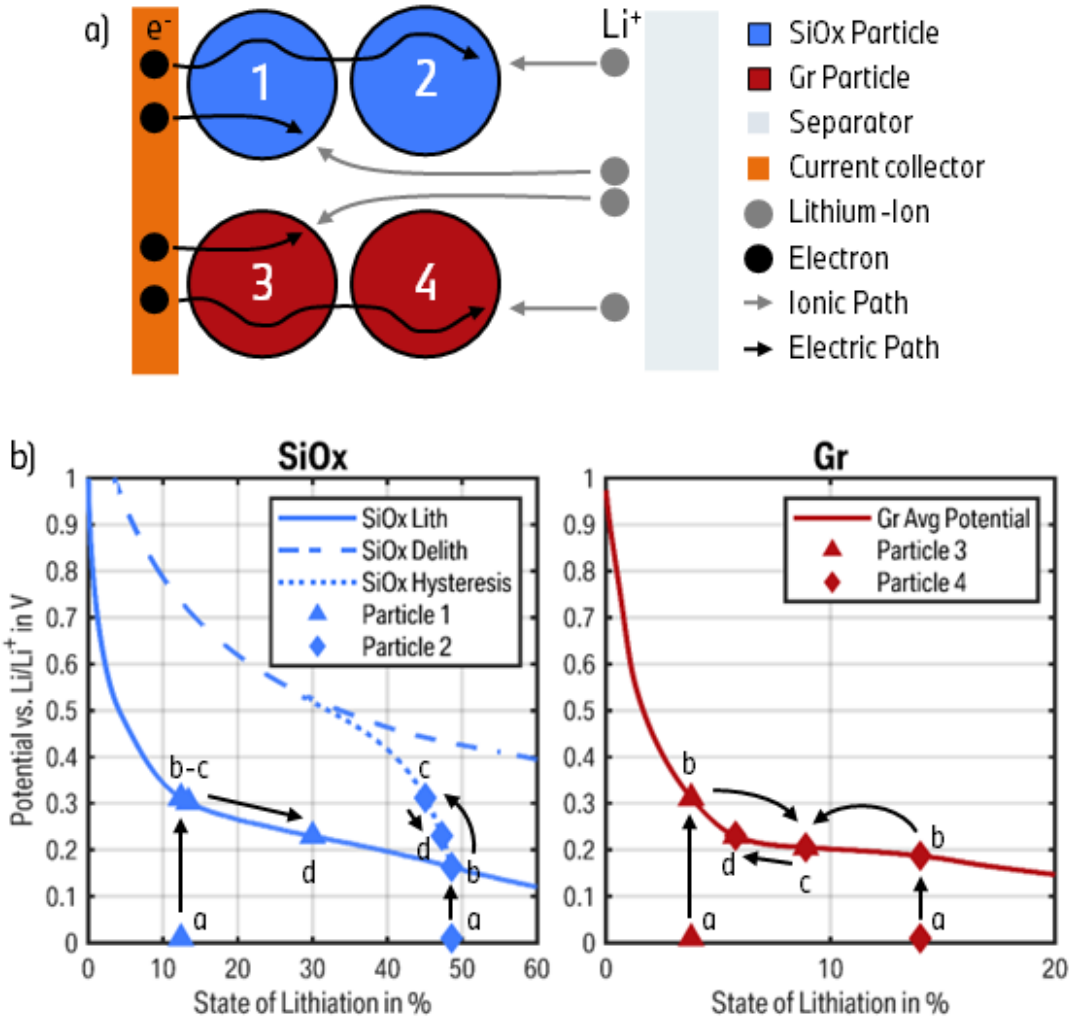

Figure 5. Illustration of the balancing effect after 1C lithiation, which exceeds the reference SiOx lithiation. a) Four-particle model of a blend anode with indicated ionic and electric paths. b) Expected particle potential during the 1C lithiation step and the consecutive balancing effect during the relaxation. The presented particles correspond to the model above. Point (a) shows the potential at the end of the lithiation step including polarization, point (b) shows the potential without polarization effects, point (c) shows the potential after balancing effects between the particles of each active material and point (d) shows the potential after the balancing effects between Gr and SiOx.

Simulation results. – The test procedure is repeated in simulation using the described p2D model to transfer the measurements of the parallel setup to the blend electrode. Fig. 6 compares the potential and charge obtained from simulation and measurement. The results for the lithiation rate C/40 (Fig. 6a and Fig. 6b) and 1C (Fig. 6c and Fig 6d) are displayed in detail. The remaining lithiation rates are presented in an overview plot in Fig. 6e. The parameterization focuses on matching the lithiation potential adequately. When comparing the charge throughput, it is evident that the parallel setup of two pure material half-cells is suitable for measuring the lithiation behavior of blend electrodes. There is almost no deviation visible in the C/40 case. In contrast, the 1C case shows the highest deviation between simulation and measurements in

the charge throughput. This discrepancy is most pronounced during the 1h relaxation, but it gradually diminishes towards the end of the relaxation.

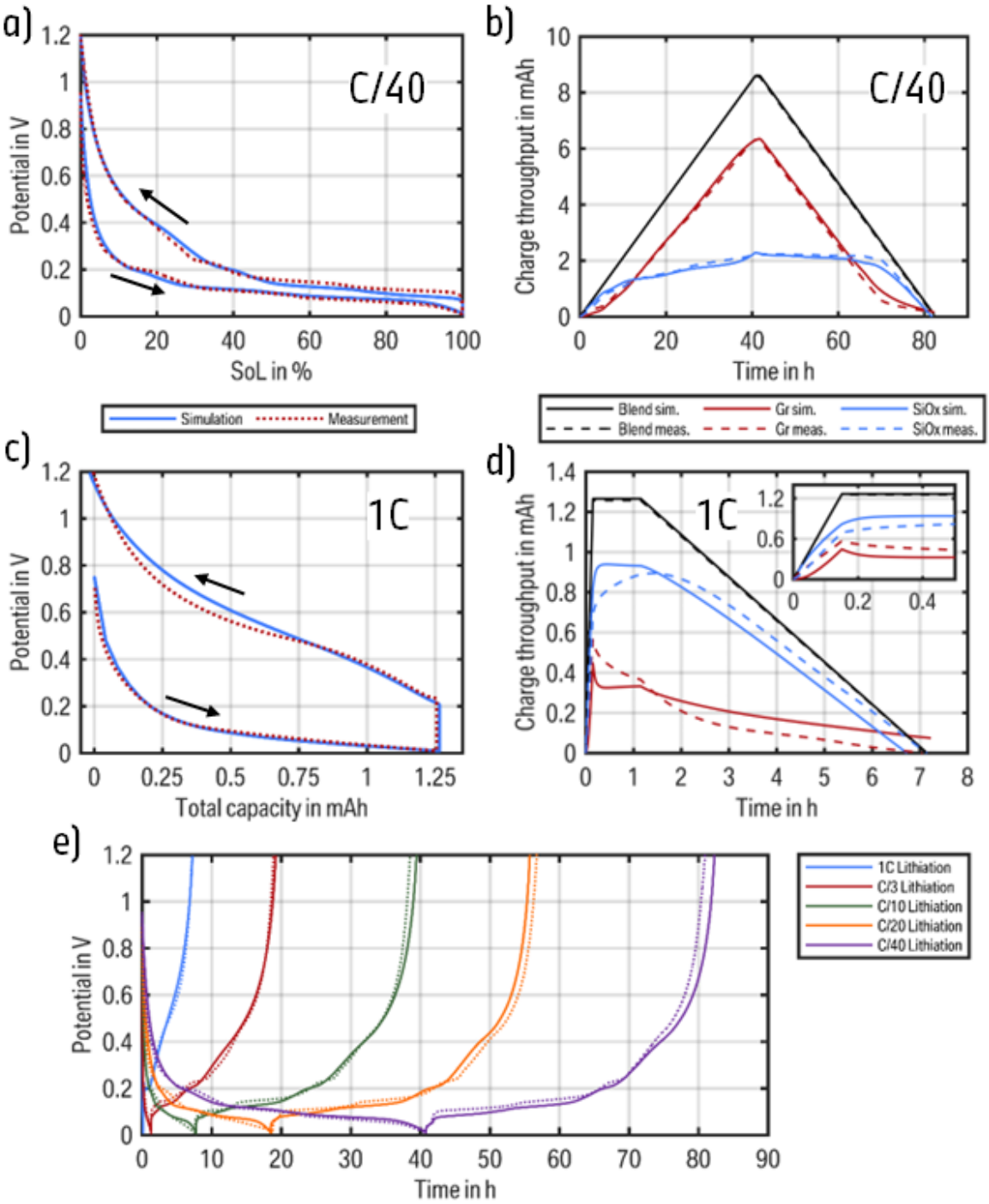

Figure 6. Comparison between the measurements (dotted lines) and the p2D simulation results (solid lines). a) Potential vs. Li/Li^+ during the C/40 (de-)lithiation. b) Charge throughput of Gr, SiOx and the total setup during the C/40 (de-)lithiation. c) Potential vs. Li/Li^+ during the 1C lithiation and the subsequent C/40 delithiation. d) Charge throughput of Gr, SiOx and the total setup during the 1C lithiation and the subsequent C/40 delithiation. e) Potential vs. Li/Li^+ for all lithiation rates and the subsequent C/40 delithiation.

There are two highly probable explanations for the discrepancies observed in the 1C case. Firstly, the p2D model does not account for the high volume expansion of the SiOx particles. Combined with the lower porosity in the simulation model, as explained earlier, this is the most likely reason for the differences observed during the 1C lithiation step. Secondly, the relaxation step appears to be slower in the measurement compared to the simulation. This behavior is expected due to the experimental setup. In the simulation, similar to real blend electrodes, a charge exchange between Gr and SiOx is possible through the relatively short ionic path inside the electrode structure. In the parallel setup, this exchange is only possible by lithium deposition and stripping on the pure Li counter electrode. The longer path through the entire cell structure of both half-cells results in an increased impedance, which explains the slower balancing effect in the measurement setup. However, as the discrepancy diminishes towards the end of the relaxation, it can be inferred that the overall charge throughput is comparable.
These results demonstrate that the parallel setup can be employed to estimate the lithiation behavior of blend electrodes, provided that the limitations of the setup are taken into account in the interpretation of the results. With this understanding, the simulation can be used to generate results that extend beyond the experimental setup. Fig. 7a illustrates the charge throughput at the end of the lithiation step for the measurements and the simulation at different C-rates. The rate capability of the total setup is highly dependent on the performance of the Gr cell. Until a rate of C/3, the SiOx charge throughput remains almost constant while the Gr charge throughput declines significantly. At a lithiation rate of 1C, the SiOx contribution even exceeds the Gr contribution, despite the Gr half-cell having three times the capacity of the SiOx half-cell. Increasing the SiOx content in a blend electrode is a complex process, particularly in the parallel half-cell setup with pure SiOx. However, the simulation allows to easily change this parameter. In this work, the SiOx content is increased while the overall capacity of the cell is kept constant. This decreases the anode thickness due to the higher specific capacity of SiOx. Fig. 7b shows the results of the rate capability with twice the amount of SiOx, compared to the reference case, while keeping the total blend capacity constant. Fig. 7c increases the SiOx content to three times the amount of the reference case. It can be observed from the simulation results that a higher amount of SiOx in the blend electrode increases the rate capability at lithiation rates above C/10. At a rate of 1C, the rate capability increases about three times, similar to the increase in the SiOx content. The overall higher OCP resulting from the increased SiOx content, the better kinetics of Si[11], or a combination of both may be responsible for this improved rate capability. Further measurements with corresponding blend electrodes are necessary to confirm this. However, the simulation provides a rapid solution for investigating the effects of a varying SiOx content.

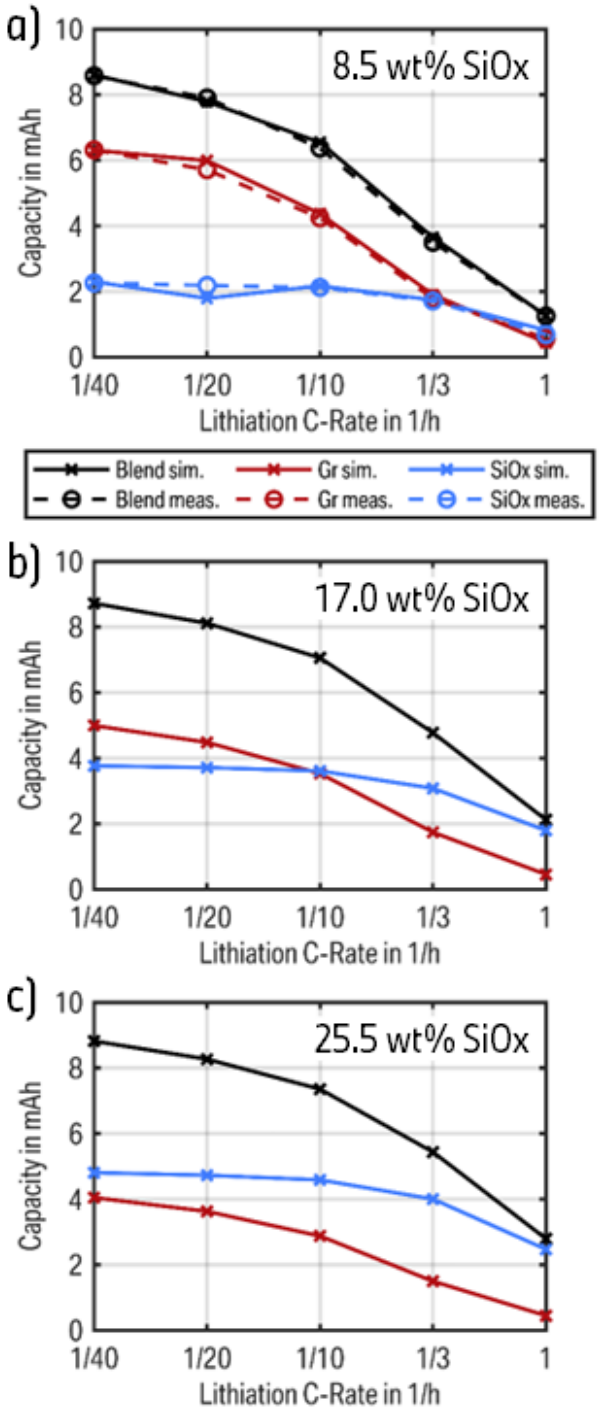

Figure 7. Simulated rate capacity of all lithiation rates at different SiOx contents. The total capacity (black) is also shown separated into the Gr (red) and SiOx (blue) content. a) Rate capacity of the reference case as used in the measurement with a SiOx content of 8.5 wt%. The solid lines represent the simulated values, while the dashed lines represent the measured values. b) Simulated rate capacity of twice the amount of SiOx at a similar total cell capacity. c) Simulated rate capacity of triple the amount of SiOx at a similar total cell capacity.

Conclusions

This study analyzes the lithiation behavior of Gr/SiOx blend anodes in a parallel half-cell setup of the active anode materials. Different lithiation rates are employed to determine the lithiation behavior of SiOx and Gr at increasing rates in blend electrodes. Two pure material half-cells in T-cell format are assembled, one with pure SiOx and one with pure Gr. The two half-cells are connected in parallel to represent the electric contact in a blend electrode. Current measurements of each active material enable the direct calculation of the SoL of each material. To transfer the results to blend electrodes, a p2D Doyle-Fuller-Newman model of a blend anode is parameterized. The simulation results are in good agreement with the measurements, except for a faster balancing effect, since direct lithium exchange between the active materials is possible in the simulated blend electrode. Moreover, the parameterized simulation model allows for changes in the electrode design without having to assemble new cells. The blend electrode's SiOx content is varied up to three times the original amount, resulting in an enhanced rate capability of the cell with a higher SiOx content.
The increased SoL of SiOx at higher rates demonstrates a clear trend in the kinetic behavior of silicon-based anode materials in comparison to graphite. Nevertheless, this must be validated individually for other particle sizes and material concepts, such as nano-Si particles or silicon embedded in a carbon matrix. Additionally, it is anticipated that an electrode design that hinders the kinetics of SiOx will results in a higher Gr lithiation, for instance, by the use of very large SiOx particles.

Abbreviations

C-rate	Charge-rate
CE	Coulombic efficiency
DFN	Doyle-Fuller-Newman
DMC	Dimethyl carbonate
EMC	Ethyl methyl carbonate
EC	Ethylene carbonate
FEC	Fluoroethylene carbonate
Gr	Graphite
Li	Lithium
LIB	Lithium-ion battery
OCP	open-circuit potential
SEI	Solid-electrolyte-interface
SEM	Scanning electron microscopy
Si	Silicon
SiOx	Silicon oxide
SoC	State-of-Charge
SoL	State-of-Lithiation
SoL_{Gr}	State-of-Lithiation of graphite
SoL_{SiOx}	State-of-Lithiation of silicon oxide

References

1. Y. Jin, B. Zhu, Z. Lu, N. Liu, and J. Zhu, *Advanced Energy Materials*, **7**, 1700715 (2017).

2. S. Chae, M. Ko, K. Kim, K. Ahn, and J. Cho, *Joule*, **1**, 47–60 (2017).

3. M. Ashuri, Q. He, and L. L. Shaw, *Nanoscale*, **8**, 74–103 (2016).

4. G. X. Wang, J. H. Ahn, J. Yao, S. Bewlay, and H. K. Liu, *Electrochemistry Communications*, **6**, 689–692 (2004).

5. M. Jiao et al., *Journal of Alloys and Compounds*, **842**, 155774 (2020).

6. G. Liang et al., *Carbon*, **127**, 424–431 (2018).

7. J. Asenbauer et al., *Sustainable Energy Fuels*, **4**, 5387–5416 (2020).

8. S. Bazlen, P. Heugel, O. von Kessel, W. Commerell, and J. Tübke, *Journal of Energy Storage*, **49**, 104044 (2022).

9. S. Yoshida et al., *Electrochemistry*, **85**, 403–408 (2017).

10. K. P. Yao, J. S. Okasinski, K. Kalaga, J. D. Almer, and D. P. Abraham, *Advanced Energy Materials*, **9**, 1803380 (2019).

11. C. Heubner et al., *Batteries & Supercaps*, **5**, e202100182 (2022).

12. K. Richter et al., *ChemSusChem*, **13**, 529–538 (2020).

13. C. Heubner, T. Liebmann, C. Lämmel, M. Schneider, and A. Michaelis, *Journal of Power Sources*, **363**, 311–316 (2017).

14. C. Heubner, T. Liebmann, C. Lämmel, M. Schneider, and A. Michaelis, *ChemElectroChem*, **5**, 425–428 (2018).

15. T. Liebmann, C. Heubner, C. Lämmel, M. Schneider, and A. Michaelis, *ChemElectroChem*, **6**, 5728–5734 (2019).

16. D. Chatzogiannakis et al., *Journal of Power Sources*, **591**, 233804 (2024).

17. J. Knorr et al., *Journal of Energy Storage*, **86**, 111151 (2024).

18. A. Franco Gonzalez, N.-H. Yang, and R.-S. Liu, *The Journal of Physical Chemistry C*, **121**, 27775–27787 (2017).

19. K. Sato, M. Noguchi, A. Demachi, N. Oki, and M. Endo, *Science*, **264**, 556–558 (1994).

20. J. R. Dahn, T. Zheng, Y. Liu, and J. S. Xue, *Science*, **270**, 590–593 (1995).

21. J. R. Dahn, *Physical Review B*, **44**, 9170 (1991).

22. F. Kong et al., *Journal of Power Sources*, **97–98**, 58–66 (2001).

23. S. C. Jung, H.-J. Kim, J.-H. Kim, and Y.-K. Han, *J. Phys. Chem. C*, **120**, 886–892 (2016).

24. T. Chen, J. Wu, Q. Zhang, and X. Su, *Journal of Power Sources*, **363**, 126–144 (2017).

25. M. Miyachi, H. Yamamoto, H. Kawai, T. Ohta, and M. Shirakata, *Journal of the electrochemical society*, **152**, A2089 (2005).

26. T. Kim, S. Park, and S. M. Oh, *Journal of The Electrochemical Society*, **154**, A1112 (2007).

27. W. Wu et al., *Journal of Power Sources*, **464**, 228244 (2020).

28. M. Doyle, T. F. Fuller, and J. Newman, *J. Electrochem. Soc.*, **140**, 1526–1533 (1993).

29. J. Newman and W. Tiedemann, *AIChE Journal*, **21**, 25–41 (1975).

30. J. Schmalstieg, C. Rahe, M. Ecker, and D. U. Sauer, *J. Electrochem. Soc.*, **165**, A3799–A3810 (2018).

31. S. V. Erhard et al., *J. Electrochem. Soc.*, **162**, A2707–A2719 (2015).

32. W. Ai et al., *Journal of Power Sources*, **527**, 231142 (2022).

33. G. L. Plett, *Journal of Power Sources*, **134**, 262–276 (2004).

34. V. J. Ovejas and A. Cuadras, *Sci Rep*, **9**, 14875 (2019).

35. S. Rodríguez-Cadavid et al., in *2020 5th International Conference on Smart and Sustainable Technologies (SpliTech)*,, p. 1–6, IEEE (2020).

36. D. Allart, M. Montaru, and H. Gualous, *Journal of The Electrochemical Society*, **165**, A380 (2018).

37. B. Lu et al., *Phys. Chem. Chem. Phys.*, **18**, 4721–4727 (2016).

38. L. Köbbing, A. Latz, and B. Horstmann, *arXiv preprint arXiv:2305.17533* (2023).

39. A. Durdel, S. Friedrich, L. Hüsken, and A. Jossen, *Batteries*, **9**, 558 (2023).

40. F. Katzer and M. A. Danzer, *Journal of Power Sources*, **503**, 230009 (2021).

41. M. Hahn, A. Schiela, P. Mößle, F. Katzer, and M. A. Danzer, *Journal of Power Sources*, **477**, 228672 (2020).

Supplementary Material:

Fig. S1 shows a photograph of the entire parallel half-cell setup, similar to the schematic illustration in Fig 1.

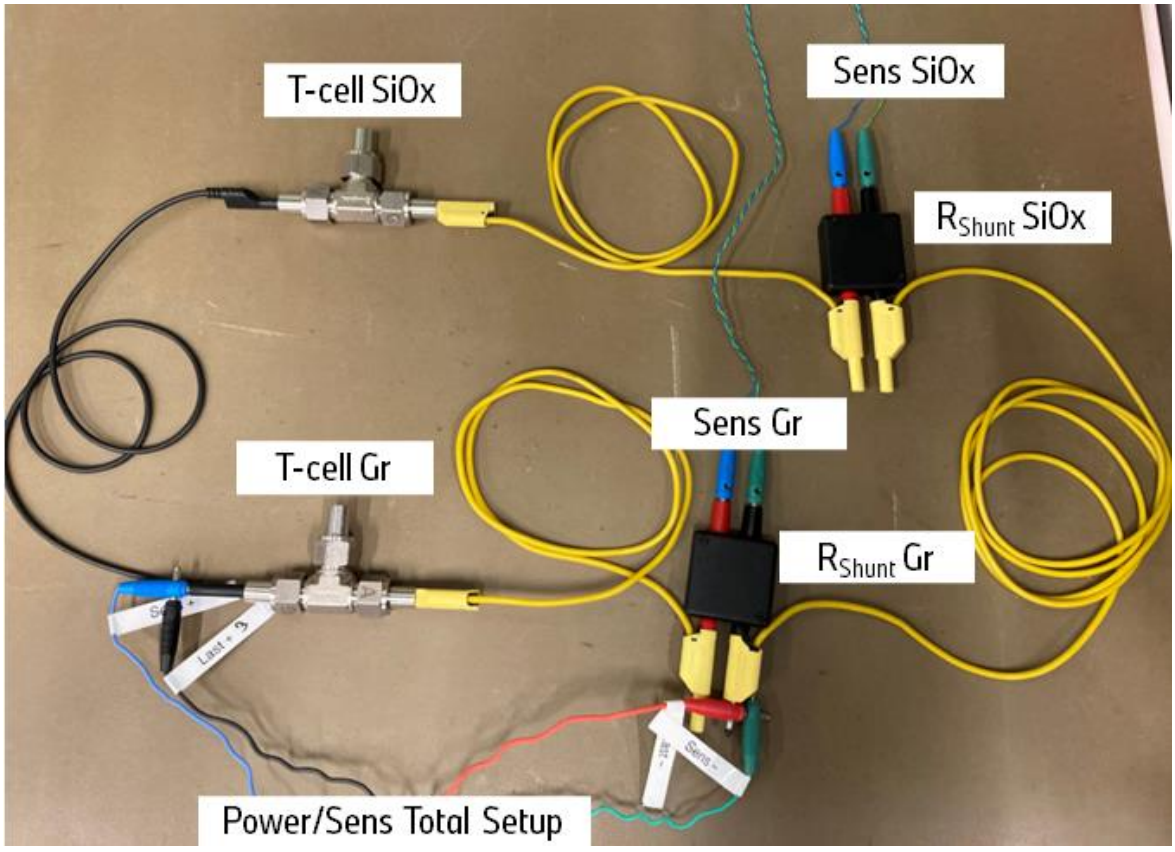

Figure S1. Photograph of the experimental test setup outside of the climate chamber, similar to the schematic illustration shown in Figure 1. The power line of the total setup is used to set I_1 and the sensor line of the total setup is used to measure the voltage U_1. The 1Ω shunt resistances are connected to additional sensor lines to measure the voltages U_2 and U_3.

Fig. S2 and Fig. S3 show the measurements of the second set of parallel connected half-cells. The structure of the figures is identical to Fig. 3 and Fig. 4, respectively.

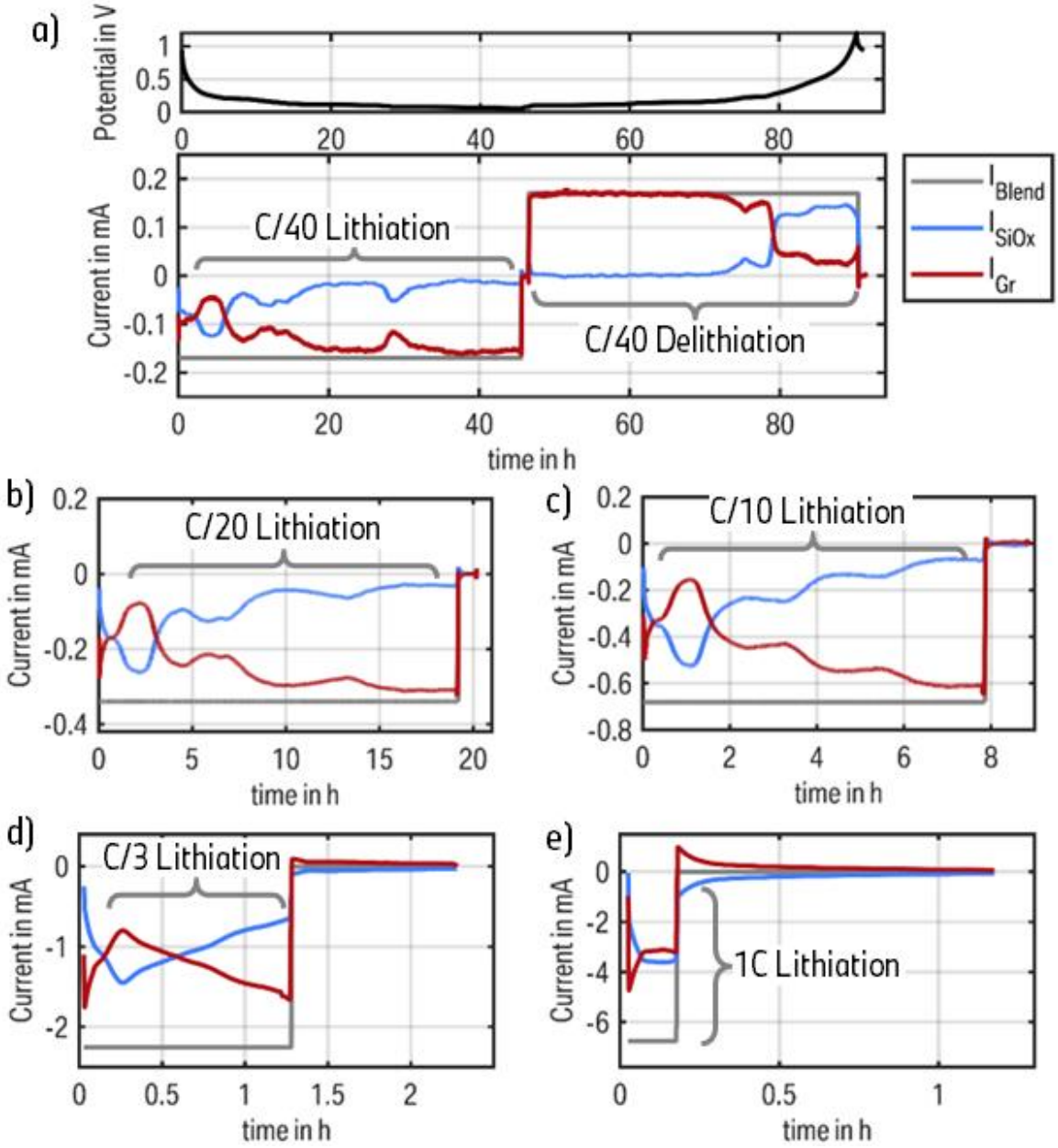

Figure S2. Measurements of all lithiation rates for the active material currents over time, with SiOx in blue and Gr in red. The set total current of the parallel setup is shown in grey. The measurements are conducted with the second set of half-cells, as a validation of the presented results in the main work. a) Current measurement of the C/40 lithiation step, followed by the C/40 delithiation step. The anode potential is displayed above the current measurement at different rates of the lithiation step: b) C/20, c) C/10, d) C/3, e) 1C. Subsequent to each lithiation step, a 1 h relaxation period is implemented.

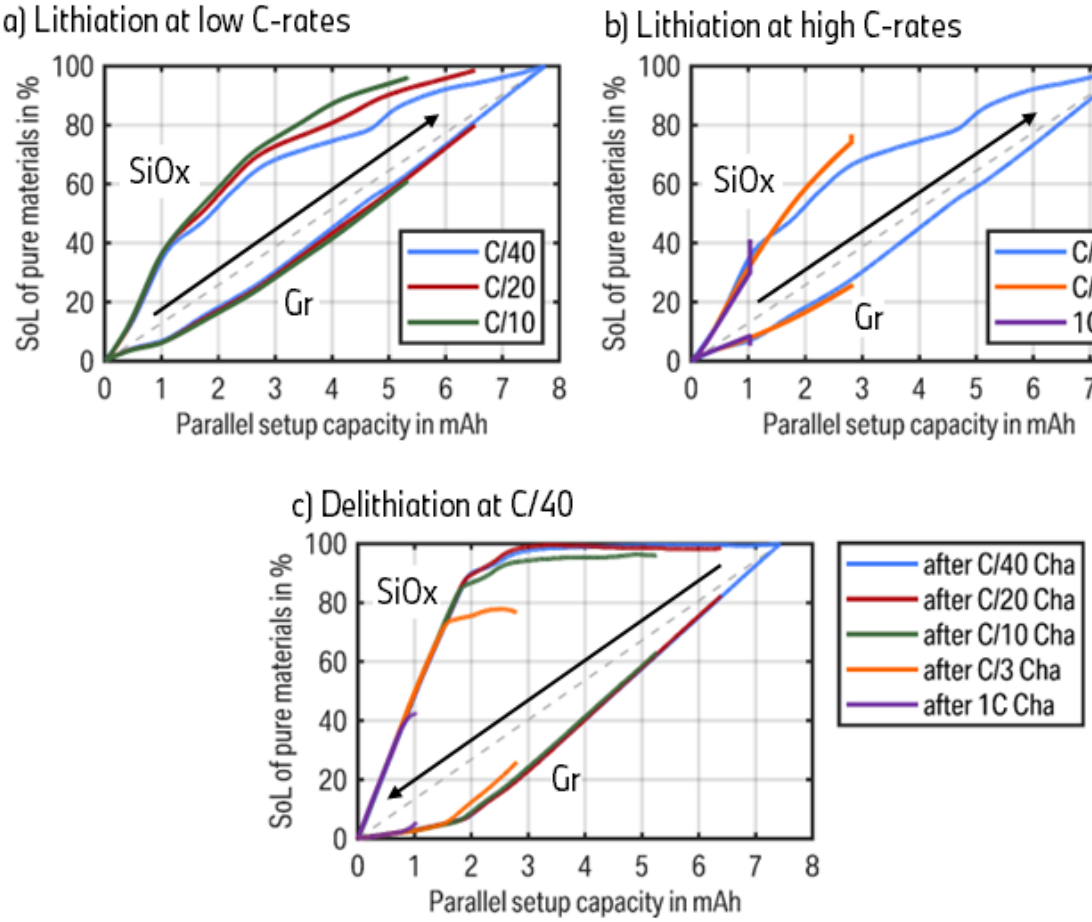

Figure S3. Continuous SoL of Gr and SiOx over the capacity throughput of the whole parallel setup for the second set of half-cells, as a validation of the presented results in the main work. The SoLs are normalized to the results of the C/40 measurement. The black arrow indicates the chronological procedure of the tests. a) Lithiation with low rates of C/40, C/20 and C/10. b) Lithiation with high rates of C/3 and 1C with C/40 as a reference. c) Delithiation with a rate of C/40 after all different lithiation steps.

3 Discussion and summary

This chapter presents a comprehensive discussion of the research articles within the broader context of understanding the thermodynamic and kinetic effects influencing the lithiation behavior of Gr/SiO_x blend anodes. It elucidates the specific contributions of each study to the research questions addressed in this work, and ultimately demonstrates how this thesis advances the performance of high-energy LIBs.

3.1 Discussion of thermodynamic effects

The thermodynamics of pure graphite are relatively straightforward when compared to the effects presented in this thesis for Gr/SiO_x blend electrodes. The clearly distinguishable potential plateaus of the graphite phase transitions, with a negligible potential hysteresis between lithiation and delithiation, permits a clear mapping of the electrochemical processes with the potential or the cell voltage. The sole disadvantage is the uncertainty regarding the precise degree of lithiation within one of the three potential plateaus. However, this issue is only problematic on full cell level with an LFP cathode, as this material also exhibits a significant potential plateau [63; 71]. In addition to the increased complexity of incorporating a second active material, pure silicon or SiO_x exhibit a number of thermodynamic effects that impact the lithiation behavior and the resulting potential. The most evident effect is the considerable intrinsic hysteresis between lithiation and delithiation of approximately 300 mV [47]. Furthermore, the silicon phase transition from amorphous to crystalline introduces a second species of silicon active material with a diverging delithiation potential profile, resulting in an additional asymmetric hysteresis.
It is evident that the hysteresis plays a pivotal role in the thermodynamics of Gr/SiO_x blend electrodes. It is thus essential to gain an understanding of the impact of the hysteresis on the voltage behavior of cells comprising a Gr/SiO_x blend anode, in order to enhance the performance of this cell type. Accordingly, this section provides a concise overview of the hysteresis and the hysteresis transition between lithiation and delithiation. This explanation is necessary since all of the presented research articles incorporate the hysteresis in some way. Given that the oxide in SiO_x reacts to inactive side products, pure silicon serves as the reversible source of Li-ion storage in SiO_x [21; 143]. Consequently, similar hysteresis effects exist for both active materials.
The hysteresis behavior of two distinct anode half-cells is provided, namely a pure SiO_x electrode and a Gr/SiO_x blend electrode with a high SiO_x content of 19 wt%. The anode half-cells

are assembled and subjected to a formation process in accordance with the description provided in Section 2.3. Two cells are tested simultaneously for each type, and the results show no significant deviation. A full cycle is conducted between a lower and upper cutoff voltage of 10 mV and 1.5 V, respectively, commencing with lithiation and followed by delithiation. The C-rate is set to C/10 for both processes and is defined based on the available delithiation capacity observed in the third formation cycle. The results of the hysteresis measurements are displayed in Fig. 3.1. Fig. 3.1 a) and b) illustrate the C/10 lithiation and delithiation pseudo OCP for pure SiO_x and the Gr/SiO_x blend electrode, respectively. The absolute voltage hysteresis between delithiation and lithiation for both anode types is displayed below in Fig. 3.1 c) and d).

The hysteresis of pure SiO_x demonstrates a consistent decline with increasing SoL. A minor

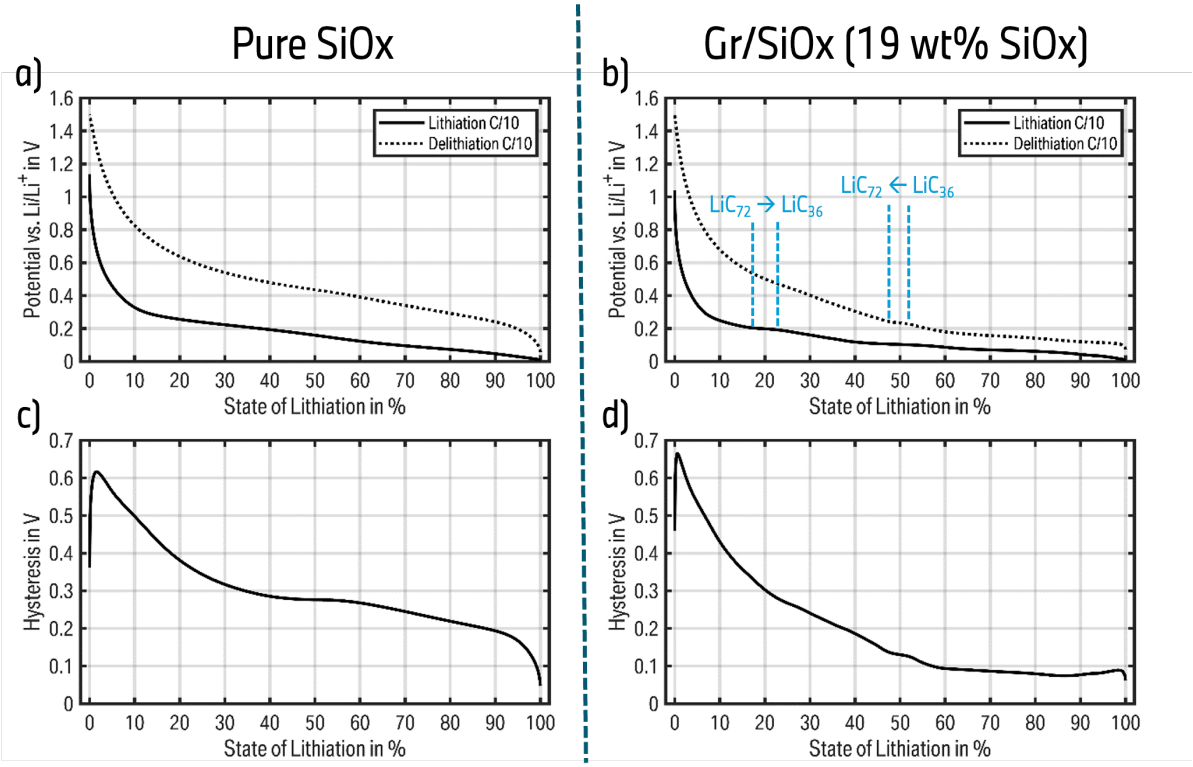

Figure 3.1: OCP and voltage hysteresis of a pure SiO_x electrode and a Gr/SiO_x blend electrode with 19 wt% SiO_x. a) Lithiation and delithiation potential of the pure SiO_x anode. b) Lithiation and delithiation potential of the Gr/SiO_x blend anode. c) Hysteresis between the delithiation and lithiation potential of the pure SiO_x anode. d) Hysteresis between the delithiation and lithiation potential of the Gr/SiO_x blend anode.

plateau is observable between 40 to 50 % SoL. The mean hysteresis across the entire SoL range is 305 mV. However, a minor proportion of the hysteresis can be ascribed to polarization, which is considerably low but persists at C/10 for the T-cell configuration. The impact of polarization is also observable for the Gr/SiO_x blend anode, where the graphite plateaus allow for a more precise identification. Given that graphite exhibits a negligible intrinsic hysteresis of approximately 20 mV [47; 127; 154], the marked plateau of the phase transition from LiC_{72}

to LiC_{36} in Fig. 3.1 b) should be at the same potential. Nevertheless, the measurements indicate a discrepancy of 35 mV between lithiation and delithiation.
The graphite plateau of the LiC_{72} to LiC_{36} phase transition marks the potential below which graphite is predominantly active. It can thus be concluded that the lithiation at increased potentials in the blend electrode can be attributed almost exclusively to SiO_x. For the given blend electrode with a SiO_x content of 19 wt%, the initial 18 % SoL at potentials above 0.2 V are attributed to the lithiation of SiO_x, which reaches an SoL of 40 % at this potential. This is visible by comparing the SiO_x potential in Fig. 3.1 a). As a consequence of the increased delithiation potential of SiO_x, the Si-range during delithiation is augmented, in this particular case to SoLs below 47 %. The delithiation of SiO_x at potentials above the plateau accounts for ~95 % of the total SoL-range. Accordingly, the blend electrode has a silicon capacity share of approximately 45 %.
As illustrated in Fig. 3.1 d), the hysteresis of the blend electrode begins to increase when the Si-range is reached during delithiation, at SoLs below 47 %. The maximum hysteresis is consistent with the findings for the pure SiO_x electrode. Comparing the region below 18 % SoL of the blend electrode (where both lithiation and delithiation is dominated by silicon) with the region below 30 % of the pure SiO_x electrode reveals that the hysteresis curves exhibits a similar qualitative behavior.
A hysteresis transition, as it is used to determine the changes in lithiation at increased C-rates in Section 2.2, is observed in cycles that do not reach the lower or upper cutoff voltage for lithiation or delithiation, respectively. In the event of switching from lithiation to delithiation at an SoL < 100 % in a partial cycle, the transition commences at the lithiation OCP and is terminated upon reaching the delithiation OCP. It should be noted that a hysteresis transition also occurs at 0 and 100 % SoL during a full cycle. However, it is difficult to ascertain when the transition is complete, given that the opposing OCP is unknown for these states. Fig. 3.2 displays the hysteresis transition in both directions for the pure SiO_x anode half-cell. Fig. 3.2 a) shows the transitions from the lithiation pseudo OCP to the delithiation pseudo OCP for varying initial SoLs. Additionally, the C/10 pseudo OCP for lithiation and delithiation are provided as an indicator of when the transition is complete. For the sake of comparability, the transition employs the same C-rate of C/10. Similarly, Fig. 3.2 b) displays the opposing hysteresis transitions from delithiation to lithiation at the identical initial SoLs.

In general, the hysteresis transition for pure SiO_x exhibits a similar behavior regardless of the direction at the start SoL. The potential converges towards the full cycle potential within the first 10–20 % SoL of the transition. However, a slight discrepancy persists until the upper or lower cutoff potential for delithiation and lithiation, respectively, is reached. The sole exception to this behavior is the transition from lithiation to delithiation, that starts at an SoL of 80 %. This transition exhibits a slower convergence towards the full cycles delithiation potential. The process is largely completed after a Δ SoL of approximately 30 %. An explanation for this observation is provided by the crystalline phase transition of silicon, which occurs below potentials of 60 mV during lithiation and therefore only exists in the full cycle delithiation potential. A detail discussion of this phenomenon was provided in Sections 1.2.2

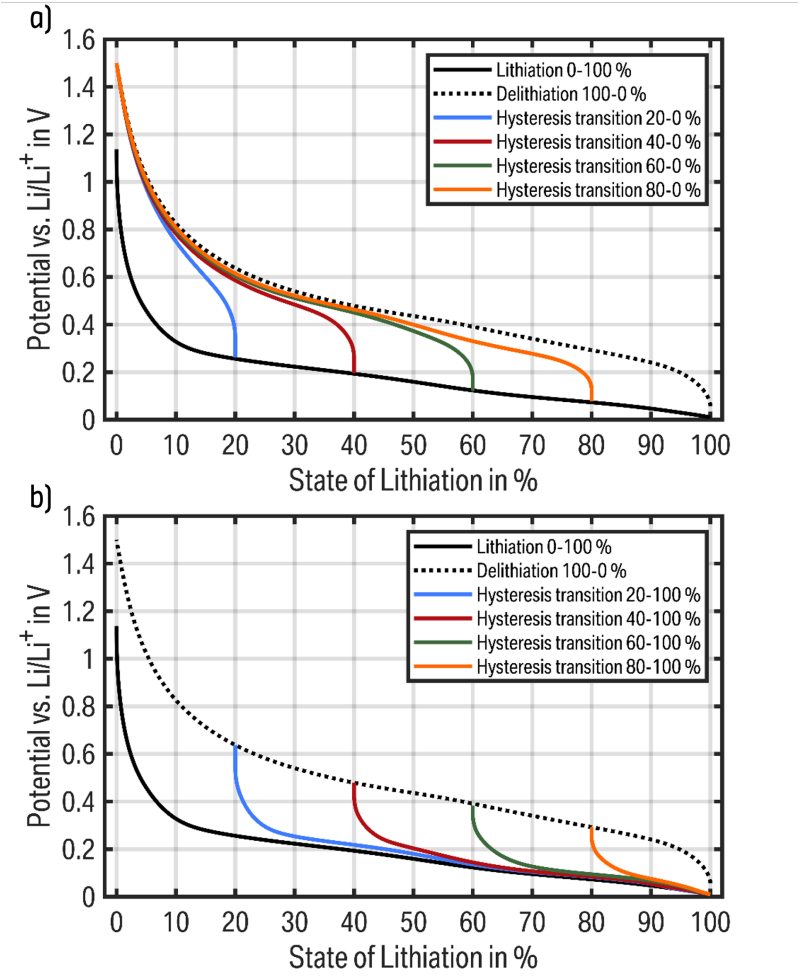

Figure 3.2: Hysteresis transition of partial cycles for a pure SiO_x anode half-cell, with evenly spread start SoLs. Additionally, the pseudo OCP for lithiation and delithiation with the same C-rate as the hysteresis transition is presented for a reference. a) Hysteresis transition from lithiation to delithiation. b) Hysteresis transition from delithiation to lithiation.

and 2.1.

The hysteresis transition of the Gr/SiO_x blend anode half-cell is presented in Fig. 3.3 in a similar manner to that of pure SiO_x. Fig. 3.3 a) depicts the transitions from lithiation to delithiation, while Fig. 3.3 b) illustrates the transitions in the opposite direction, from delithiation to lithiation. The number of conducted transitions increases, with start SoLs in the range of 15–75 % for every 15 % of SoL.

The results can be classified into two categories. In the first category, the transitions occur within a range where only silicon is active, with no participation of graphite. This category comprises only those transitions that start at 15 % SoL. Both, the lithiation and delithiation transitions converge quickly towards the opposing pseudo OCP over approximately 5 % of SoL. The reduced SoL delta until the hysteresis transition is complete is attributed to the reduced capacity share of silicon in the blend electrode. As previously stated, the SiO_x

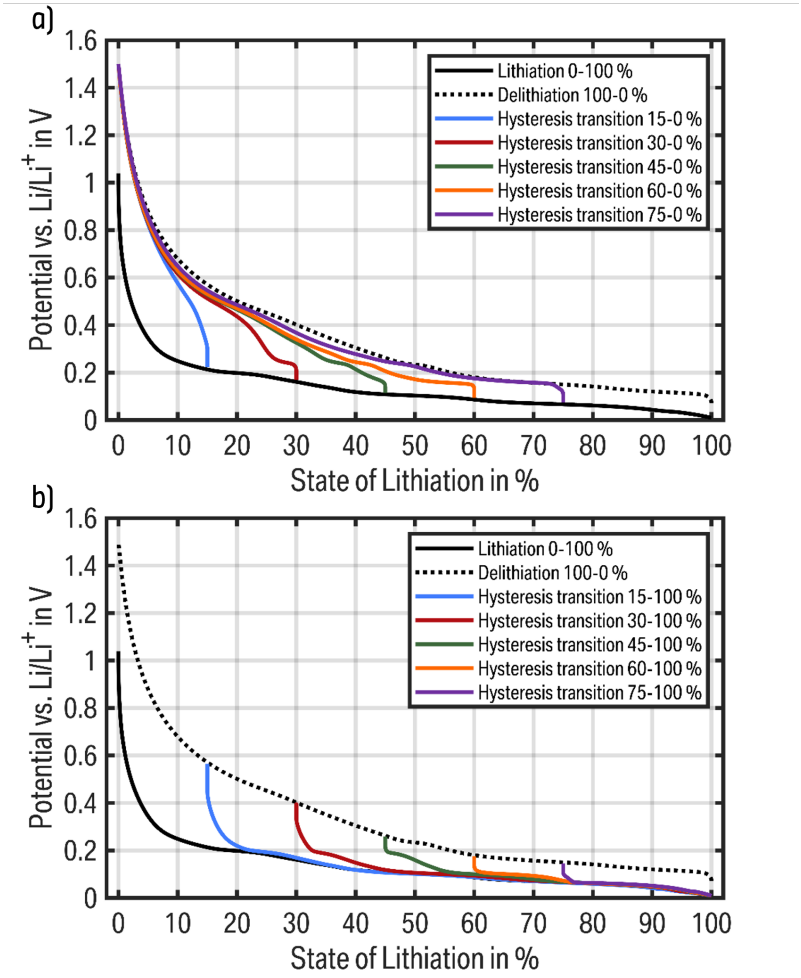

Figure 3.3: Hysteresis transition of partial cycles for a Gr/SiO_x anode half-cell with an SiO_x content of 19 wt%. The start SoL varies with a higher density in the lower SoL range, where silicon is mainly active. Additionally, the pseudo OCP for lithiation and delithiation with the same C-rate as the hysteresis transition is presented for a reference. a) Hysteresis transition from lithiation to delithiation. b) Hysteresis transition from delithiation to lithiation.

contributes approximately 45 % to the total capacity. Therefore, the hysteresis transition is anticipated and observed to be twice as fast, with an even greater speed in cells with a lower SiO_x share.

The second category contains the remaining transitions, in which both silicon and graphite are active during the transition process. These transitions exhibit at least one plateau that can clearly be attributed to the (de-)lithiation of graphite. During these plateaus, graphite is primarily (de-)lithiated. As silicon is responsible of a hysteresis, the hysteresis transition pauses in these graphite regions. The SoL-wise length of the hysteresis transition is thus dependent on two factors. Firstly, at least 10 % SoL of silicon must undergo (de-)lithiation in order to perform the general silicon hysteresis transition, which is known from pure SiO_x and the transitions of the first category. This is exemplified by the transition from lithiation to delithiation, which starts at 30 % SoL in Fig. 3.3 a). In this instance, the silicon hysteresis

transition starts at approximately 25 % SoL, which coincides with the end of the graphite plateau. Over the subsequent 5 % of SoL the potential converges towards the potential observed in full cycles. For the second factor, it is necessary that the composition of lithiated silicon and graphite is identical to that of the full cycle in the corresponding direction. An illustrative example is the transition from delithiation to lithiation at 45 % SoL, as depicted in Fig. 3.3 b). This transition commences at an SoL, situated at the threshold between the region where graphite delithiation ceases and SiO_x delithiation begins. Therefore, SiO_x remains fully lithiated and is thus inactive during the hysteresis transition. Given that SiO_x is also active at higher SoLs during lithiation, the hysteresis transition persists until silicon is fully lithiated in the full cycle. At approximately 75 % SoL, the discrepancies become negligible, and no substantial deviation in the potential is discernible. In conclusion, this type of hysteresis transition is not rooted in the intrinsic hysteresis of silicon but rather in disparities in the lithiation distribution between the lithiation and delithiation processes of Gr/SiO_x blend anodes.

This assumption regarding the separation of (de-)lithiation processes in accordance with the OCP of the active materials is contingent upon the assumption that all particles are connected in parallel. This parallel connection is either given through direct particle contact, the connection through conductive additives, or the electrical path through the current collector. Consequently, any OCP discrepancies between the particles will result in a balancing effect until such differences are resolved. However, this assumption is not applicable in the case of increased currents, where the additional polarization must be taken into account. Given that each particle exhibits a different polarization, particularly as a consequence of varying ionic paths through the porous electrode structure, slight discrepancies in the lithiation behavior and hysteresis transition are anticipated. At the considerably low C-rate of C/10, this assertion permits an approximation of the hysteresis transition based on the pseudo OCP of the pure active materials.

As the primary tool to analyze the kinetics in Section 2.2, the general thermodynamics of the hysteresis transition from charging to discharging for the Molicel M35A are presented in Fig. 3.4 in a manner similar to that previously employed for the anode half-cell in Fig. 3.3. The transition from charging to discharging is illustrated in Fig. 3.4 a), while the corresponding opposite transition from discharging to charging is depicted in Fig. 3.4 b). For the purposes of comparison, the pseudo OCV of the full cycle is once more provided as a reference. The selection of the start SoCs for the hysteresis transition is focused more on lower SoCs, with the objective of emphasizing on the transitions where only silicon is active. The plateau of the graphite phase transition from LiC_{72} to LiC_{36} during discharging occurs within the specific SoC range of 30–35 %, as indicated in Fig. 3.4 a). Accordingly, the Si-range of this cell encompasses the lower 30 % of SoC.

The results demonstrate a transition behavior comparable to that observed in the blend anode half-cell, as illustrated in Fig. 3.3. The hysteresis transitions that commence below 20 % SoC are classified as category one, wherein only silicon is active. These transitions can be approximated by an exponential function that converges towards the opposite full cycle

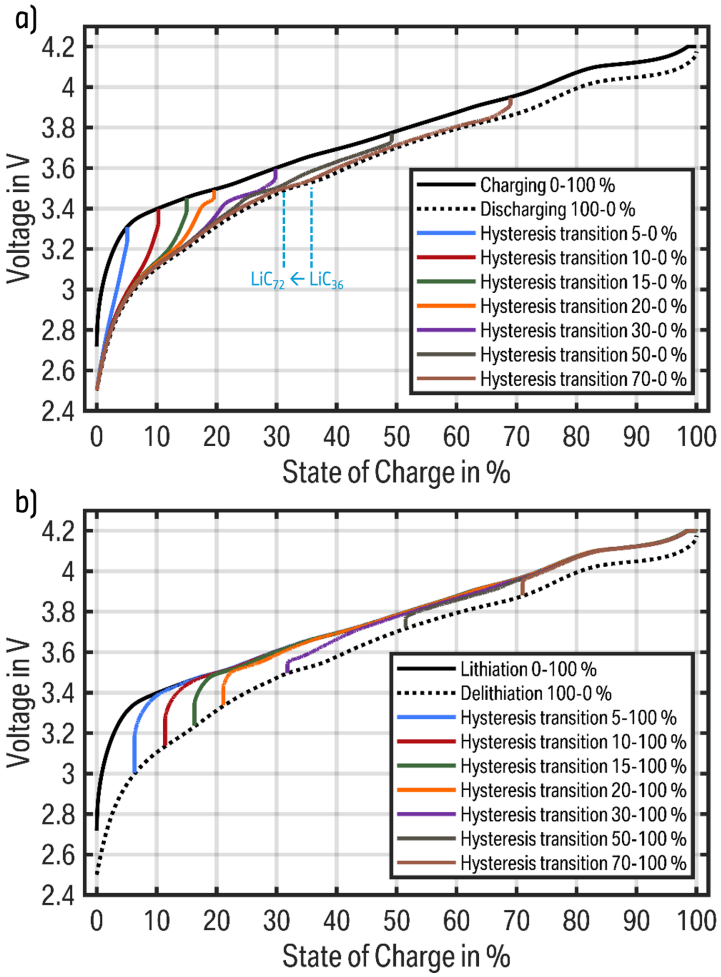

Figure 3.4: Hysteresis transition of partial cycles for a full cell (Molicel M35A) with a Gr/SiO_x blend anode. The start SoC varies with a higher density in the lower SoC range, where silicon is mainly active. Additionally, the pseudo OCV for charging and discharging with the same C-rate as the hysteresis transition is presented as a reference. a) Hysteresis transition from charging to discharging. b) Hysteresis transition from discharging to charging.

OCV [129; 155]. The hysteresis transition starting at higher SoCs once more illustrates the impact of graphite (de-)lithiation, wherein the hysteresis transition pauses during periods where graphite is active. The transition is complete when the SoL of both graphite and silicon is identical to that observed in the full cycle.

As previously stated, graphite is delithiated prior to SiO_x, due to the overall lower delithiation potential of graphite in comparison to SiO_x. Based on this information, it is possible to give an approximation, what percentage of the SiO_x is lithiated at the end of a partial charging step. As illustrated in Fig. 3.4 a), the Si-range of the full discharge step starts at 30 %. The hysteresis transition in Fig. 3.4 a) clearly depicts this graphite plateau for start SoCs above 15 % SoC, indicating the end of the Gr-range. However, this plateau is shifted towards lower SoCs, compared to the appearance of the plateau between 30–35 % in the full discharge cycle. For example, in the hysteresis transition from charging to discharging at 20 % SoC,

the graphite plateau terminates at approximately 17 % SoC, thereby defining the remaining Si-range. Comparing this value with the 30 % of the full cycle indicates that SiO_x reaches 57 % of the full cycle lithiation when charging to 20 % SoC. This method is not applicable to lower start SoCs, as no discernible graphite plateau is observable. However, since the first graphite plateau is not yet reached during charging, the charged SoC is equal to the Si-range in the subsequent discharge step.
In summary, Gr/SiO_x blend anodes in both half and full cells demonstrate a comparable hysteresis transition to that observed in pure SiO_x electrodes, provided that the SoL of the two active materials exhibits no discrepancy between the full cycle lithiation and delithiation curves at the respective SoC. Once there exists a discrepancy between the full cycle lithiation and delithiation, the hysteresis transition continues until the discrepancy is resolved. In general, it is not feasible to determine a definitive SoC-voltage mapping for Gr/SiO_x blend anodes, due to the hysteresis of silicon. This introduces the first challenges in the estimation of the SoC and the SoH in the operation of battery cells, which is often voltage based [96–98; 156].
The provided insights indicate that the silicon hysteresis only proceeds upon lithiation or delithiation. This further affirms the findings from Sections 2.2 and 2.3 that an increased SiO_x lithiation remains present during relaxation. An increase in SiO_x lithiation during charging results in a reduction in anode potential compared to that observed in a standard full cycle. Consequently, as previously outlined in the aforementioned sections, the resulting balancing force facilitates the delithiation of SiO_x and the lithiation of graphite. However, due to the rapid potential increase associated with this hysteresis transition, as illustrated in Fig. 3.2 a), an equilibrium potential is reached almost immediately without a significant charge transfer. This summarizes the fundamental thermodynamic effects of amorphous silicon, which establish a basis for understanding the lithiation behavior and how multiple SoCs can result in the same cell voltage. However, in addition to this hysteresis effect, the phase transition from amorphous to crystalline also introduces further complexity to the thermodynamics of Gr/SiO_x blend anodes. A detailed discussion of this influence on the lithiation behavior can be found in Section 2.1. Given that the presented memory effect is independent of temperature and C-rate, it can be concluded that this effect is solely a consequence of thermodynamic processes.

The crystalline phase transition occurs at high SoCs or anode potentials below 60 mV, resulting in the formation of c-$Li_{3.75}Si$ from a-$Li_{3.5}Si$, as previously outlined in Section 1.2.2 [18; 133; 139]. This phase transition gives rise to an additional asymmetrical hysteresis, which is observed at significantly elevated potentials above 440 mV [12; 139]. In full cells with Gr/SiO_x blend anodes, these high potentials are typically reached at SoCs below 10 %. Until this potential is reached, the discharging voltage profile in the silicon region undergoes a notable shift towards lower values. This introduces a second type of thermodynamic effect, in addition to the standard silicon hysteresis, that affects the cell voltage.

However, as the study in Section 2.1 describes, the consequences of this memory effect become significant only after repeated partial cycling without fully discharging the battery cell or reverting the crystalline phase back to the amorphous state. As a result of repeated partial cycling, an increasing proportion of the amorphous silicon undergoes the crystalline phase transition and is subsequently trapped in this state until the cell reaches a low SoC once more. These cycles are of particular significance for electric vehicles, as a fully discharged battery pack invariably necessitates the provision of towing services.
Without adequate compensation for the voltage fluctuations in the BMS, errors in the internal state estimation arise, leading to an underestimation of the SoC and SoH. This is due to the fact that the discharged capacity, until reaching a certain voltage during discharging, is reduced. This temporary capacity loss can be fully recovered during the first discharge cycle above anode potentials of 440 mV. However, the reduction in the voltage level results in a slight decrease in the discharged energy. As demonstrated in Section 2.1, a notable correlation exists between the memory effect and both the cycle number and the SoC range of the partial cycles. The most critical SoC range is that which fully charges the battery and discharges it as far as possible without increasing the anode potential above the threshold of 440 mV. A slight improvement of the memory effect is discernible with augmented degradation. As previously stated, no significant correlation between the memory effect and either temperature or the C-rate can be observed.
To circumvent this additional complication in matching SoC and cell voltage, it is recommended to limit the upper SoC during charging. This will reduce the amount of trapped lithium, as less crystalline silicon is formed within each cycle. Furthermore, it is advised that regular deep discharging is employed to reverse any crystalline silicon back to its amorphous state.
In order to provide an accurate description of the thermodynamic lithiation behavior of graphite, amorphous SiO_x, and crystalline SiO_x in Gr/SiO_x blend anodes, it is essential to consider all presented effects. These include the pure material anode potentials, the rate-independent hysteresis of silicon, and the amount of present crystalline silicon. As such, an accurate state estimation can only be assured through the consideration of all thermodynamic effects.

3.2 Discussion of kinetic effects

In order to provide a comprehensive description of the lithiation behavior of Gr/SiO_x blend anodes, it is necessary to extend the findings about the thermodynamics with an analysis of the kinetic behavior. This section elucidates the impact of the kinetics on the lithiation distribution between graphite and SiO_x, which is addressed in this thesis at the full cell and half-cell levels in Sections 2.2 and 2.3, respectively.
The research article in Section 2.2 examines the lithiation behavior, with the objective of acquiring information regarding the active material that is preferably lithiated at elevated

charging currents in full cells. A non-destructive method is presented that allows for the determination of the lithiation of both active materials, when charging with different C-rates to a specific SoC. This method employs the aforementioned hysteresis transition from charging to discharging that occurs subsequently to the charging process. The length of the region in which graphite is delithiated during the hysteresis transition can be measured and compared for the different charging rates prior to the hysteresis transition. The specific SoC with the greatest significance is observed at a relatively low SoC, at a degree of lithiation within the first graphite plateau that is attributed to the phase transition of LiC_{72} to LiC_{36}. Minor alterations in graphite lithiation have a notable impact on the hysteresis transition within this specific SoC range. Reducing or increasing the SoC, at which the charging process terminates allows for the same determination, however, with a reduced characteristic. This is because the first graphite plateau is either not lithiated at all for some C-rates or already fully lithiated for all C-rates. This is illustrated in the Appendix in Fig. A.1, where three distinct SoCs are compared for the Molicel M35A.

The analysis of the graphite plateau length in the hysteresis transition indicates that an elevated charging current results in a shorter graphite plateau, which consequently implies an increase in the SiO_x lithiation. This leads to the conclusion that the relative polarization of SiO_x is expected to be reduced in comparison to graphite, and that SiO_x is therefore preferentially lithiated at increased C-rates. The results of the electrochemical cell tests are corroborated by XRD analysis, which enables the determination of the graphite lithiation. The feasibility of both methods is contingent upon the absence of a balancing effect between SiO_x and graphite at an increased SiO_x lithiation. This previously described thermodynamic effect is due to the hysteresis of silicon and the resulting higher delithiation potential, which terminates any balancing process after a minor charge exchange between the active materials. In order to extend the findings of an increased SiO_x lithiation at increased charging currents from a single specific SoC to the entire SoC range, an experimental half-cell setup is employed within the research article in Section 2.3. The experimental setup comprises a pure SiO_x and a pure graphite anode half-cell. Subsequently, the two half-cells are connected in parallel, which represents the electrical contact in a blend electrode. The addition of current measurements for each pure active material enables the determination of the current distribution between each active material and the calculation of the individual SoL of SiO_x and graphite. This allows for the definition of regions in which each material is predominantly undergoing lithiation or delithiation, which aligns with the anticipated outcomes based on the anode potentials. During the lithiation process, SiO_x exhibits increased lithiation in the initial stages of the lithiation process at elevated potentials and between the characteristic graphite plateaus. During the delithiation process, graphite is initially delithiated almost entirely, followed by the delithiation of SiO_x. As in the first project regarding the kinetic behavior, an increase in the lithiation rate results in a notable enhancement in SiO_x lithiation throughout the entirety of the lithiation process. It is only at a significantly enhanced current with large polarization that a small region exists where graphite exhibits increased lithiation due to the extended polarization at this C-rate. However, should the lithiation process cease in this region, an

increased SiO_x lithiation will ensue during the subsequent relaxation process, which can be explained by the hysteresis of SiO_x. Despite the differences between this experimental setup and a blend electrode, the results allow conclusions to be drawn about the lithiation behavior in blend electrodes and confirm the findings from the full cell experiments.
To gain a comprehensive understanding of the kinetic behavior, it is essential to investigate the impact of temperature on the lithiation behavior. In general, all electrochemical processes, with the exception of electron transport, proceed at a slower rate at reduced temperatures. Nevertheless, it is necessary to determine the manner in which way the kinetic behavior of both active materials declines in comparison to one another. Repeating the experiment described in Section 2.2 at varying ambient temperatures permits an analysis of the temperature influence on the kinetics of Gr/SiO_x blend anodes.

A comparison of the ambient temperatures of 0 °C, 10 °C, 25 °C, and 40 °C is illustrated in Fig. 3.5. Multiple effects are observable in the hysteresis transition subsequent to the charging process with varying C-rates. The first phenomenon is commonly known for pure graphite anodes, namely that the graphite plateaus become less discernible at reduced temperatures. This phenomenon can be attributed to the enhanced polarization of the ionic transport at reduced temperatures, which gives rise to considerable lithiation gradients across the electrode thickness. As a result, the graphite plateau exhibits an enhanced slope, rendering the determination of alterations during lithiation more challenging.
Another general effect is the kinetic behavior of the hysteresis transition. It is evident that the hysteresis transition proceeds at a faster rate at elevated temperatures. At 0 °C, the transition persists until the lower cutoff voltage is reached, before aligning with the reference of the full cycle pseudo OCV at this temperature. On the contrary, the hysteresis transition reaches the voltage of the full cycle after approximately 8 % at 40 °C. As the root cause of the silicon hysteresis remains undetermined [128; 131], any potential explanation for this temperature effect would only be mere conjecture.
In consideration of the objective of this test, a discernible trend emerges at lower temperatures, indicating a diminished sensitivity of the C-rate on the lithiation distribution between graphite and silicon. The dispersion effect of the voltage during the hysteresis transition is significantly reduced at 10 °C, and is barely perceptible at 0 °C. This implies that the SiO_x is not preferentially lithiated over graphite at elevated charge rates at low temperatures. This finding is in accordance with the results presented by Richter et al. [45], which demonstrate a preferred graphite lithiation at ambient temperatures below 0 °C. No significant deviation is observed at elevated temperatures of 25 °C and 40 °C. Under the assumption that the graphite and SiO_x particles are distributed evenly across the electrode thickness, the reduced kinetics observed at lower temperatures for SiO_x must emerge from the particle level. A potential explanation for this phenomenon is the increased SEI thickness of SiO_x, which results from the substantial volume expansion of these particles. Another possibility is that the charge transfer process is slowed down, or that there is a reduction in speed of the solid diffusion within the SiO_x particles. One or a combination of multiple factors is responsible for the prolonged increase in polarization observed for the SiO_x particles relative to the graphite

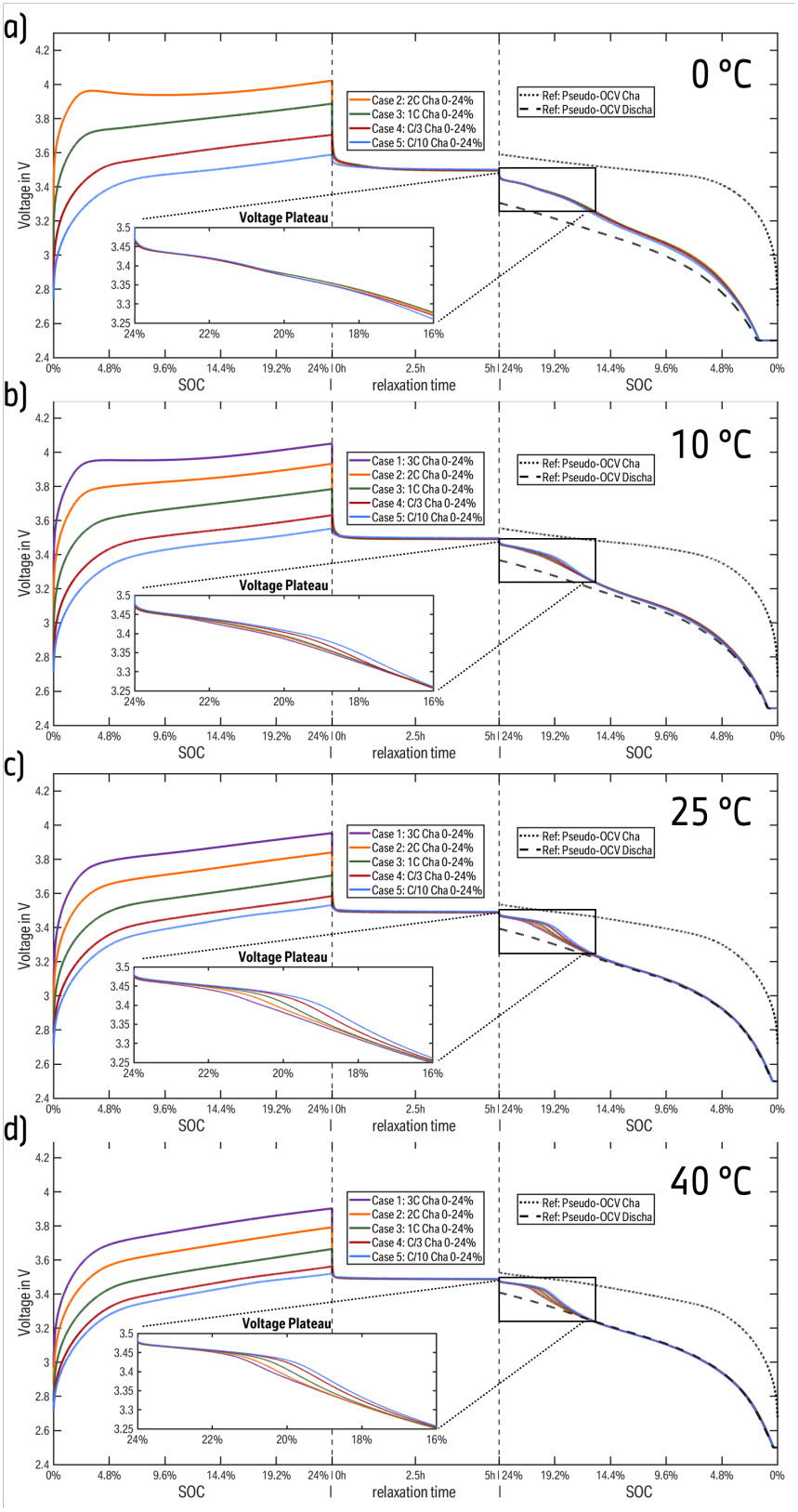

Figure 3.5: Comparison between varying ambient temperatures of the hysteresis transition after charging with different currents to 25 % SoC for the MoliCel M35A. The compared temperatures include a) 0 °C, b) 10 °C, c) 25 °C, and d) 40 °C.

particles at low ambient temperatures.
The test scenario is repeated for the MoliCel P45B, which provides a high power density, and the SDI 30Q, which contains nano-Si in place of SiO_x as a secondary active material. The voltage measurements are presented in the Appendix in Figures A.2 and A.3, respectively. The graphite plateau in both of these cells exhibits a more discernible characteristic, most likely due to the reduced energy density compared to the Molicel M35A, which results in diminished lithium concentration gradients across the electrode thickness. A comparison of the length of the graphite plateaus after charging with C/10 at different temperatures reveals a reduction in the plateau length at elevated temperatures. This supports the hypothesis that SiO_x and pure silicon exhibit overall reduced kinetics at lower temperatures in comparison to graphite. Nevertheless, the dispersion effect in the hysteresis transition subsequent to charging at disparate C-rates is barely discernible in the cell containing nano-Si. This supports the statement that the side product Li_2O of SiO_x serves as a Li-ion diffusion channel, thereby enhancing the rate capability [21]. Nevertheless, to substantiate this hypothesis, a larger sample size than three cells is required.
It has been demonstrated that the kinetics exert a significant influence on the lithiation behavior of Gr/SiO_x blend anodes. At room temperature or above, an increase in the charging current results in enhanced lithiation of SiO_x. This enhanced SiO_x lithiation is observed throughout the entire charging process, either directly during lithiation for the majority of the time or in certain special scenarios following a relaxation period. This dependency on the C-rate diminishes with decreasing temperature, becoming barely visible at 0 °C. Moreover, an overall trend of an increased SiO_x lithiation at elevated temperatures was observed. It can thus be concluded that SiO_x exhibits an enhanced kinetic behavior at elevated temperatures and C-rate in comparison to graphite, which exerts a considerable influence on the lithiation behavior of blend anodes.

3.3 Conclusion and Outlook

The use of silicon as an anode active material has the potential to markedly enhance the specific energy of lithium-ion batteries, thereby providing the requisite increase in driving range for BEVs. However, the substantial volume expansion that occurs upon lithiation of silicon represents a significant challenge with regard to the battery's lifetime. In order to incorporate the high energy density of silicon while providing a sufficient lifetime, a promising solution is the use of blend electrodes consisting primarily of graphite with small amounts of a silicon-based material. This approach has the potential to enhance the performance of LIBs. However, the use of blend anodes comprising two distinct active materials gives rise to new challenges, particularly with regard to the lithiation behavior of both materials during cycling. This includes the determination of which active material provides enhanced kinetic behavior during fast charging and an investigation of the distinct voltage hysteresis effects of silicon on the cell voltage. A comprehensive understanding is essential to achieve the

optimal performance of this type of battery, including an accurate estimation of its internal states.

The objective of this thesis is to examine the interaction between the two active materials in Gr/SiO_x blend anodes and to determine the thermodynamic and kinetic effects on the lithiation behavior. The results demonstrate that a specific SoC can be achieved through a multitude of combinations of graphite and SiO_x lithiation, while also exhibiting disparate OCVs. The presented causes include the intrinsic hysteresis of SiO_x and a memory effect induced by trapped lithium in the crystalline phase of silicon, which can be classified as thermodynamic effects. Furthermore, the increased kinetics of SiO_x compared to graphite at room temperature or above can result in further alterations in the lithiation distribution between the two active materials.

The following provides a concise summary of the methods used to address each of the four research questions in this work. The first research question, "How much lithium is stored in each active material throughout the entirety of the charging and discharging process?", concentrates on the interaction between the two active materials and how their thermodynamics can be incorporated. The primary factor influencing the lithiation distribution between the active materials is the hysteresis of silicon. Although SiO_x exhibits an overall increased working potential compared to graphite, the active potential range overlaps during lithiation but is predominantly separated during delithiation. During lithiation, this results in the formation of regions where SiO_x is lithiated and regions where graphite is active, mostly in the range of the graphite plateaus. During delithiation, the majority of graphite is initially delithiated, followed by the subsequent delithiation of SiO_x. Accordingly, the lithiation distribution between charging and discharging varies significantly. This principle also applies to partial cycles, wherein the transition from lithiation to delithiation and vice versa at any point of partial anode lithiation introduces further challenges. As a result of this phenomenon, an infinite number of combinations of SiO_x and graphite lithiation at a specific SoL are technically possible.

This leads us directly to the second research question, which is: "What is the effect of the charging and discharging history on the lithiation behavior?". It is essential to understand the lithiation distribution between the active materials when switching between charging and discharging. This start point of the hysteresis transition is crucial in order to accurately estimate the lithiation of SiO_x and graphite during this transition. As indicated by its designation, the memory effect of crystalline silicon represent an additional phenomenon that is contingent upon on the cycling history. As outlined in Section 2.1, repetitive cycling within a specific SoC range that induces the formation of this crystalline phase at high SoCs but fails to revert it back to the original amorphous phase by avoiding very low SoCs, results in the continuous trapping of lithium. This introduces crystalline silicon as a third active material species with distinct thermodynamic properties, which consequently affect the lithiation distribution between the now three active materials.

As the third research question, "What is the impact of the charge rate (slow charging vs. fast charging) on the lithiation behavior?", already implies, the kinetics also significantly alter

the lithiation behavior. The investigations in Sections 2.2 and 2.3 demonstrate, through the use of multiple approaches, that an increased C-rate, as is present during fast-charging, shifts the lithiation distribution towards an enhanced SiO_x lithiation at room temperature. Due to the hysteresis of silicon, this shift even persists during relaxation periods. It can thus be concluded that SiO_x exhibits superior kinetics in comparison to graphite, which results in a reduced polarization. However, it was demonstrated that the effect is diminished at lower temperatures.
The fourth and most pertinent research question regarding the operation of LIBs with Gr/SiO_x blend anodes is: "How is the cell voltage influenced in Gr/SiOx blend electrodes?". This question is influenced by all of the previous effects. As the primary input for the state estimation in a BMS is the cell voltage, it is crucial to comprehend the underlying effects that impact the cell voltage. In addition to the polarization inherent to all LIBs, the lithiation distribution among the three different active materials in Gr/SiO_x blend anodes (graphite, amorphous silicon and crystalline silicon) significantly influences the voltage profile. The thermodynamic properties of each of these species are distinct, and the precise composition is crucial for aligning the cell voltage with the SoC. As evidenced by the disparate studies, a multitude of potential SoCs are plausible for a specific cell voltage, especially in the lower SoC range where SiO_x is predominantly active.
Considering the aforementioned effects, it is feasible to make more precise state estimations, thereby ensuring the seamless operation of Gr/SiO_x blend electrodes in LIBs and guaranteeing the high performance that is promised by this type of electrode.

In the context of this research, it becomes pertinent to consider the manner in which the insights gained into the lithiation behavior may be leveraged to enhance the operation of LIBs and how these insights can be extended through future research. The most significant extension would be to modify simulation models of Gr/SiO_x blend anodes with the findings on the lithiation behavior, in a manner analogous to that described in Section 2.2. This comprises a model of the SiO_x hysteresis on particle level, which provides an adequate representation of the hysteresis transition in Gr/SiO_x blend anodes. The hysteresis transition observed subsequent to elevated charge rates (Section 2.2) can then be employed to validate the parameterization of the polarization for both active anode materials. A comparison of this simulation model with the measurements from the parallel connected half-cell setup (Section 2.3) enables the results from the experimental setup to be transferred to real blend electrodes. Inclusion of the crystalline phase transition of fully lithiated silicon and the resulting voltage changes in Gr/SiO_x blend electrodes (Section 2.1) ensure that the simulation model encompasses all effects described in this work, thereby facilitating precise estimation of the SoC and the active material lithiation. However, the interplay between graphite and silicon may be influenced by additional lithiation behavior effects, which have not yet been investigated. Once discovered, these effects should be incorporated into the model.
As this work focused on SiO_x as a silicon-based active material, is it necessary to investigate

the lithiation behavior of other silicon-based materials, such as pure silicon or SiC in combination with graphite. As evidenced by the assessment of the lithiation behavior of Gr/nano-Si blend anodes in Section 3.2, the lithiation behavior of SiO_x cannot be directly transferred to the other materials. In particular, it has been reported that the lithium diffusivity of SiO_x is enhanced by the formation of Li_2O, which acts as a diffusion channel for lithium ions [21]. This may result in a reduction of the polarization, which does not exist for other silicon-based active materials. Another intriguing topic for future research is to ascertain how these findings can be applied to different blend electrodes, not only for anodes but also for cathodes. It is essential to investigate whether some of the presented methods can be utilized to enhance the understanding of other blend electrodes and accelerate battery development.

References

[1] *New EV record in Norway*. electrive.com. URL: https://www.electrive.com/2024/10/01/new-ev-record-in-norway-2/ (visited on 11/22/2024).

[2] X. Zhao, Y. Ma, S. Shao, and T. Ma. "What determines consumers' acceptance of electric vehicles: A survey in Shanghai, China". In: *Energy Economics* 108 (2022), p. 105805. DOI: 10.1016/j.eneco.2021.105805.

[3] E. Higueras-Castillo, A. Guillén, L.-J. Herrera, and F. Liébana-Cabanillas. "Adoption of electric vehicles: Which factors are really important?" In: *International Journal of Sustainable Transportation* 15.10 (2021), pp. 799–813. DOI: 10.1080/15568318.2020.1818330.

[4] V. Singh, V. Singh, and S. Vaibhav. "A review and simple meta-analysis of factors influencing adoption of electric vehicles". In: *Transportation Research Part D: Transport and Environment* 86 (2020), p. 102436. DOI: 10.1016/j.trd.2020.102436.

[5] W. Li, R. Long, H. Chen, and J. Geng. "A review of factors influencing consumer intentions to adopt battery electric vehicles". In: *Renewable and Sustainable Energy Reviews* 78 (2017), pp. 318–328. DOI: 10.1016/j.rser.2017.04.076.

[6] *S&P Global Mobility Survey Finds EV Affordability tops Charging and Range Concerns in Slowing EV Demand*. News Release Archive. URL: https://press.spglobal.com/2023-11-08-S-P-Global-Mobility-Survey-Finds-EV-Affordability-tops-Charging-and-Range-Concerns-in-Slowing-EV-Demand (visited on 11/22/2024).

[7] S. Link, C. Neef, and T. Wicke. "Trends in Automotive Battery Cell Design: A Statistical Analysis of Empirical Data". In: *Batteries* 9.5 (2023), p. 261. DOI: 10.3390/batteries9050261.

[8] *A new EV survey: What consumers want in charging — McKinsey*. URL: https://www.mckinsey.com/features/mckinsey-center-for-future-mobility/our-insights/exploring-consumer-sentiment-on-electric-vehicle-charging (visited on 11/22/2024).

[9] S. Chae, M. Ko, K. Kim, K. Ahn, and J. Cho. "Confronting issues of the practical implementation of Si anode in high-energy lithium-ion batteries". In: *Joule* 1.1 (2017), pp. 47–60. DOI: 10.1016/j.joule.2017.07.006.

[10] Y. Jiang, G. Offer, J. Jiang, M. Marinescu, and H. Wang. "Voltage Hysteresis Model for Silicon Electrodes for Lithium Ion Batteries, Including Multi-Step Phase Transformations, Crystallization and Amorphization". In: *Journal of The Electrochemical Society* 167.13 (2020), p. 130533. DOI: 10.1149/1945-7111/abbbba.

[11] N. Kirkaldy, M. A. Samieian, G. J. Offer, M. Marinescu, and Y. Patel. "Lithium-Ion Battery Degradation: Measuring Rapid Loss of Active Silicon in Silicon–Graphite Composite Electrodes". In: *ACS Applied Energy Materials* 5.11 (2022), pp. 13367–13376. DOI: 10.1021/acsaem.2c02047.

[12] T. Schott, R. Robert, P. A. Ulmann, P. Lanz, S. Zürcher, M. E. Spahr, P. Novák, and S. Trabesinger. "Cycling Behavior of Silicon-Containing Graphite Electrodes, Part A: Effect of the Lithiation Protocol". In: *The Journal of Physical Chemistry C* 121.34 (2017), pp. 18423–18429. DOI: 10.1021/acs.jpcc.7b05919.

[13] A. Franco Gonzalez, N.-H. Yang, and R.-S. Liu. "Silicon anode design for lithium-ion batteries: progress and perspectives". In: *The Journal of Physical Chemistry C* 121.50 (2017), pp. 27775–27787. DOI: 10.1021/acs.jpcc.7b07793.

[14] Y. Jin, B. Zhu, Z. Lu, N. Liu, and J. Zhu. "Challenges and recent progress in the development of Si anodes for lithium-ion battery". In: *Advanced Energy Materials* 7.23 (2017), p. 1700715. DOI: 10.1002/aenm.201700715.

[15] A. Durdel, S. Friedrich, L. Hüsken, and A. Jossen. "Modeling Silicon-Dominant Anodes: Parametrization, Discussion, and Validation of a Newman-Type Model". In: *Batteries* 9.11 (2023), p. 558. DOI: 10.3390/batteries9110558.

[16] Z. Yang, S. E. Trask, X. Wu, and B. J. Ingram. "Effect of Si Content on Extreme Fast Charging Behavior in Silicon–Graphite Composite Anodes". In: *Batteries* 9.2 (2023), p. 138. DOI: 10.3390/batteries9020138.

[17] Q. Huang, M. J. Loveridge, R. Genieser, M. J. Lain, and R. Bhagat. "Electrochemical evaluation and phase-related impedance studies on silicon–few layer graphene (FLG) composite electrode systems". In: *Scientific Reports* 8.1 (2018), p. 1386. DOI: 10.1038/s41598-018-19929-3.

[18] M. Wetjen, S. Solchenbach, D. Pritzl, J. Hou, V. Tileli, and H. A. Gasteiger. "Morphological Changes of Silicon Nanoparticles and the Influence of Cutoff Potentials in Silicon-Graphite Electrodes". In: *Journal of The Electrochemical Society* 165.7 (2018), A1503–A1514. DOI: 10.1149/2.1261807jes.

[19] M. Miyachi, H. Yamamoto, H. Kawai, T. Ohta, and M. Shirakata. "Analysis of SiO anodes for lithium-ion batteries". In: *Journal of the electrochemical society* 152.10 (2005), A2089. DOI: 10.1149/1.2013210.

[20] T. Chen, J. Wu, Q. Zhang, and X. Su. "Recent advancement of SiOx based anodes for lithium-ion batteries". In: *Journal of Power Sources* 363 (2017), pp. 126–144. DOI: 10.1016/j.jpowsour.2017.07.073.

[21] X. Zhu, B. Liu, J. Shao, Q. Zhang, Y. Wan, C. Zhong, and J. Lu. "Fundamental Mechanisms and Promising Strategies for the Industrial Application of SiO_x Anode". In: *Advanced Functional Materials* 33.17 (2023), p. 2213363. DOI: 10.1002/adfm.202213363.

[22] K. Liu, Y. Liu, D. Lin, A. Pei, and Y. Cui. "Materials for lithium-ion battery safety". In: *Science Advances* 4.6 (2018), eaas9820. DOI: 10.1126/sciadv.aas9820.

[23] Y. Sanusi, F. T. Radityan, F. A. F. Adnan, J. S. Rhee, and D. Ginting. "Performance Evaluation and Economic Analysis of Lithium Iron Phosphate (LFP) and Nickel Manganese Cobalt (NMC) Batteries in Electric Vehicles in Indonesia". In: *ASEAN Journal on Science and Technology for Development* 43.1 (2025). DOI: https://doi.org/10.61931/ajstd.2224-9028.1639.

[24] X.-G. Yang and C.-Y. Wang. "Understanding the trilemma of fast charging, energy density and cycle life of lithium-ion batteries". In: *Journal of Power Sources* 402 (2018), pp. 489–498. DOI: 10.1016/j.jpowsour.2018.09.069.

[25] F. M. N. U. Khan, M. G. Rasul, A. S. M. Sayem, and N. Mandal. "Maximizing energy density of lithium-ion batteries for electric vehicles: A critical review". In: *Energy Reports*. Proceedings of 2022 7th International Conference on Renewable Energy and Conservation 9 (2023), pp. 11–21. DOI: 10.1016/j.egyr.2023.08.069.

[26] S. K. Sharma, G. Sharma, A. Gaur, A. Arya, F. Sadat Mirsafi, R. Abolhassani, H.-G. Rubahn, J.-S. Yu, and Y. Kumar Mishra. "Progress in electrode and electrolyte materials: path to all-solid-state Li-ion batteries". In: *Energy Advances* 1.8 (2022), pp. 457–510. DOI: 10.1039/D2YA00043A.

[27] M. H. Hossain, M. A. Chowdhury, N. Hossain, M. A. Islam, and M. H. Mobarak. "Advances of lithium-ion batteries anode materials—A review". In: *Chemical Engineering Journal Advances* 16 (2023), p. 100569. DOI: 10.1016/j.ceja.2023.100569.

[28] J. Lu, Z. Chen, F. Pan, Y. Cui, and K. Amine. "High-Performance Anode Materials for Rechargeable Lithium-Ion Batteries". In: *Electrochemical Energy Reviews* 1.1 (2018), pp. 35–53. DOI: 10.1007/s41918-018-0001-4.

[29] M. Jiao, Y. Wang, C. Ye, C. Wang, W. Zhang, and C. Liang. "High-capacity SiOx (0≤ x≤ 2) as promising anode materials for next-generation lithium-ion batteries". In: *Journal of Alloys and Compounds* 842 (2020), p. 155774. DOI: 10.1016/j.jallcom.2020.155774.

[30] H. Cheng, J. G. Shapter, Y. Li, and G. Gao. "Recent progress of advanced anode materials of lithium-ion batteries". In: *Journal of Energy Chemistry* 57 (2021), pp. 451–468. DOI: 10.1016/j.jechem.2020.08.056.

[31] Y. Mekonnen, A. Sundararajan, and A. I. Sarwat. "A review of cathode and anode materials for lithium-ion batteries". In: *SoutheastCon 2016*. Norfolk, VA, USA: IEEE, Mar. 2016, pp. 1–6. DOI: 10.1109/SECON.2016.7506639.

[32] P. U. Nzereogu, A. D. Omah, F. I. Ezema, E. I. Iwuoha, and A. C. Nwanya. "Anode materials for lithium-ion batteries: A review". In: *Applied Surface Science Advances* 9 (2022), p. 100233. DOI: 10.1016/j.apsadv.2022.100233.

[33] X. Yang, C. Zhan, D. Xu, D. Nan, R. Lv, W. Shen, F. Kang, and Z.-H. Huang. "SiOx@ Si-graphite microspheres for high-stable anode of lithium-ion batteries". In: *Electrochimica Acta* 426 (2022), p. 140795. DOI: 10.2139/ssrn.4118143.

[34] M. Klett, J. A. Gilbert, K. Z. Pupek, S. E. Trask, and D. P. Abraham. "Layered oxide, graphite and silicon-graphite electrodes for lithium-ion cells: effect of electrolyte composition and cycling windows". In: *Journal of The Electrochemical Society* 164.1 (2016), A6095. DOI: 10.1149/2.0131701jes.

[35] M. Wetjen, D. Pritzl, R. Jung, S. Solchenbach, R. Ghadimi, and H. A. Gasteiger. "Differentiating the Degradation Phenomena in Silicon-Graphite Electrodes for Lithium-Ion Batteries". In: *Journal of The Electrochemical Society* 164.12 (2017), A2840–A2852. DOI: 10.1149/2.1921712jes.

[36] N.-H. Yang, Y.-S. Wu, J. Chou, H.-C. Wu, and N.-L. Wu. "Silicon oxide-on-graphite planar composite synthesized using a microwave-assisted coating method for use as a fast-charging lithium-ion battery anode". In: *Journal of Power Sources* 296 (2015), pp. 314–317. DOI: 10.1016/j.jpowsour.2015.07.066.

[37] W. Wu, Y. Kang, M. Wang, D. Xu, J. Wang, Y. Cao, C. Wang, and Y. Deng. "An ultrahigh-areal-capacity SiOx negative electrode for lithium ion batteries". In: *Journal of Power Sources* 464 (2020), p. 228244. DOI: 10.1016/j.jpowsour.2020.228244.

[38] Z. Hu, S. Zhang, C. Zhang, and G. Cui. "High performance germanium-based anode materials". In: *Coordination Chemistry Reviews* 326 (2016), pp. 34–85. DOI: 10.1016/j.ccr.2016.08.002.

[39] P. Li, H. Kim, S.-T. Myung, and Y.-K. Sun. "Diverting exploration of silicon anode into practical way: a review focused on silicon-graphite composite for lithium ion batteries". In: *Energy Storage Materials* 35 (2021), pp. 550–576. DOI: 10.1016/j.ensm.2020.11.028.

[40] S. Bazlen, P. Heugel, O. von Kessel, W. Commerell, and J. Tübke. "Influence of charging protocols on the charging capability and aging of lithium-ion cells with silicon-containing anodes". In: *Journal of Energy Storage* 49 (2022), p. 104044. DOI: 10.1016/j.est.2022.104044.

[41] K. Yao, J. P. Zheng, and Z. Liang. "Self-Healing Phenomenon Observed During Capacity-Control Cycling of Freestanding Si-Based Composite Paper Anodes for Li-Ion Batteries". In: *ACS Applied Materials & Interfaces* 10.8 (2018), pp. 7155–7161. DOI: 10.1021/acsami.7b19246.

[42] J. W. Wang et al. "Two-Phase Electrochemical Lithiation in Amorphous Silicon". In: *Nano Letters* 13.2 (2013), pp. 709–715. DOI: 10.1021/nl304379k.

[43] D. Rehnlund, Z. Wang, and L. Nyholm. "Lithium-Diffusion Induced Capacity Losses in Lithium-Based Batteries". In: *Advanced Materials* 34.19 (2022), p. 2108827. DOI: 10.1002/adma.202108827.

[44] S. Solchenbach et al. “Electrolyte motion induced salt inhomogeneity – a novel aging mechanism in large-format lithium-ion cells”. In: *Energy & Environmental Science* 17.19 (2024), pp. 7294–7317. DOI: 10.1039/D4EE03211J.

[45] K. Richter, T. Waldmann, N. Paul, N. Jobst, R.-G. Scurtu, M. Hofmann, R. Gilles, and M. Wohlfahrt-Mehrens. “Low-Temperature Charging and Aging Mechanisms of Si/C Composite Anodes in Li-Ion Batteries: An Operando Neutron Scattering Study”. In: *ChemSusChem* 13.3 (2020), pp. 529–538. DOI: 10.1002/cssc.201903139.

[46] X. Gao, S. Li, J. Xue, D. Hu, and J. Xu. “A Mechanistic and Quantitative Understanding of the Interactions between SiO and Graphite Particles”. In: *Advanced Energy Materials* 13.2 (2023), p. 2202584. DOI: 10.1002/aenm.202202584.

[47] S. Rodríguez-Cadavid, N. Bless, J. Poehler, J. Sabatier, P. Lanusse, and C. Farges. “BMS-oriented model for Li-ion batteries with mixed SiOx/graphite anodes”. In: *2020 5th International Conference on Smart and Sustainable Technologies (SpliTech)*. IEEE, 2020, pp. 1–6. DOI: 10.23919/splitech49282.2020.9243758.

[48] F. Reuter, A. Baasner, J. Pampel, M. Piwko, S. Dörfler, H. Althues, and S. Kaskel. “Importance of Capacity Balancing on The Electrochemical Performance of Li[Ni $_{0.8}$ Co $_{0.1}$ Mn $_{0.1}$]O $_2$ (NCM811)/Silicon Full Cells”. In: *Journal of The Electrochemical Society* 166.14 (2019), A3265–A3271. DOI: 10.1149/2.0431914jes.

[49] M. Ashuri, Q. He, and L. L. Shaw. “Silicon as a potential anode material for Li-ion batteries: where size, geometry and structure matter”. In: *Nanoscale* 8.1 (2016), pp. 74–103. DOI: 10.1039/c5nr05116a.

[50] W. Liu, J. Jiang, H. Wang, C. Deng, F. Wang, and G. Peng. “Influence of graphene oxide on electrochemical performance of Si anode material for lithium-ion batteries”. In: *Journal of energy chemistry* 25.5 (2016), pp. 817–824. DOI: 10.1016/j.jechem.2016.06.006.

[51] D. Rehnlund et al. “Lithium trapping in alloy forming electrodes and current collectors for lithium based batteries”. In: *Energy & Environmental Science* 10.6 (2017), pp. 1350–1357. DOI: 10.1039/C7EE00244K.

[52] H.-W. Yang, W. S. Kang, and S.-J. Kim. “A significant enhancement of cycling stability at fast charging rate through incorporation of Li3N into LiF-based SEI in SiO anode for Li-ion batteries”. In: *Electrochimica Acta* 412 (2022), p. 140107. DOI: 10.1016/j.electacta.2022.140107.

[53] S. Yoshida, T. Okubo, Y. Masuo, Y. Oba, D. Shibata, M. Haruta, T. Doi, and M. Inaba. “High Rate Charge and Discharge Characteristics of Graphite/SiOx Composite Electrodes”. In: *Electrochemistry* 85.7 (2017), pp. 403–408. DOI: 10.5796/electrochemistry.85.403.

[54] C. Li, X. Zhang, K. Wang, X. Sun, and Y. Ma. “A 29.3 Wh kg–1 and 6 kW kg–1 pouch-type lithium-ion capacitor based on SiOx/graphite composite anode”. In: *Journal of Power Sources* 414 (2019), pp. 293–301. DOI: 10.1016/j.jpowsour.2018.12.090.

[55] Y. Yamada, Y. Iriyama, T. Abe, and Z. Ogumi. "Kinetics of Electrochemical Insertion and Extraction of Lithium Ion at SiO". In: *Journal of The Electrochemical Society* 157.1 (2010), A26. DOI: 10.1149/1.3247598.

[56] M. Su, Z. Wang, H. Guo, X. Li, S. Huang, W. Xiao, and L. Gan. "Enhancement of the Cyclability of a Si/Graphite@Graphene composite as anode for Lithium-ion batteries". In: *Electrochimica Acta* 116 (2014), pp. 230–236. DOI: 10.1016/j.electacta.2013.10.195.

[57] J. Guo, A. Sun, X. Chen, C. Wang, and A. Manivannan. "Cyclability study of silicon–carbon composite anodes for lithium-ion batteries using electrochemical impedance spectroscopy". In: *Electrochimica Acta* 56.11 (2011), pp. 3981–3987. DOI: 10.1016/j.electacta.2011.02.014.

[58] J. Sturm, A. Rheinfeld, I. Zilberman, F. B. Spingler, S. Kosch, F. Frie, and A. Jossen. "Modeling and simulation of inhomogeneities in a 18650 nickel-rich, silicon-graphite lithium-ion cell during fast charging". In: *Journal of Power Sources* 412 (2019), pp. 204–223. DOI: 10.1016/j.jpowsour.2018.11.043.

[59] E. Radvanyi, K. Van Havenbergh, W. Porcher, S. Jouanneau, J.-S. Bridel, S. Put, and S. Franger. "Study and modeling of the Solid Electrolyte Interphase behavior on nano-silicon anodes by Electrochemical Impedance Spectroscopy". In: *Electrochimica Acta* 137 (2014), pp. 751–757. DOI: 10.1016/j.electacta.2014.06.069.

[60] S. J. An, J. Li, C. Daniel, D. Mohanty, S. Nagpure, and D. L. Wood. "The state of understanding of the lithium-ion-battery graphite solid electrolyte interphase (SEI) and its relationship to formation cycling". In: *Carbon* 105 (2016), pp. 52–76. DOI: 10.1016/j.carbon.2016.04.008.

[61] J. B. Goodenough and Y. Kim. "Challenges for Rechargeable Li Batteries". In: *Chemistry of Materials* 22.3 (2010), pp. 587–603. DOI: 10.1021/cm901452z.

[62] J. C. Stallard, L. Wheatcroft, S. G. Booth, R. Boston, S. A. Corr, M. F. L. D. Volder, B. J. Inkson, and N. A. Fleck. "Mechanical properties of cathode materials for lithium-ion batteries". In: *Joule* 6.5 (2022), pp. 984–1007. DOI: 10.1016/j.joule.2022.04.001.

[63] N. Mohamed and N. K. Allam. "Recent advances in the design of cathode materials for Li-ion batteries". In: *RSC Advances* 10.37 (2020), pp. 21662–21685. DOI: 10.1039/D0RA03314F.

[64] J. Liu, J. Wang, Y. Ni, K. Zhang, F. Cheng, and J. Chen. "Recent breakthroughs and perspectives of high-energy layered oxide cathode materials for lithium ion batteries". In: *Materials Today* 43 (2021), pp. 132–165. DOI: 10.1016/j.mattod.2020.10.028.

[65] R. Schmuch, R. Wagner, G. Hörpel, T. Placke, and M. Winter. "Performance and cost of materials for lithium-based rechargeable automotive batteries". In: *Nature Energy* 3.4 (2018), pp. 267–278. DOI: 10.1038/s41560-018-0107-2.

[66] D. Andre, S.-J. Kim, P. Lamp, S. F. Lux, F. Maglia, O. Paschos, and B. Stiaszny. "Future generations of cathode materials: an automotive industry perspective". In: *Journal of Materials Chemistry A* 3.13 (2015), pp. 6709–6732. DOI: 10.1039/C5TA00361J.

[67] H.-J. Noh, S. Youn, C. S. Yoon, and Y.-K. Sun. "Comparison of the structural and electrochemical properties of layered Li[NixCoyMnz]O2 (x = 1/3, 0.5, 0.6, 0.7, 0.8 and 0.85) cathode material for lithium-ion batteries". In: *Journal of Power Sources* 233 (2013), pp. 121–130. DOI: 10.1016/j.jpowsour.2013.01.063.

[68] X. Zhang, Z. Cui, E. Jo, and A. Manthiram. "Inhibition of transition-metal dissolution with advanced electrolytes in batteries with silicon-graphite anodes and high-nickel cathodes". In: *Energy Storage Materials* 56 (2023), pp. 562–571. DOI: 10.1016/j.ensm.2023.01.048.

[69] E. Evenstein, S. Taragin, A. Saha, M. Noked, and Rosy. "Investigating the Temperature Dependency of Trimethyl Aluminum Assisted Atomic Surface Reduction of Li and Mn-Rich NCM". In: *Journal of The Electrochemical Society* 171.7 (2024), p. 070531. DOI: 10.1149/1945-7111/ad6293.

[70] D. Schreiner et al. "Comparative Evaluation of LMR-NCM and NCA Cathode Active Materials in Multilayer Lithium-Ion Pouch Cells: Part I. Production, Electrode Characterization, and Formation". In: *Journal of The Electrochemical Society* 168.3 (2021), p. 030507. DOI: 10.1149/1945-7111/abe50c.

[71] M. A. Roscher, J. Vetter, and D. U. Sauer. "Characterisation of charge and discharge behaviour of lithium ion batteries with olivine based cathode active material". In: *Journal of Power Sources* 191.2 (2009), pp. 582–590. DOI: 10.1016/j.jpowsour.2009.02.024.

[72] C. Lin, Q. Yu, R. Xiong, and L. Y. Wang. "A study on the impact of open circuit voltage tests on state of charge estimation for lithium-ion batteries". In: *Applied Energy* 205 (2017), pp. 892–902. DOI: 10.1016/j.apenergy.2017.08.124.

[73] R. Korthauer. *Handbuch Lithium-Ionen-Batterien*. Springer, 2013.

[74] J. Zhang, X. Yao, R. K. Misra, Q. Cai, and Y. Zhao. "Progress in electrolytes for beyond-lithium-ion batteries". In: *Journal of Materials Science & Technology* 44 (2020), pp. 237–257. DOI: 10.1016/j.jmst.2020.01.017.

[75] K. Xu. "Nonaqueous Liquid Electrolytes for Lithium-Based Rechargeable Batteries". In: *Chemical Reviews* 104.10 (2004), pp. 4303–4418. DOI: 10.1021/cr030203g.

[76] T. Kim, S. Park, and S. M. Oh. "Solid-state NMR and electrochemical dilatometry study on Li+ uptake/extraction mechanism in SiO electrode". In: *Journal of The Electrochemical Society* 154.12 (2007), A1112. DOI: 10.1149/1.2790282.

[77] C. Bubulinca, N. E. Kazantseva, V. Pechancova, N. Joseph, H. Fei, M. Venher, A. Ivanichenko, and P. Saha. "Development of All-Solid-State Li-Ion Batteries: From Key Technical Areas to Commercial Use". In: *Batteries* 9.3 (2023), p. 157. DOI: 10.3390/batteries9030157.

[78] N. Boaretto, I. Garbayo, S. Valiyaveettil-SobhanRaj, A. Quintela, C. Li, M. Casas-Cabanas, and F. Aguesse. "Lithium solid-state batteries: State-of-the-art and challenges for materials, interfaces and processing". In: *Journal of Power Sources* 502 (2021), p. 229919. DOI: 10.1016/j.jpowsour.2021.229919.

[79] C. F. J. Francis, I. L. Kyratzis, and A. S. Best. "Lithium-Ion Battery Separators for Ionic-Liquid Electrolytes: A Review". In: *Advanced Materials* 32.18 (2020), p. 1904205. DOI: 10.1002/adma.201904205.

[80] X. Huang. "Separator technologies for lithium-ion batteries". In: *Journal of Solid State Electrochemistry* 15.4 (2011), pp. 649–662. DOI: 10.1007/s10008-010-1264-9.

[81] H. Lee, M. Yanilmaz, O. Toprakci, K. Fu, and X. Zhang. "A review of recent developments in membrane separators for rechargeable lithium-ion batteries". In: *Energy & Environmental Science* 7.12 (2014), pp. 3857–3886. DOI: 10.1039/C4EE01432D.

[82] J. Chen, T. Kang, Y. Cui, J. Xue, H. Xu, and J. Nan. "Nonflammable and thermally stable glass fiber/polyacrylate (GFP) separator for lithium-ion batteries with enhanced safety and lifespan". In: *Journal of Power Sources* 496 (2021), p. 229862. DOI: 10.1016/j.jpowsour.2021.229862.

[83] P. Zhu, D. Gastol, J. Marshall, R. Sommerville, V. Goodship, and E. Kendrick. "A review of current collectors for lithium-ion batteries". In: *Journal of Power Sources* 485 (2021), p. 229321. DOI: 10.1016/j.jpowsour.2020.229321.

[84] S.-T. Myung, Y. Hitoshi, and Y.-K. Sun. "Electrochemical behavior and passivation of current collectors in lithium-ion batteries". In: *Journal of Materials Chemistry* 21.27 (2011), pp. 9891–9911. DOI: 10.1039/C0JM04353B.

[85] G. Zubi, R. Dufo-López, M. Carvalho, and G. Pasaoglu. "The lithium-ion battery: State of the art and future perspectives". In: *Renewable and sustainable energy reviews* 89 (2018), pp. 292–308. DOI: 10.1016/j.rser.2018.03.002.

[86] S. Baazouzi, N. Feistel, J. Wanner, I. Landwehr, A. Fill, and K. P. Birke. "Design, Properties, and Manufacturing of Cylindrical Li-Ion Battery Cells—A Generic Overview". In: *Batteries* 9.6 (2023), p. 309. DOI: 10.3390/batteries9060309.

[87] B. Xu, J. Lee, D. Kwon, L. Kong, and M. Pecht. "Mitigation strategies for Li-ion battery thermal runaway: A review". In: *Renewable and Sustainable Energy Reviews* 150 (2021), p. 111437. DOI: 10.1016/j.rser.2021.111437.

[88] P. Nur Halimah, S. Rahardian, and B. A. Budiman. "Battery Cells for Electric Vehicles". In: *International Journal of Sustainable Transportation Technology* 2.2 (2019), pp. 54–57. DOI: 10.31427/IJSTT.2019.2.2.3.

[89] T. Schabenberger, S. Kücher, A. Aufschläger, and A. Jossen. "Impact of applied and preceding pressure on performance and reversible swelling of lithium-ion pouch cells with varying microporous separators". In: *Journal of Energy Storage* 102 (2024), p. 113910. DOI: 10.1016/j.est.2024.113910.

[90] A. Tomaszewska et al. "Lithium-ion battery fast charging: A review". In: *eTransportation* 1 (2019), p. 100011. DOI: 10.1016/j.etran.2019.100011.

[91] V. Müller, R. Bernhard, J. Wegener, J. Pfeiffer, S. Rössler, R.-G. Scurtu, M. Memm, M. A. Danzer, and M. Wohlfahrt-Mehrens. "Evaluation of Scalable Porous Si-Rich Si/C Composites with Low Volume Expansion in Coin Cells to Prismatic Cell Formats". In: *Energy Technology* 8.7 (2020), p. 2000217. DOI: 10.1002/ente.202000217.

[92] E. Petursdottir, M. Kohlhuber, and H. Ehrenberg. "Influence from Mechanical Stress on State of Health of Large Prismatic Lithium-Ion-Cells under Various Temperatures". In: *Journal of The Electrochemical Society* 171.7 (2024), p. 070510. DOI: 10.1149/1945-7111/ad5d1c.

[93] C. Essl, A. W. Golubkov, and A. Fuchs. "Comparing Different Thermal Runaway Triggers for Two Automotive Lithium-Ion Battery Cell Types". In: *Journal of The Electrochemical Society* 167.13 (2020), p. 130542. DOI: 10.1149/1945-7111/abbe5a.

[94] J. Lu, Y. Liu, P. Yao, Z. Ding, Q. Tang, J. Wu, Z. Ye, K. Huang, and X. Liu. "Hybridizing poly(vinylidene fluoride-co-hexafluoropropylene) with Li6.5La3Zr1.5Ta0.5O12 as a lithium-ion electrolyte for solid state lithium metal batteries". In: *Chemical Engineering Journal* 367 (2019), pp. 230–238. DOI: 10.1016/j.cej.2019.02.148.

[95] M. Rashid and A. Gupta. "Experimental assessment and model development of cycling behavior in Li-ion coin cells". In: *Electrochimica Acta* 231 (2017), pp. 171–184. DOI: 10.1016/j.electacta.2017.02.040.

[96] D. N. T. How, M. A. Hannan, M. S. H. Hossain Lipu, and P. J. Ker. "State of Charge Estimation for Lithium-Ion Batteries Using Model-Based and Data-Driven Methods: A Review". In: *IEEE Access* 7 (2019), pp. 136116–136136. DOI: 10.1109/ACCESS.2019.2942213.

[97] Z. Liu, X. Dang, and B. Jing. "A Novel Open Circuit Voltage Based State of Charge Estimation for Lithium-Ion Battery by Multi-Innovation Kalman Filter". In: *IEEE Access* 7 (2019), pp. 49432–49447. DOI: 10.1109/ACCESS.2019.2910882.

[98] C. Weng, J. Sun, and H. Peng. "A unified open-circuit-voltage model of lithium-ion batteries for state-of-charge estimation and state-of-health monitoring". In: *Journal of Power Sources* 258 (2014), pp. 228–237. DOI: 10.1016/j.jpowsour.2014.02.026.

[99] M. M. Kabir and D. E. Demirocak. "Degradation mechanisms in Li-ion batteries: a state-of-the-art review". In: *International Journal of Energy Research* 41.14 (2017), pp. 1963–1986. DOI: 10.1002/er.3762.

[100] J. Gomez, R. Nelson, E. E. Kalu, M. H. Weatherspoon, and J. P. Zheng. "Equivalent circuit model parameters of a high-power Li-ion battery: Thermal and state of charge effects". In: *Journal of Power Sources* 196.10 (2011), pp. 4826–4831. DOI: 10.1016/j.jpowsour.2010.12.107.

[101] E. J. F. Dickinson and A. J. Wain. "The Butler-Volmer equation in electrochemical theory: Origins, value, and practical application". In: *Journal of Electroanalytical Chemistry*. Dr. Richard Compton 65th birthday Special issue 872 (2020), p. 114145. DOI: 10.1016/j.jelechem.2020.114145.

[102] M. Alkhedher, A. B. Al Tahhan, J. Yousaf, M. Ghazal, R. Shahbazian-Yassar, and M. Ramadan. "Electrochemical and thermal modeling of lithium-ion batteries: A review of coupled approaches for improved thermal performance and safety lithium-ion batteries". In: *Journal of Energy Storage* 86 (2024), p. 111172. DOI: 10.1016/j.est.2024.111172.

[103] C. Heubner, M. Schneider, and A. Michaelis. "Investigation of charge transfer kinetics of Li-Intercalation in LiFePO4". In: *Journal of Power Sources* 288 (2015), pp. 115–120. DOI: 10.1016/j.jpowsour.2015.04.103.

[104] M. Doyle, T. F. Fuller, and J. Newman. "Modeling of Galvanostatic Charge and Discharge of the Lithium/Polymer/Insertion Cell". In: *Journal of The Electrochemical Society* 140.6 (1993), pp. 1526–1533. DOI: 10.1149/1.2221597.

[105] J. Newman and W. Tiedemann. "Porous-electrode theory with battery applications". In: *AIChE Journal* 21.1 (1975), pp. 25–41. DOI: 10.1002/aic.690210103.

[106] S. V. Erhard, P. J. Osswald, J. Wilhelm, A. Rheinfeld, S. Kosch, and A. Jossen. "Simulation and Measurement of Local Potentials of Modified Commercial Cylindrical Cells". In: *Journal of The Electrochemical Society* 162.14 (2015), A2707. DOI: 10.1149/2.0431514jes.

[107] X. He, B. Sun, W. Zhang, X. Fan, X. Su, and H. Ruan. "Multi-time scale variable-order equivalent circuit model for virtual battery considering initial polarization condition of lithium-ion battery". In: *Energy* 244 (2022), p. 123084. DOI: 10.1016/j.energy.2021.123084.

[108] C. Plank, T. Rüther, L. Jahn, M. Schamel, J. P. Schmidt, F. Ciucci, and M. A. Danzer. "A review on the distribution of relaxation times analysis: A powerful tool for process identification of electrochemical systems". In: *Journal of Power Sources* 594 (2024), p. 233845. DOI: 10.1016/j.jpowsour.2023.233845.

[109] C. R. Birkl, M. R. Roberts, E. McTurk, P. G. Bruce, and D. A. Howey. "Degradation diagnostics for lithium ion cells". In: *Journal of Power Sources* 341 (2017), pp. 373–386. DOI: 10.1016/j.jpowsour.2016.12.011.

[110] X. Han, L. Lu, Y. Zheng, X. Feng, Z. Li, J. Li, and M. Ouyang. "A review on the key issues of the lithium ion battery degradation among the whole life cycle". In: *eTransportation* 1 (2019), p. 100005. DOI: 10.1016/j.etran.2019.100005.

[111] D. Anseán, G. Baure, M. González, I. Cameán, A. García, and M. Dubarry. "Mechanistic investigation of silicon-graphite/LiNi0.8Mn0.1Co0.1O2 commercial cells for non-intrusive diagnosis and prognosis". In: *Journal of Power Sources* 459 (2020), p. 227882. DOI: 10.1016/j.jpowsour.2020.227882.

[112] F. Katzer and M. A. Danzer. "Analysis and detection of lithium deposition after fast charging of lithium-ion batteries by investigating the impedance relaxation". In: *Journal of Power Sources* 503 (2021), p. 230009. DOI: 10.1016/j.jpowsour.2021.230009.

[113] A. Adam, J. Wandt, E. Knobbe, G. Bauer, and A. Kwade. "Fast-Charging of Automotive Lithium-Ion Cells: In-Situ Lithium-Plating Detection and Comparison of Different Cell Designs". In: *Journal of The Electrochemical Society* 167.13 (2020), p. 130503. DOI: 10.1149/1945-7111/abb564.

[114] T. Waldmann, B.-I. Hogg, and M. Wohlfahrt-Mehrens. "Li plating as unwanted side reaction in commercial Li-ion cells – A review". In: *Journal of Power Sources* 384 (2018), pp. 107–124. DOI: 10.1016/j.jpowsour.2018.02.063.

[115] S. Schindler, M. Bauer, M. Petzl, and M. A. Danzer. "Voltage relaxation and impedance spectroscopy as in-operando methods for the detection of lithium plating on graphitic anodes in commercial lithium-ion cells". In: *Journal of Power Sources* 304 (2016), pp. 170–180. DOI: 10.1016/j.jpowsour.2015.11.044.

[116] U. R. Koleti, T. Q. Dinh, and J. Marco. "A new on-line method for lithium plating detection in lithium-ion batteries". In: *Journal of Power Sources* 451 (2020), p. 227798. DOI: 10.1016/j.jpowsour.2020.227798.

[117] D. Allart, M. Montaru, and H. Gualous. "Model of lithium intercalation into graphite by potentiometric analysis with equilibrium and entropy change curves of graphite electrode". In: *Journal of The Electrochemical Society* 165.2 (2018), A380. DOI: 10.1149/2.1251802jes.

[118] J. Asenbauer, T. Eisenmann, M. Kuenzel, A. Kazzazi, Z. Chen, and D. Bresser. "The success story of graphite as a lithium-ion anode material – fundamentals, remaining challenges, and recent developments including silicon (oxide) composites". In: *Sustainable Energy & Fuels* 4.11 (2020), pp. 5387–5416. DOI: 10.1039/D0SE00175A.

[119] M. Winter, J. O. Besenhard, M. E. Spahr, and P. Novák. "Insertion Electrode Materials for Rechargeable Lithium Batteries". In: *Advanced Materials* 10.10 (1998), pp. 725–763. DOI: 10.1002/(SICI)1521-4095(199807)10:10<725::AID-ADMA725>3.0.CO;2-Z.

[120] J. R. Dahn. "Phase diagram of Li x C 6". In: *Physical Review B* 44.17 (1991), p. 9170. DOI: 10.1103/PhysRevB.44.9170.

[121] F. Grimsmann, T. Gerbert, F. Brauchle, A. Gruhle, J. Parisi, and M. Knipper. "Hysteresis and current dependence of the graphite anode color in a lithium-ion cell and analysis of lithium plating at the cell edge". In: *Journal of Energy Storage* 15 (2018), pp. 17–22. DOI: 10.1016/j.est.2017.10.015.

[122] U. Hofmann and W. Rüdorff. "The formation of salts from graphite by strong acids". In: *Transactions of the Faraday Society* 34.0 (1938), pp. 1017–1021. DOI: 10.1039/TF9383401017.

[123] N. Daumas and A. Herold. "Relations between phase concept and reaction mechanics in graphite insertion compounds". In: *Comptes Rendus Hebdomadaires Des Seances De L Academie Des Sciences Serie C* 268.5 (1969), p. 373.

[124] D. P. Finegan et al. "Spatially Resolving Lithiation in Silicon–Graphite Composite Electrodes via in Situ High-Energy X-ray Diffraction Computed Tomography". In: *Nano Letters* 19.6 (2019), pp. 3811–3820. DOI: 10.1021/acs.nanolett.9b00955.

[125] J. Schmitt, M. Schindler, and A. Jossen. "Change in the half-cell open-circuit potential curves of silicon–graphite and nickel-rich lithium nickel manganese cobalt oxide during cycle aging". In: *Journal of Power Sources* 506 (2021), p. 230240. DOI: 10.1016/j.jpowsour.2021.230240.

[126] J. Knorr, A. Gomez-Martin, H.-C. Hsiao, A. Adam, B. Rödl, and M. A. Danzer. "Effect of different charge rates on the active material lithiation of Gr/SiOx blend anodes in lithium-ion cells". In: *Journal of Energy Storage* 86 (2024), p. 111151. DOI: 10.1016/j.est.2024.111151.

[127] V. J. Ovejas and A. Cuadras. "Effects of cycling on lithium-ion battery hysteresis and overvoltage". In: *Scientific Reports* 9.1 (2019), p. 14875. DOI: 10.1038/s41598-019-51474-5.

[128] C. P. Graells, M. S. Trimboli, and G. L. Plett. "Differential hysteresis models for a silicon-anode Li-ion battery cell". In: *2020 IEEE Transportation Electrification Conference & Expo (ITEC)*. Chicago, IL, USA: IEEE, June 2020, pp. 175–180. DOI: 10.1109/ITEC48692.2020.9161591.

[129] V. A. Sethuraman, V. Srinivasan, and J. Newman. "Analysis of Electrochemical Lithiation and Delithiation Kinetics in Silicon". In: *Journal of The Electrochemical Society* 160.2 (2012), A394. DOI: 10.1149/2.008303jes.

[130] L. Köbbing, A. Latz, and B. Horstmann. "Voltage Hysteresis of Silicon Nanoparticles: Chemo-Mechanical Particle-SEI Model". In: *Advanced Functional Materials* 34.7 (2024), p. 2308818. DOI: 10.1002/adfm.202308818.

[131] D. R. Baker, M. W. Verbrugge, and X. Xiao. "An approach to characterize and clarify hysteresis phenomena of lithium-silicon electrodes". In: *Journal of Applied Physics* 122.16 (2017), p. 165102. DOI: 10.1063/1.4995277.

[132] B. Lu, Y. Song, Q. Zhang, J. Pan, Y.-T. Cheng, and J. Zhang. "Voltage hysteresis of lithium ion batteries caused by mechanical stress". In: *Physical Chemistry Chemical Physics* 18.6 (2016), pp. 4721–4727. DOI: 10.1039/C5CP06179B.

[133] K. Ogata, E. Salager, C. Kerr, A. Fraser, C. Ducati, A. Morris, S. Hofmann, and C. Grey. "Revealing lithium–silicide phase transformations in nano-structured silicon-based lithium ion batteries via in situ NMR spectroscopy". In: *Nature Communications* 5.1 (2014), p. 3217. DOI: 10.1038/ncomms4217.

[134] K. Ogata et al. "Evolving affinity between Coulombic reversibility and hysteretic phase transformations in nano-structured silicon-based lithium-ion batteries". In: *Nature Communications* 9.1 (2018), p. 479. DOI: 10.1038/s41467-018-02824-w.

[135] E. Sivonxay, M. Aykol, and K. A. Persson. "The lithiation process and Li diffusion in amorphous SiO 2 and Si from first-principles". In: *Electrochimica Acta* 331 (2020), p. 135344. DOI: 10.1016/j.electacta.2019.135344.

[136] Y. Li, X. Zheng, Z. Cao, Y. Wang, Y. Wang, L. Lv, W. Huang, Y. Huang, and H. Zheng. "Unveiling the mechanisms into Li-trapping induced (ir) reversible capacity loss for silicon anode". In: *Energy Storage Materials* 55 (2023), pp. 660–668. DOI: 10.1016/j.ensm.2022.12.032.

[137] M. N. Obrovac and L. Christensen. "Structural Changes in Silicon Anodes during Lithium Insertion/Extraction". In: *Electrochemical and Solid-State Letters* 7.5 (2004), A93. DOI: 10.1149/1.1652421.

[138] E. Moyassari, T. Roth, S. Kücher, C.-C. Chang, S.-C. Hou, F. B. Spingler, and A. Jossen. "The role of silicon in silicon-graphite composite electrodes regarding specific capacity, cycle stability, and expansion". In: *Journal of The Electrochemical Society* 169.1 (2022), p. 010504. DOI: 10.1149/ma2022-012421mtgabs.

[139] S. Wen, B. Lu, Y. Zhao, Y. Song, and J. Zhang. "Feigned death induced by partial delithiation in silicon composite electrodes". In: *Journal of Power Sources* 495 (2021), p. 229763. DOI: 10.1016/j.jpowsour.2021.229763.

[140] K. Kitada, O. Pecher, P. C. M. M. Magusin, M. F. Groh, R. S. Weatherup, and C. P. Grey. "Unraveling the Reaction Mechanisms of SiO Anodes for Li-Ion Batteries by Combining *in Situ* ^{7} Li and *ex Situ* ^{7} Li/ ^{29} Si Solid-State NMR Spectroscopy". In: *Journal of the American Chemical Society* 141.17 (2019), pp. 7014–7027. DOI: 10.1021/jacs.9b01589.

[141] J. Li and J. R. Dahn. "An in situ X-ray diffraction study of the reaction of Li with crystalline Si". In: *Journal of The Electrochemical Society* 154.3 (2007), A156. DOI: 10.1149/1.2409862.

[142] J. Saint, M. Morcrette, D. Larcher, L. Laffont, S. Beattie, J.-P. Pérès, D. Talaga, M. Couzi, and J.-M. Tarascon. "Towards a Fundamental Understanding of the Improved Electrochemical Performance of Silicon–Carbon Composites". In: *Advanced Functional Materials* 17.11 (2007), pp. 1765–1774. DOI: 10.1002/adfm.200600937.

[143] S. C. Jung, H.-J. Kim, J.-H. Kim, and Y.-K. Han. "Atomic-Level Understanding toward a High-Capacity and High-Power Silicon Oxide (SiO) Material". In: *The Journal of Physical Chemistry C* 120.2 (2016), pp. 886–892. DOI: 10.1021/acs.jpcc.5b10589.

[144] K. Yasuda, Y. Kashitani, S. Kizaki, K. Takeshita, T. Fujita, and S. Shimosaki. "Thermodynamic analysis and effect of crystallinity for silicon monoxide negative electrode for lithium ion batteries". In: *Journal of Power Sources* 329 (2016), pp. 462–472. DOI: 10.1016/j.jpowsour.2016.08.110.

[145] H. Yamamura, K. Nobuhara, S. Nakanishi, H. Iba, and S. Okada. "Investigation of the irreversible reaction mechanism and the reactive trigger on SiO anode material for lithium-ion battery". In: *Journal of the Ceramic Society of Japan* 119.1395 (2011), pp. 855–860. DOI: 10.2109/jcersj2.119.855.

[146] R. Barnard, G. T. Crickmore, J. A. Lee, and F. L. Tye. "The cause of residual capacity in nickel oxyhydroxide electrodes". In: *Journal of Applied Electrochemistry* 10.1 (1980), pp. 61–70. DOI: 10.1007/BF00937339.

[147] G. Davolio and E. Soragni. "The 'memory effect' on nickel oxide electrodes: electrochemical and mechanical aspects". In: *Journal of Applied Electrochemistry* 28.12 (1998), pp. 1313–1319. DOI: 10.1023/A:1003452327919.

[148] R. A. Huggins. "Mechanism of the memory effect in "Nickel" electrodes". In: *Solid State Ionics*. Solid State Ionics 15: Proceedings of the 15th International Conference on Solid State Ionics, Part II 177.26 (2006), pp. 2643–2646. DOI: 10.1016/j.ssi.2006.03.005.

[149] Y. Sato, S. Takeuchi, and K. Kobayakawa. "Cause of the memory effect observed in alkaline secondary batteries using nickel electrode". In: *Journal of Power Sources* 93.1 (2001), pp. 20–24. DOI: 10.1016/S0378-7753(00)00506-1.

[150] J. Knorr, H.-C. Hsiao, A. Adam, B. Rödl, T. Waldmann, M. Hölzle, and M. A. Danzer. "Lithium trapping induced memory effect of Gr/SiOx blend anodes in lithium-ion batteries subjected to repeated partial cycling". In: *Journal of Power Sources* 629 (2025), p. 235936. DOI: 10.1016/j.jpowsour.2024.235936.

[151] C. Heubner, T. Liebmann, O. Lohrberg, S. Cangaz, S. Maletti, and A. Michaelis. "Understanding Component-Specific Contributions and Internal Dynamics in Silicon/-Graphite Blended Electrodes for High-Energy Lithium-Ion Batteries". In: *Batteries & Supercaps* 5.1 (2022), e202100182. DOI: 10.1002/batt.202100182.

[152] J. Knorr, J. Li, M. Schamel, T. Kufner, A. Adam, and M. A. Danzer. "Active Material Lithiation in Gr/SiOx Blend Anodes at Increased C-Rates". In: *Journal of The Electrochemical Society* 171.8 (2024), p. 080512. DOI: 10.1149/1945-7111/ad68a9.

[153] J. Knorr, T. Kufner, A. Adam, and M. A. Danzer. "Experimental Analysis of the Current Distribution between Graphite and SiOx in Blend Electrodes for Lithium-Ion Cells". In: *ECS Meeting Abstracts* MA2023-02.2 (2023), p. 303. DOI: 10.1149/MA2023-022303mtgabs.

[154] J. Schmitt, I. Horstkötter, and B. Bäker. "A novel approach for modelling voltage hysteresis in lithium-ion batteries demonstrated for silicon graphite anodes: Comparative evaluation against established Preisach and Plett model". In: *Journal of Power Sources Advances* 26 (2024), p. 100139. DOI: 10.1016/j.powera.2024.100139.

[155] Feng Xuyun and Sun Zechang. “A battery model including hysteresis for State-of-Charge estimation in Ni-MH battery”. In: *2008 IEEE Vehicle Power and Propulsion Conference*. Harbin, Hei Longjiang, China: IEEE, Sept. 2008, pp. 1–5. DOI: 10.1109/VPPC.2008.4677449.

[156] Y. Xing, W. He, M. Pecht, and K. L. Tsui. “State of charge estimation of lithium-ion batteries using the open-circuit voltage at various ambient temperatures”. In: *Applied Energy* 113 (2014), pp. 106–115. DOI: 10.1016/j.apenergy.2013.07.008.

List of Figures

List of Tables

Appendix

A Additional results

The following figure (Fig. A.1) presents the SoCs variation of the hysteresis transition after different C-rates to strengthen the statement for the selection of 25 % as the optimal SoCs for this experiment.

The following figures present the temperature variation of the hysteresis transition after different C-rates for the Molicel P45A (Fig. A.2) and the SDI 30Q (Fig. A.3). The results are discussed in Section 3.2 and the figures are similar to Fig. 3.5 for the Molicel M35A.

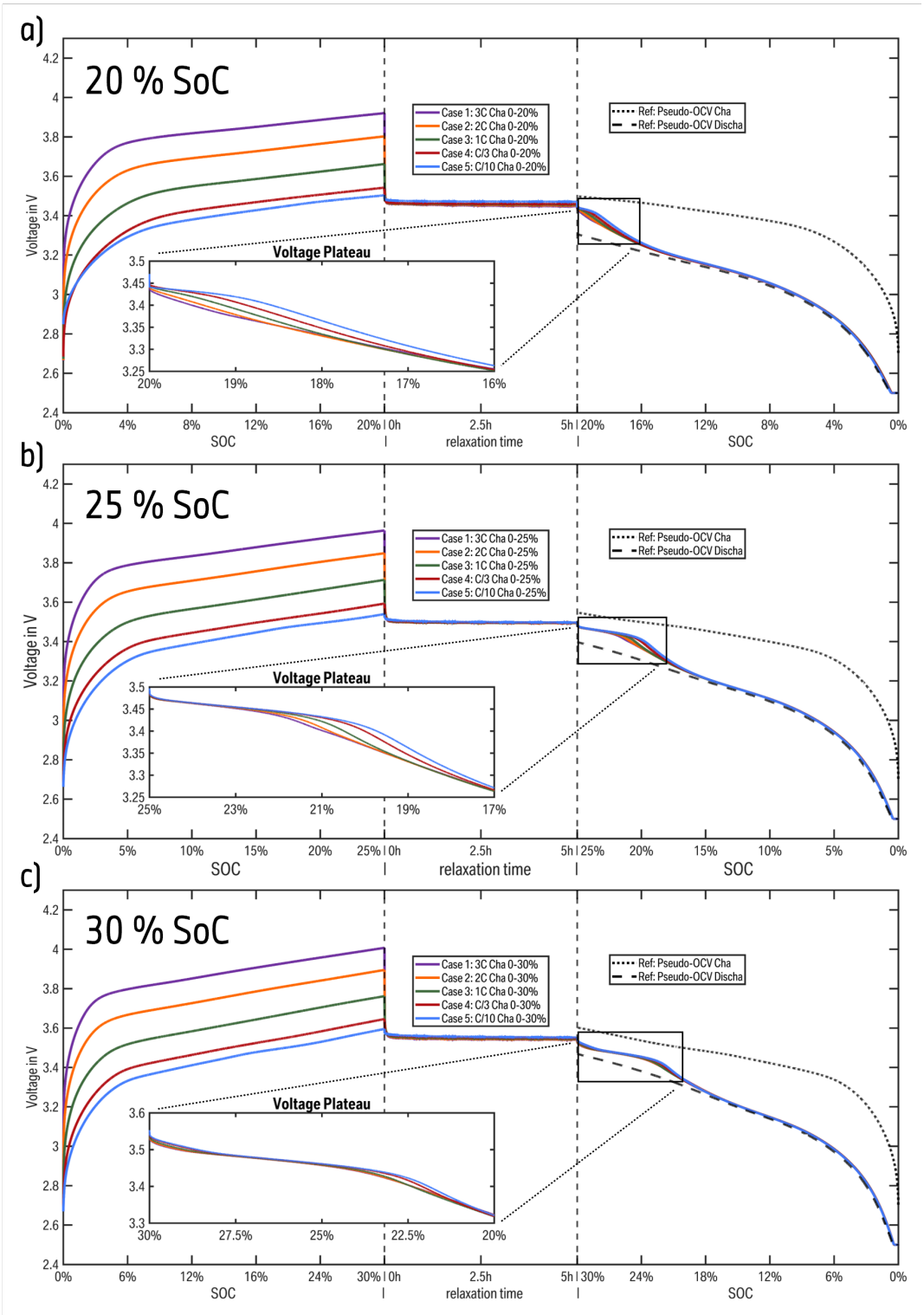

Figure A.1: Comparison between varying SoCs of the hysteresis transition after charging with different currents to the specific SoC. The compared SoCs are in the range of the first graphite plateau at a) 20 %, b) 25 %, and c) 30 %.

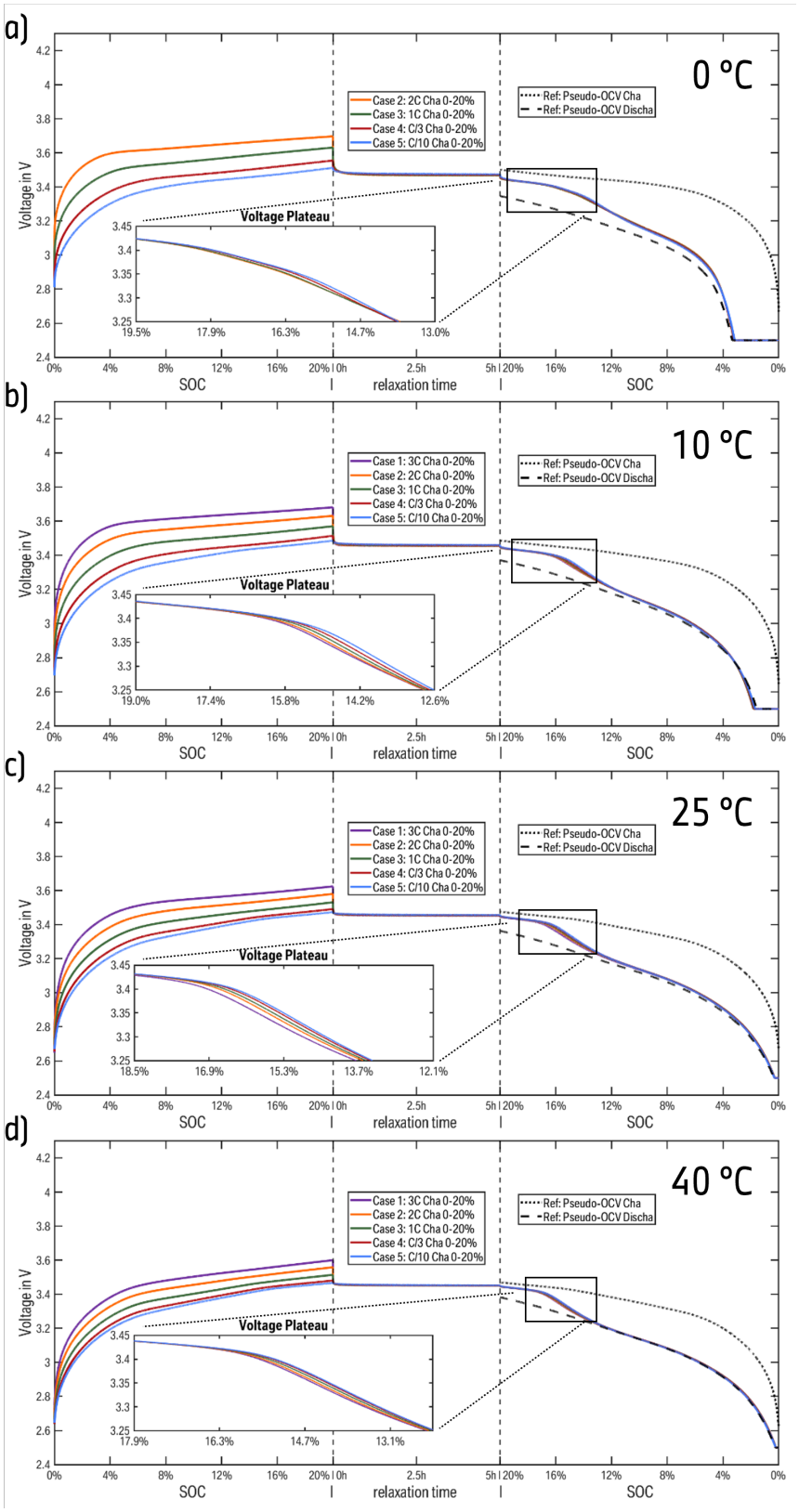

Figure A.2: Comparison between varying ambient temperatures of the hysteresis transition after charging with different currents to 20 % SoC for the MoliCel P45B. The compared temperatures include a) 0 °C, b) 10 °C, c) 25 °C, and d) 40 °C.

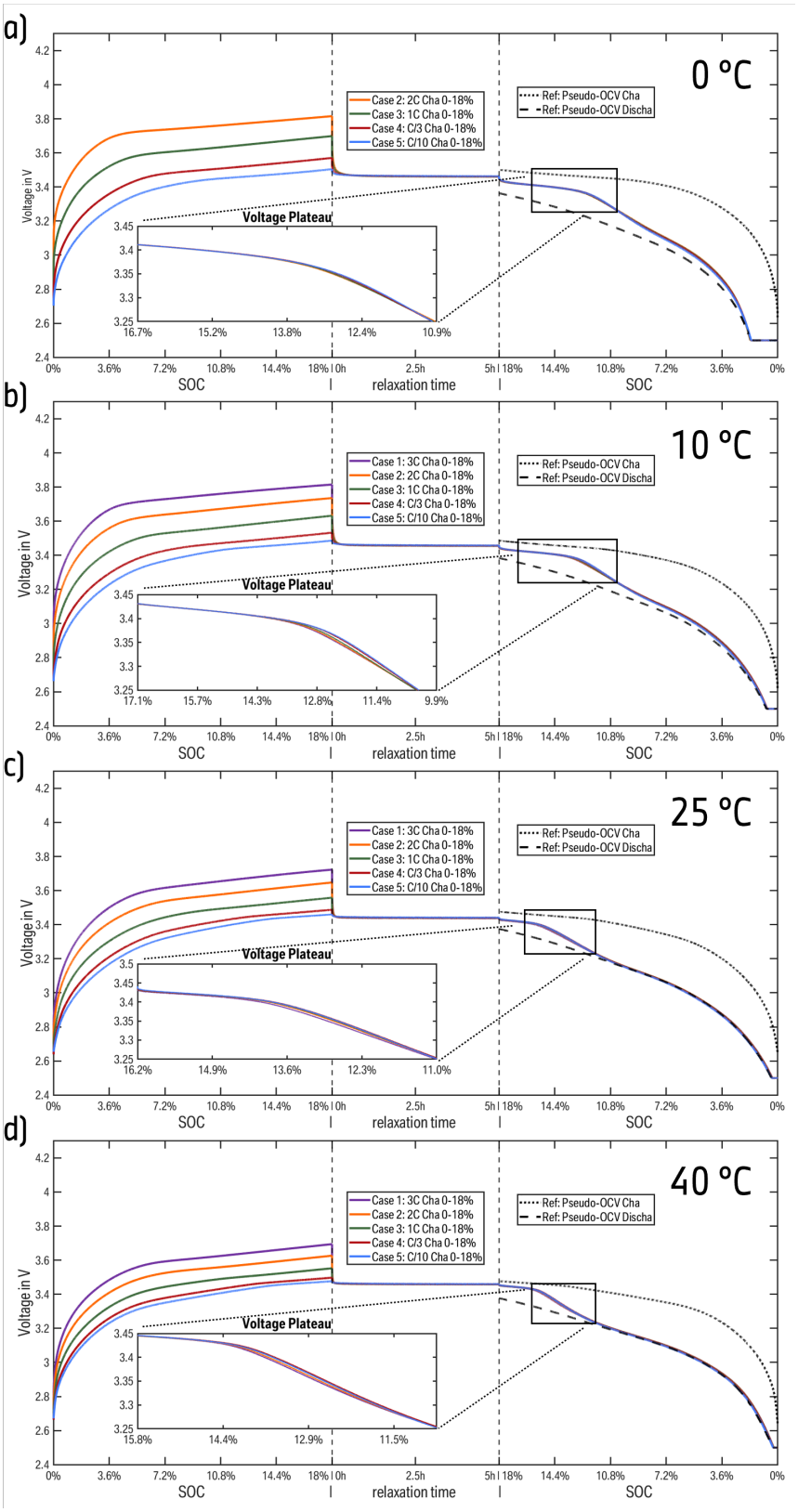

Figure A.3: Comparison between varying ambient temperatures of the hysteresis transition after charging with different currents to 18 % SoC for the SDI 30Q. The compared temperatures include a) 0 °C, b) 10 °C, c) 25 °C, and d) 40 °C.